LITHIUM AND SODIUM SOLID ELECTROLYTES FOR NEXT-GENERATION BATTERIES: BRIDGING MECHANISTIC UNDERSTANDING AND THEIR PERFORMANCE

A Dissertation
Presented to
The Academic Faculty

by

Zachary D. Hood

In Partial Fulfillment
of the Requirements for the Degree
of Doctor of Philosophy in the
School of Chemistry and Biochemistry

Georgia Institute of Technology
August 2018

LITHIUM AND SODIUM SOLID ELECTROLYTES FOR NEXT-GENERATION BATTERIES: BRIDGING MECHANISTIC UNDERSTANDING AND THEIR PERFORMANCE

Dr. Younan Xia, Advisor
Department of Biomedical Engineering
Georgia Institute of Technology

Dr. Miaofang Chi, Co-advisor
Center for Nanophase Materials Sciences
Oak Ridge National Laboratory

Dr. Angus P. Wilkinson, Chair
School of Chemistry and Biochemistry
Georgia Institute of Technology

Dr. Z. John Zhang
School of Chemistry and Biochemistry
Georgia Institute of Technology

Dr. Hui Wang
Department of Mechanical Engineering
University of Louisville

Date Approved: Feb. 9, 2018

To those who inspired it

ACKNOWLEDGEMENTS

The production of this dissertation would not be possible without the contribution of many scientists. Although my name appears first on this dissertation, I would like to acknowledge a number of individuals who have continuously motivated this work, mentored my research, and pushed the overall understanding of new materials. I would first like to acknowledge my Ph.D. advisors, Prof. Younan Xia and Dr. Miaofang Chi, for granting me the freedom to continue studying solid-state ion conductors throughout graduate school and learning alongside me about their interesting syntheses, properties, and phenomena. Their knowledge and insight has greatly improved my critical thinking, my scientific writing skills, and my overall independence in research. My interest in solid-state ion conductors was initially sparked by Prof. Natalie Holzwarth during my undergraduate studies at Wake Forest University (WFU). Since graduating from WFU in 2013, I have continuously collaborated with her and her group; Prof. Holzwarth's motivation, mentorship, and enthusiasm has stuck with me throughout the years. I am incredibly grateful for her guidance and for always believing in my abilities as a scientist. I am also grateful for Prof. Abdou Lachgar, Prof. Keerthi Senevirathne and Dr. Shiba Adhikari of WFU for my early training in materials chemistry; the training I gained through them motivated my further studies in chemistry, and for their mentorship, I am incredibly grateful. Before starting graduate school at Georgia Tech, I worked on solid-state ion conductors under the direction of Dr. Chengdu Liang at the Center for Nanophase Materials Sciences (CNMS) at Oak Ridge National Laboratory (ORNL). Dr. Liang's guidance, enthusiasm, and motivation was instrumental in my training as a chemist. He constantly

and continuously promotes my career development; his enthusiasm has been carried throughout my graduate school career and will be for years to come. I would also like to extend my gratitude to a number of scientists and collaborators at ORNL who provided the necessary guidance to jumpstart my graduate school career, namely Prof. Hui Wang, Dr. Amaresh Samuthira Pandian, Dr. Nancy Dudney, Dr. Juchuan Li, Dr. Yunchao Li, Dr. M. Parans Paranthaman, Dr. Jagjit Nanda, Dr. Frank Delnick, Dr. Gabriel Veith, Dr. Gayatri Sahu, Dr. Ezhiylmurugan Rangasamy, Dr. Rui Peng, Dr. Zili Wu, Dr. Uma Tumuluri, Dr. Jong Kahk Keum, Dr. Ibrahim Ilgaz Soykal, Dr. Amanda Mann, Matt Rager, Dr. Tolga Aytug, Dr. Adam Rondinone, Dr. Ian Anderson, Dr. Karren More, Dr. Melanie Kirkham, and Michelle Pawel.

Throughout graduate school, many individuals at different institutions have contributed to my training. Here, I would like to thank the multiple individuals who aided in expanding my knowledge to new fields like biomedicine, catalysis, photonics, photocatalysis, biofuels, carbon, microscopy, materials science, and beyond. At Georgia Tech, I am grateful for the support of many individuals, including Dr. Kyle Gilroy, Dr. Legna Figuroa-Cosme, Dr. Xuan Yang, Dr. Miaoxin Yang, Dr. Madeline Vara, Prof. Stanislav Emelianov, Kelsey Kubelick, Dr. Thenner Silva Rodrigues, Dr. Anderson Gabriel Marques da Silva, Dr. Shixiong Bao, Shan Zhou, Ming Zhao, Dr. Xue Wang, Sujin Lee, Chi-Ta Lee, Ming Zhou, Qiuxiang Wang, Dr. Aleksey Ruditskiy, Walter Henderson, Todd Walters, Eric Woods, Prof. Matt McDowell, Prof. Hailong Chen, Dr. Jinho Park, Michael Tanes, Dr. Hsin-Chieh Peng, Dr. Jiajia Xue, Dr. Da Huo, Ziheng Lyu, Dr. Song Shen, Dr. Jing Qian, Xiaohuan Zhao, Wenjuan (Jessica) Shang, and Whitney Breech. At ORNL, I am grateful for the support of many individuals in projects related to materials

for solid-state batteries, catalysts, and beyond, including Prof. Hui Wang, Dr. Amaresh Samuthira Pandian, Dr. Xiaoming Liu, Dr. Nancy Dudney, Dr. Gabriel Vieth, Dr. Frank Delnick, Dr. Jong Kahk Keum, Dr. Wenpei Gao, Dr. Yunchao Li, Dr. M. Parans Paranthaman, Dr. Amit Naskar, Dr. Jajgit Nanda, Prof. Sujuan Wu (and her students Yunfan Xu and Piaopiao Wan), Dr. Jihua Chen, Dr. David Cullen, Dr. Karren More, Dr. Larry Allard, Dr. Yan Chen, Dr. Ke An, Dr. Zili Wu, Dr. Uma Tumuluri, Dr. Guo-Shiou Foo, Dr. Yang Song, Dr. Kuibo Yin, Minghao Zhang, Tongming Su, Xiaofei Liu, Xi Chen, Dr. Xi (Chelsea) Chen, Dr. Christopher Nelson, Dr. Shi-Ze Yang, Dr. Chengcheng Tian, Dr. Yongqiang Cheng, Dr. Michael Naguib, Dr. Andrew Westover, Dr. Robert Sacci, Dr. Robert Schmidt, Dr. Guang Yang, Dr. Zhijiang Tang, Dr. Ilia Ivanov, Eric Muckley Dr. Brad Lokitz, Sam Evans, Shawn Reeves, and Zachary Gosser. At WFU, I am grateful for the collaborations related to solid-state electrolytes and various systems of catalysts with Prof. Natalie Holzwarth, Prof. Abdou Lachgar, Dr. Shiba Adhikari, Prof. Marcus Wright, Cameron Kates, Hunter Dean, Jason Howard, Larry Rush Jr., and Ahmad Al-Qawasmeh. I am additionally appreciative for some of my early training related to organic chemistry at WFU from Prof. Ulrich Bierbach, Dr. Amanda Pickard, Dr. Mu Yang, and Dr. Song Ding. I am also grateful for the collaborations during my Ph.D. research with Dr. William West, Prof. Munekazu Motoyama, and Prof. Yasutoshi Iriyama at Nagoya University in Japan. Of course, I would like to extend my gratitude to Professors Angus Wilkinson, Z. John Zhang, and Hui Wang for serving on my Ph.D. dissertation committee, for their encouragement, and for being supportive throughout graduate school.

This work would not be possible without the financial support of the National Science Foundation Graduate Research Fellowship Program, the Georgia Tech-ORNL

Fellowship, the Center for Nanophase Materials Sciences at ORNL, the Spallation Neutron Source at ORNL, and the Higher Education Research Experiences (HERE) at ORNL. These resources have been incredible throughout my graduate studies. I truly appreciate the support from each of these institutions and funding agencies.

Of course, I would like to thank my family and friends for their endless support, love, and humor throughout graduate school. There are too many of you to name, so I want to simply say thank you for all that you have done. Thank you all.

TABLE OF CONTENTS

LIST OF TABLES

LIST OF FIGURES

LIST OF SYMBOLS AND ABBREVIATIONS

A	constant related to the lattice structure
ACN	acetonitrile
ALD	atomic layer deposition
bcc	body-centered cubic
c-LLZO	cubic $Li_{7-3x}Al_xLa_3Zr_2O_{12}$
CPMEA	cross-linked poly(ethylene glycol) methyl ether acrylate
CV	cyclic voltammogram
DFT	density functional theory
DI	deionized
E_a	Arrhenius activation energy
EDS	energy-dispersive X-ray spectroscopy
EELS	electron energy loss spectroscopy
EIS	electrochemical impedance spectroscopy
fcc	Face-centered cubic
GB	grain boundary
HAADF	high-angle annular dark field
hcp	hexagonal close-packed
HSAB	hard and soft acids and bases
HRTEM	high-resolution transmission electron microscopy
k	Boltzmann constant
LAGP	$Li_{1+x}Al_xGe_{2-x}(PO_4)_3$
LCO	$LiCoO_2$
LiPON	lithium phosphorus oxynitride

LiSICON	Lithium superionic conductor
LGPS	$Li_{10}GeP_2S_{12}$
LLTO	$Li_{3x}La_{2/3-x}TiO_3$
LLZO	$Li_7La_3Zr_2O_{12}$
LMN	$LiMn_{1.485}Ni_{0.45}Cr_{0.05}O_4$
LNO	$LiNbO_3$
LPS	β-Li_3PS_4
LZNO	$Li_6ZnNb_4O_{14}$
MD	molecular dynamics
NaSICON	sodium superionic conductor
n_c	mobile-ion site occupancy available
NEB	nudged elastic band
NED	nano-electron diffraction
NMR	nuclear magnetic resonance
PCPSE	polymer/ceramic/polymer sandwich electrolyte
PDOS	partial density of states
PLD	pulsed laser deposition
RF	radio frequency
SE	solid electrolyte
SEI	solid electrolyte interphase
SPM	scanning probe microscopy
STEM	scanning transmission electron microscopy
T	absolute temperature
TEM	transmission electron microscopy
THF	tetrahydrofuran

XAS	X-ray absorption spectroscopy
XPS	X-ray photoelectron spectroscopy
XRD	X-ray diffraction
σ_o	temperature independent ionic conductivity

SUMMARY

Solid electrolytes have attracted growing research interest for their promise to offer the safety and energy density necessary for future battery systems. Not only being the primary component in all-solid-state batteries, solid electrolyte materials also demonstrate their importance as a protector for lithium or sodium metal anodes in novel battery configurations, such as Li-S, Li-air, and flow batteries. The impedance at interfaces associated with solid electrolytes, *i.e.* internal grain and phase boundaries, and their interfacial stability with electrodes, are currently two key factors limiting the performance of solid electrolyte in batteries. Only will a mechanistic understanding of the root origin of these interfacial resistance and potential instability pave the way to the design of high-performance solid electrolyte-based batteries. In this Dissertation, I start with an introduction to the fundamentals of solid electrolytes and challenges associated with tuning their physical properties and their interfaces. I also discuss techniques that allow for an atomic-scale understanding of ion transport and stability in solid electrolytes and at their interfaces. I have selected representative examples from current literature that exemplify recent fundamental insights gained through advanced characterization techniques and high-throughput theoretical methods. Different strategies for improving ion conduction and stability in solid electrolytes and interfaces are discussed. In the following chapters, several solid electrolytes are introduced and discussed in detail, including β-Li_3PS_4, $Li_4P_2S_6$, Li_2OHCl, and $Na_4P_2S_6$. Different synthetic and processing methods were employed to prepare these new solid electrolytes and understand their electrochemical performance with metallic lithium or sodium anode. In the case of β-Li_3PS_4, I describe a strategy for

improving ion conduction in nanostructured β-Li_3PS_4 through the formation of nanocomposites with ion conducting and non-conducting oxide-based fillers. The work related to β-Li_3PS_4 is further extended to the fabrication of thin membranes (<50 μm) via tiled assembly of shape-controlled, nanoscale building blocks. This method is based on facile and low-cost solution-based soft chemistry to create membranes with tunable thicknesses. Next, I discuss $Li_4P_2S_6$, a largely overlooked material that appears as a decomposition product in the Li-P-S system, on the basis of combined experimental and theoretical investigations. I also discuss the LiOH-LiCl system of electrolytes and their compatibility with metallic lithium anode; I show that Li_2OHCl solid electrolyte forms a stable solid electrolyte interphase layer with a metallic lithium anode, even past the melting point of lithium metal. I subsequently discuss a new sulfide-based sodium conductor, $Na_4P_2S_6$. The design of the solid electrolyte $Na_4P_2S_6$ is described, realizing excellent air stability and an economic soft chemistry synthetic approach in the presence of water. This Dissertation concludes by highlighting opportunities and perspectives for future research that will achieve an enhanced understanding of solid electrolytes and bridge the gap between the mechanistic understanding of solid electrolytes and their electrochemical performance in different battery configurations.

CHAPTER 1

INTRODUCTION

1.1 Introduction to Crystalline Solid Electrolytes

Ion transport in solids and their associated interfaces forms the basis of various current and next-generation energy storage technologies. In conventional state-of-the-art Li-ion batteries, the lithium ion transport within solid-state electrode materials and at the interfaces of solid electrodes and liquid electrolyte dictates the battery performance. In batteries involving solid electrolyte (SE) materials, such as all-solid-state batteries where SE is used as a primary component or some future battery configurations (*i.e.* Li-S and Li-air, and Li-flow) where SE is the crucial protecting layer for lithium metal anodes, the ion transport within SE and at SE interfaces directly determines the rate capability and energy density of the battery. Three major types of SEs have been intensively studied: polymers, glasses, and crystalline electrolytes [1-2]. Polymer electrolytes offer the advantage of facile processability and flexibility over glassy or crystalline SEs, and thus are useful for flexible lithium batteries. However, they often bring problems associated with their lower mechanical strength and poor chemical stability. Crystalline SEs are often more stable at increased temperatures. The mechanical strength of crystalline SEs is often a desirable property, potentially preventing the growth of dendrites from high capacity anodes such as metallic Li or Na. In line with this Dissertation, this chapter mainly focuses on the crystalline SEs, while literature detailing polymer and glassy materials can be found in several good reviews [3-6].

Li^+ and Na^+ transport in crystalline solids is primarily based on mobile ions hopping among energetically favorable sites in a surrounding potential. The motion of the surrounding ions provides the activation energy for mobile ions to move through channels in the crystalline framework under an externally applied electrical field. The activation associated with the movement of ions within a crystalline lattice is often higher than that in liquid, and as a result, the ionic conductivity in SEs is generally lower. Owing to the concerted efforts from both experimentalists and theorists, designing superionics from the atomic scale is emerging, as several fast-conducting materials were recently discovered that exhibit ionic conductivities comparable to those of organic liquid electrolytes.

Crystalline SEs of current interest can be broadly classified in three major categories: sulfides, oxides, and nitrides, each with different structural families. Sulfide-based SEs in the thio-LISICON (lithium superionic conductor) and argyrodite structural families received much attention from the scientific community due to their enhanced room-temperature ionic conductivity and technologically viable Arrhenius activation energy when compared to other families of solid electrolytes. Prime examples of the thio-LISICON and argyrodite ionic conductors include β-Li_3PS_4 (0.16 mS/cm at RT, E_a = 0.35 eV), $Li_7P_3S_{11}$ (17 mS/cm at RT, E_a = 0.18 eV), $Li_{10}GeP_2S_{12}$ (12 mS/cm at RT, E_a = 0.22-0.25 eV) and Li_6PS_5Br (6.8 mS/cm at RT, E_a = 0.32 eV) [7-14]. Experimental studies detailing these sulfide-based SEs inspired multiple recent theoretical reports [15-25]. Oxide-based SEs, on the other hand, fall into three main structural families: garnet, perovskite, and NASICON-like (sodium superionic conductor). Some prime examples of oxide-based ion conductors include tetragonal $Li_7La_3Zr_2O_{12}$ (0.11 mS/cm at RT, E_a = 0.41 eV), $Li_{6.24}La_3Zr_2Al_{0.24}O_{11.98}$ (0.40 mS/cm at RT, E_a = 0.26 eV), $Li_{1.3}Al_{0.3}Ti_{1.7}(PO_4)_3$ (0.7

mS/cm at RT, E_a = 0.20 – 0.35 eV), and $Li_{3x}La_{2/3-x}TiO_3$ (10^{-2} – 1.0 mS/cm at RT, E_a = 0.26 – 0.40 eV) [26-30]. Amongst the reported lithium nitrides, Li_3N holds the highest ionic conductivity (0.66 mS/cm at room temperature, E_a = 0.25 eV) [31]. In terms of sodium ion conductors, the ionic conductivity of β-alumina ($NaAl_{11}O_{17}$) is amongst the highest (14 mS/cm at RT, E_a = 0.16 eV) [32].

The mass and charge transfer at solid-solid interfaces are complex yet performance-limiting for the electrochemical energy systems involving SEs [1, 33]. In comparison to liquid/solid interfaces, ion transport through solid-solid interfaces are inherently different and often dictate the overall battery performance. Not only the structural heterogeneity and the electrochemical stability, but the inherent space-charge layer, the potential discontinuous contact, and interfacial strain induced between the two adjacent materials before and during electrochemical cycling can also significantly influence the ion conduction at solid-solid interfaces. However, our fundamental understanding of mass transport and charge transfer at solid-solid interfaces is very limited, significantly hindering rational designs of interfaces with desirable ion conductivity and cycling stability.

Developing a precise understanding of ion transport behavior at solid-solid interfaces is challenging. Since solid-solid interfaces are often spatially confined and embedded, not many characterization techniques can clearly reveal the structural and chemical nature of interfaces at an adequate spatial resolution. Studying ion transport at ionic solid interfaces is equally challenging to theoretical calculations, as practical interfacial structure is often non-centrosymmetric and unpredictable. The strong interaction among charge carriers and between charge carriers and the lattice further complicates theoretical calculations. Nevertheless, recent rapid developments in characterization

techniques and computations have brought unprecedented opportunities to investigate interfacial mass and charge transfer related to SEs. The intention of this chapter is to highlight the fundamental understanding of ion transport and stability of SEs and their interfaces, by emphasizing recent atomic-scale insights gained through advanced characterization techniques and cutting-edge theoretical calculations. It should be noted that, in the past few years, several good reviews have emerged that discuss bulk solid-state ion conducting materials in general, including both inorganic SEs [3,5,6,34-43] and polymer-based electrolytes [3-5]. This chapter focuses on the atomic-scale understanding and the design of SEs and their interfaces towards optimized ion conductivity and electrochemical stability, underlining the knowledge recently developed by the integration of high-resolution microscopy and spectroscopic characterization methods and theoretical approaches. Different strategies to improve ion conduction and stability in SEs and their interfaces are also discussed. This chapter highlights different experimental and theoretical approaches that will bridge the gap between our fundamental understanding of different SEs and their performance.

1.2 Challenges of Solid Electrolytes and Their Interfaces

Solid electrolytes, also known as solid-state superionic conductors, are characterized by high ionic conductivity and low electronic conductivity. In the last several decades, many fast ion conducting materials have been introduced in the literature, including oxide-based, sulfide-based, fluoride-ion, silver ion conductors, amongst others [1], which have paved the way towards the development of new and improved technologies, including solid-state batteries, Li-air batteries, fuel cells, capacitors, sensors, implantable medical

devices, and electrochromic devices [44-56]. Solid electrolytes are especially of interest for energy storage technologies where enhanced energy density is requisite, such as mobile electronic devices or electric vehicles.

Though several superionic conductors have been recently discovered, the ionic conductivity in most SEs is still lower than that of organic liquid electrolytes [37]. In particular, only a very few compounds show a room temperature ion conductivity higher than 10^{-4} S/cm, which presents a number of limitations towards their practical applications. The other major concern associated to many current SEs is their chemical stability towards ambient conditions. So far, sulfide-based lithium SEs have shown the highest Li^{+} conductivities at room temperature. However, many of these compounds are extremely unstable under ambient atmospheres and such instability becomes one of the major hurdles for their practical applications. The discovery of new superionic conductors with sufficient ion conduction and desirable chemical stability is therefore crucial.

Perhaps the greatest challenge in the application of solid electrolytes is preserving low interfacial resistance at the electrode/SE and SE/SE interfaces while maintaining high ionic conductivity through the SE membrane. High resistivity is often unexpectedly found at interfaces involving SE materials. Overcoming this challenge requests a clear understanding of complex interfacial phenomena at the atomic to microscopic scale in model SE-based systems as well as a reliable link between the atomic phenomena with macroscopic performance at these local features. Various interfaces are involved in batteries employing SE, schematically illustrated in Fig. 1.1. Crystalline electrolytes are often processed into membranes that are polycrystalline in nature and contain a high concentration of grain boundaries, where the grain boundary conductivity could

significantly influence the overall bulk ionic conductivity in SEs. On the other hand, in many cases, a SE could be composed of multiple phases in the format of a composite or a lamellar layered structure, in order to enhance the ion conductivity, mechanical stability, or chemical stability with electrodes; the interface between the two heterogeneous SE materials, therefore, becomes vital [38,57]. The most important and challenging interface associated with SE materials are those with electrodes. Due to the large dissimilarity in the structural, chemical, mechanical, and electrical properties between SEs and electrodes, multiple interfacial mechanisms can be involved in the charge transport, such as chemical/electrochemical decomposition, elemental interfusion, structural deformation of the crystal lattice, and changes in the mechanical integrity [58-60]. These mechanisms can influence each other and may evolve during different stages of charging, complicating the analysis of interfaces with SEs. A fundamental understanding of which mechanisms are at play and how they influence each other is the key to develop descriptors of design for chemically stable and highly conductive SEs and their interfaces at the atomic to microscopic scale. In the following sections, I review and discuss some of the most recent advances in probing different interfaces with SEs at the atomic scale as well as strategies to improve ionic transport, chemical stability, and interfaces within systems involving SEs.

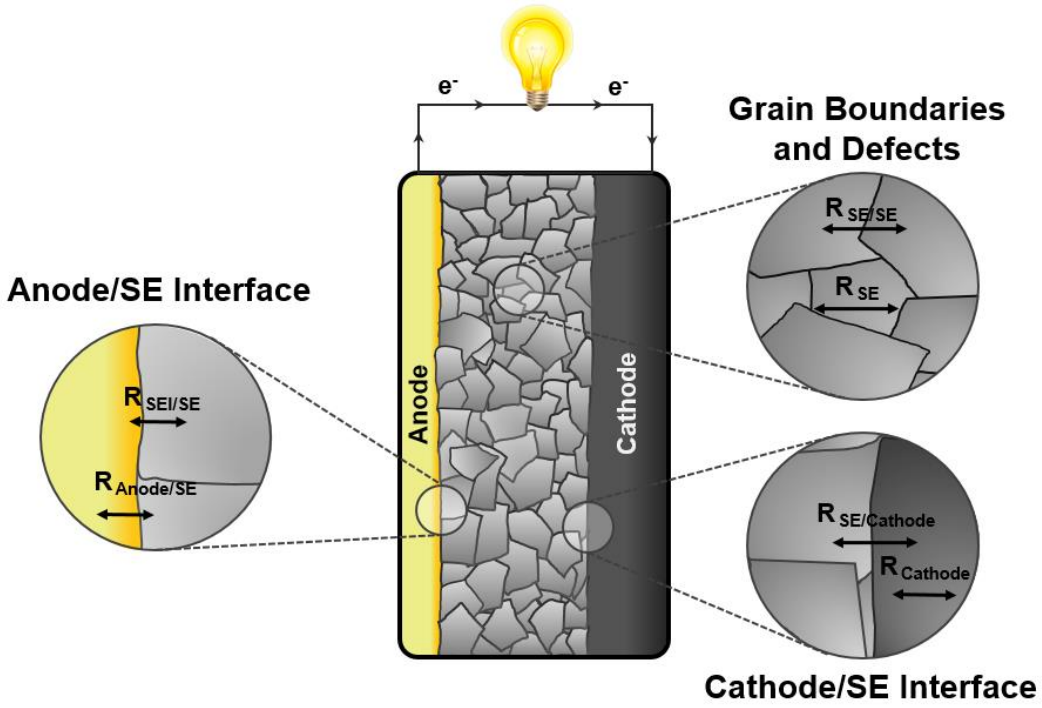

Figure 1.1 Schematic configuration of a typical battery employing solid electrolyte (SE), detailing the different interfaces associated with SEs. Different interfaces within such batteries hold altered resistances, which change the overall performance of the battery.

1.3 Atomistic Understanding of Ion Transport Within Solid Electrolytes and at Their Interfaces

Limited characterization techniques are present for probing atomistic mechanism of ion transport in solids and their interfaces. Conventionally, nuclear magnetic resonance (NMR) spectroscopy [29, 61-64], electrochemical impedance spectroscopy (EIS) [65-69], cyclic voltammetry (CV), and scanning probe microscopy (SPM) are broadly used and provide valuable averaged information of ion conduction in SEs. However, directly

probing ion conduction behavior at the atomic scale or at individual interfaces using these methods is challenging. This section mainly focuses on the recent insights gained from characterization techniques that have broadened our understanding of conductivity and stability at the atomic scale. In particular, knowledge recently gained by state-of-art transmission electron microscopy (TEM), X-ray photoelectron spectroscopy (XPS), and a number of other characterization techniques are discussed. Computational approaches often compliment different characterization techniques, which have greatly enhanced our understanding of different SE systems. Significant efforts towards the design of novel materials with fast ion conduction and the prediction of electrochemical stability of SE interfaces have recently been reported. In the following sections, I discuss recent investigations of SEs from the unit cell structure to different types of interfaces using theoretical calculations and experimental characterization techniques.

1.3.1 Design of fast ion conduction using the unit cell structure

1.3.1.1 Basis for design at the unit cell level

Though different types of SEs can contain different mobile ion species, the principle detailing how these mobile ions move in a crystalline lattice is the same. Ion diffusion in solids describes the movement from one site to another through different defects in a crystal lattice or solid, which determines some of the key electrochemical properties in SE-based batteries [70]. For a given lattice structure, the ion conductivity can be expressed by Equation 1:

$$\sigma = n_c ze\mu = \frac{A}{T} n_c(1 - n_c)\exp\left(-\frac{E_a}{kT}\right) \qquad (1)$$

where n_c is a mobile-ion site occupancy available to the mobile ions, E_a is the activation energy for the transport of the mobile ions, T is absolute temperature, k is Boltzmann constant, and A is a constant related to the lattice structure. The main criteria to enhance the ionic conductivity in a SE is (1) to correlatively optimize concentration ratio of mobile ions and vacancies, (2) to construct well-connected ion conduction channels, and (3) to arrange the unit cell atoms in a way with low activation energy. Based on these criteria, fast ion conduction within a framework at the unit cell level can essentially be designed and optimized. For example, in oxide-based SEs, Li-O bonding is often strong, leading to lower ionic conductivity. One strategy is to weaken the Li-O bond by bonding O^{2-} ions to network cations to form tetrahedral covalent bonds, such as in SiO_4^{4-} or PO_4^{3-}. The four sp^3 orbitals are therefore occupied and the oxygen charges are polarized away from the Li^+ ions, allowing for higher ionic conductivity [71]. Another good example is the design of NASICON by Hong and Goodenough, where a rigid 3D framework is interwoven with a 3D interstitial space, which enables the movement of Na^+ ions with a lower activation energy [72,73].

In $Li_{3x}La_{2/3-x}TiO_3$ (LLTO) perovskite oxides, the cation ordering, *i.e.* the ordering of Li-rich and Li-poor layers, provides an enhanced probability for Li^+ ions to find nearby vacancy sites, giving an improved ion conductivity compared to the structure with randomly distributed cations [74]. Thanks to the significant developments of computation techniques, the atomic framework at the unit cell can be predicted and designed to allow for fast ion conduction. Recently, the body-centered cubic (*bcc*) framework was found to allow for superior ionic conductivity and decreased activation energy in lithium superionic conductors from first principles calculations in sulfide-based SEs [15]. In comparison to

face-centered cubic (*fcc*) and hexagonal close-packed (*hcp*) frameworks, the topology of the anion host matrix in the bcc framework was found to be a key factor in allowing for facile lithium ion transport in superionic conductors, such as $Li_7P_3S_{11}$ and $Li_{10}GeP_2S_{12}$. Fig. 1.2 shows the Li-ion migration through a typical *bcc* lattice with the corresponding migration energies using density functional theory (DFT) and the nudged elastic band (NEB) method [75]. In the *bcc* and *bcc*-like frameworks, Li ions prefer to move within a network of interconnected tetrahedral sites that possess equivalent energies. In correlation to previously reported studies detailing ion conductors, the volume of the different Li sites was found to be a critical factor in determining the ion mobility in solid-state materials [76]. The tetrahedral site in the *bcc* lattice was found to hold the lowest relative energy for all volumes when surveying *bcc*, *hcp*, and *fcc* materials, where the Li-ion migration barrier was well below 0.4 eV across all bcc unit cell volumes. This trend is assumed to be primarily influenced by the anion host-matrix; therefore, the choice of the anion network is critical when designing solid-state superionic conducting materials.

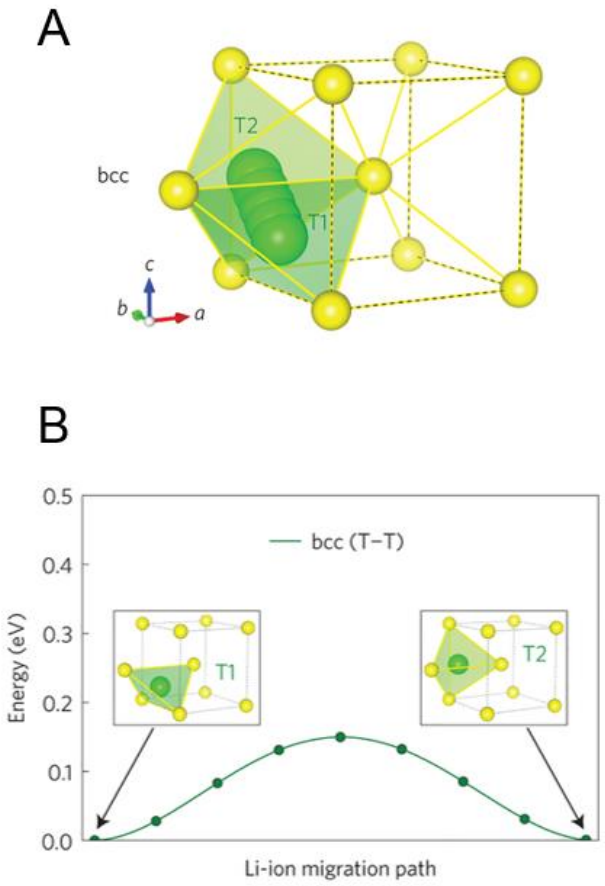

Figure 1.2 A) Li-ion migration pathway through a body centered cubic (*bcc*) anion lattice and B) calculated energy path for Li-ion migration [15]. Reprinted with permission; © 2015 Nature Publishing Group.

1.3.1.2 Grain boundaries of SEs

Grain boundaries in polycrystalline materials represent a critical feature influencing their overall mechanical, thermal and conducing properties. From the microscopic perspective of SEs, the grain boundary (GB) characterizes structural and chemical discontinuity, which can significantly influence the ion conductivity of the SE. In fact, many current ion conductors show high GB resistivity with a 2-3 orders of magnitude

higher than grain interior. The GB resistance is recognized in the literature, yet the exact structural and chemical origins of large GB resistance for a number of classes of SEs are unknown [30, 77-81]. Understanding the origin of high GB resistivity in these materials is crucial, but challenging. Many of these GBs are confined to nanoscale lengths, and in some cases, these interfaces consist of only a few unit cells.

A recent microscopy study demonstrates the power of atomic resolution electron microscopy imaging and electron energy loss spectroscopy (EELS) towards a clear understanding of grain boundary resistance at atomic scale [82]. Atomic-scale analysis of LLTO GBs revealed different atomic arrangements for the boundary when compared to the grain interior. Figure 1.3A shows a high-angle annular dark-field (HAADF) scanning transmission electron microscopy (STEM) image of LLTO, displaying the alternative stacking of the La-rich and La-poor A-site layers, a feature exhibited by most LLTO materials [28, 82-84]. Figure 1.3B displays a representative HAADF-STEM image of a LLTO GB, where two different variations of GB structure: the majority of GBs showing darker contrast in HAADF-STEM images (labeled Type I), and some of the GBs showing a limited feature with a relatively reduced contrast difference across the GB (labeled Type II). Type II GBs are often terminated with La rich atomic layers (deficient in mobile carriers and vacancies) at the GBs, which do not permit fast ion conduction. In Type I GBs, increased chemical deficiencies in both La^{3+} and Li^{+} were observed, resulting in a binary Ti-O layer of 2-3 unit cells at the GB core (Figure 1.3C). This feature is not energetically preferred for lithium transport, which presents higher GB resistivity. Such S/TEM studies allow for a mechanistic understanding of often overlooked features of SEs such as GB resistance.

Here, it must be emphasized that the origin of high GB resistivity in different types of SEs may vary and further characterizations are necessary to develop a general understanding for various SEs [85, 86]. A universal strategy, equivalent to the criteria of designing fast ion conduction at the unit cell level, must be developed. Furthermore, garnet structured oxides, *i.e.* $Li_7La_3Zr_2O_{12}$ (LLZO), gives an acceptable GB conductivity which is comparable to that of the grain [87-91]. Such benign GBs deserve particular attention in order to develop our strategies towards the design of grain boundaries with high ionic conductivity.

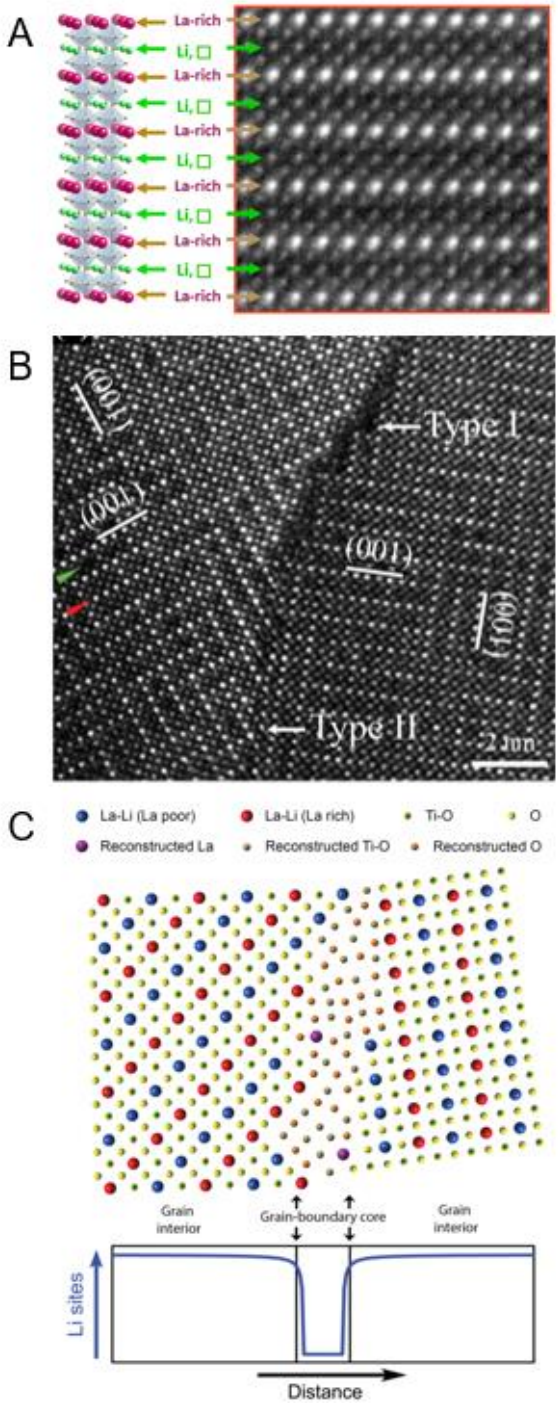

Figure 1.3 A) HAADF-STEM image of LLTO, with a schematic showing the La and Li rich layers. B) HAADF-STEM image of an LLTO GB, with green and red arrows displaying the La-rich and La-poor layers, respectively. C) Schematic illustration of the Type I GB based on HAADF-STEM images and EELS analysis, depicting a Li-depleted GB [82]. Reprinted with permission; © 2014 Royal Society of Chemistry.

1.3.2 Ion conduction at the anode/SE interface

The anode/SE interface, in many cases, presents high interfacial resistance due to poor interfacial contact, the formation of a lithium depleted space-charge layer, or interfacial degradation; any combination of these problems will ultimately limit the power and rate performance in solid-state batteries [92-98]. High-throughput modeling of interfaces between SEs and the different anode materials is expected to play a critical role in evaluating the thermodynamics of the interfacial electrochemical and chemical stability. To evaluate the interfacial stability, the electrochemical stability of the electrolyte is first evaluated by introducing the Li chemical potentials (μ_{Li}) observed at the anode. The model is then extended to allow for any interfacial reactions to occur. Calculated electrochemical stability ranges for different SEs with metallic lithium anode are presented in Fig. 1.4. In these calculations, the anodic stability window was largely correlated with the related binary system from decomposition products. For example, the anodic stability of $Li_{10}GeP_2S_{12}$ was related with the stability of Li_2S with metallic lithium anode, and since lithium is removed from the electrolyte during the simulation, a Li_nX (n = 1, 2, 3, X = anion) forms as a decomposition product at the interface while the energy of mixing causes other elements to react with the binary [57]. Most of these calculations take into account of the stability of the polyanion matrix, where more energy is required to dissociate stronger polyanion bonds, yet some of these calculations do not match electrochemical window achieved experimentally for some SEs, such as LiPON, Li_3PS_4, and Li_3PO_4 [11, 46, 99]. From these simulations, passivation layers are expected to form at the interface, which, in some cases, are ionically conductive and can protect the SE or anode from further

interfacial decomposition. For instance, simulations show that Li_3P and Li_2S form at the Li/γ-Li_3PS_4 interface when applying first principles calculations (Fig. 1.5) [100]. The calculated partial density of states (PDOS) for the Li slab, the interface, and electrolyte region for the Li/γ-Li_3PS_4 interface clearly show that a buffer layer forms at the interface, which agrees with other more recent simulations [22]. The PDOS of the Li slab in the top panel and the γ-Li_3PS_4 interface in the bottom panel closely resemble that of the ideal crystals. The PDOS for the Li/γ-Li_3PS_4 interface clearly show the reaction products, where γ-Li_3PS_4 forms a number of compounds at the interface. When applied to a broad range of materials, these simulations give insight as to the possible stability and decomposition reactions that can occur at the interface between anode and SE materials. Until recently, experimental characterizations have not been able to confirm theoretical modeling at such interfaces due to the poor resolution of different techniques and the inability to acquire elemental and compositional data at the atomic scale.

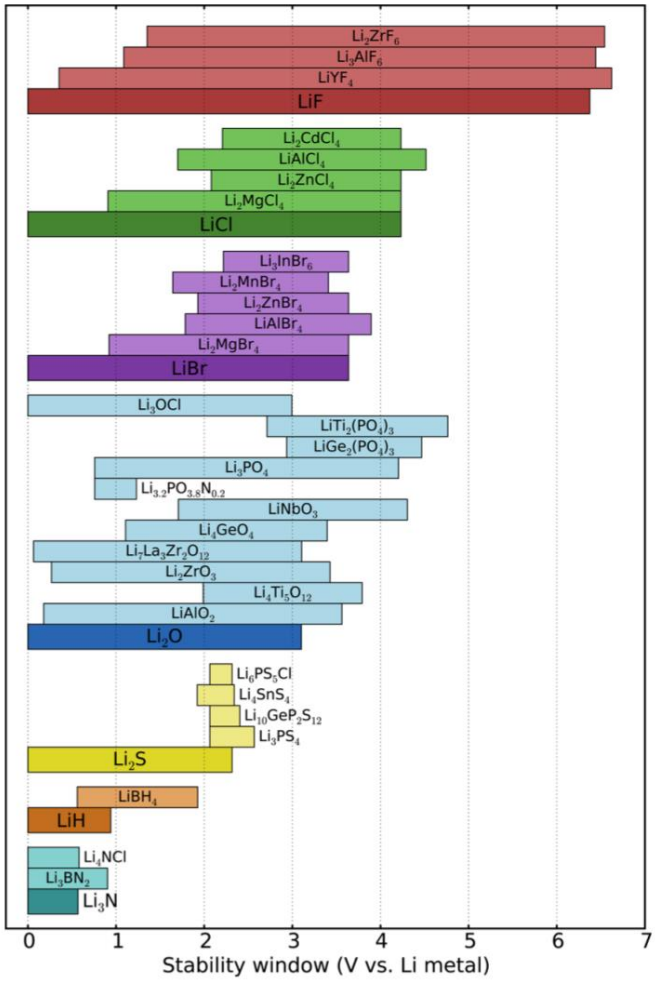

Figure 1.4 Calculated electrochemical stability range of reported lithium SEs with metallic lithium anode, where the anion determines the high-voltage stability [57]. Reprinted with permission; © 2015 American Chemical Society.

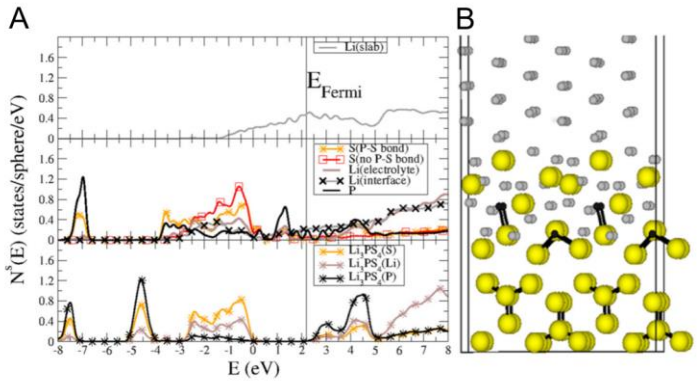

Figure 1.5 A) Calculated partial density of states for the Li slab, the interface, and electrolyte region for the Li/γ-Li_3PS_4 interface and B) schematic model of optimized structure [100]. Reprinted with permission; © 2015 American Physical Society.

Since interfaces between SEs and electrode materials hold inherently complicated chemical and structural features, most investigations detailing the atomic-scale features of electrode/SE interfaces at the atomic scale have been limited to theoretical modeling. It is requisite that these interfaces maintain low interfacial resistance, though many studies lack a clear mechanistic understanding of the dynamic nature of the interface. Such a mechanistic understanding will assist researchers to develop rational design principles for interfaces. Therefore, the structural and chemical features must be examined using techniques that hold high spatial and temporal resolution, such as *in situ* S/TEM or XPS.

STEM, EDS, and nano-electron diffraction (NED) were previously utilized to observe the interface between LLZO and a $LiCoO_2$ (LCO) cathode [93]. The specimen was prepared *ex situ* by using pulsed laser deposition to deposit LCO onto LLZO. The combination TEM techniques exposed an interfacial buffer layer of about 50 nm thick that contained La_2CO_4, which hinders lithium diffusion across the interface. Similar studies were also applied to the Li_2S-P_2S_5 SEs, where $LiMn_2O_4$ and LCO cathodes were both

investigated [101, 102]. These studies reveal that reaction layers occur between the cathode and SE particles due to elemental inter-diffusion, which lead to an increase in charge transfer resistance. More recent studies using XPS and EIS also reveal the elemental inter-diffusion between LLZO and LCO [103]. Though many these studies reveal the existence of reaction layers, limited studies exist that detail the *in situ* behavior of the electrode/SE interface with atomic resolution.

Due to advancements in different *in situ* S/TEM techniques, the interfacial behavior between SEs and different electrode materials can now be directly observed [104-107]. Fig. 1.6 shows results from the first STEM study of the interface between cubic $Li_{7-3x}Al_xLa_3Zr_2O_{12}$ (c-LLZO) and metallic lithium anode [104]. Though c-LLZO was experimentally found to hold enhanced room temperature ionic conductivity and stability with metallic lithium anode, the reason for this stability was previously unknown [108-110]. Using a unique *in situ* STEM setup, metallic lithium was contacted with c-LLZO and the resulting interfacial behavior was probed. EELS analysis reveal that a localized phase transition occurs at the Li/c-LLZO interface, which was found to be ~6 nm or ~5 unit cells thick (Fig. 1.6C,D). This phase transition was attributed to the formation of a slightly reduced surface on c-LLZO, leading to an ultrathin interfacial layer containing tetragonal LLZO. This observation provides an important mechanistic understanding of the SE interface where the key to designing high-performance SEs relies on forming stable and conductive interfaces with high capacity anodes such as metallic lithium.

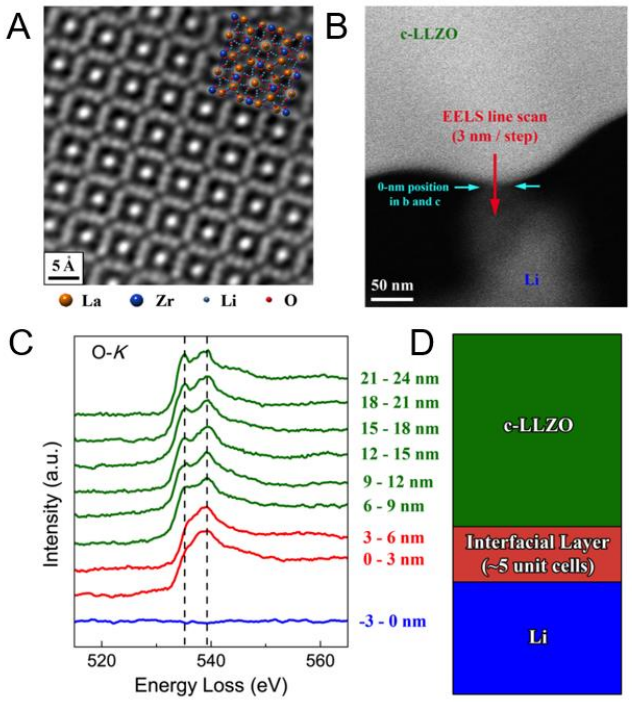

Figure 1.6 A) High-resolution HAADF-STEM image of the cubic LLZO specimen. B) HAADF-STEM image of LLZO in contact with a metallic lithium anode. C) O K-edges acquired in the EELS scan from (B). D) Schematic of the behavior at the Li/LLZO interface [111]. Reprinted with permission; © 2016 American Chemical Society.

In situ XPS investigations have recently allowed for direct detection of possible decomposition reactions at the anode/SE [112-114]. This technique has a number of advantages, including the surface and elemental sensitivity, the ability to detect light elements such as Li, and the ability to ascertain chemical bonding information. Of the different surface characterization techniques, XPS is regarded as the most quantitative and interpretable with regards to the chemical information. Different ion conductors, such as LiPON, LLTO, NASICON-like, and LISICON-like SEs, have been explored using XPS to determine the local structures and the possible decomposition product when placed in contact with metallic lithium or sodium anodes [112, 113, 115-117]. A number of

considerations must be made before analyzing SEs with XPS. Due to the high vacuum of the system, some materials, such as sulfide-based SEs, need to be cooled to temperatures < -80 °C to avoid elemental loss. Additionally, the decreased operating temperature is also known to slow down the reaction kinetics when exploring sensitive interfaces between anodes and SEs [113, 118].

Taking advantage of the surface sensitivity and quantitative nature of XPS, Wezel *et al.* recently reported the existence of a SEI between lithium metal and $Li_{10}GeP_2S_{12}$ (LGPS) with nanometer resolution [113]. Using a unique stage for sequential Li deposition and XPS data acquisition [112], the S2p, Ge3d, and P2p spectra were collected while 31 nm of metallic lithium was deposited on the surface of a LGPS pellet (Fig. 1.7A). As the reaction progressed, the XPS displayed a clear change in the oxidation state of Ge and the formation of Li_3P and Li_2S. These results are in good agreement with theoretical studies and also explain the increased interfacial resistance at the Li/LGPS interface over time [57]. Although XPS techniques provide excellent chemical information at the nanoscale, SEs currently cannot be examined *in operando* using such techniques. As a result, time-resolved electrochemical measurements, such as EIS and cyclic voltammetry, are necessary to elucidate how the interfaces will affect ion conduction in practical cells [68]. Hence, XPS analysis is a very useful tool for analyzing interfaces and allows for an enhanced mechanistic understanding when combined with other techniques.

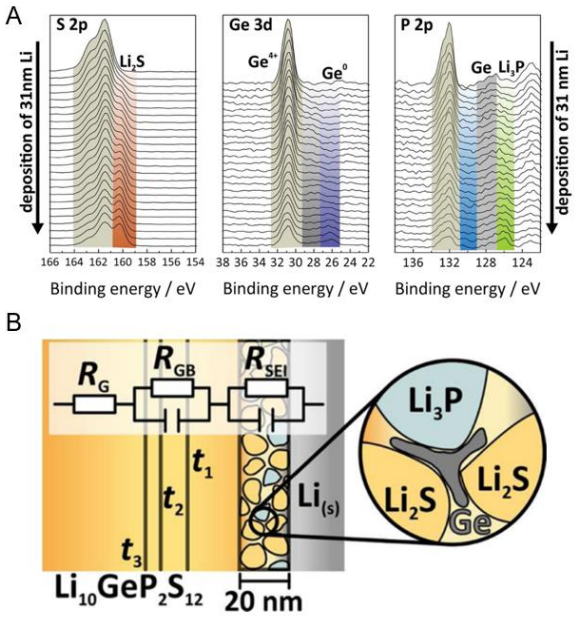

Figure 1.7 A) XPS spectra for the S2p, Ge3d, and P2p regions during the deposition of 31 nm film of metallic lithium on LGPS, displaying a clear decomposition into an interphase layer. B) Schematic representation of the interphase formation between metallic lithium and LGPS [113]. Reprinted with permission; © 2016 American Chemical Society.

1.3.3 Ion conduction at the cathode/SE interface

Experimental and theoretical investigations detailing the cathode/SE interface largely use similar calculations when compared to that of the anode/SE interface. In most cases, however, the charge-transfer resistance is high at the cathode/SE interface due to the following issues: (1) electrochemical reactions, (2) strong reduction or oxidation of the SE at an applied potential, (3) chemical reactions between the SE and the cathode material, and (4) space-charge layer effects. The combination of these issues has guided researchers in exploring and explaining the propagation of high interfacial resistance at the cathode/SE interface. By way of example, recent studies suggest that oxide-based SEs have better

chemical and electrochemical stability than sulfide-based SEs when interfaced with transition metal intercalation-type cathodes such as lithium cobalt oxide (LCO), as an exothermic chemical reaction could occur without an applied voltage [15, 57, 100, 119]. It was predicted that the phase equilibrium for sulfide-based SEs favors the formation of Co_9S_8, Li_2SO_4, and Li_3PO_4 at the LCO interface, which contributes to the high interfacial resistance. In order to decrease charge-transfer resistance at the cathode/SE interface, it was experimentally demonstrated that thin buffer layers could be deposited by various methods [120-125]. Some of the most common coating materials include LiPON, Li_3PO_4, $LiSiO_3$, $LiNbO_3$, $Li_4Ti_5O_{12}$, and $LiTaO_3$ [120-125]. Fig. 1.8 displays the calculated electrochemical window for some of these different coating materials, where many of these coating materials hold a theoretical reduction potential of less than 2 V and an oxidation potential of ~ 4 V. Artificial passivation layers hold two separate interfaces, one with SE and one with the cathode material, and calculations detailing the decomposition products at these respective interfaces show that only a few nanometers of materials are necessary to protect the cathode and SE from chemical or electrochemical reactions. The wide electrochemical window and low interfacial resistance are obvious advantages of applying a coating later between the SE and interaction cathodes.

Space-charge layer effects were more recently investigated as a form of interfacial resistance at the cathode/SE interface. Using LCO, $LiNbO_3$ (LNO), and β-Li_3PS_4 (LPS) as an example, the DFT + U framework method was applied to investigate the LCO/LPS and LCO/LNO/LPS interfaces (Fig. 1.9) [126, 127]. At the LCO/LPS interface, a disordered structure forms due to Li adsorption on the CoO_6 sites of LCO, leading to a space-charge layer. When a LNO buffer layer was deposited between the LCO and LPS layers, Li

adsorption space and Li inhomogeneity were effectively suppressed leading to an overall enhanced interface. These calculations suggest that the onset of space-charge growth occurs with charging and explains the high interfacial resistance measured for LCO/LPS interfaces while providing useful improvement for oxide/sulfide interfaces.

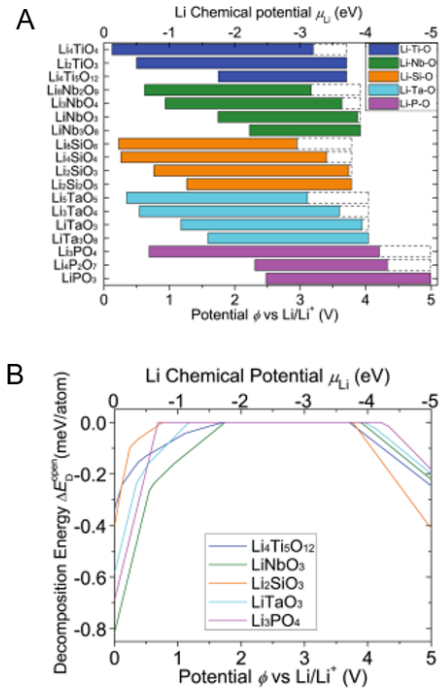

Figure 1.8 A) Calculated electrochemical stability and B) decomposition energy of reported lithium coating materials for SEs with cathode materials [119]. Reprinted with permission; © 2016 Royal Society of Chemistry.

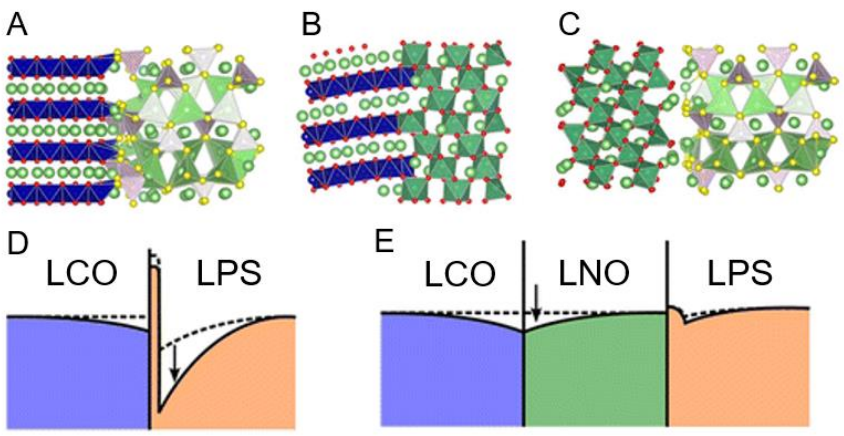

Figure 1.9 Calculated interface structures between A) LCO(110)/ LPS(010) B) LCO(110)/ LNO(1$\bar{1}$0) C) LNO (1$\bar{1}$0)/LPS(010). Schematics in D) and F) describe the lithium concentration change at the initial stage of charging for the LCO/LPS and LCO/LNO/LPS interfaces, respectively [126]. Reprinted with permission; © 2014 American Chemical Society.

1.3.4 Importance of linking microscopic phenomena with macroscopic performance

The above-discussed work has and will continue to provide invaluable insights of atomistic understanding of the structure, chemistry and even their evolution at different interfaces. The role of these interfaces can only be elucidated by reliably linking the atomistic/microscopic parameters revealed with macroscopic performance of individual interfaces. In such regards, *in situ* and *in operando* characterizations at different length scales and various properties are still needed to better understand SE materials.

The structural evolutions of SEs in their bulk form aids in linking the microscopic phenomena with the macroscopic performance. For example, recent developments in x-ray diffraction (XRD) techniques, such as *in situ* synchrotron XRD, have allowed researchers to better understand the phase formation in different SEs. By way of example, *in situ*

synchrotron XRD was applied to the synthesis of $Li_{1+x}Al_xGe_{2-x}(PO_4)_3$ (LAGP) SE and the identification of the glass to ceramic structural evolutions of materials with different dopant concentrations, which aids in improving the synthesis of NaSICON-type LAGP ceramics to maximize their ionic conductivity [128]. Neutron scattering has been widely used to characterize Li-ion conductors, for its several unique advantages. Unlike X-rays, which scatter through interaction with electrons, neutrons interact directly with neuclei, thus can penetrate deep into the material. Also, neutron scattering cross-sections are relatively high for the light elements such as H/D, Li, O, N, etc. which are more difficult to see with X-rays. Neutrons can also distinguish different isotopes of an element, making it possible to solve complicated (local) structure with isotopic labeling. Since thermal neutrons have the desired combination of momentum and energy, it is an ideal probe to the atomic/molecular dynamics such as vibration and diffusion. All these make neutron scattering a powerful technique for the study of ion conduction in Li-ion conductors. On the other hand, Raman investigations have been important for the study of their chemical bonding information in both amorphous SEs, such as LiPON and polymer-based electrolytes, and in crystalline SEs, such as LISICON-based and NASICON-based electrolytes [11, 120, 129-131]. In polymer/ceramic composites, Raman mapping can reveal interfacial degradation of SE membranes in their bulk form, which can be linked to their performance [132].

Directly probing local and long-range ion mobility *in situ* has recently been demonstrated for a number of researchers. In a recent example, Deng *et al.* recently revealed mechanistic insights involving Li^+ conduction in Li_4SiO_4-Li_3PO_4 SEs using solid-state ^6Li, ^7Li, and ^{31}P NMR experiments [133]. The enhanced Li^+ dynamics and atomic disorder found in the Li_4SiO_4-Li_3PO_4 SEs were correlated with the lithium diffusivity,

which were also in agreement with simulations. Similarly, multinuclear (^{1}H. ^{6}Li, ^{7}Li, and ^{31}P) solid-state NMR was used to show the structural evolution and Li dynamics of nanostructured Li_3PS_4, confirming high ionic conductivity on the order of 10^{-3} S/cm at 100 °C [62]. Scanning probe microscopy (SPM) approaches have also allowed for the study of voltage-controlled dynamics in ionically conductive solids with a spatial resolution below 10 nm [134]. In force-based SPM approaches, a cantilevered tip interacts with the surface of the SE or electrode, which serves as a mobile electrode and confines a small electrochemical potential to a nano-sized volume [65]. Using these newly-developed SPM approaches, Li^+ transport could be effectively mapped in Si/LiPON/$LiCoO_2$ thin-film batteries. Neutron powder diffraction has also played a key role in solving the long-range and local structure of many Li-ion conductors, especially the structural order associated with light elements [135], as well as the ordering between multiple transition metals [136]. Such detailed structural information provides the basis for the understanding of the Li conduction mechanism.

Different techniques have been particularly useful in interrogating the interface between electrodes and SEs. X-ray absorption spectroscopy **(**XAS) was used to investigate the local and electronic structure of the interface between LATP and LCO using depth-resolved XAS with a resolution of ~7 nm. This technique allowed for the interrogation of the chemical and electronic structure and the identification of decomposition products at the LATP/LCO interface [137]. Such interfaces also benefit from CV investigations, which provide valuable data relevance to the electrochemical window, performance, and processes occurring within an electrochemical system [9, 10, 138]. Recent *in situ* Raman scattering experiments have detailed the interface between sulfide-based solid electrolytes

and Au during lithium deposition and stripping, highlighting the dynamic interfacial structure evolution where the ionic framework breaks and reforms at the SE/electrode interface [131]. Small angle neutron scattering has also detailed the nanostructures formed within SE and at the SE/electrode interfaces [139], by which the size, morphology, and evolution of the nanostructure can be revealed. The formation of an SEI layer has also been observed *in situ* with neutron reflectometry [140]. The dynamical behavior in Li-ion conductors can be measured by quasielastic neutron scattering (for diffusion) [141] and inelastic neutron scattering (for vibration) [142], and the information obtained can be directly related to the local structure as well as Li ion transport.

1.4 Strategies to Improve Ionic Transport and Chemical Stability of Solid Electrolytes and Interfaces

SEs take part in multiple interfaces within electrochemical cells. As a result, different strategies must be employed to effectively reduce charge-transfer resistance at these interfaces. This section focused on potential strategies to improve ion transport, chemical stability, and interfaces of SEs. Strategies to improve ion conduction at the unit scale level are first discussed. The importance of mesoscale features and nanocomposite fabrication for SEs are elucidated. Lastly, passivation layers and their promise for reducing charge-transfer resistance at the interface in different SE systems are discussed.

1.4.1 Tuning ion conduction within SE materials

1.4.1.1 At the unit cell level

Manipulating the structure of a SE at the unit cell level is arguably the most common method of tuning its electrolyte properties. In most cases, cation substitution and/or cation or anion doping are exploited to tune the lattice volume, interstitial sites, and vacancies within different classes of SEs. In several structural families of SEs including NASICON-like [27, 143], LISICON-like [9, 144-147], garnet [26, 108, 148, 149], perovskite [28, 30, 150], antiperovskite [151, 152], amongst other families, the ionic size for cation diffusion and lattice volume play essential roles in governing the trends of ionic conductivity [153]. When the ionic radius and lattice volume achieve an optimal size, the diffusion coefficient for ion conduction reaches a maximum, boosting the ionic conductivity.

Of the reported descriptors of ionic conductivity, lattice dynamics and the volume of diffusion pathway represent some of the most commonly accepted parameters that govern ion conduction. Lattice dynamics refers to the study of atomic vibrations within a crystal lattice, which has been central to the branch of condensed matter physics. On the other hand, the volume of diffusion pathway refers to the volume accessible to the mobile ion within a crystal lattice, which can then be correlated to observed properties within solid-state ion conductors. The combination of these descriptors have allowed for a general understanding of SEs, where different material systems were screened to find new ion conductors [15, 18, 154-156]. The volume of diffusion pathway was also interrogated by bond valence method, where the main idea involves determining the valence of the chemical bonds within a crystalline or amorphous lattice and relating these bonds to the

percolating region through the solid [157-159]. The key to the bond valence method is to determine the bond valence mismatch of the mobile species in relation to the threshold for ion diffusion.

The careful choice of the anion host matrix and mobile ion can fine-tune the lattice dynamics and the volume of diffusion pathway within different SEs. By way of example, Aono *et al.* synthesized SEs based on the lithium titanium phosphate were synthesized with compositions $Li_{1+x}M_xTi_{2-x}(PO_4)_3$ (M = Al^{3+}, Cr^{3+}, Ga^{3+}, Fe^{3+}, Sc^{3+}, In^{3+}, Lu^{3+}, Y^{3+} and La^{3+}) where $Li_{1.3}M_{0.3}Ti_{1.7}(PO_4)_3$ (M = Al and Sc) holds the highest ionic conductivity of 0.7 mS/cm at 298 K [27]. Though GBs and density enhancement associated with the aliovelent cation substations affect the ionic conductivity, the concentration of lithium ions within the crystal lattice also plays a major role in tuning the ionic conductivity [160]. Within SE, there is a critical concentration of aliovalent cation substitution that will enhance the ionic conductivity, but past this concentration, the ionic conductivity will be suppressed due to passing the optimal concentration of mobile ions or extrinsic defects and increasing the migration energy for the mobile ion.

A more recent example of tuning the lattice dynamics and the volume of diffusion pathway involves anion exchange within the antiperovskite Li_2OHCl [152, 161]. At room temperature, Li_2OHCl holds an orthorhombic structure at room temperature and a cubic structure at increased temperatures. This phase transition was found to increase the ionic conductivity by at least two orders of magnitude [151, 152]. Li *et al.* have shown that substitution of OH^- with F^- to form $Li_2(OH)_{0.9}F_{0.1}Cl$ stabilizes the cubic phase at room temperature, standing in good agreement with the increased antiperovskite tolerance factor. The cubic Li_2OHCl phase has clear Li^+ vacancies through the structure, which form

triangular $O^{2-}(Cl)_2^-$ sites (Fig. 1.10B). In comparison to triangular $O^{2-}(Br)_2^-$ sites (Fig. 1.10C), the Cl-based structure has less steric hindrance and coulomb repulsion of the H ions, and when some OH^- is substituted with F^-, the number of hindering H^+ is also reduced, which explains the increased ionic conductivity of cubic $Li_2(OH)_{0.9}F_{0.1}Cl$.

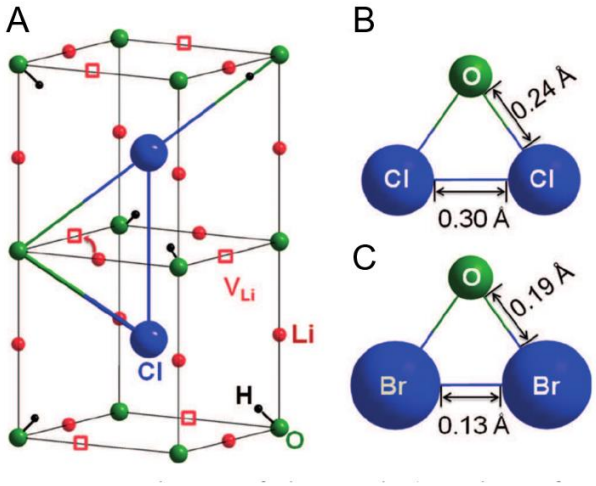

Figure 1.10 A) Crystal structure representation of cubic Li_2OHCl. Schematic of exchanging Cl with Br within the unit cell of Li_2OHCl [152]. Reprinted with permission; © 2016 WILEY-VCH Verlag GmbH & Co. KGaA, Weinheim.

1.4.1.2 Integration of mesoscopic features

Another general strategy for enhancing ionic conductivity in SE has involved optimizing the annealing or sintering temperatures, which was largely correlated with improving the density, grain size, and GBs of various SEs [26, 82, 153]. However, it turns out there is more to the story. Ma *et al.* recently demonstrated that LLTO holds mesoscopic features when annealed at different temperatures, revealing a new paradigm of general strategies for optimizing Li^+ transport [74]. Using a series of state-of-the-art STEM techniques, different percolation pathways were found within two LLTO samples, one with

a lower ionic conductivity annealed at 800 and one with a higher ionic conductivity annealed at 1350 °C (Fig. 1.11) [74]. Taking advantage of the high special resolution of STEM, the size of the percolation pathways could be measured with sub-Å resolution. Sophisticated molecular dynamics (MD) simulations were able to unambiguously reveal the pathways that the charge carrier would migrate through the different percolation sizes within the LLTO material (Fig. 1.11B), where Li^+ migration is more facile when the domain size for the percolation is minimal. It should be noted that the mesoscopic scale is rarely explored for SEs and necessitates future research for such features to be better understood [162-164].

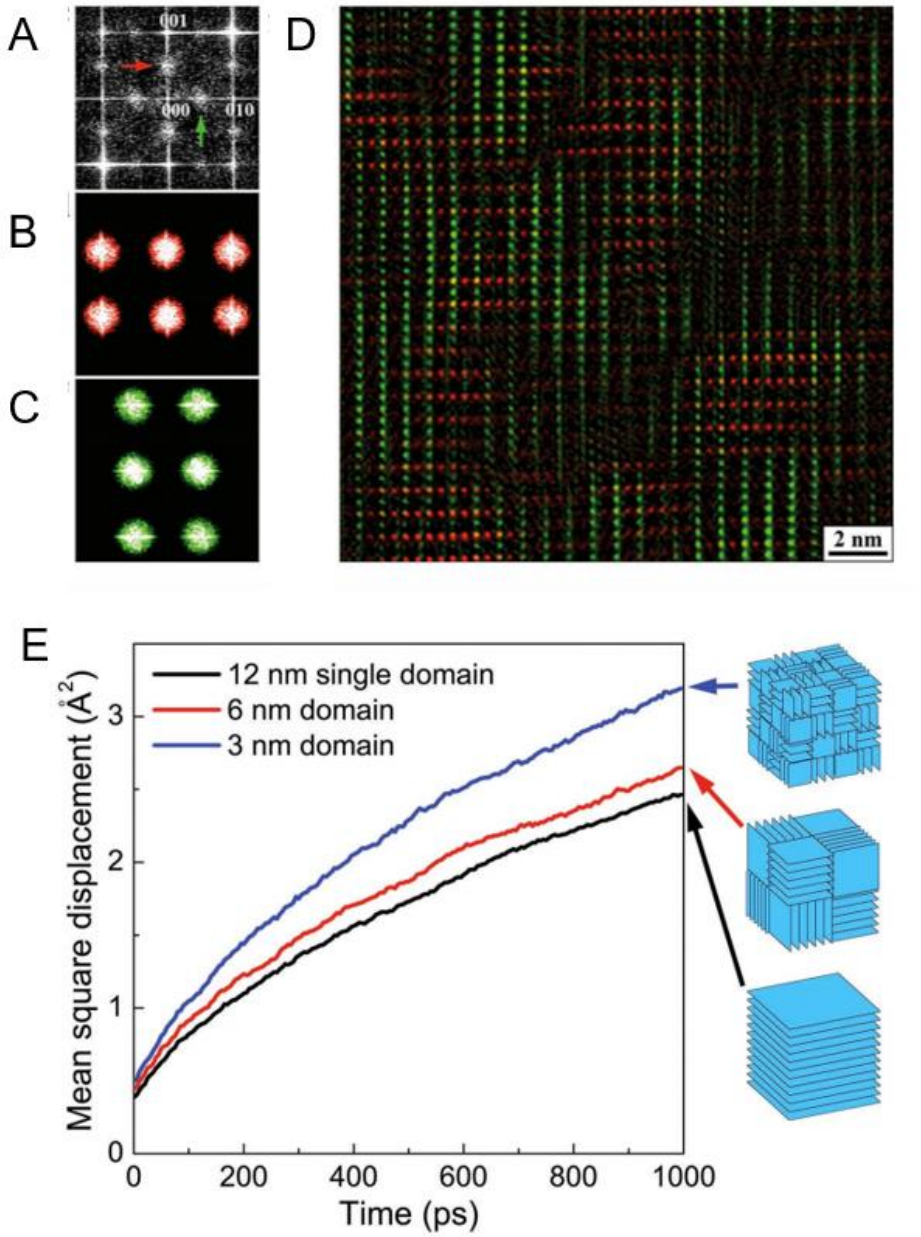

Figure 1.11 A) FFT pattern of LLTO with representative 1/2(eeo) and 1/2(eoe) spots donated with red and green arrows, respectively. B) Masked FFT pattern in (A), showing only 1/2(eeo) spots. C) Masked FFT pattern in (A), showing only 1/2(eoe) spots. D) Reconstructed atomic-resolution image by overlapping the inverse FFT in (B) and (C), displaying a clear mesoscopic framework. E) Molecular dynamics simulation of LLTO with different domain sizes, revealing that domain size affects the mobility of the mobile ion [74]. Reprinted with permission; © 2016 WILEY-VCH Verlag GmbH & Co. KGaA, Weinheim.

1.4.1.3 Integration of highly conductive interfaces

Beyond individual phases, forming nanocomposites between an ion conductor and an insoluble second phase represents another strategy to enhance ion conduction and stability of SEs, which has been reported by many groups. This approach takes advantage of the rich interfacial phenomena, including (1) interfacial phase formation, (2) enhanced ion conduction within the interfacial core, and (3) enhanced charge carrier concentration within the space-charge layer [165-174]. Nanocomposites of SEs are well-known for their enhanced lithium ion conductivity, where their ionic conductivity has been increased by one to three orders of magnitude [175-177]. The main concept, here, is that fine particles of a SE are processed with an insoluble second phase that enhances the charge carrier distribution or mobility, as shown in Fig. 1.12 [178]. Creating composites of SEs and electrode materials have also enhanced the battery performance in different all-solid-state battery configurations [101, 121, 179-182]. The combination of the different interfacial phenomena have been observed in more recent examples of composite SEs [178, 183-186], where the bulk ion conductivity and Arrhenius activation energy can be controllably tuned by varying the vol. % or wt. % of the insoluble second phase. The atomic origin of the interface between a SE and insoluble second phase could benefit from a closer examination with STEM with EELS, as these analyses are yet to be reported in literature.

The formation of polymer/ceramic nanocomposite electrolytes have also gained increased attention in recent years [3, 132, 187-192]. In some cases, inorganic lithium SEs can sometimes hold high interfacial resistance with metallic lithium anode, which is the case for some garnet-based electrolytes like LLZO [193, 194]. To mitigate this issue, a number of polymer/ceramic electrolytes have been successfully applied to stabilize a metallic lithium anode, with minimal interfacial resistance [61, 190, 195-197]. For

example, Zheng *et al.* recently demonstrated the utility of a PEO-LLZO-$LiClO_4$ composite electrolyte in a symmetric cell configuration (Fig. 1.13) [61]. Using solid-state NMR spectroscopy, the diffusion of ^6Li could be probed through the polymer/ceramic membranes, where the ^6Li ions preferentially moved through the ceramic rather than the interface or polymer fractions of the membrane. Altogether, the synergy between the different fractions within polymer/ceramic nanocomposites have improved battery performance for systems that utilize metallic lithium anode, yet such membranes necessitate closer examination with techniques with enhanced spatial resolution to resolve the ion conduction pathway.

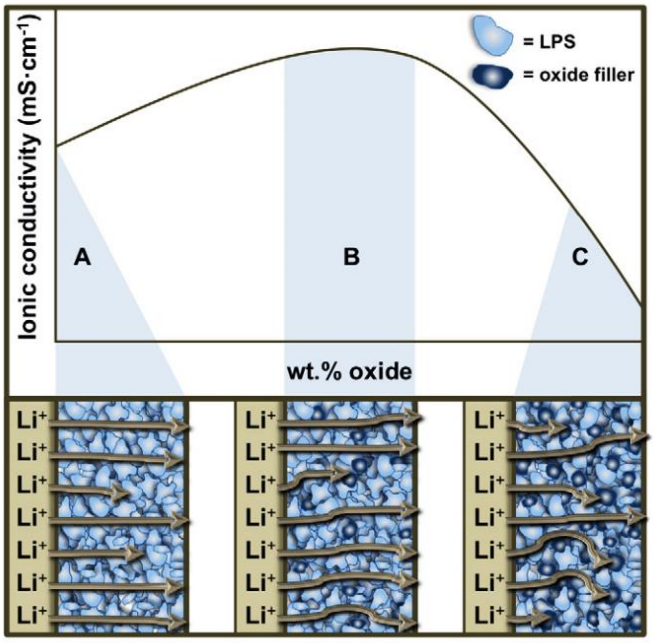

Figure 1.12 Schematic of the space-charge effect within the SE matrix when including oxide fillers in composite with nanoporous β-Li_3PS_4 (A: no oxide filler; B: enough oxide filler to improve ionic conduction; C: blocking effects of the oxide filler) [178]. Reprinted with permission; © 2015 Elsevier.

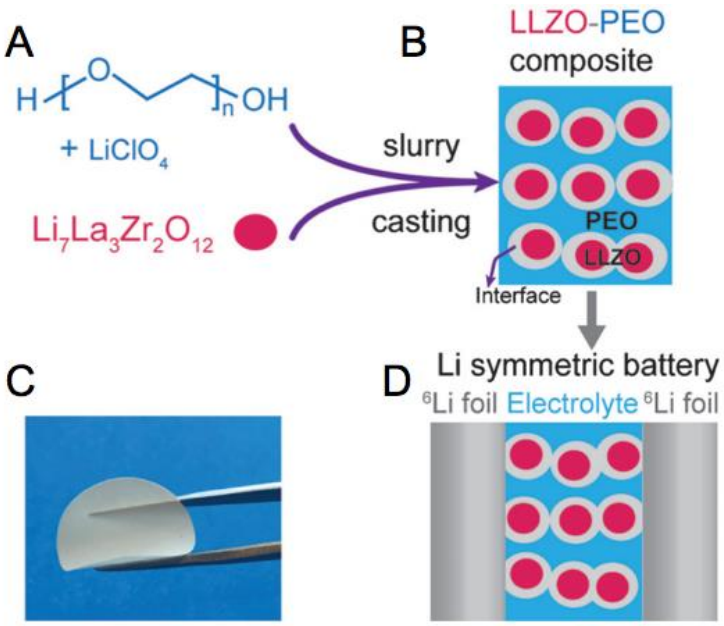

Figure 1.13 A-B) Schematic of PEO-LLZO-$LiClO_4$ composite fabrication through slurry casting of the materials in anhydrous acetonitrile. C) Image of the flexible SE membrane and D) Schemtic of the symmetric cell used for solid-state NMR studies [61]. Reprinted with permission; © 2016 WILEY-VCH Verlag GmbH & Co. KGaA, Weinheim.

1.4.2 Forming conductive and stable electrode/SE interfaces

1.4.2.1 Li/SE interfaces using self-forming passivation layers

Of the reported descriptors for SEs, parameters that describe the interface between a SE and different electrode materials are still necessitated. One of the most important properties is the electrochemical stability window for SEs, which largely dictates how the resulting electrochemical device will perform. At the interface between SEs and electrodes, interfacial reactions are prone to occur that can form a SEI layer, yet theory cannot accurately predict the thickness of such layers. For batteries employing lithium conducting SEs, a metallic lithium anode is used for its increased theoretical capacity (3860 mAh g^{-1})

and low electrochemical potential [198, 199]. However, the strong reducing power of the metallic lithium anode can cause the electrolyte to become an electronic conductor, an interface layer with high impedance may form, or an interface layer with low impedance may form, where the latter is the ideal situation. A recent example of this phenomenon is presented in Fig. 1.14, where Li_2OHCl was used as a SE with metallic lithium anode [151]. After cycling in a symmetric cell configuration at 195 °C using a current density of 1.0 mA/cm^2, the SE membrane was able to cycle without a significant increase in the interfacial resistance. A relatively thick SEI layer of ~50 μm existed between the metallic lithium anode and Li_2OHCl, which was found to stabilize the molten lithium anode. A much thinner passivation layer was recently found for the Li/c-LLZO interface, as described in Section 3.2, which was also found to stabilize a metallic lithium anode [104]. Though theory predicts that a number of decomposition reactions will form at interfaces between different electrodes and SEs, SEI layers have been theoretically predicted and experimentally shown to improve the electrochemical stability window of multiple SEs [57, 100, 119, 200].

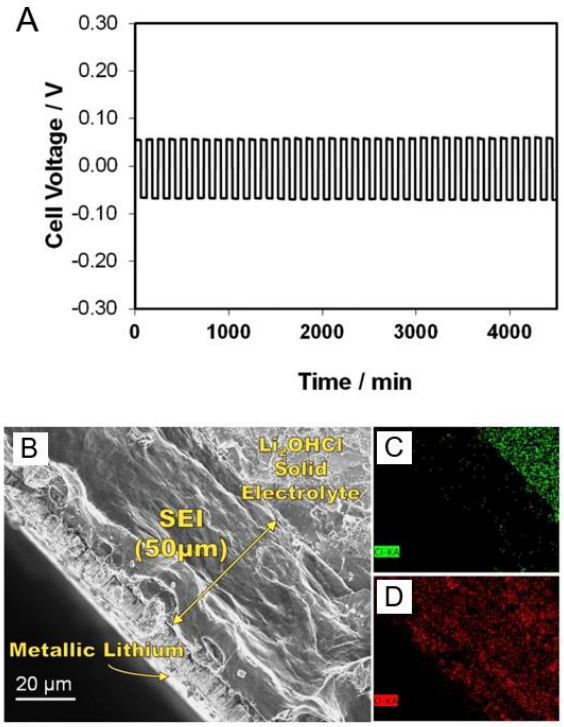

Figure 1.14 Formation of a stable SEI *in situ* with molten lithium anode. A) Symmetric Li/Li_2OHCl/Li cell cycling at 195 °C using a current density of 1.0 mA/cm^2. B) SEM image of the Li/Li_2OHCl interface displaying clear SEI formation. EDS elemental mapping of C) Cl and D) O shows that the SEI is oxygen rich [151]. Reprinted with permission; © 2016 American Chemical Society.

1.4.2.2 Intentionally adding a passivation layer at SE/electrode interface to push the electrochemical window

Different techniques have been employed to fabricate thin passivation layers at the interface between SEs and electrodes, including radio frequency (RF) sputtering [201-203], pulsed laser deposition (PLD) [120, 204, 205], atomic layer deposition (ALD) [206-209], chemical vapor deposition (CVD) [210], sol-gel methods [101], and coating polymers or different ceramics using hot pressing or wet chemical methods [211-213]. The main goal of these passivation layers is to reduce the charge-transfer resistance at the interface, extend the electrochemical window, and improving the wettability between the SE and the anode

material. A recent example of the combination of these ideal properties was shown by Han *et al.*, where a thin Al_2O_3 interlayer was grown by ALD on the garnet-based $Li_7La_{2.75}Ca_{0.25}Zr_{1.75}Nb_{0.25}O_{12}$, improving the charge-transfer between a lithium anode and the SE (Fig. 1.15) [206]. This reduction in interfacial impedance was evidenced by both EIS and symmetric cell cycling experiments to test the lithium stripping and plating at the interface. At a current density of 0.2 mS/cm^2, the materials were able to cycle well when the thin Al_2O_3 interlayer was present, agreeing with reports of sodiated and lithiatied Al_2O_3 [214-217]. Other recent reports of improving the lithium wetting have also shown the enhancing cycling performance of SEs with metallic lithium anodes [69, 208, 210, 218]. It is expected that similar ALD methodology will allow for careful tuning of the interfacial chemistry with different SEs.

Artificial passivation layers composed of LiPON have also been successfully used to improve charge-transfer resistance in different electrochemical systems, one of which involves Si electrodes (Fig. 1.16). A major concern with Si as an electrode material is the electrochemical degradation, which general compromises the reversible capacity in different battery cells. To avert these problems, Li *et al.* demonstrated that an artificial SEI layer composed of LiPON from RF sputtering could circumvent the electrochemical degradation of Si anodes [202]. A critical thickness of 45-50 nm of LiPON coatings were necessary to suppress the electrochemical degradation of Si anodes. At thicknesses <50 nm, LiPON was found to be a mixed conductor, which allows for the flow of both electrons and Li ions to the Si anode, explaining the electrolyte decomposition and reduction in reversible capacity in cells [202]. The deposition of LiPON was also recently shown to suppress charge-transfer resistance in thin-film batteries at the cathode. Using a nitrogen-

rich Li_2PO_2N source, West *et al.* demonstrated that thin layers of LiPON could be deposited onto high-capacity cathodes such as $LiMn_{1.485}Ni_{0.45}Cr_{0.05}O_4$ (LMN) using PLD, which significantly reduced the charge-transfer resistance [120, 219]. This reduction in charge-transfer resistance was attributed to a careful control of the chemistry of the LiPON film while forming a strongly bound interface between the SE and cathode.

Polymers have also been widely investigated to improve the stability between SEs and high-capacity anodes such as metallic lithium [1]. A cross-linked poly(ethylene glycol) methyl ether acrylate (CPMEA) polymer was recently developed by Zhou *et al.* and employed in a novel polymer/ceramic/polymer sandwich electrolyte (PCPSE), as shown in Fig. 1.17 [189]. This sandwich electrolyte combines the high ionic conductivity of the NASICON-like $Li_{1.3}Al_{0.3}Ti_{1.7}(PO_4)_3$ and the electrochemical compatibility of the polymer. Notably, the ceramic membrane also blocked the polymer salt anion from degrading the interface at the lithium anode, which improved electrochemical cycling using this unique architecture [189].

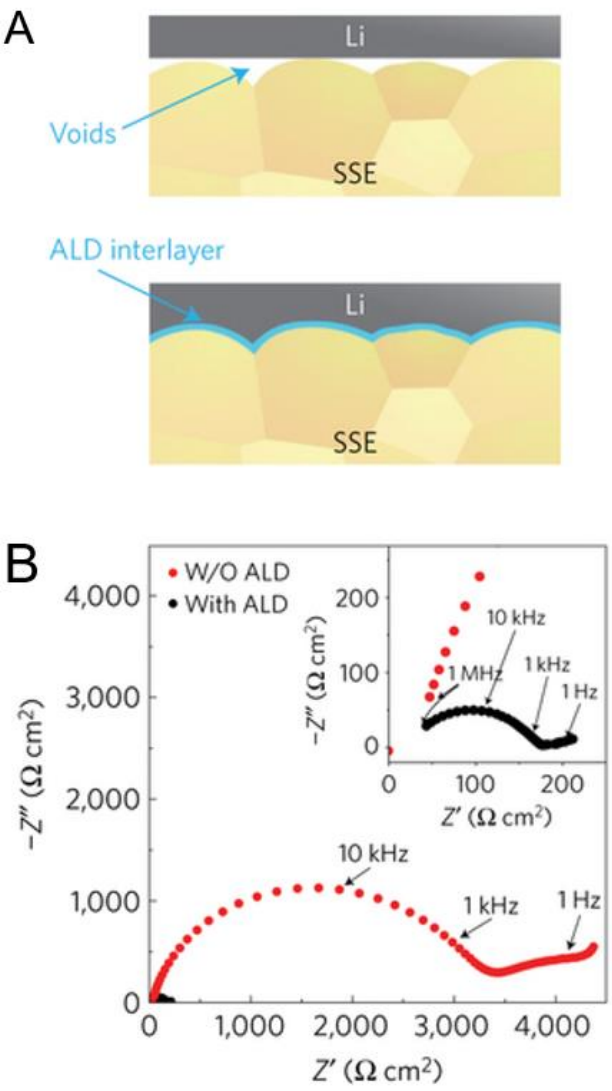

Figure 1.15 A) Illustration of the metallic lithium wetting behavior on a garnet-based solid-state electrolyte with and without an Al_2O_3 layer deposited by ALD. B) EIS profiles of symmetric Li non-blocking garnet cells with and without an Al_2O_3 layer deposited by ALD [206]. Reprinted with permission; © 2017 Nature Publishing Group.

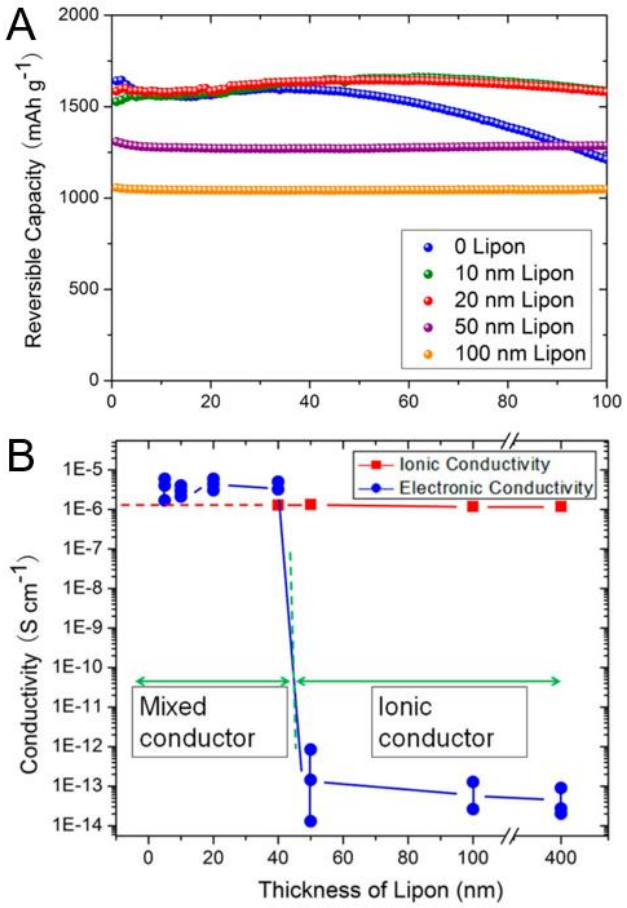

Figure 1.16 Artificial LiPON coatings for Si anodes. A) Reversible (delithiation) capacity for Si anodes with different thickness of LiPON coating; B) ionic and electron conductivities of ultrathin LiPON [202]. Reprinted with permission; © 2014 American Chemical Society.

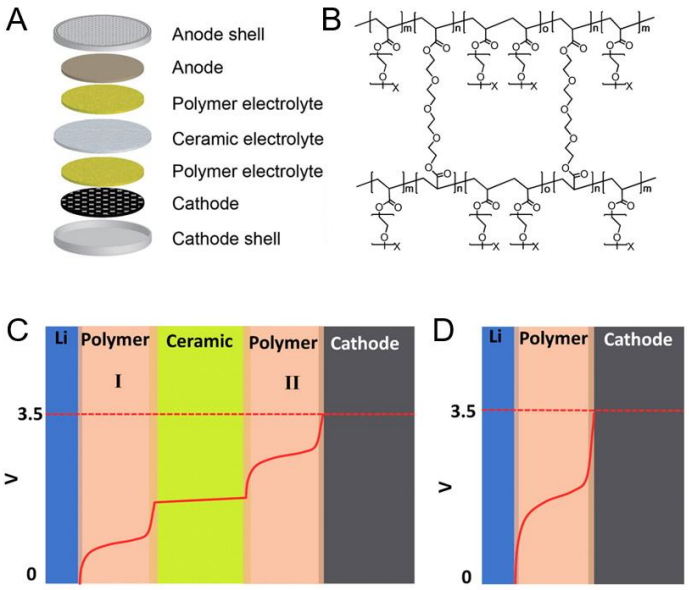

Figure 1.17 A) Schematic of all-solid-state battery design and B) structure of the PCPSE electrolyte. C) Illustration of the electrical potential profile when using the C) sandwich polymer electrolyte and D) individual polymer electrolyte in a typical Li/$LiFePO_4$ cell [189]. Reprinted with permission; © 2016 American Chemical Society.

1.4.2.3 Minimizing the conduction barrier by modifying space charge

Different mechanisms have been reported in the literature to explain the interfacial resistance at the electrode/SE interface [96, 194, 220-225]. One of these mechanisms includes the formation of space charge layers at the interface between oxide-based cathodes and sulfide-based SEs. An example of such a layer was computationally demonstrated with the LPS/LCO interface, where juxtaposing an LNO layer between the cathode and SE suppresses the growth of the space charge layer which improves the overall lithium conduction at this interface, as discussed in Section 1.3.3 of this chapter [126]. Upon the initial charge of LPS/LCO interfaces, first principles calculations suggest that a space charge layer growth increases the interfacial resistance between the cathode and SE, which

hinders ionic diffusion at this interface. Still, direct measurements of space charge layers have been difficult due to the limited atomic resolution of many experimental techniques, and further closer examination of electrode/SE interfaces will only the mechanistic understanding of the interfacial phenomena.

Strategies to improve the interfaces associated with SE have not only enhanced battery performance, but have also outlined practical methods to advance our mechanistic understanding of interfacial phenomena, which is currently far underdeveloped. In fact, much is still unknown as to the root interfacial phenomena at electrode/SE interfaces and their correlation with chemical, electrochemical, and mechanical stabilities at interfaces. Additionally, little is known as to the correlation between interfacial phenomena occurring during the formation of interfaces or interfacial layers, and more crucially, the dynamic behavior of the interfacial phenomena during electrochemical cycling.

1.5 Scope of this Work

The aim of this work is to achieve a mechanistic understanding of different oxide- and sulfide-based solid electrolytes in order to pave the way to the design of high-performance SE-based batteries. Despite the significant progress in the last few decades, the increased impedance at interfaces associated with SEs, *i.e.*, internal grain and phase boundaries, and their interfacial stability with electrodes, are currently two key factors limiting the performance of batteries involving SEs. In this Dissertation, different strategies and materials were investigated to improve ion conduction and stability in SEs and at interfaces. This Dissertation largely focuses on new sulfide- and oxide-based SEs, including β-Li_3PS_4, $Li_4P_2S_6$, Li_2OHCl, and $Na_4P_2S_6$. Different synthetic and processing

strategies were employed to synthesize these new SEs and understand their electrochemical performance in all-solid-state batteries with metallic lithium or sodium anode.

In Chapter 2, I describe a strategy for improving ion conduction in nanostructured β-Li_3PS_4 through the formation of nanocomposites with oxide-based fillers. Nanostructured LPS was recently shown to have anomalous high ionic conductivity, and it was found that this property could be further enhanced. This study examines the effect of three solid oxide fillers ($Li_6ZnNb_4O_{14}$, Al_2O_3, and SiO_2) in composites with β-Li_3PS_4 for the enhancement of the parent electrolyte. The processability, ionic conductivity, activation energy and stability against metallic lithium of each composite electrolyte are presented to gain a deep understanding of the effect of solid oxide fillers on LPS while elucidating the significant enhancement of β-Li_3PS_4 through the addition of $Li_6ZnNb_4O_{14}$ and Al_2O_3.

In Chapter 3, I describe a new method for the production of ultrathin films of β-Li_3PS_4. The potential of using ultrathin films is among the best merits of solid electrolytes that can considerably reduce the weight and volume of each battery unit, therefore, significantly enhancing the energy density, which is notably important for electric vehicles. However, it is generally challenging to fabricate ultrathin solid electrolyte membranes using low-cost methodologies. In this chapter, I report a new strategy for fabricating submicron-thick membranes of β-Li_3PS_4 solid electrolytes via tiled assembly of shape-controlled, nanoscale building blocks. This method is based on facile and low-cost solution-based soft chemistry to create membranes with tunable thicknesses. These ultrathin β-Li_3PS_4 membranes show desirable ionic conductivity and necessary compatibility with metallic lithium anode. These results highlight a new strategy of

creating ultrathin, dense solid electrolytes with high ionic conductivities for next-generation energy storage and conversion systems.

In Chapter 4, I investigate the structural and electrolyte properties of $Li_4P_2S_6$ through a combination of experimental and theoretical investigations. Experiment and simulations are used to investigate the structural and electrolyte properties of $Li_4P_2S_6$. Compared with other thiophosphate materials, $Li_4P_2S_6$ is quite stable, maintaining its crystal structure up to temperatures as high as 950 °C in vacuum and up to 280 °C in air. While its ionic conductivity is low, 2.38×10^{-7} S/cm at 25 °C and 2.33×10^{-6} S/cm at 100 °C, its Arrhenius activation energy of 0.29 eV is similar to technologically viable electrolytes. Computer simulations provide insight into the causes and effects of disorder in this material and also suggest that the mechanism of the ion conduction is dominated by interstitial sites.

In Chapter 5, I investigate the LiOH-LiCl system of electrolytes and their compatibility with metallic lithium anode. In a classic example of stability from instability, it is shown that Li_2OHCl solid electrolyte forms a stable solid electrolyte interphase (SEI) layer with a metallic lithium anode. Li_2OHCl solid electrolyte can be readily achieved through simple mixing of LiOH and LiCl precursors at a mild processing temperature <400 °C. Additionally, it is shown that continuous, dense Li_2OHCl membranes can be fabricated at temperatures <400 °C, standing in great contrast to current processing temperatures of >1600 °C for most oxide-based solid electrolytes. The ionic conductivity and Arrhenius activation energy were explored for the LiOH–LiCl system of crystalline solid electrolytes, where Li_2OHCl with increased crystal defects was found to have the highest ionic conductivity and reasonable Arrhenius activation energy. The Li_2OHCl solid

electrolyte displays stability against metallic lithium, even in extreme conditions past the melting point of lithium metal. To understand this excellent stability, it is shown that SEI formation is critical in stabilizing the interface between metallic lithium and the Li_2OHCl solid electrolyte.

In Chapter 6, I explore a new sulfide-based sodium conductor, $Na_4P_2S_6$. The design of the solid electrolyte $Na_4P_2S_6$ is described, realizing excellent air stability and an economic soft chemistry synthetic approach in the presence of water. This material is also shown to reversibly exchange water without degradation of its electrochemical performance. Nanocrystalline $Na_4P_2S_6$ is also shown to hold compatibility with high-capacity metallic sodium anode. Solution-based soft-chemistry approaches to synthesizing nanostructured sodium solid electrolytes has a far-reaching impact on next-generation Na-ion technologies with a broad range of applications, including batteries, sensors, photovoltaic devices, and so on.

This Dissertation concludes by highlighting opportunities and perspectives for future research that will achieve an enhanced understanding of SEs and bridge the gap between the mechanistic understanding of SEs and their electrochemical performance in different battery configurations.

1.6 Notes to Chapter 1

Part of this chapter is adapted from the following references: [12, 151, 178]

1.7 References

[1] Dudney, N. J.; West, W. C.; Nanda, J. Handbook of Solid State Batteries; *World Scientific*, **2016**.

[2] Hagenmuller, P.; Van Gool, W. Solid Electrolytes: General Principles, Characterization, Materials, Applications; *Elsevier*, **2015**.

[3] Quartarone, E.; Mustarelli, P. Electrolytes for solid-state lithium rechargeable batteries: recent advances and perspectives. *Chemical Society Reviews* **2011**, *40*, 2525-2540.

[4] Ngai, K. S.; Ramesh, S.; Ramesh, K.; Juan, J. C. A review of polymer electrolytes: fundamental, approaches and applications. *Ionics* **2016**, *22*, 1259-1279.

[5] Barghamadi, M.; Best, A. S.; Bhatt, A. I.; Hollenkamp, A. F.; Musameh, M.; Rees, R. J.; Rüther, T. Lithium–sulfur batteries—the solution is in the electrolyte, but is the electrolyte a solution? *Energy & Environmental Science* **2014**, *7*, 3902-3920.

[6] Berbano, S. S.; Mirsaneh, M.; Lanagan, M. T.; Randall, C. A. Lithium Thiophosphate Glasses and Glass–Ceramics as Solid Electrolytes: Processing, Microstructure, and Properties. *International Journal of Applied Glass Science* **2013**, *4*, 414-425.

[7] Yamane, H.; Shibata, M.; Shimane, Y.; Junke, T.; Seino, Y.; Adams, S.; Minami, K.; Hayashi, A.; Tatsumisago, M. Crystal structure of a superionic conductor, $Li_7P_3S_{11}$. *Solid State Ionics* **2007**, *178*, 1163-1167.

[8] Kuhn, A.; Duppel, V.; Lotsch, B. V. Tetragonal $Li_{10}GeP_2S_{12}$ and Li_7GePS_8–exploring the Li ion dynamics in LGPS Li electrolytes. *Energy & Environmental Science* **2013**, *6*, 3548-3552.

[9] Kamaya, N.; Homma, K.; Yamakawa, Y.; Hirayama, M.; Kanno, R.; Yonemura, M.; Kamiyama, T.; Kato, Y.; Hama, S.; Kawamoto, K. A lithium superionic conductor. *Nature Materials* **2011**, *10*, 682-686.

[10] Seino, Y.; Ota, T.; Takada, K.; Hayashi, A.; Tatsumisago, M. A sulphide lithium super ion conductor is superior to liquid ion conductors for use in rechargeable batteries. *Energy & Environmental Science* **2014**, *7*, 627-631.

[11] Liu, Z.; Fu, W.; Payzant, E. A.; Yu, X.; Wu, Z.; Dudney, N. J.; Kiggans, J.; Hong, K.; Rondinone, A. J.; Liang, C. Anomalous high ionic conductivity of nanoporous *β*-Li_3PS_4. *Journal of the American Chemical Society* **2013**, *135*, 975-978.

[12] Hood, Z. D.; Kates, C.; Kirkham, M.; Adhikari, S.; Liang, C.; Holzwarth, N. Structural and electrolyte properties of $Li_4P_2S_6$. *Solid State Ionics* **2016**, *284*, 61-70.

[13] Wang, H.; Hood, Z. D.; Xia, Y.; Liang, C. Fabrication of ultrathin solid electrolyte membranes of β-Li_3PS_4 nanoflakes by evaporation-induced self-assembly for all-solid-state batteries. *Journal of Materials Chemistry A* **2016**, *4*, 8091-8096.

[14] Rao, R. P.; Adams, S. Studies of lithium argyrodite solid electrolytes for all-solid-state batteries. *Physica Status Solidi (a)* **2011**, *208*, 1804-1807.

[15] Wang, Y.; Richards, W. D.; Ong, S. P.; Miara, L. J.; Kim, J. C.; Mo, Y.; Ceder, G. Design principles for solid-state lithium superionic conductors. *Nature Materials* **2015**.

[16] Lepley, N.; Holzwarth, N.; Du, Y. A. Structures, Li^+ mobilities, and interfacial properties of solid electrolytes Li_3PS_4 and Li_3PO_4 from first principles. *Physical Review B* **2013**, *88*, 104103.

[17] Dathar, G. K. P.; Balachandran, J.; Kent, P. R.; Rondinone, A. J.; Ganesh, P. Li-ion site disorder driven superionic conductivity in solid electrolytes: a first-principles investigation of β-Li_3PS_4. *Journal of Materials Chemistry A* **2017**.

[18] Richards, W. D.; Wang, Y.; Miara, L. J.; Kim, J. C.; Ceder, G. Design of $Li_{1+2x}Zn_{1-x}PS_4$, a new lithium ion conductor. *Energy & Environmental Science* **2016**, *9*, 3272-3278.

[19] Howard, J.; Holzwarth, N. First-principles simulations of the porous layered calcogenides $Li_{2+x}SnO_3$ and $Li_{2+x}SnS_3$. *Physical Review B* **2016**, *94*, 064108.

[20] Al-Qawasmeh, A.; Howard, J.; Holzwarth, N. Li_4SnS_4 and Li_4SnSe_4: Simulations of Their Structure and Electrolyte Properties. *Journal of The Electrochemical Society* **2017**, *164*, A6386-A6394.

[21] Mo, Y.; Ong, S. P.; Ceder, G. First principles study of the $Li_{10}GeP_2S_{12}$ lithium super ionic conductor material. *Chemistry of Materials* **2011**, *24*, 15-17.

[22] Yang, Y.; Wu, Q.; Cui, Y.; Chen, Y.; Shi, S.; Wang, R.-Z.; Yan, H. Elastic Properties, Defect Thermodynamics, Electrochemical Window, Phase Stability, and Li^+ Mobility of Li_3PS_4: Insights from First-Principles Calculations. *ACS Applied Materials & Interfaces* **2016**, *8*, 25229-25242.

[23] (23) Wang, X.; Xiao, R.; Li, H.; Chen, L. Oxygen-driven transition from two-dimensional to three-dimensional transport behaviour in β-Li_3PS_4 electrolyte. *Physical Chemistry Chemical Physics* **2016**, *18*, 21269-21277.

[24] Holzwarth, L. E. R. J.; N.A.W. First Principles invesitgation of the structural and electrochemical properties of $Na_4P_2S_6$ and $Li_4P_2S_6$. *Solid State Ionics* **2016**, *286*, 45-50.

[25] Weber, D. A.; Senyshyn, A.; Weldert, K. S.; Wenzel, S.; Zhang, W.; Kaiser, R.; Berendts, S.; Janek, J. r.; Zeier, W. G. Structural insights and 3D diffusion pathways within the lithium superionic conductor $Li_{10}GeP_2S_{12}$. *Chemistry of Materials* **2016**, *28*, 5905-5915.

[26] Wolfenstine, J.; Rangasamy, E.; Allen, J. L.; Sakamoto, J. High conductivity of dense tetragonal $Li_7La_3Zr_2O_{12}$. *Journal of Power Sources* **2012**, *208*, 193-196.

[27] Aono, H.; Sugimoto, E.; Sadaoka, Y.; Imanaka, N.; Adachi, G. y. Ionic conductivity of solid electrolytes based on lithium titanium phosphate. *Journal of the Electrochemical Society* **1990**, *137*, 1023-1027.

[28] Inaguma, Y.; Liquan, C.; Itoh, M.; Nakamura, T.; Uchida, T.; Ikuta, H.; Wakihara, M. High ionic conductivity in lithium lanthanum titanate. *Solid State Communications* **1993**, *86*, 689-693.

[29] Bohnke, O.; Bohnke, C.; Fourquet, J. Mechanism of ionic conduction and electrochemical intercalation of lithium into the perovskite lanthanum lithium titanate. *Solid State Ionics* **1996**, *91*, 21-31.

[30] Stramare, S.; Thangadurai, V.; Weppner, W. Lithium lanthanum titanates: a review. *Chemistry of materials* **2003**, *15*, 3974-3990.

[31] Boukamp, B.; Huggins, R. Fast ionic conductivity in lithium nitride. *Materials Research Bulletin* **1978**, *13*, 23-32.

[32] Whittingham, M. S.; Huggins, R. A. Measurement of sodium ion transport in beta alumina using reversible solid electrodes. *The Journal of Chemical Physics* **1971**, *54*, 414-416.

[33] Li, J.; Ma, C.; Chi, M.; Liang, C.; Dudney, N. J. Solid Electrolyte: the Key for High-Voltage Lithium Batteries. *Advanced Energy Materials* **2015**, *5*.

[34] Goodenough, J. B.; Singh, P. Review—Solid Electrolytes in Rechargeable Electrochemical Cells. *Journal of The Electrochemical Society* **2015**, *162*, A2387-A2392.

[35] Thangadurai, V.; Narayanan, S.; Pinzaru, D. Garnet-type solid-state fast Li ion conductors for Li batteries: critical review. *Chemical Society Reviews* **2014**, *43*, 4714-4727.

[36] Wu, B.; Wang, S.; Evans IV, W. J.; Deng, D. Z.; Yang, J.; Xiao, J. Interfacial behaviours between lithium ion conductors and electrode materials in various battery systems. *Journal of Materials Chemistry A* **2016**, *4*, 15266-15280.

[37] Bachman, J. C.; Muy, S.; Grimaud, A.; Chang, H.-H.; Pour, N.; Lux, S. F.; Paschos, O.; Maglia, F.; Lupart, S.; Lamp, P. Inorganic Solid-State Electrolytes for Lithium Batteries: Mechanisms and Properties Governing Ion Conduction. *Chemical Reviews* **2015**, *116*, 140-162.

[38] Lin, Z.; Liang, C. Lithium–sulfur batteries: from liquid to solid cells. *Journal of Materials Chemistry A* **2015**, *3*, 936-958.

[39] Park, J. H.; Suh, K.; Rohman, M. R.; Hwang, W.; Yoon, M.; Kim, K. Solid lithium electrolytes based on an organic molecular porous solid. *Chemical Communications* **2015**, *51*, 9313-9316.

[40] Ren, Y.; Chen, K.; Chen, R.; Liu, T.; Zhang, Y.; Nan, C. W. Oxide electrolytes for lithium batteries. *Journal of the American Ceramic Society* **2015**, *98*, 3603-3623.

[41] Varzi, A.; Raccichini, R.; Passerini, S.; Scrosati, B. Challenges and prospects of the role of solid electrolytes in the revitalization of lithium metal batteries. *Journal of Materials Chemistry A* **2016**, *4*, 17251-17259.

[42] Sun, C.; Liu, J.; Gong, Y.; Wilkinson, D. P.; Zhang, J. Recent advances in all-solid-state rechargeable lithium batteries. *Nano Energy* **2017**.

[43] Chen, R.; Qu, W.; Guo, X.; Li, L.; Wu, F. The pursuit of solid-state electrolytes for lithium batteries: from comprehensive insight to emerging horizons. *Materials Horizons* **2016**, *3*, 487-516.

[44] Minh, N. Q. Ceramic fuel cells. *Journal of the American Ceramic Society* **1993**, *76*, 563-588.

[45] Traversa, E. Ceramic sensors for humidity detection: the state-of-the-art and future developments. *Sensors and Actuators B: Chemical* **1995**, *23*, 135-156.

[46] Bates, J.; Dudney, N.; Neudecker, B.; Ueda, A.; Evans, C. Thin-film lithium and lithium-ion batteries. *Solid State Ionics* **2000**, *135*, 33-45.

[47] Jensen, J.; Krebs, F. C. From the bottom up–flexible solid state electrochromic devices. *Advanced Materials* **2014**, *26*, 7231-7234.

[48] Armand, M.; Tarascon, J.-M. Building better batteries. *Nature* **2008**, *451*, 652-657.

[49] Girishkumar, G.; McCloskey, B.; Luntz, A.; Swanson, S.; Wilcke, W. Lithium−air battery: Promise and challenges. *The Journal of Physical Chemistry Letters* **2010**, *1*, 2193-2203.

[50] Rao, Z.; Wang, S. A review of power battery thermal energy management. *Renewable and Sustainable Energy Reviews* **2011**, *15*, 4554-4571.

[51] Dunn, B.; Kamath, H.; Tarascon, J.-M. Electrical energy storage for the grid: a battery of choices. *Science* **2011**, *334*, 928-935.

[52] Subbarao, E. Solid electrolytes and their applications. *Springer Science & Business Media*, 2012.

[53] Pearse, A. J.; Schmitt, T. E.; Fuller, E. J.; El-Gabaly, F.; Lin, C.-F.; Gerasopoulos, K.; Kozen, A. C.; Talin, A. A.; Rubloff, G.; Gregorcyzck, K. E. Nanoscale Solid State Batteries Enabled By Thermal Atomic Layer Deposition of a Lithium Polyphosphazene Solid State Electrolyte. *arXiv preprint arXiv:1702.04009* **2017**.

[54] Wan, T.; Zhang, L.; Du, H.; Lin, X.; Qu, B.; Xu, H.; Li, S.; Chu, D. Recent Developments in Oxide-Based Ionic Conductors: Bulk Materials, Nanoionics, and Their Memory Applications. *Critical Reviews in Solid State and Materials Sciences* **2016**, 1-36.

[55] Dudney, N. J. Solid-state thin-film rechargeable batteries. *Materials Science and Engineering: B* **2005**, *116*, 245-249.

[56] Lai, W.; Erdonmez, C. K.; Marinis, T. F.; Bjune, C. K.; Dudney, N. J.; Xu, F.; Wartena, R.; Chiang, Y. M. Ultrahigh-Energy-Density Microbatteries Enabled by New Electrode Architecture and Micropackaging Design. *Advanced Materials* **2010**, *22*.

[57] Richards, W. D.; Miara, L. J.; Wang, Y.; Kim, J. C.; Ceder, G. Interface stability in solid-state batteries. *Chemistry of Materials* **2015**, *28*, 266-273.

[58] Janek, J.; Zeier, W. G. A solid future for battery development. *Nature Energy* **2016**, *1*, 16141.

[59] Luntz, A. C.; Voss, J.; Reuter, K. Interfacial Challenges in Solid-State Li Ion Batteries. *The Journal of Physical Chemistry Letters* **2015**, *6*, 4599-4604.

[60] Zhu, Y.; He, X.; Mo, Y. Origin of outstanding stability in the lithium solid electrolyte materials: insights from thermodynamic analyses based on first-principles calculations. *ACS Applied Materials & Interfaces* **2015**, *7*, 23685-23693.

[61] Zheng, J.; Tang, M.; Hu, Y. Y. Lithium Ion Pathway within $Li_7La_3Zr_2O_{12}$-Polyethylene Oxide Composite Electrolytes. *Angewandte Chemie* **2016**, *128*, 12726-12730.

[62] Gobet, M.; Greenbaum, S.; Sahu, G.; Liang, C. Structural Evolution and Li Dynamics in Nanophase Li_3PS_4 by Solid-State and Pulsed-Field Gradient NMR. *Chemistry of Materials* **2014**, *26*, 3558-3564.

[63] Blanc, F.; Leskes, M.; Grey, C. P. In situ solid-state NMR spectroscopy of electrochemical cells: batteries, supercapacitors, and fuel cells. *Accounts of Chemical Research* **2013**, *46*, 1952-1963.

[64] Pecher, O.; Carretero-González, J.; Griffith, K. J.; Grey, C. P. Materials' methods: NMR in battery research. **2017**.

[65] Black, J.; Strelcov, E.; Balke, N.; Kalinin, S. V. Electrochemistry at the Nanoscale: The Force Dimension. *The Electrochemical Society Interface* **2014**, *23*, 53-59.

[66] Balke, N.; Jesse, S.; Kim, Y.; Adamczyk, L.; Tselev, A.; Ivanov, I. N.; Dudney, N. J.; Kalinin, S. V. Real space mapping of Li-ion transport in amorphous Si anodes with nanometer resolution. *Nano Letters* **2010**, *10*, 3420-3425.

[67] Kobayashi, T.; Yamada, A.; Kanno, R. Interfacial reactions at electrode/electrolyte boundary in all solid-state lithium battery using inorganic solid electrolyte, thio-LISICON. *Electrochimica Acta* **2008**, *53*, 5045-5050.

[68] Bron, P.; Roling, B.; Dehnen, S. Impedance characterization reveals mixed conducting interphases between sulfidic superionic conductors and lithium metal electrodes. *Journal of Power Sources* **2017**, *352*, 127-134.

[69] Basappa, R. H.; Ito, T.; Yamada, H. Contact between Garnet-Type Solid Electrolyte and Lithium Metal Anode: Influence on Charge Transfer Resistance and Short Circuit Prevention. *Journal of The Electrochemical Society* **2017**, *164*, A666-A671.

[70] Mehrer, H.: *Diffusion in solids: fundamentals, methods, materials, diffusion-controlled processes*; Springer Science & Business Media, 2007; Vol. 155.

[71] Hong, H.-P. Crystal structure and ionic conductivity of $Li_{14}Zn(GeO_4)_4$ and other new Li^+ superionic conductors. *Materials Research Bulletin* **1978**, *13*, 117-124.

[72] Goodenough, J.; Hong, H.-P.; Kafalas, J. Fast Na^+-ion transport in skeleton structures. *Materials Research Bulletin* **1976**, *11*, 203-220.

[73] Hong, H.-P. Crystal structures and crystal chemistry in the system $Na_{1+x}Zr_2Si_xP_{3-x}O_{12}$. *Materials Research Bulletin* **1976**, *11*, 173-182.

[74] Ma, C.; Cheng, Y.; Chen, K.; Li, J.; Sumpter, B. G.; Nan, C. W.; More, K. L.; Dudney, N. J.; Chi, M. Mesoscopic Framework Enables Facile Ionic Transport in Solid Electrolytes for Li Batteries. *Advanced Energy Materials* **2016**, *6*.

[75] Henkelman, G.; Uberuaga, B. P.; Jónsson, H. A climbing image nudged elastic band method for finding saddle points and minimum energy paths. *The Journal of Chemical Physics* **2000**, *113*, 9901-9904.

[76] Ong, S. P.; Mo, Y.; Richards, W. D.; Miara, L.; Lee, H. S.; Ceder, G. Phase stability, electrochemical stability and ionic conductivity of the $Li_{10\pm1}MP_2X12$ (M= Ge, Si, Sn, Al or P, and X= O, S or Se) family of superionic conductors. *Energy & Environmental Science* **2013**, *6*, 148-156.

[77] Mariappan, C. R.; Yada, C.; Rosciano, F.; Roling, B. Correlation between micro-structural properties and ionic conductivity of $Li_{1.5}Al_{0.5}Ge_{1.5}(PO_4)_3$ ceramics. *Journal of Power Sources* **2011**, *196*, 6456-6464.

[78] Mariappan, C. R.; Gellert, M.; Yada, C.; Rosciano, F.; Roling, B. Grain boundary resistance of fast lithium ion conductors: Comparison between a lithium-ion conductive Li–Al–Ti–P–O-type glass ceramic and a $Li_{1.5}Al_{0.5}Ge_{1.5}P_3O_{12}$ ceramic. *Electrochemistry Communications* **2012**, *14*, 25-28.

[79] Gellert, M.; Gries, K. I.; Yada, C.; Rosciano, F.; Volz, K.; Roling, B. Grain boundaries in a lithium aluminum titanium phosphate-type fast lithium ion

conducting glass ceramic: microstructure and nonlinear ion transport properties. *The Journal of Physical Chemistry C* **2012**, *116*, 22675-22678.

[80] Yamada, H.; Tsunoe, D.; Shiraishi, S.; Isomichi, G. Reduced grain boundary resistance by surface modification. *The Journal of Physical Chemistry C* **2015**, *119*, 5412-5419.

[81] Yamada, H.; Takemoto, K. Local structure and composition change at surface of lithium-ion conducting solid electrolyte. *Solid State Ionics* **2016**, *285*, 41-46.

[82] Ma, C.; Chen, K.; Liang, C.; Nan, C.-W.; Ishikawa, R.; More, K.; Chi, M. Atomic-scale origin of the large grain-boundary resistance in perovskite Li-ion-conducting solid electrolytes. *Energy & Environmental Science* **2014**, *7*, 1638-1642.

[83] Catti, M. First-Principles Modeling of Lithium Ordering in the LLTO ($Li_xLa_{2/3-x/3}TiO_3$) Superionic Conductor. *Chemistry of Materials* **2007**, *19*, 3963-3972.

[84] Inaguma, Y.; Katsumata, T.; Itoh, M.; Morii, Y.; Tsurui, T. Structural investigations of migration pathways in lithium ion-conducting $La_{2/3-x}Li_{3x}TiO_3$ perovskites. *Solid State Ionics* **2006**, *177*, 3037-3044.

[85] Ma, C.; Chi, M. Novel solid electrolytes for Li-ion batteries: a perspective from electron microscopy studies. *Frontiers in Energy Research* **2016**, *4*, 23.

[86] Qian, D.; Ma, C.; More, K. L.; Meng, Y. S.; Chi, M. Advanced analytical electron microscopy for lithium-ion batteries. *NPG Asia Materials* **2015**, *7*, e193.

[87] Cheng, L.; Chen, W.; Kunz, M.; Persson, K.; Tamura, N.; Chen, G.; Doeff, M. Effect of surface microstructure on electrochemical performance of garnet solid electrolytes. *ACS Applied Materials & Interfaces* **2015**, *7*, 2073-2081.

[88] David, I. N.; Thompson, T.; Wolfenstine, J.; Allen, J. L.; Sakamoto, J. Microstructure and Li-Ion Conductivity of Hot-Pressed Cubic $Li_7La_3Zr_2O_{12}$. *Journal of the American Ceramic Society* **2015**, *98*, 1209-1214.

[89] Tenhaeff, W. E.; Rangasamy, E.; Wang, Y.; Sokolov, A. P.; Wolfenstine, J.; Sakamoto, J.; Dudney, N. J. Resolving the Grain Boundary and Lattice Impedance of Hot-Pressed $Li_7La_3Zr_2O_{12}$ Garnet Electrolytes. *ChemElectroChem* **2014**, *1*, 375-378.

[90] Ramakumar, S.; Deviannapoorani, C.; Dhivya, L.; Shankar, L. S.; Murugan, R. Lithium garnets: synthesis, structure, Li^+ conductivity, Li^+ dynamics and applications. *Progress in Materials Science* **2017**.

[91] Yu, S.; Schmidt, R. D.; Garcia-Mendez, R.; Herbert, E.; Dudney, N. J.; Wolfenstine, J. B.; Sakamoto, J.; Siegel, D. J. Elastic Properties of the Solid Electrolyte $Li_7La_3Zr_2O_{12}$ (LLZO). *Chemistry of Materials* **2015**, *28*, 197-206.

[92] Takada, K. Progress and prospective of solid-state lithium batteries. *Acta Materialia* **2013**, *61*, 759-770.

[93] Kim, K. H.; Iriyama, Y.; Yamamoto, K.; Kumazaki, S.; Asaka, T.; Tanabe, K.; Fisher, C. A.; Hirayama, T.; Murugan, R.; Ogumi, Z. Characterization of the interface between $LiCoO_2$ and $Li_7La_3Zr_2O_{12}$ in an all-solid-state rechargeable lithium battery. *Journal of Power Sources* **2011**, *196*, 764-767.

[94] Nam, Y. J.; Cho, S.-J.; Oh, D. Y.; Lim, J.-M.; Kim, S. Y.; Song, J. H.; Lee, Y.-G.; Lee, S.-Y.; Jung, Y. S. Bendable and thin sulfide solid electrolyte film: A new electrolyte opportunity for free-standing and stackable high-energy all-solid-state lithium-ion batteries. *Nano Letters* **2015**, *15*, 3317-3323.

[95] Ohta, S.; Kobayashi, T.; Seki, J.; Asaoka, T. Electrochemical performance of an all-solid-state lithium ion battery with garnet-type oxide electrolyte. *Journal of Power Sources* **2012**, *202*, 332-335.

[96] Takada, K.; Ohta, N.; Zhang, L.; Xu, X.; Hang, B. T.; Ohnishi, T.; Osada, M.; Sasaki, T. Interfacial phenomena in solid-state lithium battery with sulfide solid electrolyte. *Solid State Ionics* **2012**, *225*, 594-597.

[97] Pan, J.; Cheng, Y.-T.; Qi, Y. General method to predict voltage-dependent ionic conduction in a solid electrolyte coating on electrodes. *Physical Review B* **2015**, *91*, 134116.

[98] Han, F.; Zhu, Y.; He, X.; Mo, Y.; Wang, C. Electrochemical Stability of $Li_{10}GeP_2S_{12}$ and $Li_7La_3Zr_2O_{12}$ Solid Electrolytes. *Advanced Energy Materials* **2016**.

[99] Yu, X.; Bates, J.; Jellison, G.; Hart, F. A Stable Thin-Film Lithium Electrolyte: Lithium Phosphorus Oxynitride. *Journal of the Electrochemical Society* **1997**, *144*, 524-532.

[100] Lepley, N.; Holzwarth, N. Modeling interfaces between solids: Application to Li battery materials. *Physical Review B* **2015**, *92*, 214201.

[101] Sakuda, A.; Hayashi, A.; Tatsumisago, M. Interfacial observation between $LiCoO_2$ electrode and $Li_2S{-}P_2S_5$ solid electrolytes of all-solid-state lithium secondary batteries using transmission electron microscopy. *Chemistry of Materials* **2009**, *22*, 949-956.

[102] Kitaura, H.; Hayashi, A.; Tadanaga, K.; Tatsumisago, M. All-solid-state lithium secondary batteries using $LiMn_2O_4$ electrode and $Li_2S–P_2S_5$ solid electrolyte. *Journal of The Electrochemical Society* **2010**, *157*, A407-A411.

[103] Zarabian, M.; Bartolini, M.; Pereira-Almao, P.; Thangadurai, V. X-ray Photoelectron Spectroscopy and AC Impedance Spectroscopy Studies of Li-La-Zr-O Solid Electrolyte Thin Film/$LiCoO_2$ Cathode Interface for All-Solid-State Li Batteries. *Journal of The Electrochemical Society* **2017**, *164*, A1133-A1139.

[104] Ma, C.; Cheng, Y.; Yin, K.; Luo, J.; Sharafi, A.; Sakamoto, J.; Li, J.; More, K. L.; Dudney, N. J.; Chi, M. Interfacial Stability of Li Metal–Solid Electrolyte Elucidated via in Situ Electron Microscopy. *Nano Letters* **2016**.

[105] Wang, Z.; Santhanagopalan, D.; Zhang, W.; Wang, F.; Xin, H. L.; He, K.; Li, J.; Dudney, N. J.; Meng, Y. S. In situ STEM/EELS Observation of Nanoscale Interfacial Phenomena in All-Solid-State Batteries. *Nano Letters* **2016**.

[106] Gong, Y.; Zhang, J.-N.; Jiang, L.; Shi, J.-A.; Zhang, Q.; Yang, Z.; Zou, D.; Wang, J.; Yu, X.; Xiao, R. In Situ Atomic-Scale Observation of Electrochemical Delithiation Induced Structure Evolution of $LiCoO_2$ Cathode in a Working All-Solid-State Battery. *Journal of the American Chemical Society* **2017**.

[107] Brazier, A.; Dupont, L.; Dantras-Laffont, L.; Kuwata, N.; Kawamura, J.; Tarascon, J.-M. First cross-section observation of an all solid-state lithium-ion “nanobattery” by transmission electron microscopy. *Chemistry of materials* **2008**, *20*, 2352-2359.

[108] Murugan, R.; Thangadurai, V.; Weppner, W. Fast Lithium Ion Conduction in Garnet-Type $Li_7La_3Zr_2O_{12}$. *Angewandte Chemie International Edition* **2007**, *46*, 7778-7781.

[109] Cussen, E. J. Structure and ionic conductivity in lithium garnets. *Journal of Materials Chemistry* **2010**, *20*, 5167-5173.

[110] Wolfenstine, J.; Allen, J.; Read, J.; Sakamoto, J. Chemical stability of cubic $Li_7La_3Zr_2O_{12}$ with molten lithium at elevated temperature. *Journal of Materials Science* **2013**, *48*, 5846-5851.

[111] Ma, C.; Cheng, Y.; Yin, K.; Luo, J.; Sharafi, A.; Sakamoto, J.; Li, J.; More, K. L.; Dudney, N. J.; Chi, M. Interfacial Stability of Li Metal–Solid Electrolyte Elucidated via in Situ Electron Microscopy. *Nano Letters* **2016**, *16*, 7030-7036.

[112] Wenzel, S.; Leichtweiss, T.; Krüger, D.; Sann, J.; Janek, J. Interphase formation on lithium solid electrolytes—an in situ approach to study interfacial reactions by photoelectron spectroscopy. *Solid State Ionics* **2015**, *278*, 98-105.

[113] Wenzel, S.; Randau, S.; Leichtweiß, T.; Weber, D. A.; Sann, J.; Zeier, W. G.; Janek, J. r. Direct observation of the interfacial instability of the fast ionic conductor $Li_{10}GeP_2S_{12}$ at the lithium metal anode. *Chemistry of Materials* **2016**, *28*, 2400-2407.

[114] Auvergniot, J.; Cassel, A.; Foix, D.; Viallet, V.; Seznec, V.; Dedryvère, R. Redox activity of argyrodite Li_6PS_5Cl electrolyte in all-solid-state Li-ion battery: An XPS study. *Solid State Ionics* **2017**, *300*, 78-85.

[115] Hartmann, P.; Leichtweiss, T.; Busche, M. R.; Schneider, M.; Reich, M.; Sann, J.; Adelhelm, P.; Janek, J. r. Degradation of NASICON-type materials in contact with lithium metal: formation of mixed conducting interphases (MCI) on solid electrolytes. *The Journal of Physical Chemistry C* **2013**, *117*, 21064-21074.

[116] Schwöbel, A.; Hausbrand, R.; Jaegermann, W. Interface reactions between LiPON and lithium studied by in-situ X-ray photoemission. *Solid State Ionics* **2015**, *273*, 51-54.

[117] Li, Y.; Zhou, W.; Chen, X.; Lü, X.; Cui, Z.; Xin, S.; Xue, L.; Jia, Q.; Goodenough, J. B. Mastering the interface for advanced all-solid-state lithium rechargeable batteries. *Proceedings of the National Academy of Sciences* **2016**, 201615912.

[118] Wenzel, S.; Weber, D. A.; Leichtweiss, T.; Busche, M. R.; Sann, J.; Janek, J. Interphase formation and degradation of charge transfer kinetics between a lithium metal anode and highly crystalline $Li_7P_3S_{11}$ solid electrolyte. *Solid State Ionics* **2016**, *286*, 24-33.

[119] Zhu, Y.; He, X.; Mo, Y. First principles study on electrochemical and chemical stability of solid electrolyte–electrode interfaces in all-solid-state Li-ion batteries. *Journal of Materials Chemistry A* **2016**, *4*, 3253-3266.

[120] West, W. C.; Hood, Z. D.; Adhikari, S. P.; Liang, C.; Lachgar, A.; Motoyama, M.; Iriyama, Y. Reduction of charge-transfer resistance at the solid electrolyte–electrode interface by pulsed laser deposition of films from a crystalline Li_2PO_2N source. *Journal of Power Sources* **2016**, *312*, 116-122.

[121] Ohta, N.; Takada, K.; Zhang, L.; Ma, R.; Osada, M.; Sasaki, T. Enhancement of the High-Rate Capability of Solid-State Lithium Batteries by Nanoscale Interfacial Modification. *Advanced Materials* **2006**, *18*, 2226-2229.

[122] Ohta, N.; Takada, K.; Sakaguchi, I.; Zhang, L.; Ma, R.; Fukuda, K.; Osada, M.; Sasaki, T. $LiNbO_3$-coated $LiCoO_2$ as cathode material for all solid-state lithium secondary batteries. *Electrochemistry communications* **2007**, *9*, 1486-1490.

[123] Takada, K.; Ohta, N.; Zhang, L.; Fukuda, K.; Sakaguchi, I.; Ma, R.; Osada, M.; Sasaki, T. Interfacial modification for high-power solid-state lithium batteries. *Solid State Ionics* **2008**, *179*, 1333-1337.

[124] Kitaura, H.; Hayashi, A.; Tadanaga, K.; Tatsumisago, M. Improvement of electrochemical performance of all-solid-state lithium secondary batteries by surface modification of $LiMn_2O_4$ positive electrode. *Solid State Ionics* **2011**, *192*, 304-307.

[125] Kato, T.; Hamanaka, T.; Yamamoto, K.; Hirayama, T.; Sagane, F.; Motoyama, M.; Iriyama, Y. In-situ $Li_7La_3Zr_2O_{12}/LiCoO_2$ interface modification for advanced all-solid-state battery. *Journal of Power Sources* **2014**, *260*, 292-298.

[126] Haruyama, J.; Sodeyama, K.; Han, L.; Takada, K.; Tateyama, Y. Space–Charge Layer Effect at Interface between Oxide Cathode and Sulfide Electrolyte in All-Solid-State Lithium-Ion Battery. *Chemistry of Materials* **2014**, *26*, 4248-4255.

[127] Anisimov, V. I.; Zaanen, J.; Andersen, O. K. Band theory and Mott insulators: Hubbard U instead of Stoner I. *Physical Review B* **1991**, *44*, 943.

[128] Safanama, D.; Sharma, N.; Rao, R. P.; Brand, H. E.; Adams, S. Structural evolution of NASICON-type $Li_{1+x}Al_xGe_{2-x}(PO_4)_3$ using in situ synchrotron X-ray powder diffraction. *Journal of Materials Chemistry A* **2016**, *4*, 7718-7726.

[129] Otoyama, M.; Ito, Y.; Hayashi, A.; Tatsumisago, M. Raman imaging for LiCoO 2 composite positive electrodes in all-solid-state lithium batteries using Li_2S–P_2S_5 solid electrolytes. *Journal of Power Sources* **2016**, *302*, 419-425.

[130] Wang, H.; Chen, Y.; Hood, Z. D.; Sahu, G.; Pandian, A. S.; Keum, J. K.; An, K.; Liang, C. An Air-Stable Na_3SbS_4 Superionic Conductor Prepared by a Rapid and Economic Synthetic Procedure. *Angewandte Chemie International Edition* **2016**.

[131] Sang, L.; Haasch, R. T.; Gewirth, A. A.; Nuzzo, R. G. Evolution at the Solid Electrolyte/Au Electrode Interface during Lithium Deposition and Stripping. *Chemistry of Materials* **2017**.

[132] Li, Y.; Xu, B.; Xu, H.; Duan, H.; Lü, X.; Xin, S.; Zhou, W.; Xue, L.; Fu, G.; Manthiram, A. Hybrid Polymer/Garnet Electrolyte with a Small Interfacial Resistance for Lithium-Ion Batteries. *Angewandte Chemie* **2017**, *129*, 771-774.

[133] Deng, Y.; Eames, C.; Chotard, J.-N. l.; Lalère, F.; Seznec, V.; Emge, S.; Pecher, O.; Grey, C. P.; Masquelier, C.; Islam, M. S. Structural and mechanistic insights into fast lithium-ion conduction in Li_4SiO_4–Li_3PO_4 solid electrolytes. *Journal of the American Chemical Society* **2015**, *137*, 9136-9145.

[134] Balke, N.; Jesse, S.; Kim, Y.; Adamczyk, L.; Ivanov, I. N.; Dudney, N. J.; Kalinin, S. V. Decoupling electrochemical reaction and diffusion processes in ionically-conductive solids on the nanometer scale. *ACS Nano* **2010**, *4*, 7349-7357.

[135] Sacci, R. L.; Bañuelos, J. L.; Veith, G. M.; Littrell, K. C.; Cheng, Y. Q.; Wildgruber, C. U.; Jones, L. L.; Ramirez-Cuesta, A. J.; Rother, G.; Dudney, N. J. Structure of spontaneously formed solid-electrolyte interphase on lithiated graphite determined using small-angle neutron scattering. *The Journal of Physical Chemistry C* **2015**, *119*, 9816-9823.

[136] Chen, Y.; Rangasamy, E.; dela Cruz, C. R.; Liang, C.; An, K. A study of suppressed formation of low-conductivity phases in doped $Li_7La_3Zr_2O_{12}$ garnets by in situ neutron diffraction. *Journal of Materials Chemistry A* **2015**, *3*, 22868-22876.

[137] Okumura, T.; Nakatsutsumi, T.; Ina, T.; Orikasa, Y.; Arai, H.; Fukutsuka, T.; Iriyama, Y.; Uruga, T.; Tanida, H.; Uchimoto, Y. Depth-resolved X-ray absorption spectroscopic study on nanoscale observation of the electrode–solid electrolyte

interface for all solid state lithium ion batteries. *Journal of Materials Chemistry* **2011**, *21*, 10051-10060.

[138] Rangasamy, E.; Liu, Z.; Gobet, M.; Pilar, K.; Sahu, G.; Zhou, W.; Wu, H.; Greenbaum, S.; Liang, C. An Iodide-Based Li7P2S8I Superionic Conductor. *Journal of the American Chemical Society* **2015**, *137*, 1384-1387.

[139] Chen, Y.; Rangasamy, E.; Liang, C.; An, K. Origin of high Li^+ conduction in doped $Li_7La_3Zr_2O_{12}$ garnets. *Chemistry of Materials* **2015**, *27*, 5491-5494.

[140] Kawaura, H.; Harada, M.; Kondo, Y.; Kondo, H.; Suganuma, Y.; Takahashi, N.; Sugiyama, J.; Seno, Y.; Yamada, N. L. Operando Measurement of Solid Electrolyte Interphase Formation at Working Electrode of Li-Ion Battery by Time-Slicing Neutron Reflectometry. *ACS Applied Materials & Interfaces* **2016**, *8*, 9540-9544.

[141] Owejan, J. E.; Owejan, J. P.; DeCaluwe, S. C.; Dura, J. A. Solid electrolyte interphase in Li-ion batteries: Evolving structures measured in situ by neutron reflectometry. *Chemistry of Materials* **2012**, *24*, 2133-2140.

[142] Mori, K.; Enjuji, K.; Murata, S.; Shibata, K.; Kawakita, Y.; Yonemura, M.; Onodera, Y.; Fukunaga, T. Direct Observation of Fast Lithium-Ion Diffusion in a Superionic Conductor: $Li_7P_3S_{11}$ Metastable Crystal. *Physical Review Applied* **2015**, *4*, 054008.

[143] Martínez-Juárez, A.; Pecharromán, C.; Iglesias, J. E.; Rojo, J. M. Relationship between Activation Energy and Bottleneck Size for Li^+ Ion Conduction in NASICON Materials of Composition LiMM ‘$(PO_4)_3$; M, M ‘= Ge, Ti, Sn, Hf. *The Journal of Physical Chemistry B* **1998**, *102*, 372-375.

[144] Kanno, R.; Murayama, M. Lithium Ionic Conductor Thio-LISICON: The Li_2S-GeS_2-P_2S_5 System. *Journal of The Electrochemical Society* **2001**, *148*, A742-A746.

[145] Sun, Y.; Suzuki, K.; Hara, K.; Hori, S.; Yano, T.-a.; Hara, M.; Hirayama, M.; Kanno, R. Oxygen substitution effects in $Li_{10}GeP_2S_{12}$ solid electrolyte. *Journal of Power Sources* **2016**, *324*, 798-803.

[146] Hirayama, M.; Kanno, R. Synthesis, structure, and electrochemical properties of crystalline Li–P–S–O solid electrolytes: Novel lithium-conducting oxysulfides of $Li_{10}GeP_2S_{12}$ family. **2016**.

[147] Deng, Y.; Eames, C.; Fleutot, B.; David, R.; Chotard, J.-N. l.; Suard, E.; Masquelier, C.; Islam, M. S. Enhancing the Lithium Ion Conductivity in Lithium Superionic Conductor (LISICON) Solid Electrolytes through a Mixed Polyanion Effect. *ACS Applied Materials & Interfaces* **2017**, *9*, 7050-7058.

[148] Rangasamy, E.; Wolfenstine, J.; Sakamoto, J. The role of Al and Li concentration on the formation of cubic garnet solid electrolyte of nominal composition $Li_7La_3Zr_2O_{12}$. *Solid State Ionics* **2012**, *206*, 28-32.

[149] Thompson, T.; Wolfenstine, J.; Allen, J. L.; Johannes, M.; Huq, A.; David, I. N.; Sakamoto, J. Tetragonal vs. cubic phase stability in Al–free Ta doped $Li_7La_3Zr_2O_{12}$ (LLZO). *Journal of Materials Chemistry A* **2014**, *2*, 13431-13436.

[150] Huang, B.; Xu, B.; Li, Y.; Zhou, W.; You, Y.; Zhong, S.; Wang, C.-A.; Goodenough, J. B. Li-ion conduction and stability of perovskite $Li_{3/8}Sr_{7/16}Hf_{1/4}Ta_{3/4}O_3$. *ACS applied materials & interfaces* **2016**, *8*, 14552-14557.

[151] Hood, Z. D.; Wang, H.; Samuthira Pandian, A.; Keum, J. K.; Liang, C. Li_2OHCl Crystalline Electrolyte for Stable Metallic Lithium Anodes. *Journal of the American Chemical Society* **2016**, *138*, 1768-1771.

[152] Li, Y.; Zhou, W.; Xin, S.; Li, S.; Zhu, J.; Lü, X.; Cui, Z.; Jia, Q.; Zhou, J.; Zhao, Y. Fluorine-Doped Antiperovskite Electrolyte for All-Solid-State Lithium-Ion Batteries. *Angewandte Chemie International Edition* **2016**, *55*, 9965-9968.

[153] Hull, S. Superionics: crystal structures and conduction processes. *Reports on Progress in Physics* **2004**, *67*, 1233.

[154] Richards, W. D.; Tsujimura, T.; Miara, L. J.; Wang, Y.; Kim, J. C.; Ong, S. P.; Uechi, I.; Suzuki, N.; Ceder, G. Design and synthesis of the superionic conductor $Na_{10}SnP_2S_{12}$. *Nature Communications* **2016**, *7*.

[155] Du, Y. A.; Holzwarth, N. First-principles study of LiPON and related solid electrolytes. *Physical Review B* **2010**, *81*, 184106.

[156] Lepley, N.; Holzwarth, N. Computer modeling of crystalline electrolytes-lithium thiophosphates and phosphates. *ECS Transactions* **2011**, *35*, 39-51.

[157] Swenson, J. Determining ionic conductivity from structural models of fast ionic conductors. *Physical Review Letters* **2000**, *84*, 4144.

[158] Adams, S.; Swenson, J. Migration pathways in Ag-based superionic glasses and crystals investigated by the bond valence method. *Physical Review B* **2000**, *63*, 054201.

[159] Adams, S.; Swenson, J. Bond valence analysis of transport pathways in RMC models of fast ion conducting glasses. *Physical Chemistry Chemical Physics* **2002**, *4*, 3179-3184.

[160] McWhan, D.; Allen Jr, S.; Remeika, J.; Dernier, P. Ion-Ion Correlations and Diffusion in *β*-Alumina. *Physical Review Letters* **1975**, *35*, 953.

[161] Schwering, G.; Hönnerscheid, A.; van Wüllen, L.; Jansen, M. High Lithium Ionic Conductivity in the Lithium Halide Hydrates $Li_{3-n}(OH_n)Cl$ ($0.83 \leq n \leq 2$) and $Li_{3-n}(OH_n)Br$ ($1 \leq n \leq 2$) at Ambient Temperatures. *ChemPhysChem* **2003**, *4*, 343-348.

[162] Billinge, S. J.; Kanatzidis, M. Beyond crystallography: the study of disorder, nanocrystallinity and crystallographically challenged materials with pair distribution functions. *Chemical Communications* **2004**, 749-760.

[163] Juhás, P.; Cherba, D.; Duxbury, P.; Punch, W.; Billinge, S. Ab initio determination of solid-state nanostructure. *Nature* **2006**, *440*, 655-658.

[164] Billinge, S. J.; Levin, I. The problem with determining atomic structure at the nanoscale. *Science* **2007**, *316*, 561-565.

[165] Maier, J. Ionic conduction in space charge regions. *Progress in Solid State Chemistry* **1995**, *23*, 171-263.

[166] Maier, J. Space charge regions in solid two-phase systems and their conduction contribution—I. Conductance enhancement in the system ionic conductor-'inert'phase and application on AgC1: Al_2O_3 and AgC1: SiO_2. *Journal of Physics and Chemistry of Solids* **1985**, *46*, 309-320.

[167] Liang, C. Conduction Characteristics of the Lithium Iodide-Aluminum Oxide Solid Electrolytes. *Journal of The Electrochemical Society* **1973**, *120*, 1289-1292.

[168] Phipps, J. B.; Johnson, D.; Whitmore, D. Effect of composition and imperfections on ion transport in lithium iodine. *Solid State Ionics* **1981**, *5*, 393-396.

[169] Phipps, J.; Whitmore, D. Interfacial conduction in lithium iodide containing inert oxides. *Journal of Power Sources* **1983**, *9*, 373-378.

[170] Takada, K.; Ohta, N.; Tateyama, Y. Recent Progress in Interfacial Nanoarchitectonics in Solid-State Batteries. *Journal of Inorganic and Organometallic Polymers and Materials* **2015**, *25*, 205-213.

[171] Ariga, K.; Li, J.; Fei, J.; Ji, Q.; Hill, J. P. Nanoarchitectonics for Dynamic Functional Materials from Atomic-/Molecular-Level Manipulation to Macroscopic Action. *Advanced Materials* **2016**, *28*, 1251-1286.

[172] Agrawal, R.; Gupta, R. Superionic solid: composite electrolyte phase–an overview. *Journal of materials science* **1999**, *34*, 1131-1162.

[173] Maier, J. Nanoionics: ion transport and electrochemical storage in confined systems. *Nature materials* **2005**, *4*, 805-815.

[174] Maier, J. Defect chemistry and conductivity effects in heterogeneous solid electrolytes. *Journal of The Electrochemical Society* **1987**, *134*, 1524-1535.

[175] Dudney, N. J. Composite electrolytes. *Annual Review of Materials Science* **1989**, *19*, 103-120.

[176] Dudney, N. J. Enhanced ionic conductivity in composite electrolytes. *Solid State Ionics* **1988**, *28*, 1065-1072.

[177] Kumar, B.; Scanlon, L. G. Polymer-ceramic composite electrolytes. *Journal of Power Sources* **1994**, *52*, 261-268.

[178] Hood, Z. D.; Wang, H.; Li, Y.; Pandian, A. S.; Paranthaman, M. P.; Liang, C. The "filler effect": A study of solid oxide fillers with β-Li_3PS_4 for lithium conducting electrolytes. *Solid State Ionics* **2015**, *283*, 75-80.

[179] Mizuno, F.; Hayashi, A.; Tadanaga, K.; Tatsumisago, M. Effects of conductive additives in composite positive electrodes on charge-discharge behaviors of all-solid-state lithium secondary batteries. *Journal of the Electrochemical Society* **2005**, *152*, A1499-A1503.

[180] Rangasamy, E.; Li, J.; Sahu, G.; Dudney, N.; Liang, C. Pushing the theoretical limit of Li-CF_x batteries: a tale of bifunctional electrolyte. *Journal of the American Chemical Society* **2014**, *136*, 6874-6877.

[181] Hayashi, A.; Nishio, Y.; Kitaura, H.; Tatsumisago, M. Novel technique to form electrode–electrolyte nanointerface in all-solid-state rechargeable lithium batteries. *Electrochemistry Communications* **2008**, *10*, 1860-1863.

[182] Kim, D. H.; Oh, D. Y.; Park, K. H.; Choi, Y. E.; Nam, Y. J.; Lee, H. A.; Lee, S.-M.; Jung, Y. S. Infiltration of solution-processable solid electrolytes into conventional Li-ion-battery electrodes for all-solid-state Li-ion batteries. *Nano Letters* **2017**.

[183] Rangasamy, E.; Sahu, G.; Keum, J. K.; Rondinone, A. J.; Dudney, N. J.; Liang, C. A high conductivity oxide–sulfide composite lithium superionic conductor. *Journal of Materials Chemistry A* **2014**, *2*, 4111-4116.

[184] Liu, K.; Wang, C.-A. Honeycomb-alumina supported garnet membrane: Composite electrolyte with low resistance and high strength for lithium metal batteries. *Journal of Power Sources* **2015**, *281*, 399-403.

[185] Tao, X.; Liu, Y.; Liu, W.; Zhou, G.; Zhao, J.; Lin, D.; Zu, C.; Sheng, O.; Zhang, W.; Lee, H.-W. Solid-State Lithium-Sulfur Batteries Operated at 37° C with Composites of Nanostructured $Li_7La_3Zr_2O_{12}$/Carbon Foam and Polymer. *Nano Letters* **2017**.

[186] Chen, R.-J.; Zhang, Y.-B.; Liu, T.; Xu, B.-Q.; Lin, Y.-H.; Nan, C.-W.; Shen, Y. Addressing the Interface Issues in All-Solid-State Bulk-Type Lithium Ion Battery via an All-Composite Approach. *ACS Applied Materials & Interfaces* **2017**.

[187] Liu, W.; Liu, N.; Sun, J.; Hsu, P.-C.; Li, Y.; Lee, H.-W.; Cui, Y. Ionic conductivity enhancement of polymer electrolytes with ceramic nanowire fillers. *Nano Letters* **2015**, *15*, 2740-2745.

[188] Cao, C.; Li, Z.-B.; Wang, X.-L.; Zhao, X.-B.; Han, W.-Q. Recent advances in inorganic solid electrolytes for lithium batteries. *Frontiers in Energy Research* **2014**, *2*, 25.

[189] Zhou, W.; Wang, S.; Li, Y.; Xin, S.; Manthiram, A.; Goodenough, J. B. Plating a dendrite-free lithium anode with a polymer/ceramic/polymer sandwich electrolyte. *Journal of the American Chemical Society* **2016**, *138*, 9385-9388.

[190] Kim, S.-H.; Choi, K.-H.; Cho, S.-J.; Kil, E.-H.; Lee, S.-Y. Mechanically compliant and lithium dendrite growth-suppressing composite polymer electrolytes for flexible lithium-ion batteries. *Journal of Materials Chemistry A* **2013**, *1*, 4949-4955.

[191] Fu, K. K.; Gong, Y.; Dai, J.; Gong, A.; Han, X.; Yao, Y.; Wang, C.; Wang, Y.; Chen, Y.; Yan, C. Flexible, solid-state, ion-conducting membrane with 3D garnet nanofiber networks for lithium batteries. *Proceedings of the National Academy of Sciences* **2016**, *113*, 7094-7099.

[192] Baek, S.-W.; Honma, I.; Kim, J.; Rangappa, D. Solidified inorganic-organic hybrid electrolyte for all solid state flexible lithium battery. *Journal of Power Sources* **2017**, *343*, 22-29.

[193] Li, Y.; Han, J.-T.; Vogel, S. C.; Wang, C.-A. The Reaction of $Li_{6.5}La_3Zr_{1.5}Ta_{0.5}O_{12}$ with Water. *Solid State Ionics* **2015**, *269*, 57-61.

[194] Cheng, L.; Crumlin, E. J.; Chen, W.; Qiao, R.; Hou, H.; Lux, S. F.; Zorba, V.; Russo, R.; Kostecki, R.; Liu, Z. The origin of high electrolyte–electrode interfacial resistances in lithium cells containing garnet type solid electrolytes. *Physical Chemistry Chemical Physics* **2014**, *16*, 18294-18300.

[195] Liu, Y.; Lin, D.; Liang, Z.; Zhao, J.; Yan, K.; Cui, Y. Lithium-coated polymeric matrix as a minimum volume-change and dendrite-free lithium metal anode. *Nature communications* **2016**, *7*.

[196] Zhou, W.; Gao, H.; Goodenough, J. B. Low-Cost Hollow Mesoporous Polymer Spheres and All-Solid-State Lithium, Sodium Batteries. *Advanced Energy Materials* **2016**, *6*.

[197] Zhao, Y.; Wu, C.; Peng, G.; Chen, X.; Yao, X.; Bai, Y.; Wu, F.; Chen, S.; Xu, X. A new solid polymer electrolyte incorporating $Li_{10}GeP_2S_{12}$ into a polyethylene oxide matrix for all-solid-state lithium batteries. *Journal of Power Sources* **2016**, *301*, 47-53.

[198] Lv, D.; Zheng, J.; Li, Q.; Xie, X.; Ferrara, S.; Nie, Z.; Mehdi, L. B.; Browning, N. D.; Zhang, J. G.; Graff, G. L. High energy density lithium–sulfur batteries: challenges of thick sulfur cathodes. *Advanced Energy Materials* **2015**, *5*.

[199] Xu, W.; Wang, J.; Ding, F.; Chen, X.; Nasybulin, E.; Zhang, Y.; Zhang, J.-G. Lithium metal anodes for rechargeable batteries. *Energy & Environmental Science* **2014**, *7*, 513-537.

[200] Zhu, Y.; He, X.; Mo, Y. Strategies Based on Nitride Materials Chemistry to Stabilize Li Metal Anode. *Advanced Science* **2017**.

[201] Li, J.; Baggetto, L.; Martha, S. K.; Veith, G. M.; Nanda, J.; Liang, C.; Dudney, N. J. An artificial solid electrolyte interphase enables the use of a $LiNi_{0.5}Mn_{1.5}O_4$ 5 V cathode with conventional electrolytes. *Advanced Energy Materials* **2013**, *3*, 1275-1278.

[202] Li, J.; Dudney, N. J.; Nanda, J.; Liang, C. Artificial Solid Electrolyte Interphase To Address the Electrochemical Degradation of Silicon Electrodes. *ACS Applied Materials & Interfaces* **2014**, *6*, 10083-10088.

[203] Kozen, A. C.; Pearse, A. J.; Lin, C.-F.; Noked, M.; Rubloff, G. W. Atomic layer deposition of the solid electrolyte LiPON. *Chemistry of Materials* **2015**, *27*, 5324-5331.

[204] Sakuda, A.; Hayashi, A.; Ohtomo, T.; Hama, S.; Tatsumisago, M. All-solid-state lithium secondary batteries using $LiCoO_2$ particles with pulsed laser deposition coatings of Li_2S–P_2S_5 solid electrolytes. *Journal of Power Sources* **2011**, *196*, 6735-6741.

[205] Ogawa, M.; Kanda, R.; Yoshida, K.; Uemura, T.; Harada, K. High-capacity thin film lithium batteries with sulfide solid electrolytes. *Journal of Power Sources* **2012**, *205*, 487-490.

[206] Han, X.; Gong, Y.; Fu, K. K.; He, X.; Hitz, G. T.; Dai, J.; Pearse, A.; Liu, B.; Wang, H.; Rubloff, G. Negating interfacial impedance in garnet-based solid-state Li metal batteries. *Nature Materials* **2016**.

[207] Meng, X.; Yang, X. Q.; Sun, X. Emerging Applications of Atomic Layer Deposition for Lithium-Ion Battery Studies. *Advanced Materials* **2012**, *24*, 3589-3615.

[208] Wang, C.; Gong, Y.; Liu, B.; Fu, K. K.; Yao, Y.; Hitz, E.; Li, Y.; Dai, J.; Xu, S.; Luo, W. Conformal, Nanoscale ZnO Surface Modification of Garnet-Based Solid State Electrolyte for Lithium Metal Anodes. *Nano Letters* **2016**.

[209] Luo, W.; Lin, C. F.; Zhao, O.; Noked, M.; Zhang, Y.; Rubloff, G. W.; Hu, L. Ultrathin Surface Coating Enables the Stable Sodium Metal Anode. *Advanced Energy Materials* **2017**, *7*.

[210] Luo, W.; Gong, Y.; Zhu, Y.; Fu, K. K.; Dai, J.; Lacey, S. D.; Wang, C.; Liu, B.; Han, X.; Mo, Y. Transition from Superlithiophobicity to Superlithiophilicity of Garnet Solid-state electrolyte. *J. Am. Chem. Soc* **2016**, *138*, 12258-12262.

[211] Sahu, G.; Lin, Z.; Li, J.; Liu, Z.; Dudney, N.; Liang, C. Air-stable, high-conduction solid electrolytes of arsenic-substituted Li_4SnS_4. *Energy & Environmental Science* **2014**, *7*, 1053-1058.

[212] Maekawa, H.; Matsuo, M.; Takamura, H.; Ando, M.; Noda, Y.; Karahashi, T.; Orimo, S.-I. Halide-stabilized $LiBH_4$, a room-temperature lithium fast-ion conductor. *Journal of the American Chemical Society* **2009**, *131*, 894-895.

[213] Zhou, W.; Li, Y.; Xin, S.; Goodenough, J. B. Rechargeable Sodium All-Solid-State Battery. *ACS Central Science* **2017**.

[214] Han, X.; Liu, Y.; Jia, Z.; Chen, Y.-C.; Wan, J.; Weadock, N.; Gaskell, K. J.; Li, T.; Hu, L. Atomic-layer-deposition oxide nanoglue for sodium ion batteries. *Nano Letters* **2013**, *14*, 139-147.

[215] Jung, S. C.; Kim, H.-J.; Choi, J. W.; Han, Y.-K. Sodium Ion Diffusion in Al2O3: A Distinct Perspective Compared with Lithium Ion Diffusion. *Nano Letters* **2014**, *14*, 6559-6563.

[216] Lotfabad, E. M.; Kalisvaart, P.; Kohandehghan, A.; Cui, K.; Kupsta, M.; Farbod, B.; Mitlin, D. Si nanotubes ALD coated with TiO_2, TiN or Al_2O_3 as high performance lithium ion battery anodes. *Journal of Materials Chemistry A* **2014**, *2*, 2504-2516.

[217] Kohandehghan, A.; Kalisvaart, P.; Cui, K.; Kupsta, M.; Memarzadeh, E.; Mitlin, D. Silicon nanowire lithium-ion battery anodes with ALD deposited TiN coatings demonstrate a major improvement in cycling performance. *Journal of Materials Chemistry A* **2013**, *1*, 12850-12861.

[218] Fu, K. K.; Gong, Y.; Liu, B.; Zhu, Y.; Xu, S.; Yao, Y.; Luo, W.; Wang, C.; Lacey, S. D.; Dai, J. Toward garnet electrolyte–based Li metal batteries: An ultrathin, highly effective, artificial solid-state electrolyte/metallic Li interface. *Science Advances* **2017**, *3*, e1601659.

[219] Senevirathne, K.; Day, C. S.; Gross, M. D.; Lachgar, A.; Holzwarth, N. A new crystalline LiPON electrolyte: Synthesis, properties, and electronic structure. *Solid State Ionics* **2013**, *233*, 95-101.

[220] Yamada, H.; Oga, Y.; Saruwatari, I.; Moriguchi, I. Local structure and ionic conduction at interfaces of electrode and solid electrolytes. *Journal of The Electrochemical Society* **2012**, *159*, A380-A385.

[221] Takada, K. Interfacial nanoarchitectonics for solid-state lithium batteries. *Langmuir* **2013**, *29*, 7538-7541.

[222] Park, M.; Zhang, X.; Chung, M.; Less, G. B.; Sastry, A. M. A review of conduction phenomena in Li-ion batteries. *Journal of Power Sources* **2010**, *195*, 7904-7929.

[223] Haruyama, J.; Sodeyama, K.; Tateyama, Y. Cation Mixing Properties toward Co Diffusion at the $LiCoO_2$ Cathode/Sulfide Electrolyte Interface in a Solid-State Battery. *ACS Applied Materials & Interfaces* **2016**.

[224] Sakuma, M.; Suzuki, K.; Hirayama, M.; Kanno, R. Reactions at the electrode/electrolyte interface of all-solid-state lithium batteries incorporating Li–M (M= Sn, Si) alloy electrodes and sulfide-based solid electrolytes. *Solid State Ionics* **2016**, *285*, 101-105.

[225] Uhlenbruck, S.; Dornseiffer, J.; Lobe, S.; Dellen, C.; Tsai, C.-L.; Gotzen, B.; Sebold, D.; Finsterbusch, M.; Guillon, O. Cathode-electrolyte material interactions during manufacturing of inorganic solid-state lithium batteries. *Journal of Electroceramics* **2016**, 1-10.

CHAPTER 2

THE FILLER EFFECT: TUNING LITHIUM ION CONDUCTIVITY BY FORMING NANOCOMPOSITES

2.1 Introduction

In the current energy market, there exists a need for a longer-lasting battery with increased energy density [1-3]. Previously, batteries consisted of solid electrodes and a liquid electrolyte, however, this model is neither the safest nor most efficient. Liquid electrolytes are flammable and lead to dendrite formation for lithium deposition that causes the cell to short, compromising the lifetime of the battery [2]. Theoretically, solid electrolytes allow for batteries with greater energy density and in some cases, stability with lithium anode at increased voltages, making solid electrolyte superior to liquid electrolyte [3].

Recent developments in lithium superionic conductor (LiSICON) electrolytes paved the way to materials with high conductivity ($\geq 10^{-4}$ S·cm^{-1}), good processability, and high energy density [4-6]. The LiSICON solids have higher theoretical thermal and electrochemical stability in comparison to liquid electrolytes, and in the case of batteries, these solids open a new frontier for electrolyte research. One compound, in particular, is of great interest: nano-crystalline β-Li_3PS_4 (LPS) [7, 8]. With an ionic conductivity of 1.6×10^{-4} S·cm^{-1} at ambient temperature, nanostructured LPS is truly a novel addition to the LiSICON system [7]. Additionally, LPS is synthesized at room temperature, has good processability, easy membrane fabrication, and low interfacial resistance with metallic lithium electrodes. Still, further improvement of the ionic conductivity and stability of LPS

with different anodes will enhance battery performance and allow for an ionic conductivity similar to those found in liquid electrolyte.

It has been previously shown that the addition of oxide fillers into the LPS system could increase the conductivity of the electrolyte [8]. Previously, ion-conducting and non-conducting oxide fillers have been shown to enhance the ionic conductivity of solid electrolytes. However, it is unknown as to what oxide filler works best with LPS, which warrants an understanding of how oxides affect the mechanical and electrolyte properties of LPS. For this study, several oxides have been selected to analyze the filler effect: $Li_6ZnNb_4O_{14}$ (LZNO), Al_2O_3, and SiO_2. According to the hard and soft acids and bases (HSAB) theory, these hard oxides will not react with LPS, a soft base, when forming composites. Also, LZNO has an ionic conductivity of 3.28×10^{-5} $S \cdot cm^{-1}$ at 21.5 °C and 1.31×10^{-2} $S \cdot cm^{-1}$ at 250 °C [9, 10] while Al_2O_3 and SiO_2 are reported to enhance the ionic conductivity in heterogeneous composite electrolytes [9, 10], which is the reason why these solid oxide fillers were selected for this study.

This chapter presents a comparative study of ion-conducting and non-conducting oxide fillers in composites with LPS. The ionic conductivity, activation energy, and stability of electrolyte composites against metallic lithium are reported. A working understanding as to the effect of ion-conducting and non-conducting oxides on LPS facilitates the discovery of better composite electrolytes for use in Li-metal based all-solid-state batteries, which will ultimately help fabricate safer, higher energy-dense batteries.

2.2 Results and Discussion

2.2.1 Composite processability and structural analysis

The composites are simple mixtures of the oxide fillers and LPS. The oxide fillers are stable with LPS. This stability is apparent in the XRD measurements, where the 50:50 (LPS: oxide) composites display no apparent reaction (Fig. 2.1), which confirms that no solid-state reaction occurred between LPS and the oxides during ball milling processes. Additional XRD analysis also confirms that the starting materials did not react with the ball milling media (Y-ZrO_2). SEM aided in determining composite homogeneity, where particles $\leq$ 1-2 μm were found for both the LPS and the oxide filler in all composites, which confirms that simple ball milling may be used to achieve homogeneity of the LPS and oxide particles (Fig. 2.2). EDS analysis further demonstrates the composite homogeneity, where LPS and oxide particles were evenly dispersed throughout the LZNO:LPS composite (Fig. 2.3), the Al_2O_3:LPS composite (Fig. 2.4), and the SiO_2:LPS composite (Fig. 2.5).

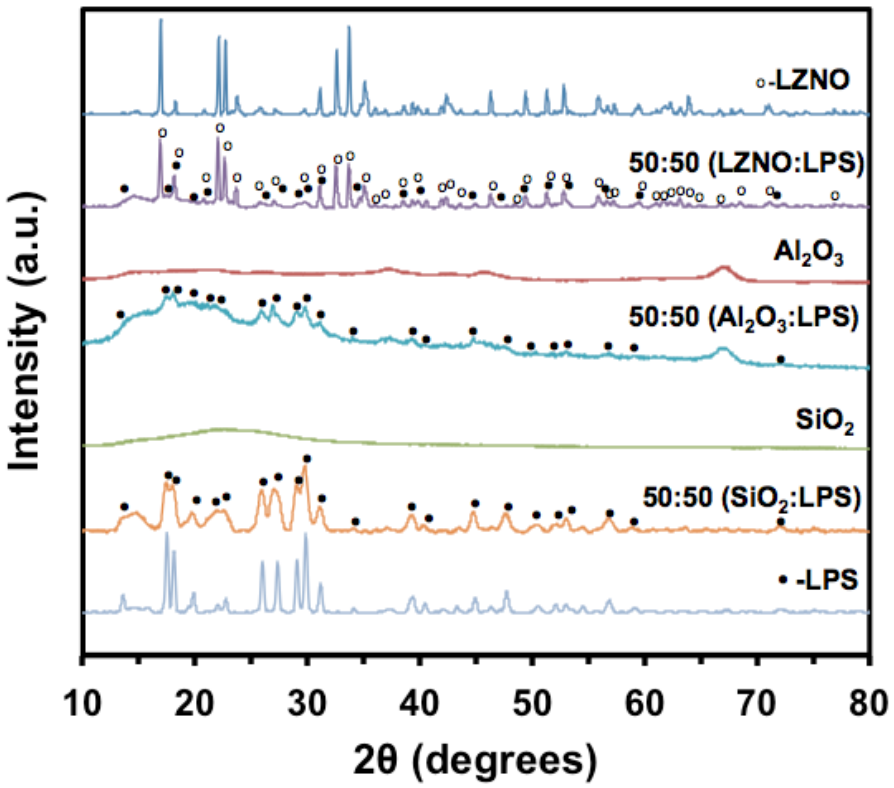

Figure 2.1 XRD patterns of composites and pristine precursors. No reaction was observed between the LPS and oxide fillers from XRD analysis, as all peaks in composites were identified as from the parent compounds [25]. Reprinted with permission; © 2015 Elsevier.

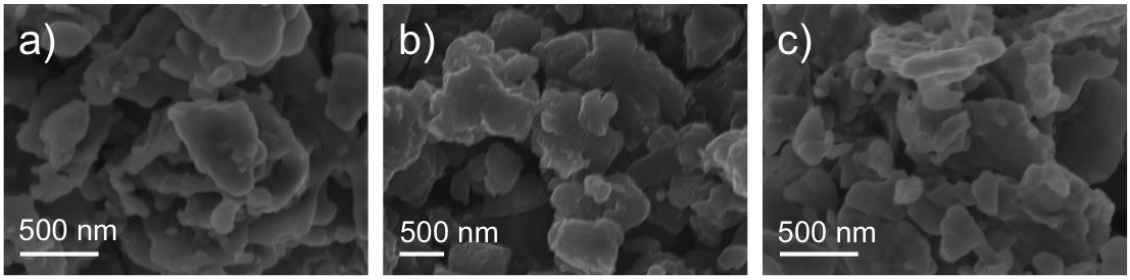

Figure 2.2 a) SEM images of 50 LZNO: 50 LPS; b) 50 Al_2O_3: 50 LPS; and c) 50 SiO_2: 50 LPS after ball milling [25]. Reprinted with permission; © 2015 Elsevier.

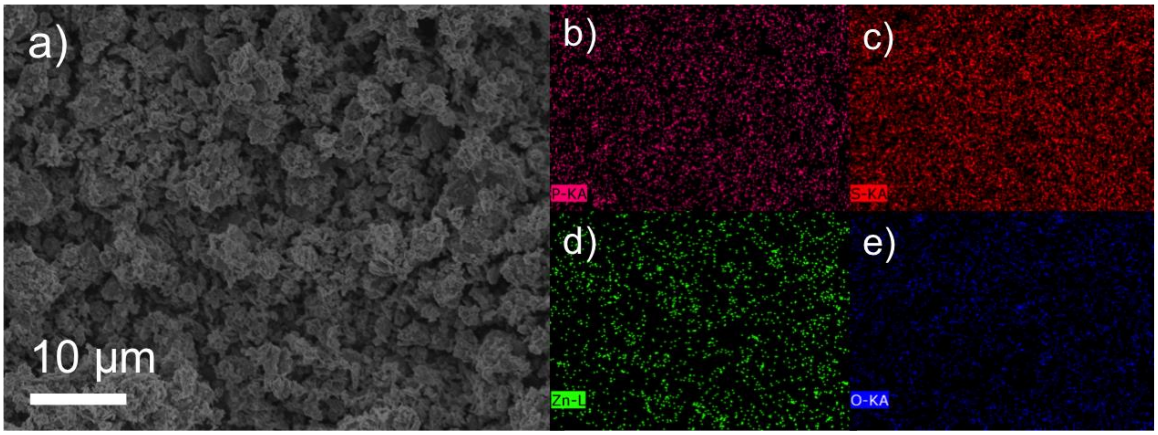

Fig. 2.3 a) SEM image of 50 LZNO: 50 LPS composite with corresponding EDS analysis showing a homogeneous distribution of b) phosphorus, c) sulfur, d) zinc and e) oxygen [25]. Reprinted with permission; © 2015 Elsevier.

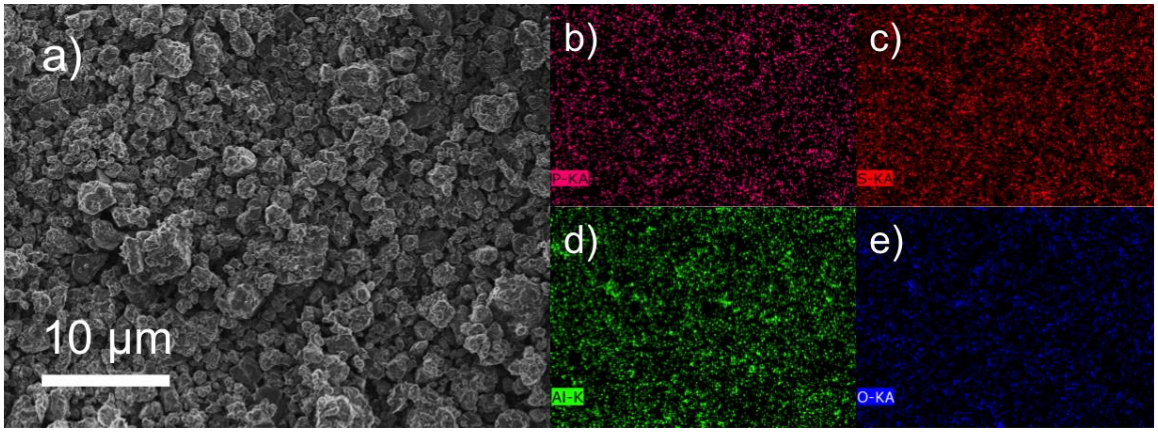

Fig. 2.4 a) SEM image of 50 Al_2O_3: 50 LPS composite with corresponding EDS analysis showing a homogeneous distribution of b) phosphorus, c) sulfur, d) aluminum and e) oxygen [25]. Reprinted with permission; © 2015 Elsevier.

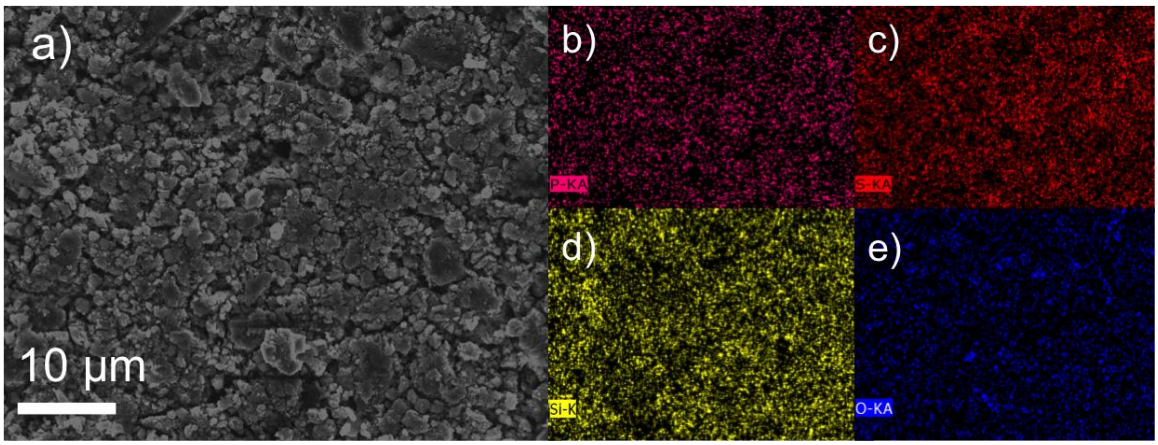

Fig. 2.5 a) SEM image of 50 SiO_2: 50 LPS composite with corresponding EDS analysis showing a homogeneous distribution of b) phosphorus, c) sulfur, d) silicon and e) oxygen [25]. Reprinted with permission; © 2015 Elsevier.

At room temperature, the oxides have poor processability; it is nearly impossible to cold-press a pellet of LZNO, Al_2O_3 or SiO_2 without the pellet partitioning or fractures forming. For this reason, the sticky LPS aids in pressing a dense pellet free from fractures (Fig. 2.6). After adding as low as 10 wt.% LPS to the oxide fillers, a dense pellet can be easily cold-pressed (density of 10 wt.% LZNO composite ~2.56 $g \cdot cm^{-3}$, 10 wt.% Al_2O_3 composite ~1.75 $g \cdot cm^{-3}$, and 10 wt.% SiO_2 composite ~1.43 $g \cdot cm^{-3}$; densities determined from gravimetric and geometric measurements). The pellet density increases for the LZNO and Al_2O_3 composites with increasing oxide content, while the pellet density decreases for the SiO_2 composites; this trend agrees with the density of the pristine oxides, as LZNO and Al_2O_3 are denser than LPS, while SiO_2 is less dense than LPS.

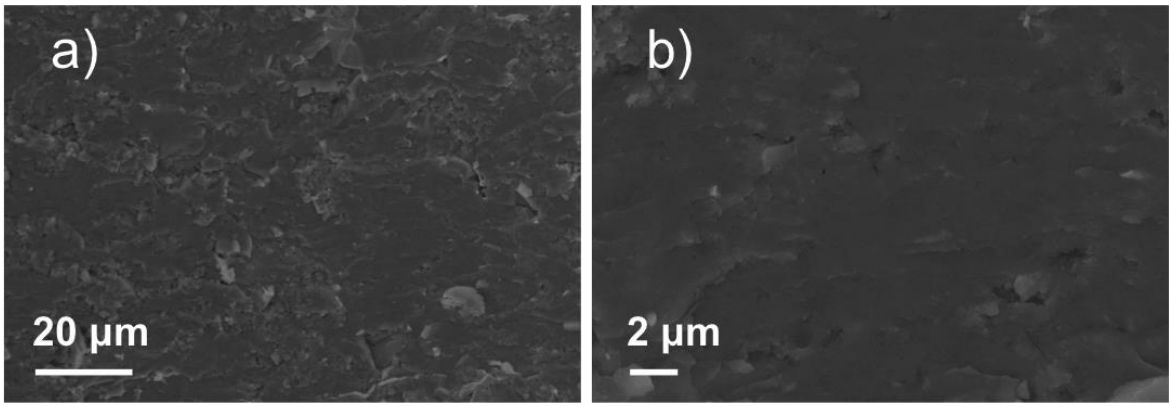

Fig. 2.6. a) Cross-sectional SEM images of cold-pressed 10:90 (LZNO:LPS) composite and b) a close-up image detailing the dense electrolyte. The sticky LPS aids in cold pressing dense pellets free from pores and cracks [25]. Reprinted with permission; © 2015 Elsevier**.**

2.2.2 Effect of solid oxide fillers on composite ionic conductivity and activation energy

Each of the oxide fillers affects the ionic conductivity of the composite with a similar trend – a relatively small fraction percent of the oxide filler enhances the ionic conductivity while higher concentrations of solid oxide cause the ionic conductivity to decrease. In the case of 10:90 (LZNO:LPS), the ionic conductivity is 2.44×10^{-4} $S\cdot cm^{-1}$, which is higher than the conductivity of the pristine parent compounds. This trend was previously observed in the case of LPS filled with $Li_7La_3Zr_2O_{12}$ (LLZO), where an addition of 30 wt.% LLZO to LPS increased the conductivity from 1.6×10^{-4} $S\cdot cm^{-1}$ to 5.36×10^{-4} $S\cdot cm^{-1}$ [8]. This enhancement in conductivity was attributed to the interface between LPS and LLZO, where the Nyquist data show both higher and lower conducting components. For the case of LZNO, this same phenomenon is observed with the 90:10 (LZNO:LPS) composite; Nyquist data show higher conducting and lower conducting processes, evidencing the

presence of an interfacial layer between the LPS and the porous non-dense oxide filler (Fig. 2.7). This phenomenon was only found in the LPS filled with ion-conducting fillers while the non-conducting fillers did not show two processes in the Nyquist data, which confirms that there is competition between the higher conducting parent electrolyte and lower conducting oxide filler throughout the composite.

In heterogeneous composite electrolytes, the conduction mechanism is expected to be influenced by both space-charge and blocking effects [8, 13-20]. The space-charge effect will account for enhancement of the parent electrolyte, causing less resistance for the charged particle, while the blocking effect will cause the conductivity to decrease, where the blocking species will impede the forward mobility of the charged particle. A model for the filler's effect on LPS is shown in Fig. 2.8, where 'A' represents the pristine LPS with no oxide filler, 'B' illustrates LPS filled with enough oxide filler to induce an enhancement in the ionic conductivity, and 'C' demonstrates the blocking effects of the oxide filler. Each oxide filler has a concentration in LPS where it enhances the ionic conductivity and a concentration where it will impede ion hopping through the material. Fig. 2.9 presents the compiled ionic conductivities and activation energies for each composite. The LZNO-filled LPS composites show a pronounced space-charge effect where the addition of 10 wt.% of LZNO increases the conductivity to 2.44×10^{-4} $S\cdot cm^{-1}$, while the addition of 2 wt.% of Al_2O_3 and SiO_2 also increases the conductivity (2 wt.% Al_2O_3 increases the conductivity to 2.28×10^{-4} $S\cdot cm^{-1}$ and 2 wt.% SiO_2 increases the conductivity to 1.84×10^{-4} $S\cdot cm^{-1}$). When comparing the SiO_2 to Al_2O_3 fillers, LPS filled with 2 wt.% Al_2O_3 shows a significant increase in conductivity while the LPS filled with 2 wt.% SiO_2 shows a slight increase. The Al_2O_3 and SiO_2 fillers have different zero charge pH values (SiO_2 is ~3 and

Al_2O_3 is ~9) where the order of oxide activity corresponds to the zero charge pH value of the oxide filler [17]. The surface acidity of the oxide filler increases the ionic conductivity by changing the charge carrier distribution in the composites. SiO_2 does not favorably enhance the charge carrier distribution in the composite, so solid oxides in composites with LPS with a zero charge pH of ~3 are expected to yield similar results. Furthermore, the particle size of SiO_2 is smaller than that of LZNO and Al_2O_3, which has previously been demonstrated to cause both favorable and unfavorable changes in the charge transfer distribution in composite electrolytes depending on pore and particle sizes [21-24]. In this study, the LZNO and Al_2O_3 fillers are composed of larger particles than the SiO_2 filler, and consequently, the ionic conductivity was enhanced with relatively larger particles. The ion-conducting LZNO filler causes a more pronounced enhancement when compared to the non-conducting Al_2O_3, even though their particle size is similar. Still, the ionic conductivity of LPS decreases after the addition of ≥ 30wt.% LZNO, ≥ 8wt.% Al_2O_3 and ≥ 5wt.% SiO_2, which corresponds to the blocking effects shown in part 'C' of Fig. 2.8. When the concentration of non-conducting oxide particles in the composite is too high, the particles will impede the forward motion of the Li ions. On the other hand, LZNO may also impede the forward motion of the Li ions since it has a lower room temperature ionic conductivity than LPS, but its effect is not as pronounced as the non-conducting oxide fillers. The results of this study agree with previous reports of space-charge and blocking effects in other systems that use Al_2O_3 and SiO_2 as fillers [14-17].

The activation energy collected from Arrhenius measurements significantly increases as LPS is filled with more SiO_2. LPS filled with LZNO or Al_2O_3 also follows a similar trend of increasing activation energy, however, the increase is not as significant as

the SiO_2:LPS composites. This increase in activation energy is attributed to grain boundaries and the blocking effects of the oxide filler. More specifically, SiO_2 significantly increases the thermal activation of ion hopping through the material, which is attributed to the small particle size and unfavorable zero charge pH. On the other hand, LPS filled with $\leq$ 5 wt.% of Al_2O_3 does not significantly change the thermal activation (0.32eV). When compared to the nonconductors, the ion-conductors (LLZO and LZNO) significantly decrease the thermal activation of ion hopping for composites with enhanced ionic conductivity [8]. The activation energy of pristine LZNO was estimated as 0.39eV [10], however, in the highest conducting LZNO:LPS composite, the activation energy was decreased to 0.31eV, significantly lower than that of LPS (0.35eV) and LZNO (0.39eV).

With a high conductivity coupled with low activation energy, the 10wt.% LZNO and 2wt.% Al_2O_3 composite electrolytes are superior to the SiO_2:LPS composite presented in this study. These composites have ionic conductivities greater than 2.2×10^{-4} $S \cdot cm^{-1}$ and activation energies lower than 0.33eV, making these electrolytes favorable for lithium-ion battery applications.

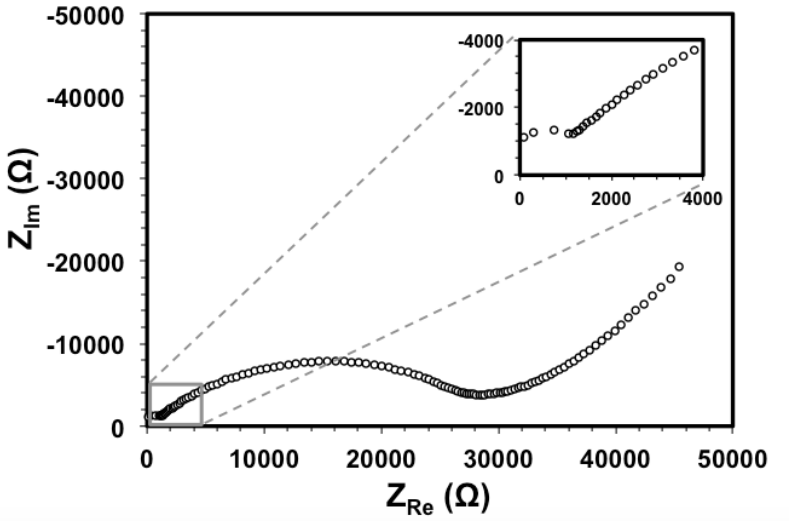

Figure 2.7 Nyquist plot of 90:10 (LZNO:LPS) composite at 25 °C. Two semicircles represent the high conduction and low conduction processes of the cold-pressed composite electrolyte [25]. Reprinted with permission; © 2015 Elsevier.

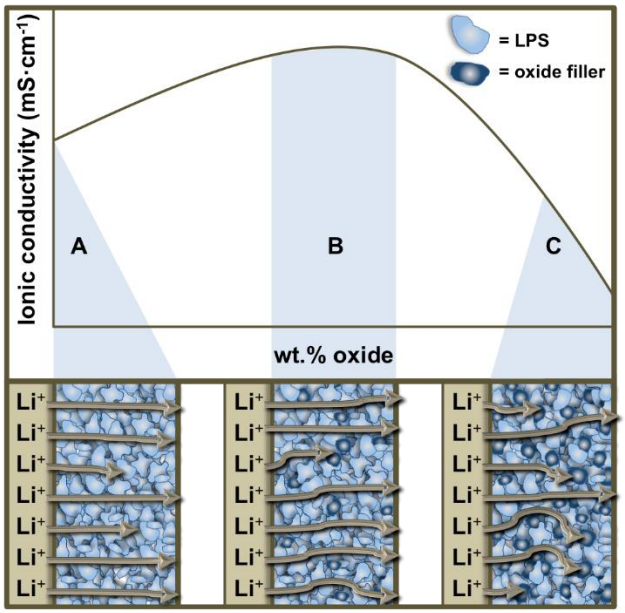

Figure 2.8 Model for the oxide filler's effect on the parent LPS electrolyte. 'A' represents the addition of no oxide filler, 'B' represents the space charge effect, and 'C' shows the blocking effect of the oxide filler [25]. Reprinted with permission; © 2015 Elsevier.

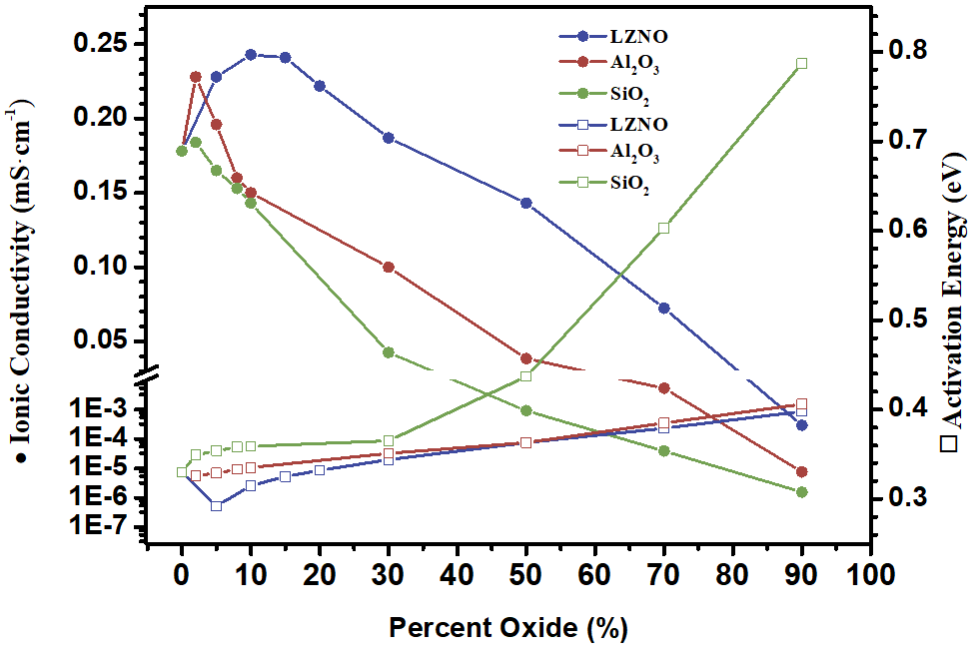

Figure 2.9 Plots of ionic conductivity (left y-axis) and activation energy (right y-axis) as a function of oxide content. The closed circles correspond to ionic conductivity and the open squares correspond to activation energy [25]. Reprinted with permission; © 2015 Elsevier.

2.2.3 Stability of the composite against metallic lithium anode

After determining the ionic conductivity enhancement of the ion-conducting and non-conducting oxide fillers on LPS, the composites with greatest ionic conductivity were selected for electrochemical stability and cell cycling measurements for each composite was evaluated. Some solid electrolytes have high ionic conductivity, however, their use in a solid-state battery is compromised by their stability with metallic lithium anode, which ultimately compromises the overall capacity. LPS alone shows stability with a metallic Li anode [7], however, it was unknown to what extent the oxide fillers compromised this stability. Cyclic voltammetry measurements show that each composite is stable up to the potential of 5V *vs.* Li/Li^+. In Fig. 2.10a, the stability of the composite is apparent in the cyclic voltammogram (CV) with the Li/LZNO:LPS/Pt cell for the 10:90 (LZNO:LPS) composite, which is also representative of LPS filled with Al_2O_3 and SiO_2. Anodic current is only present at 0 to 0.75 V while no significant current was observed between 0.75 to 5 V, which was also observed for composites filled with the selected non-conducting oxides. Additionally, no side reactions were observed between the composites and metallic lithium. Therefore, the oxide fillers do not compromise the chemical and electrochemical stability of LPS against metallic lithium anode.

To demonstrate the cyclability and long-term stability of the composite electrolytes filled with ion-conducting and non-conducting oxides, a symmetric Li/composite electrolyte/Li cell was constructed and cycled at room temperature. Fig. 2.10b displays the voltage profile for the symmetric cell with the LZNO-filled LPS, which is representative for each composite. This cell presented a voltage of 35.6 mV with a current density of 0.1 $mA \cdot cm^{-2}$, corresponding to a direct-current (dc) conductivity of 2.3×10^{-4} $S \cdot cm^{-1}$ for the

symmetric cell. The alternating current (ac) conductivity was found to be 2.4×10^{-4} $S\cdot cm^{-1}$ for the composite, agreeing with the calculated dc conductivity. The dc and ac conductivities were also similar for the LPS filled with non-conducting oxides. Negligible interfacial resistance was observed when the composite electrolytes were cycled with metallic lithium (even after 400 cycles), supporting the compatibility of the composite electrolytes with metallic lithium.

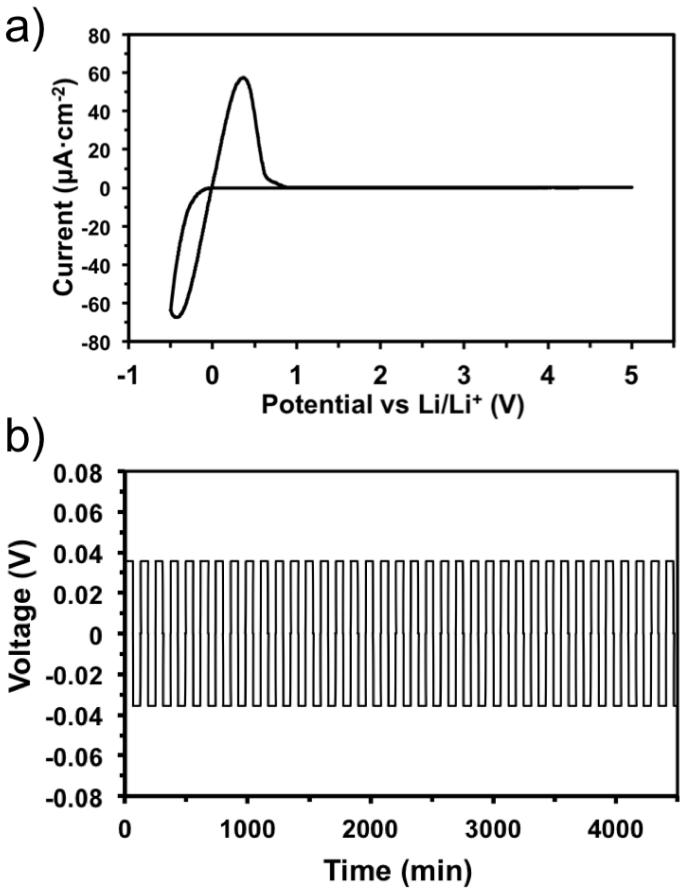

Figure 2.10 a) Representative CV of Li/LZNO:LPS/Pt cell for the 10:90 (LZNO:LPS) composite, demonstrating a wide electrochemical window of 5V; b) representative cycling data of Li/LZNO:LPS/Li symmetric cell with a current density of $0.1mA\cdot cm^{-2}$ for the 10:90 (LZNO:LPS) composite. These data are representative of the highest conducting composites with Al_2O_3 and SiO_2, as similar cyclic voltammetry and cycling data were collected [25]. Reprinted with permission; © 2015 Elsevier.

The stability between metallic lithium and the 10:90 (LZNO:LPS) composite was further confirmed by EIS at different cycle numbers and through the utilization of SEM with EDS to analyze the interface in a symmetric cell containing metallic lithium. Previously, thin films of pristine LZNO were shown to have high interfacial resistance when cycled with metallic lithium [12], however, in this study, it is demonstrated that the LZNO:LPS composite may be cycled hundreds of times with low interfacial resistance. Fig. 2.11 displays the EIS spectra collected after 25, 50, and 100 charge/ discharge cycles. The resistance through the material does not significantly change when charged/ discharged in a symmetric cell configuration. The interface between metallic lithium was analyzed using SEM and EDS elemental mapping after 0, 50, and 100 cycles (Fig. 2.12). After cycling, the composite electrolyte does not change morphology, maintaining a dense network where lithium cannot penetrate through the composite LZNO:LPS electrolyte. Interestingly, no significant buffer layer appears between the composite electrolyte and the metallic lithium anode signifying that no major side reactions occur at the interface. LPS is believed to stabilize the interface, even when LPS is in composites with oxide fillers. Therefore, the synergistic relationship between LPS and the oxide filler allows for both interfacial stability with metallic lithium (from LPS) *and* enhanced ionic conductivity in the composite electrolyte (from the oxide filler).

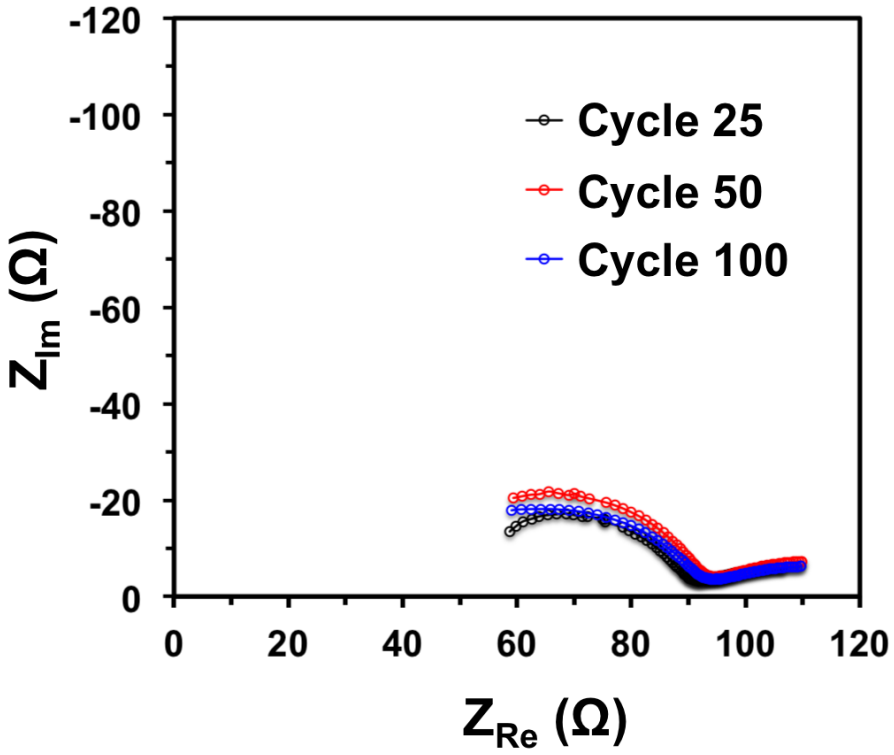

Figure 2.11 EIS of Li/LZNO:LPS/Li cell for the 10:90 (LZNO:LPS) composite at 25 °C after different cycle numbers. Negligible change in resistance between cycles 25, 50 and 100 was observed [25]. Reprinted with permission; © 2015 Elsevier.

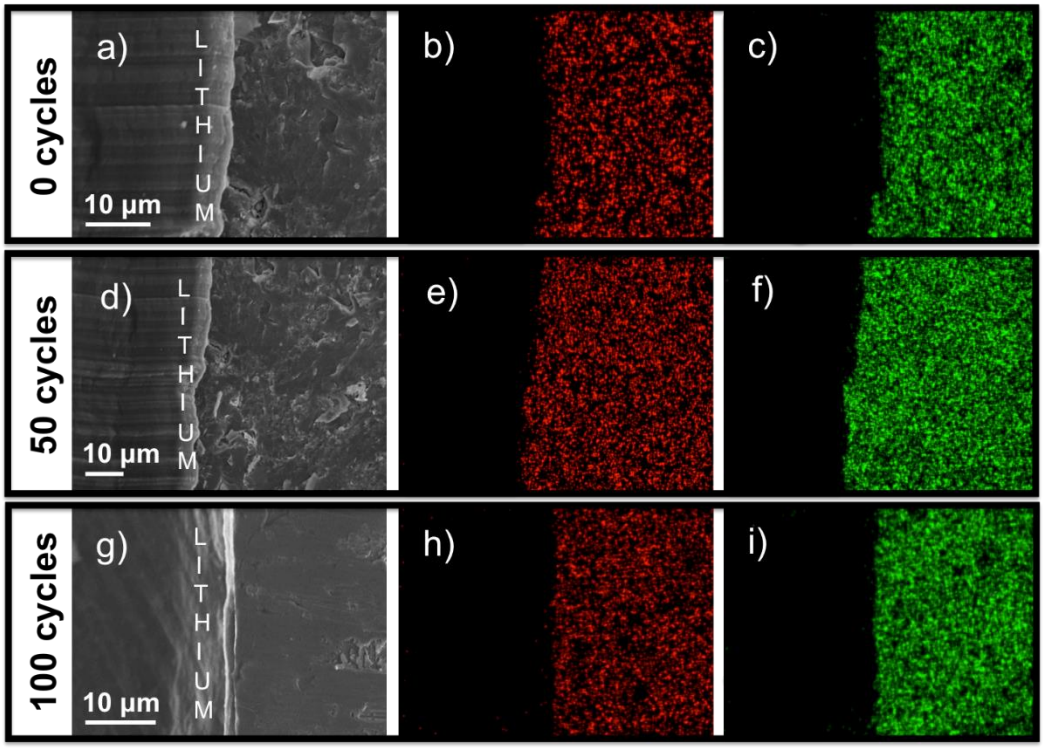

Figure 2.12 Cross-sectional SEM images of 10:90 (LZNO:LPS) interface after a) 0 charge/ discharge cycles, d) 50 charge/ discharge cycles and g) 100 charge/ discharge cycles; b,e,h) corresponding EDS elemental mapping of sulfur; c,f,i) corresponding EDS elemental mapping of phosphorus. After 100 charge/ discharge cycles, the interface between the LZNO:LPS composite maintains the same dense morphology where no major interfacial reaction was observed [25]. Reprinted with permission; © 2015 Elsevier.

2.3 Summary

Three different oxides were studied as fillers for LPS composites. Through X-ray diffraction analysis, it was shown that no reaction occurred through simple room-temperature ball-milling of the oxides with LPS. SEM images indicate that the cold-pressed pristine oxide pellets can be fabricated without fractures, breaks, and minimal open porosity. As an increased amount of oxide was added to the composite, the ionic

conductivity significantly decreases while the activation energy increases which is attributed to the blocking effects from the oxide filler. When 10 wt.% LZNO was added to LPS, the ionic conductivity increases to 2.44×10^{-4} $S\cdot cm^{-1}$, nearly doubling the ionic conductivity of the parent electrolyte.

To meet the needs of solid-state batteries, the present study will help fabricate better LiSICON composite electrolytes. As found, the addition of 10 wt.% LZNO significantly increased the conductivity of LPS while maintaining low activation energy (0.31eV) and stability against metallic lithium up to 5V. Similarly, LPS filled with 2wt.% Al_2O_3 increased the conductivity to 2.28×10^{-4} $S\cdot cm^{-1}$ while maintaining low activation energy (0.32eV) and stability against metallic lithium up to 5V. These data demonstrate that ion-conducting and non-conducting oxide fillers may be used to enhance the ionic conductivity of LPS. Also, the oxide fillers do not compromise LPS's stability against metallic lithium anode, allowing for hundreds of charge-discharge cycles. Based on the present study, the enhancement of LPS with LZNO and Al_2O_3 produced composite electrolytes with high ionic conductivity and low activation energy comparable to that of liquid electrolytes, which shows promise for the fabrication of safer, longer-lasting, all-solid state batteries in the near future.

2.4 Experimental Methods

Synthesis of composites: LZNO:LPS, Al_2O_3:LPS, and SiO_2:LPS composites were prepared by ball milling with the SPEX SamplePrep® Mixer/Mill 8000M. LPS was synthesized in a previously reported solution-based method using THF followed by subsequent heating at 140°C for 1 hour and 200°C for 2 hours [3] and LZNO was synthesized using a solid-state

reaction [11, 12]. Al_2O_3 (Sigma Aldrich, 150 mesh, pore size 58 Å) and SiO_2 (Aldrich, 99.5%, 5-15nm particle size) were used to synthesize the composites. Al_2O_3 and LZNO were ball-milled to reduce the particle size to ≤ 1-2 μm before composite fabrication. Since LZNO, Al_2O_3 and SiO_2 were previously stored in air, these powders were heated to 350°C prior to moving the powders to the glove box to remove any moisture. The oxide wt.% was varied between 2-90 wt.% when fabricating each composite. Y-ZrO_2 beads (3mm & 5mm; ~10g) were used in the ball milling process. All composites have particles size of 1-2 μm or less before pressing pellets. Since LPS is sensitive to air, all composites were synthesized under Argon.

Characterization of materials: A PANalytical X'Pert Pro Powder Diffractometer equipped with a Ni-filtered Cu K_α radiation was used for the crystallographic phase identification for the composites. Quartz slides were sealed with Kapton® films for analysis and High Score Plus was used to complete Rietveld refinement and structural analysis. All X-ray powder diffraction patterns were collected at room temperature. Scanning electron microscopy (SEM) images were collected with a Zeiss Merlin SEM at 3.0kV. Energy-dispersive X-ray spectroscopy (EDS) was completed on the composites to ensure homogeneity after ball milling. For EDS, the beam energy was 10.0kV in order to obtain the excitation of elements from LPS and the oxide fillers. Pellets were carefully fractured for cross-sectional SEM images detailing the interface between the composite electrolyte and metallic lithium anode. Prior to collecting images, all samples were placed on carbon conductive tape and sealed under Argon.

Electrochemical measurements: About 140mg of each composite was used to prepare 1/2" pellets, which were cold-pressed at 300 MPa with Al/C blocking electrodes. Swagelok®

cells were used to obtain all impedance and activation energy data. Impedance measurements were obtained using a Solartron SI 1260 Impedance Gain-Phase Analyzer from 1MHz – 1 Hz with amplitude 100.0mV. Activation energies were determined by Arrhenius measurements using the Maccor 4300 System Environmental Chamber with temperatures ranging 25-100 °C. EIS was collected for symmetric cells after cycles 25, 50 and 100 to monitor the change in interfacial resistance between the composite electrolyte and metallic lithium anode. A BioLogic MPG2 instrument equipped with EC-Lab software was utilized to collect all cyclic voltammetry and cell cycling data. Li/composite electrolyte/Pt cells were placed into Swagelok® cells for cyclic voltammetry measurements with a potential of 10 mV/s and scanned from -0.5 to 5.0 V vs. Li/Li^+. Lithium and platinum serve as counter and working electrodes, respectively. Li/composite electrolyte/Li symmetric cells were also placed into Swagelok® cells for cell cycling with a potential of $0.1mA \cdot cm^{-2}$.

2.5 Notes to Chapter 2

Part of this chapter is adapted from the paper "The "filler effect": A study of solid oxide fillers with β-Li_3PS_4 for lithium conducting electrolytes" published in *Solid State Ionics* [25].

2.6 References

[1] Armand, M. and J.M. Tarascon. Building better batteries. *Nature*, **2008**. **451**(7179): p. 652-657.

[2] Tarascon, J.M. and M. Armand. Issues and challenges facing rechargeable lithium batteries. *Nature*, 2001. **414**(6861): p. 359-367.

[3] Li, J.; Ma, C.; Chi, M.; Liang, C.; Dudney, N. J. Solid Electrolyte: the Key for High-Voltage Lithium Batteries. *Advanced Energy Materials* **2015**, *5*.

[4] Rangasamy, E., et al., *Pushing the Theoretical Limit of Li-CF_x Batteries: A Tale of Bifunctional Electrolyte.* Journal of the American Chemical Society, **2014**, 136(19), p. 6874–6877.

[5] Sahu, G., et al., Air-stable, high-conduction solid electrolytes of arsenic-substituted Li_4SnS_4. Energy & Environmental Science, **2014**. **7**(3): p. 1053-1058.

[6] Nagao, M., et al., All-solid-state Li–sulfur batteries with mesoporous electrode and thio-LISICON solid electrolyte. Journal of Power Sources, 2013. **222**: p. 237-242.

[7] Liu, Z.; Fu, W.; Payzant, E. A.; Yu, X.; Wu, Z.; Dudney, N. J.; Kiggans, J.; Hong, K.; Rondinone, A. J.; Liang, C. Anomalous high ionic conductivity of nanoporous *β*-Li_3PS_4. *Journal of the American Chemical Society* **2013**, *135*, 975-978.

[8] Rangasamy, E.; Sahu, G.; Keum, J. K.; Rondinone, A. J.; Dudney, N. J.; Liang, C. A high conductivity oxide–sulfide composite lithium superionic conductor. *Journal of Materials Chemistry A* **2014**, *2*, 4111-4116.

[9] Liang, C. Conduction Characteristics of the Lithium Iodide-Aluminum Oxide Solid Electrolytes. *Journal of The Electrochemical Society* **1973**, *120*, 1289-1292.

[10] Maier, J. Space charge regions in solid two-phase systems and their conduction contribution—I. Conductance enhancement in the system ionic conductor-'inert' phase and application on AgC1:Al_2O_3 and AgC1:SiO_2. *Journal of Physics and Chemistry of Solids*, **1985**, 46(3), 309-320.

[11] Konovalova, V.V., et al. New conducting phase in the Li_2O-ZnO-Nb_2O_5 system: Existence conditions. *Russian Journal of Inorganic Chemistry*, **2009**, 54(10), 1650-1654.

[12] Li, Yunchao, Mariappan Parans Paranthaman, Lance W. Gill, Edward W. Hagaman, Yangyang Wang, Alexi P. Sokolov, Sheng Dai et al. Conduction below 100° C in nominal $Li_6ZnNb_4O_{14}$. *Journal of Materials Science*, **2015**, 1-7. DOI 10.1007/s10853-015-9408-z.

[13] Dudney, N.J. Effect of the interfacial space-charge polarization on the ionic-conductivity of composite electrolytes. *Journal of the American Ceramic Society*, **1985**, 68(10), 538-545.

[14] Maier, J., Space-charge regions in solid 2-phase systems and their conduction contribution. 1. Conductance enhancement in the system ionic conductor-inert phase and application on $AgCl-Al_2O_3$ and $AgCl-SiO_2$. *Journal of Physics and Chemistry of Solids*, **1985**, **46**(3), 309-320.

[15] Maier, J., Space-charge regions in solid 2-phase systems and their conduction contribution. 3. Defect chemistry and ionic-conductivity in thin-films. *Solid State Ionics*, **1987**, 23(1-2), 59-67.

[16] Dudney, N.J. Composite electrolytes. *Annual Review of Materials Science*, **1989**, 19, 103-120.

[17] Maier, J., Ionic conduction in space charge regions. *Progress in Solid State Chemistry*, **1995**, 23(3), 171-263.

[18] Knauth, P. Ionic conductor composites: theory and materials. *Journal of Electroceramics*, **2000**, **5**(2), 111-125.

[19] Maier, J., Nanoionics: ion transport and electrochemical storage in confined systems. *Nature Materials*, **2005**, 4(11), 805-815.

[20] Kumar, B., et al. Ionic conduction through heterogeneous solids: Delineation of the blocking and space charge effects. *Journal of Power Sources*, **2006**, 160(2), 1329-1335.

[21] Uvarov, N. F., Isupov, V. P., Sharma, V., & Shukla, A. K. Effect of morphology and particle size on the ionic conductivities of composite solid electrolytes. *Solid State Ionics*, **1992**, 51(1), 41-52.

[22] Nagasubramanian, G., Attia, A. I., Halpert, G., & Peled, E. Composite solid electrolyte for Li battery applications. *Solid State Ionics*, **1993**, 67(1), 51-56.

[23] Wieczorek, W., Florjanczyk, Z., & Stevens, J. R. Composite polyether based solid electrolytes. *Electrochimica Acta*, **1995**, 40(13), 2251-2258.

[24] Croce, F., Appetecchi, G. B., Persi, L., & Scrosati, B. Nanocomposite polymer electrolytes for lithium batteries. *Nature*, **1998**, 394(6692), 456-458.

[25] Hood, Z. D.; Wang, H.; Li, Y.; Pandian, A. S.; Paranthaman, M. P.; Liang, C. *Solid State Ionics*, **2015**, 283, 75.

CHAPTER 3

FABRICATION OF ULTRATHIN MEMBRANES OF β-Li_3PS_4

3.1 Introduction

The rapidly growing demand for energy storage requires new battery technologies beyond current state-of-the-art lithium-ion batteries. Among all the potential solutions, Li-metal batteries, which offer the highest specific capacity of lithium and lowest negative electrochemical potential, are expected to provide a maximized capacity density and voltage window, increasing the overall energy density for the battery [1-3]. While different configurations of Li-metal batteries have been proposed, including all-solid-state, Li-air, and Li-S batteries, solid electrolytes are considered one of the critical components that will enable the use of metallic lithium in most of these designs [1, 4, 5]. Currently, solid electrolytes can be divided into three main categories for battery-related applications: polymers, sulfides, and oxides. In general, the fabrication of thin films from polymer solid electrolytes is the easiest, yet they often show problems associated with lower mechanical strength and decreased ionic conductivity [6]. Sulfides and oxides offer desirable ionic conductivity and increased mechanical strength, but they are generally difficult to be processed into ultrathin films from bulk materials.

The fabrication of solid electrolytes as ultrathin films is critical to their function because they serve as both the ion transport medium and separator material. When these membranes are too thick, it leads to an increase in the overall volume/mass of the battery and lower power and energy densities, but more critically, it limits the current density that

can pass during charging/discharging processes, especially when the solid electrolyte has a low ionic conductivity [7]. It is still challenging to fabricate thin film solid electrolytes. Typical fabrication methods include radio frequency magnetron sputtering, atomic layer deposition, or pulsed laser deposition [8, 9]. These techniques, however, require expensive and time consuming ultra-high vacuum conditions. Furthermore, controlling the stoichiometry of the thin solid electrolyte films using these techniques can be very difficult, especially for volatile elements such as Li, P, and S.

Sulfide-based solid electrolytes have shown the highest lithium ion conductivity among the three main categories of solid electrolytes for battery-related applications [10, 11]. To this end, $Li_{10}GeP_2S_{12}$ (LGPS) was reported to deliver an ionic conductivity of $\geq 10^{-3}$ $S \cdot cm^{-1}$, comparable to the ionic conductivities of organic liquid electrolyte. However, LGPS is not chemically stable with lithium metal due to the presence of reactive Ge atoms, and the propagation of such chemical reactions limits the electrochemical cycling of the battery. A number of new sulfide-based solid electrolytes have shown relatively high ionic conductivities with necessary compatibility with metallic lithium anodes, e.g., β-Li_3PS_4, $Li_7P_2S_8I$, and Li_2S-P_2S_5 glass-ceramics [12-16]. In general, sulfide-based solid electrolytes are synthesized using solid-state techniques, which require processing at temperatures >400 ℃ and the use of evacuated ampules, which add to the processing cost of the material. Several sulfide-based solid electrolytes such as β-Li_3PS_4, $Li_7P_2S_8I$, and Li_4PS_4I, have recently been synthesized through solvent-based wet-chemical techniques at mild temperatures, offering flexibility in terms of synthesis [12, 13, 17]. However, the fabrication of thin films from sulfide-based solid electrolytes is challenging. Although

many efforts have been reported, the thickness of sulfide-based solid electrolytes can only be pushed to the range of hundreds of microns to several millimeters [4, 18-21].

In this work, I use sulfide-based β-Li_3PS_4 as a model system to demonstrate a novel strategy for significantly reducing the thickness of the solid electrolyte membranes. This technique combines a new synthesis of nanoscale plates with a unique, tiled assembly process that utilizes the plates as building blocks. Thin films of β-Li_3PS_4 with submicron thicknesses have been fabricated. More importantly, the thickness of each building block can be controllably tuned using this method without the degradation of film quality. Comprehensive structural and electrochemical characterizations have also been performed on the thin films. These films hold not only high ionic conductivity but also desirable compatibility with metallic lithium anode. These results highlight a new, facile strategy for generating ultrathin, dense films of solid electrolytes with desirable ionic conductivities for the next-generation energy storage and conversion systems.

3.2 Results and Discussion

3.2.1 Synthesis of Shape-controlled Solid Electrolyte Building Blocks

The fabrication of submicron-thick membranes of β-Li_3PS_4 starts with the synthesis of $Li_3PS_4 \cdot 2ACN$ nanoscale plates, which involves solvent exchange and solution-based exfoliation. $Li_3PS_4 \cdot 3THF$ was first synthesized using a solvent-based soft chemistry technique by stirring Li_2S and P_2S_5 in anhydrous tetrahydrofuran (THF, C_4H_8O) under argon, using the same procedure as first described by Liu and co-workers [12]. The Li_2S and P_2S_5 were mixed together at a 3 to 1 molar ratio, and the powder was added into THF

under vigorous stirring. After stirring for 24 h, a white precipitate was collected and dried under vacuum at room temperature for 1 h to yield $Li_3PS_4 \cdot 3THF$. The $Li_3PS_4 \cdot 3THF$ was composed of particles with an average size of *ca.* 10 μm (Figure 3.1). $Li_3PS_4 \cdot 2ACN$ nanoscale plates were then fabricated by exchanging the co-crystallized THF with ACN by adding 200 mg of the $Li_3PS_4 \cdot 3THF$ powder in to 100 mL of anhydrous acetonitrile (ACN, C_2H_3N) under vigorous stirring to initiate the process:

$$Li_3PS_4 \cdot 3THF + 2\ ACN \rightarrow Li_3PS_4 \cdot 2ACN + 3\ THF$$

After 40 min, the ACN solution changed from white to light blue (Figure 3.2) indicating the formation of $Li_3PS_4 \cdot 2ACN$. During the stirring process, samples were collected at different time points and deposited on silicon wafers for scanning electron microscopy (SEM) imaging. Figure 3.3A shows an SEM image of the initial $Li_3PS_4 \cdot 3THF$ powder and Figure 3.3B-D shows SEM images of the Li_3PS_4 samples after 15 s, 20 min, and 40 min of stirring in ACN. After stirring for 15 s, the $Li_3PS_4 \cdot 3THF$ became exfoliated as evidenced by the formation of sheet-like structures (Figure 3.4). After 40 min of stirring in ACN, the $Li_3PS_4 \cdot 3THF$ was converted to $Li_3PS_4 \cdot 2ACN$ with a well-controlled plate-like morphology, together with a thickness around 80 nm (Figure 3.5). Energy-dispersive x-ray spectroscopy (EDS) elemental mapping shows that the nanoscale plates contain both S and P (Figure 3.5C). It is worth noting that directly reacting Li_2S and P_2S_5 in ACN could not produce shape-controlled plate-like building blocks, but rather, irregularly shaped microflakes with a wide size distribution [7]. The procedure based on exchanging the co-crystalized THF with ACN, as explored in the current work, is the key to the successful production of well-defined $Li_3PS_4 \cdot 2ACN$ rectangular-shaped thin nanoplates that could then serve as building blocks for the fabrication of ultrathin films.

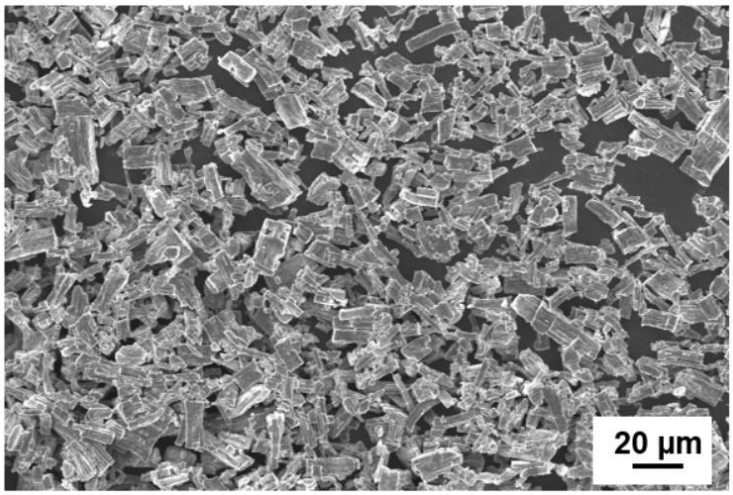

Figure 3.1 SEM image of $Li_3PS_4 \cdot 3THF$ particles [48]. Reprinted with permission; © 2018 WILEY-VCH Verlag GmbH & Co. KGaA, Weinheim.

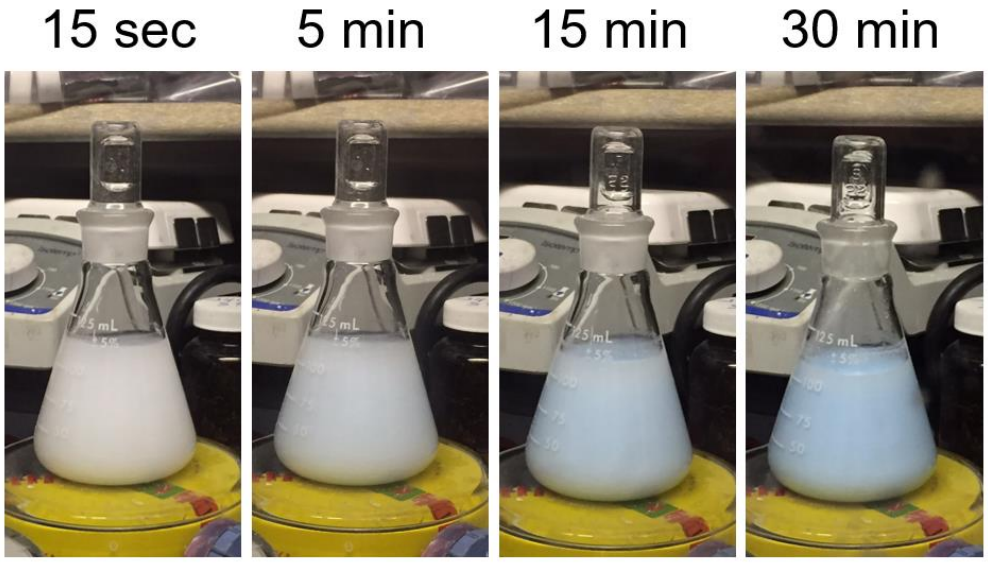

Figure 3.2 Photographs taken of the Li_3PS_4 solvent exchange reaction under vigorous stirring. As the reaction proceeded, the solution became slightly blue, indicating the formation of $Li_3PS_4 \cdot 2ACN$ [48]. Reprinted with permission; © 2018 WILEY-VCH Verlag GmbH & Co. KGaA, Weinheim.

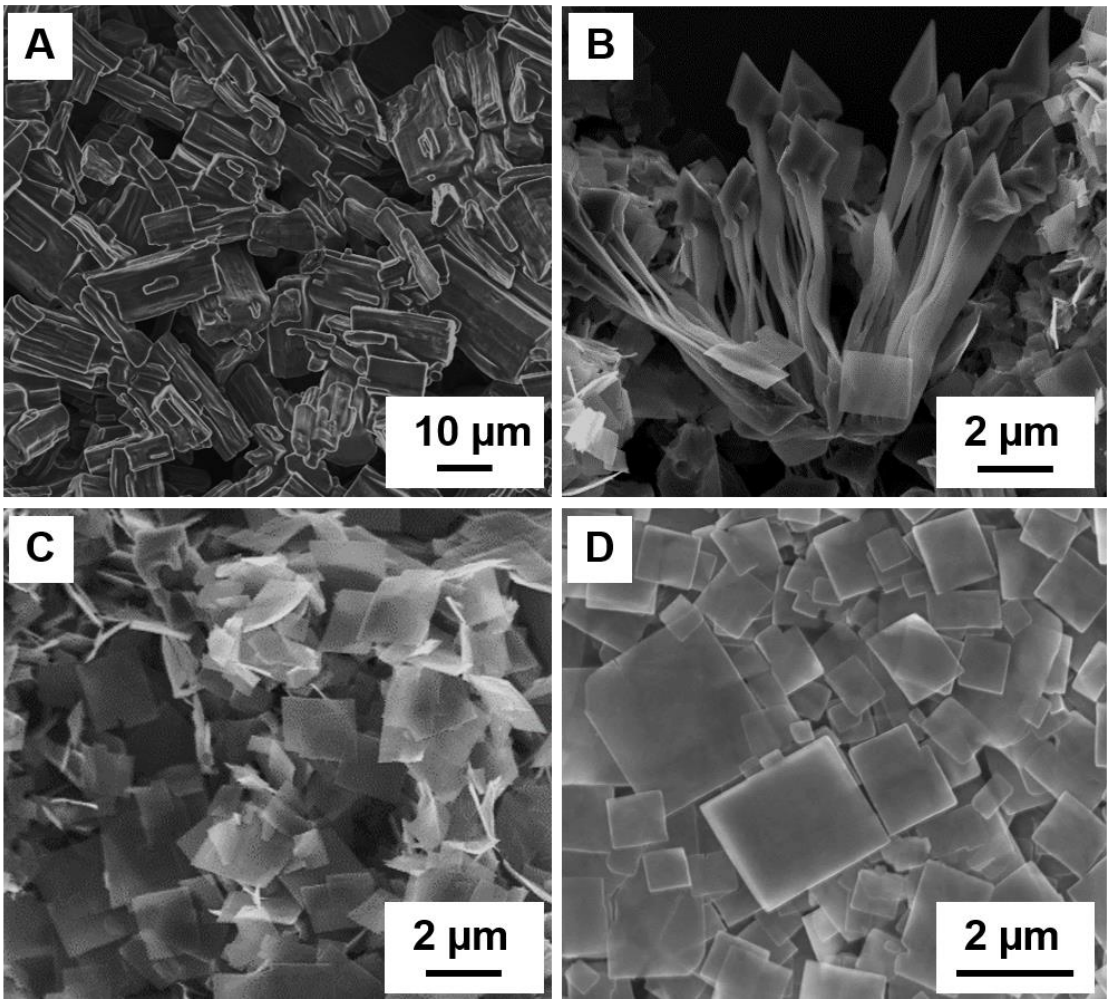

Figure 3.3 SEM images of $Li_3PS_4 \cdot 3THF$ (A) before and (B-D) after stirring $Li_3PS_4 \cdot 3THF$ in ACN for B) 15 s, C) 20 min, and D) 40 min. During this process, well-defined plates of $Li_3PS_4 \cdot 2ACN$ was precipitated out from the reaction solution [48]. Reprinted with permission; © 2018 WILEY-VCH Verlag GmbH & Co. KGaA, Weinheim.

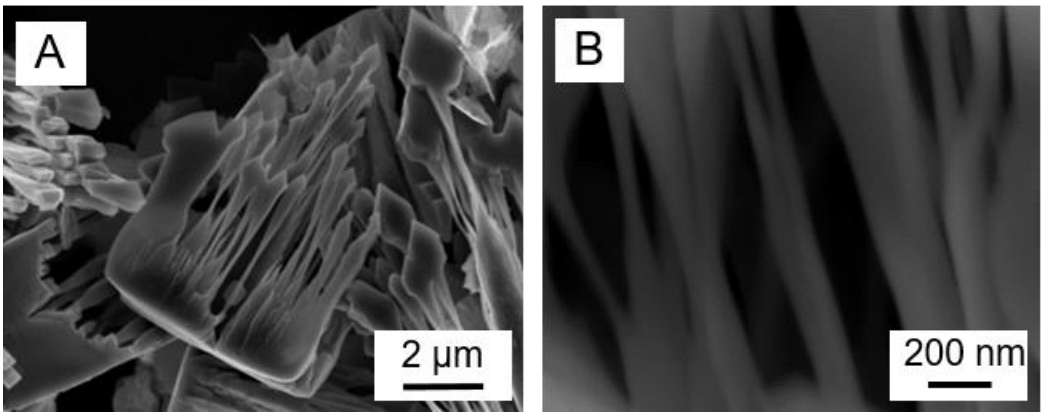

Figure 3.4 SEM images of A) an exfoliated Li_3PS_4·3THF particle and B) the formation of sheet-like structures in the exfoliated Li_3PS_4·3THF particle [48]. Reprinted with permission; © 2018 WILEY-VCH Verlag GmbH & Co. KGaA, Weinheim.

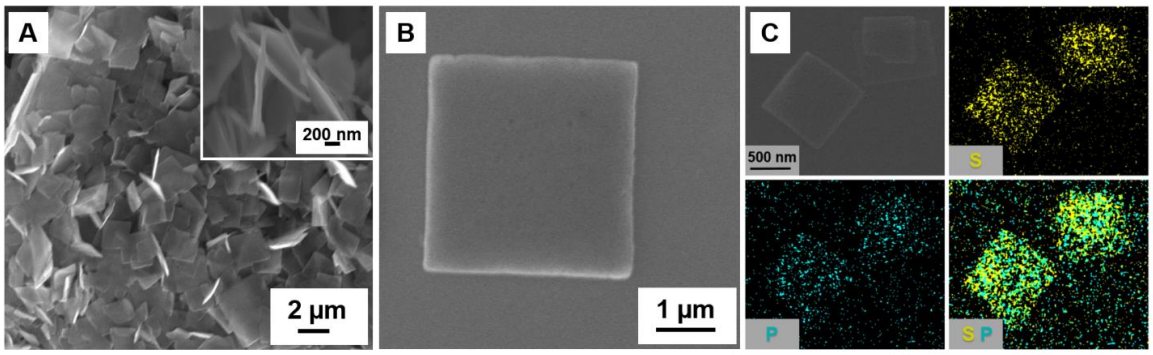

Figure 3.5 A-B) SEM images of plate-like, nanoscale building blocks of Li_3PS_4·2ACN at different magnifications. The inset reveals the thickness of around 80 nm for Li_3PS_4·2ACN. C) SEM image with EDS elemental mapping of nanoscale building blocks of Li_3PS_4·2ACN, displaying a clear distribution of phosphorus and sulfur across the Li_3PS_4·2ACN sheets [48]. Reprinted with permission; © 2018 WILEY-VCH Verlag GmbH & Co. KGaA, Weinheim.

Powder X-ray diffraction (XRD) and Raman spectroscopy confirmed the transformation of Li_3PS_4·3THF to Li_3PS_4·2ACN when the precursor is stirred in ACN (Figure 3.6). The XRD patterns of Li_3PS_4·3THF and Li_3PS_4·2ACN display distinct peaks that are in good agreement with previous reports [7, 12, 13]. The exchange of THF with

ACN happens rapidly, with nearly all the coordinated THF being replaced by ACN after about 60 s. After stirring Li_3PS_4·3THF in ACN for 40 min, X-ray diffraction reveals the complete transformation from Li_3PS_4·3THF to Li_3PS_4·2ACN. The exchange of solvent coordination with Li_3PS_4 was further proved by Raman spectroscopy. The initial Li_3PS_4·3THF displayed the characteristic peak for $\nu_s(PS_4)$ at 422 cm^{-1} and C-H vibrations of THF at 2850-3050 cm^{-1} in the Raman spectrum [12, 22-24]. After Li_3PS_4·3THF was stirred in ACN for 60 s, a series of spectral changes occurred, including: *i*) disappearance of C-H vibrations in THF; *ii*) appearance of C≡N stretch for ACN at 2240-2270 cm^{-1}; and iii) appearance of symmetric and asymmetric C-H stretching at 2942-3000 cm^{-1} [25]. These results clearly indicate that Li_3PS_4 prefers to coordinate and co-crystallize with ACN molecules over THF. The appearance of peaks at lower frequencies also confirmed the strong coordination of ACN with lithium ions in Li_3PS_4. Such preferential coordination with ACN could be attributed to the fact that ACN has twice the dipole moment as compared to THF [26]. To evaluate the temperature that was needed to remove the co-crystallized solvent, the phase evolutions of Li_3PS_4·3THF and Li_3PS_4·2ACN upon annealing was monitored using *in situ* XRD. It was found that THF could be removed from Li_3PS_4·3THF at a temperature as low as 80 °C, resulting in an amorphous Li_3PS_4 phase, similar to what was described in a previous report [12]. In comparison, a temperature >180 °C was needed to remove the co-crystallized ACN in Li_3PS_4·2ACN (Figure 3.6B). It is reasonable to conclude that the relatively high polarity, small size, and steric effects of the ACN molecules are expected to play crucial roles in strongly binding to Li_3PS_4.

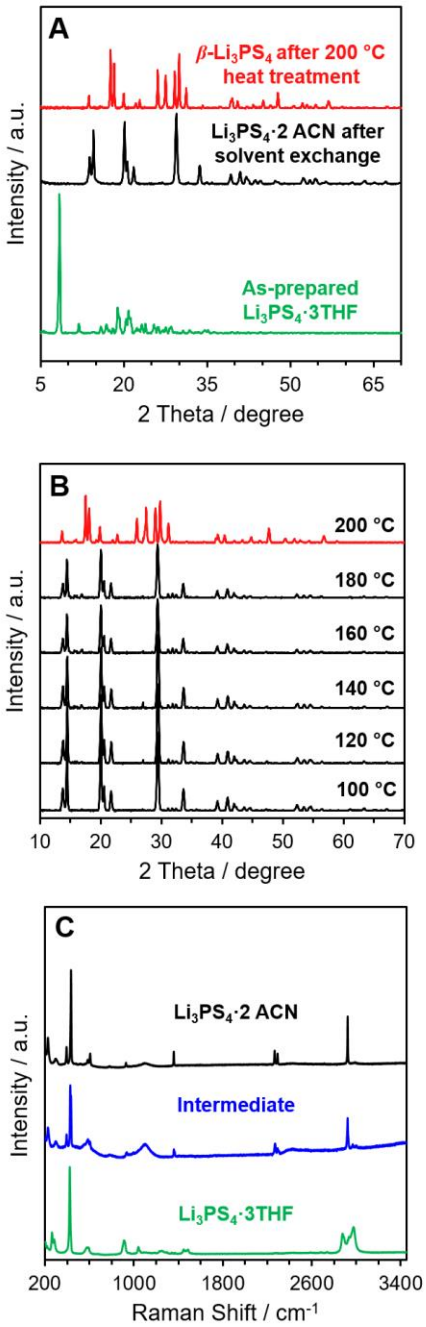

Figure 3.6 A) XRD patterns of as-prepared $Li_3PS_4 \cdot 3THF$, $Li_3PS_4 \cdot 2ACN$ (after solvent exchange and drying at 80 °C), and β-Li_3PS_4 (after heating $Li_3PS_4 \cdot 2ACN$ at 200 °C). B) XRD patterns after heating $Li_3PS_4 \cdot 2ACN$ at different temperatures, showing that a temperature of 200 °C is critical to remove ACN and thus produce β-Li_3PS_4. C) Raman spectra taken from $Li_3PS_4 \cdot 3THF$, an intermediate, and $Li_3PS_4 \cdot 2ACN$. The solvent exchange process started to occur in less than 60 s, indicating that Li_3PS_4 preferentially coordinates with ACN [48]. Reprinted with permission; © 2018 WILEY-VCH Verlag GmbH & Co. KGaA, Weinheim.

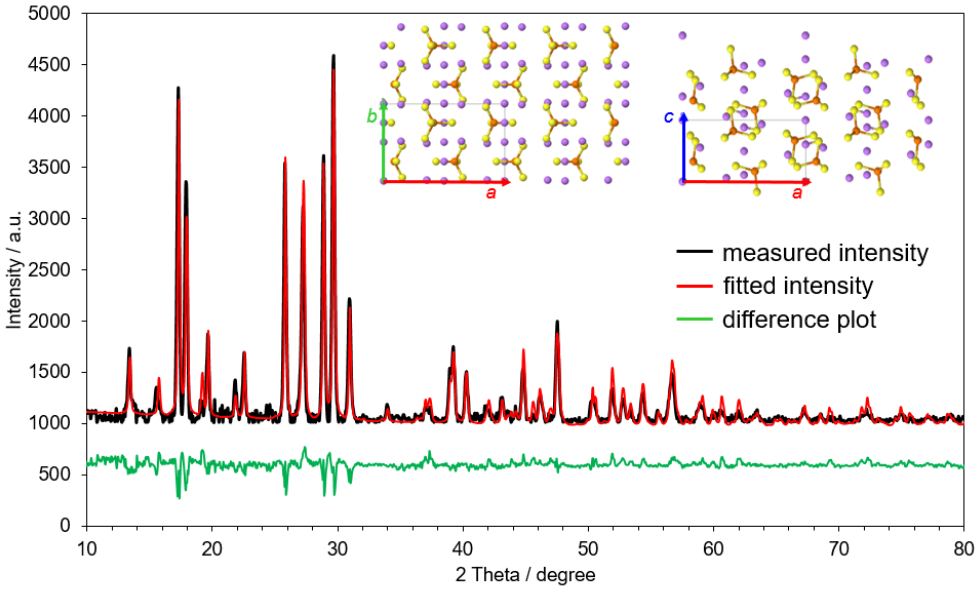

Figure 3.7 Rietveld refinement of as-prepared β-Li_3PS_4. The XRD pattern is indexed to orthorhombic β-Li_3PS_4 (space group: *Pnma*, a = 12.9758(3), b = 8.0489(2), c = 6.1238(4)). The insets show the crystal structure along the ab and ac planes [48]. Reprinted with permission; © 2018 WILEY-VCH Verlag GmbH & Co. KGaA, Weinheim.

Upon solvent removal, the product quickly converted to nanocrystalline orthorhombic β-Li_3PS_4 with an average crystallite size ranging from 80 to 120 nm, as derived using the Scherrer equation [27-29]. Rietveld refinement analysis of β-Li_3PS_4 indicated that peak broadening occurs as a result of both the crystallite size and the microstrain (Figure 3.7). The as-prepared β-Li_3PS_4 samples have a microstrain of ~0.12% for an average crystallite size ranging from 80 to 120 nm, which is comparable to the values previously reported β-Li_3PS_4 prepared from $Li_3PS_4 \cdot 3THF$ [12]. It is worth

mentioning that the XRD patterns show that the resultant film was made of pure β phase, without the existence of γ phase that gives a lower ionic conductivity [12, 22].

3.2.2 Fabrication of Solid Electrolyte Membranes

Thin membranes of β-Li_3PS_4 solid electrolyte were fabricated using a novel three-step processing method, involving *i*) assembly of the nanoscale solid electrolyte building blocks, *ii*) decomposition of $Li_3PS_4 \cdot 2ACN$ to β-Li_3PS_4, and *iii*) fusion of the solid electrolyte building blocks. By taking advantage of the solvent exchange mechanism, thin films of plate-like $Li_3PS_4 \cdot 2ACN$ building blocks were first dispersed on Ni substrates by tiled assembly, similar to what is used in evaporation-induced self-assembly (EISA), where solvent removal through evaporation directs the deposition of solid electrolyte particles [7, 30, 31]. The tiled assembly of plate-like $Li_3PS_4 \cdot 2ACN$ building blocks relies on their well-defined aspect ratios, such that the nanoscale building blocks stack face-to-face as thin films during deposition. In a typical process, Ni substrates were dipped into a suspension of plate-like $Li_3PS_4 \cdot 2ACN$ building blocks in ACN with a specific concentration (e.g., 0.01–0.8 M), followed by a heat treatment at 80 °C to remove the excess solvent. As shown by the SEM images, the surface of the $Li_3PS_4 \cdot 2ACN$ nanoscale building blocks maintained their rectangular, flaky morphology after heating to 80 °C and uniform films were produced (Figure 3.8). The key to making ultrathin films is to directly disperse suspensions of $Li_3PS_4 \cdot 2ACN$ building blocks on substrates. In order to improve the ionic conductivity of these Li_3PS_4 thin films, the remaining co-crystalized ACN must be removed. As evidenced by XRD patterns of $Li_3PS_4 \cdot 2ACN$, a temperature of greater than 180 °C was necessary to

remove the co-crystallized ACN and produce β-Li_3PS_4. After warm pressing at 200 °C and 200 MPa for 15 min, the particles in the β-Li_3PS_4 thin films fused together, yielding dense solid electrolyte membranes.

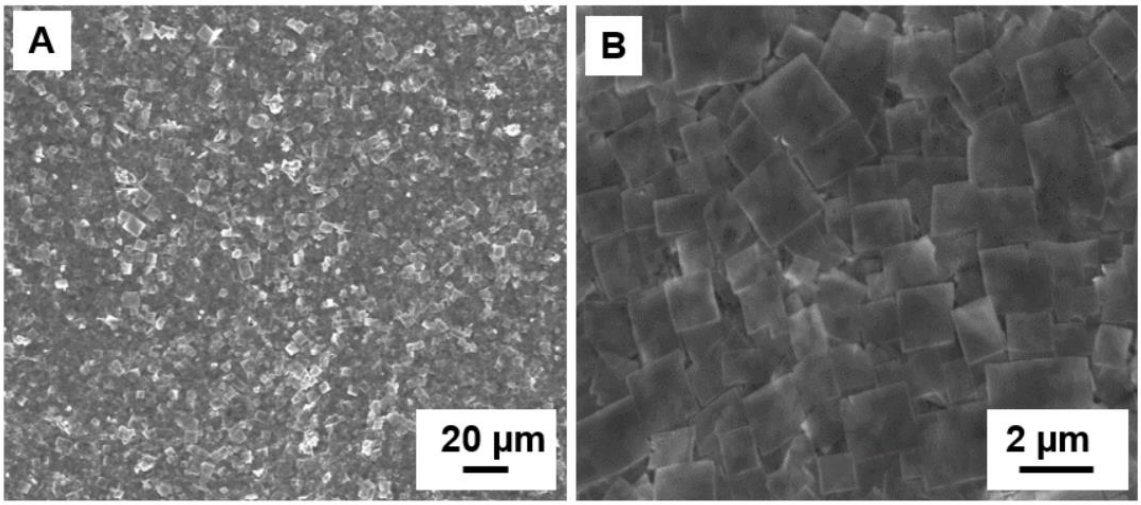

Figure 3.8 SEM images of Li_3PS_4·2ACN thin films grown by evaporation-induced self-assembly on a Ni substrate [48]. Reprinted with permission; © 2018 WILEY-VCH Verlag GmbH & Co. KGaA, Weinheim.

An interesting discovery in this work was that the thickness of the β-Li_3PS_4 solid electrolyte films could be readily tailored by tuning the concentration of the Li_3PS_4·2ACN nanoscale building blocks in ACN between 0.01 and 0.8 M, and more importantly, the thickness of these films could be pushed all the way down to the submicron scale. Figure 3.9 shows SEM images of the warm-pressed solid electrolyte membranes fabricated from suspensions of Li_3PS_4·2ACN building blocks with different concentrations. Tuning the concentration of Li_3PS_4·2ACN in ACN from 0.1 to 0.8 M allowed for the fabrication of micron-thick membranes ranging from 6 to 35 µm. When the concentration of Li_3PS_4·2ACN building blocks was further reduced to 0.01 M, a submicron-thick solid electrolyte film of β-Li_3PS_4 was obtained after warm pressing at 200 °C, which was

measured to be 0.4 μm in thickness, making it among the thinnest reported for warm-pressed sulfide-based solid electrolyte films. Figure 3.9A shows an SEM image of the cross section of the 0.4 μm β-Li_3PS_4 membrane, implying that the warm-pressed membrane was comprised of 4-5 layers of the plate-like, nanoscale building blocks. Figure 3.9B displays an SEM image of the surface of the β-Li_3PS_4 membrane, indicating that most of the flakes had fused together to form a dense, continuous membrane. After warm pressing at 200 °C, the membranes achieved densities between 95-98% of the reported bulk β-Li_3PS_4 material, implying that the warm-pressed membranes have a porosity of 2-5%. Similar densities were achieved with glassy sulfides, but the glassy sulfide membranes were generally much thicker than those highlighted in the current report [32, 33].

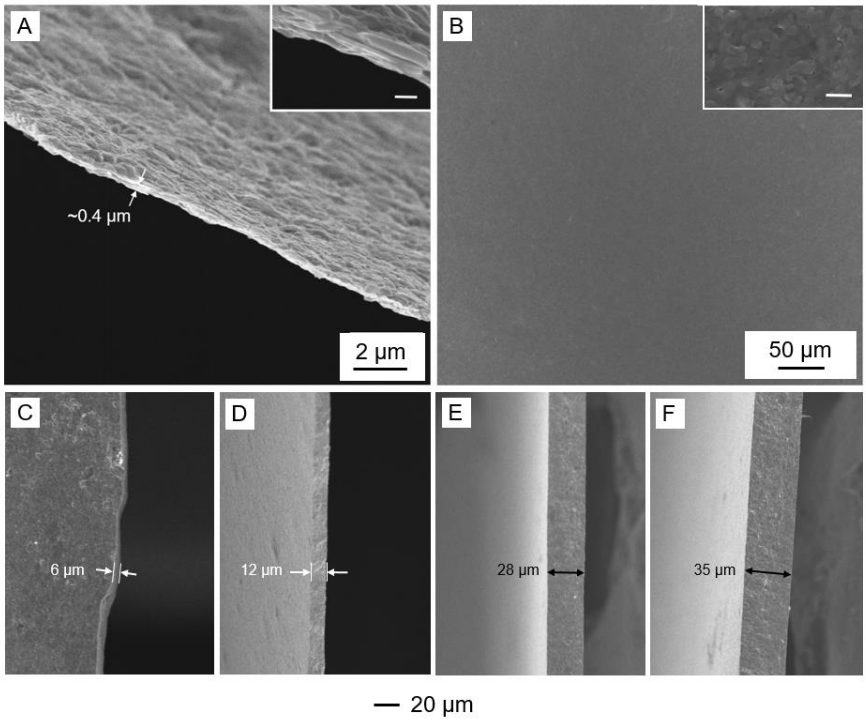

Figure 3.9 SEM images of the A) cross section and B) top surface of a β-Li_3PS_4 thin film with a thickness of 0.4 μm after warm pressing at 200 °C (inset scale bars: 100 nm). C-F) SEM images of β-Li_3PS_4 thin films with thicknesses varying from 6 and 35 μm after warm pressing at 200 °C [48]. Reprinted with permission; © 2018 WILEY-VCH Verlag GmbH & Co. KGaA, Weinheim.

3.2.3 Electrochemical Performance of β-Li_3PS_4 Membranes

The ionic conductivity of the newly formed membranes were studied using electrochemical impedance spectroscopy. Figure 3.5 shows a comparison of Nyquist and derived Arrhenius plots of Li_3PS_4·2ACN and the β-Li_3PS_4 films after warm pressing. Li_3PS_4·2ACN show a larger diameter in the semicircle of the Nyquist plot (Figure 3.10A), indicating a lower conductivity. This can be explained by the presence of solvent molecules, which lowers the Li^+ mobility. Upon the removal of ACN, the thin β-Li_3PS_4 membranes exhibited an AC ionic conductivity of 7.2×10^{-5} S·cm^{-1} at 20 °C, an improvement of four orders of magnitude over the Li_3PS_4·2ACN (Figure 3.10). Additionally, the total observed ionic conductivity displayed an Arrhenius behavior between 20 and 100 °C according to the following relationship (Equation 1):

$$\sigma = \sigma_o \cdot e^{\frac{-E_a}{kT}} \qquad (1)$$

where σ_o denotes the temperature independent ionic conductivity of the film, *k* represents the Boltzmann constant, and E_a denotes the activation energy. The Arrhenius activation energy of Li_3PS_4·2ACN and β-Li_3PS_4 were determined to be 0.69 eV and 0.36 eV, respectively [7, 12, 15]. It should be noted that the activation energy of the β-Li_3PS_4 thin film is lower than that of bulk β-Li_3PS_4, which was reported to be ~0.46 eV [22]. Such an enhancement can be attributed to *i*) the desired phase purity, *i.e.* no impurity phases such as the γ phase, $Li_4P_2S_6$, or $Li_{3.2}P_{0.96}S_4$ [34, 35], and *ii*) the small grain size that gives a larger concentration of grain boundaries concentrations along which Li^+ may have a higher mobility [12].

The compatibility of the β-Li_3PS_4 thin film with metallic lithium was evaluated using a symmetric cell configuration (Li/β-Li_3PS_4/Li) with direct current (DC)

polarization. Such configuration allows for the evaluation of interfacial stability through resistance measurements [36, 37]. As shown in Figure 3.6, the solid electrolyte membranes adopted in the present work could be cycled hundreds of times at current density between 0.1 and 0.3 $mA \cdot cm^{-2}$. The ionic conductivity from DC polarization was 6.8 10^{-5} $S \cdot cm^{-1}$ at 20 °C, which is comparable to the AC ionic conductivity of 7.2×10^{-5} $S \cdot cm^{-1}$ at 20 °C, signifying that the conductivity mainly originates from lithium ions in the thin β-Li_3PS_4 solid electrolyte membranes. This result is comparable with that of the previously reported β-Li_3PS_4 and Li_2S-P_2S_5 glass-ceramics [12, 15, 16], indicating that the thin film does not experience propagating chemical reactions with lithium metal. A slight increase in the interfacial resistance was observed in the first 3000 min (Figure 3.11), possibly due to the formation of a passivation layer and/or lithium redistribution at the interface. After cycling over 500 times (Figure 3.12), the resistance from DC polarization did not increase significantly, suggesting the desired interfacial stability of Li/β-Li_3PS_4 thin film during electrochemical cycling. As the increase in interfacial resistance happened at the beginning and became stable upon long-term cycling, it is most likely that an interphase layer that is electronically insulating forms at the interface and in turn prevents the propagation of chemical transformations at the interface. In fact, as predicted by theory, it is possible that β-Li_3PS_4 decomposes to Li_3P and Li_2S due to its electrochemical instability to metallic lithium, however, the decomposed interface layer is often self-limiting and capable of passivating further interfacial reactions [38, 39]. Such a phenomenon is not rare and has been experimentally observed [12, 40-44] and theoretically predicted [45, 46] in multiple solid electrolyte materials.

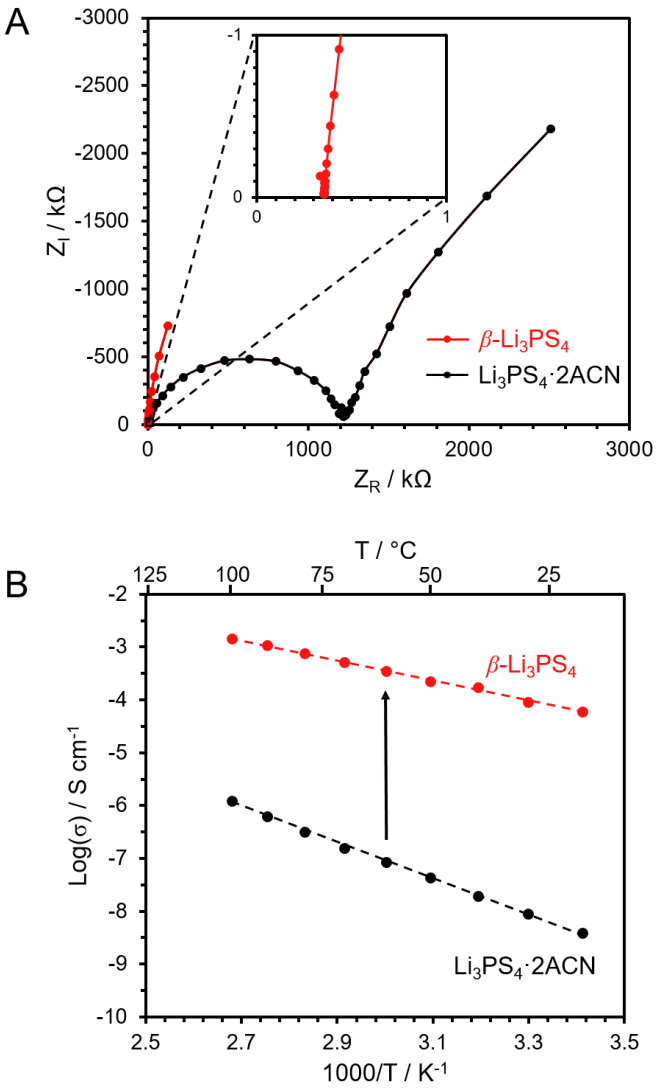

Figure 3.10 Representative A) Nyquist and B) Arrhenius plots for the as-fabricated films of Li_3PS_4·2ACN and the β-Li_3PS_4 derived from the Li_3PS_4·2ACN. The Nyquist plots were in (A) were both collected at 25 °C [48]. Reprinted with permission; © 2018 WILEY-VCH Verlag GmbH & Co. KGaA, Weinheim.

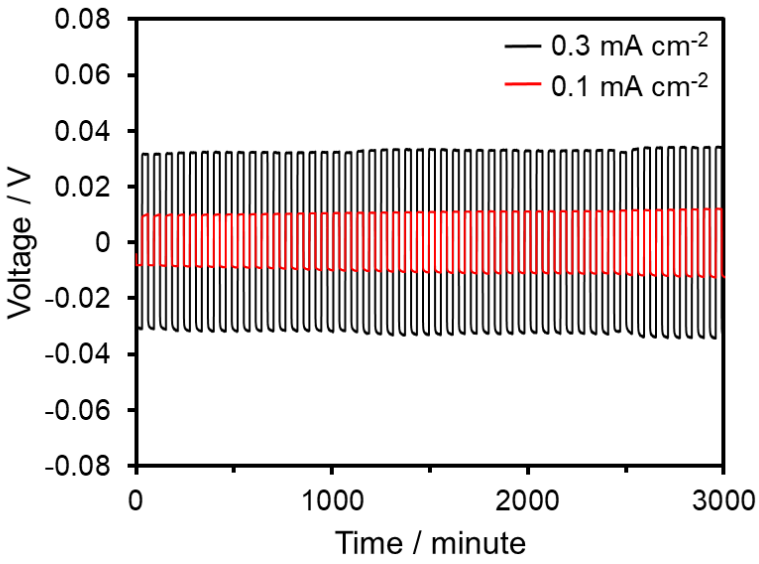

Figure 3.11 Electrochemical stability of an ultrathin film of β-Li_3PS_4 in contact with metallic lithium. Representative cycling data of a Li/β-Li_3PS_4/Li symmetric cell at current densities of 0.1 mA·cm^{-2} and 0.3 mA·cm^{-2}, respectively, at 25 °C [48]. Reprinted with permission; © 2018 WILEY-VCH Verlag GmbH & Co. KGaA, Weinheim.

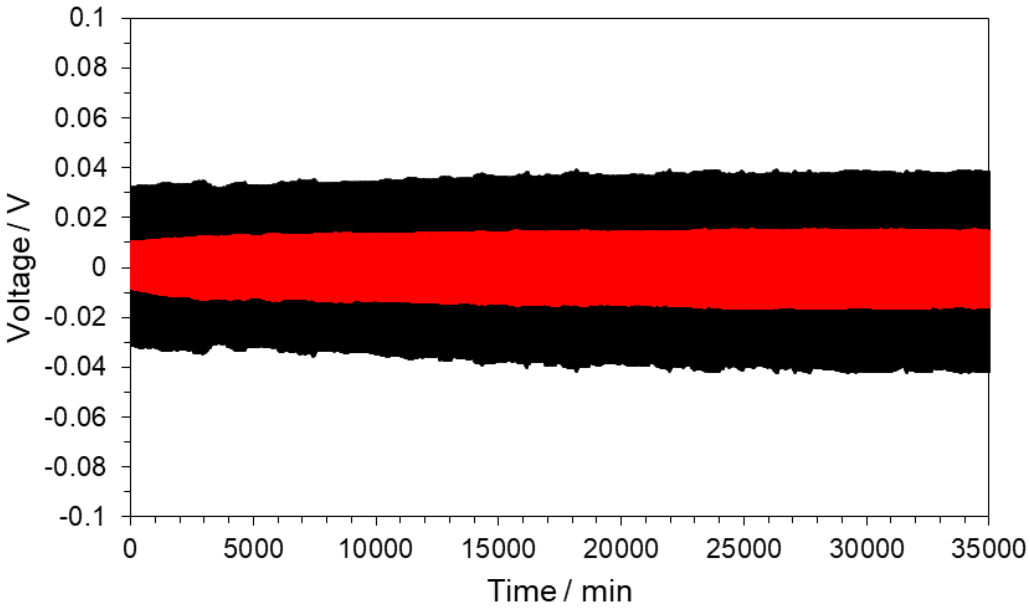

Figure 3.12 DC polarization curves for Li/β-Li_3PS_4/Li symmetric cells with current densities of 0.1 and 0.3 mA·cm^{-2}, illustrating long-term full-cell conductivity [48]. Reprinted with permission; © 2018 WILEY-VCH Verlag GmbH & Co. KGaA, Weinheim.

3.3 Summary

In summary, a new approach to fabricate ultrathin solid electrolyte membranes for all-solid-state batteries was demonstrated. This technique combines a new synthesis method of shape-controlled nanosheets of $Li_3PS_4 \cdot 2ACN$ with a unique tiled assembly process that utilizes these nanosheets as building blocks to form submicron thin membranes. This method offers the flexibility of synthesizing thin films with desired thicknesses in a controlled way. Ultrathin β-Li_3PS_4 membranes of less than 1 μm in thickness was fabricated for the first time. Apart from the desirable thickness, the ultrathin β-Li_3PS_4 films also hold additional advantages: increased ionic conductivity, a decreased Arrhenius activation energy compared with bulk Li_3PS_4, and good electrochemical compatibility with metallic lithium anode. This new solution-based soft chemistry method offers the flexibility of fabricating ultrathin solid electrolyte membranes for next-generation energy storage and conversion devices.

3.4 Experimental Methods

Synthesis of materials: Lithium sulfide (Li_2S, Alfa Aesar, 99.9%) and phosphorus pentasulfide (P_2S_5, Sigma-Aldrich, 99%) were mixed with a stoichiometry of 3 to 1 in anhydrous tetrahydrofuran (THF, Sigma-Aldrich, >99.8%) at room temperature. After stirring for 24 h, a white precipitate was observed. The precipitate was collected by filtration and dried at room temperature under vacuum for 1 h to remove excess solvent, yielding $Li_3PS_4 \cdot 3THF$. In the next step, 200 mg of the as-obtained $Li_3PS_4 \cdot 3THF$ was added into 100 mL of anhydrous acetonitrile (ACN, Sigma-Aldrich, >99.8%) and stirred

vigorously. A drop of the suspension was deposited on a Si substrate and dried under vacuum at room temperature to monitor the morphology variation after stirring for 15 s, 1 min, 5 min, 10 min, 20 min, 40 min, 60 min, and 24 h, respectively. The final product was collected by filtration and then heated at 80 °C to produce $Li_3PS_4 \cdot 2ACN$. Considering the sensitivity of the system to O_2 and moisture, all the experiments were carried out in an Argon-filled glove box.

Characterization of materials: SEM images were collected on a field-emission scanning electron microscope (SEM, Zeiss Merlin) at an acceleration voltage of 5.0 kV equipped with a custom designed stage for handling air-sensitive samples [47]. Identification of the crystalline phase was conducted on a X'pert Pro Powder Diffractometer (PANalytical) with Cu Kα radiation. All XRD samples were prepared in a glovebox and the quartz slides were sealed with Kapton® films. Rietveld refinement was performed with HighScore Plus, a software package provided by PANalytical. Raman spectra of $Li_3PS_4 \cdot 3THF$, the intermediate, and $Li_3PS_4 \cdot 2ACN$ were collected on an Acton Trivista 555 spectrometer (Princeton Instruments).

Fabrication of membranes: Thin membranes of β-Li_3PS_4 were fabricated using the $Li_3PS_4 \cdot 2ACN$ plates by following a previous report [7]. Simply put, a suspension of $Li_3PS_4 \cdot 2ACN$ plates was prepared by dispersing $Li_3PS_4 \cdot 2ACN$ plates in a beaker containing ACN. The concentration of $Li_3PS_4 \cdot 2ACN$ plates was tuned between 0.01–0.8 M to create membranes with varying thicknesses. Ni substrates were then dipped into the $Li_3PS_4 \cdot 2ACN$ suspensions, placed on a horizontal surface, transferred into a chemical dryer, and heated under vacuum at 80 °C to remove excess solvent. The membranes were then warm pressed at a temperature of 200 °C at 200 MPa between two nickel substrates

for 15 min. All processes were completed under Argon due to the sensitivity of Li_3PS_4 to moisture and air.

Electrochemical measurements and fabrication of symmetric cells: Swagolok® cells were used to complete all electrochemical impedance spectroscopy (EIS), cyclic voltammetry (CV) and cycling performance measurements. For EIS, films were prepared between two carbon-coated Al foils and measured between 1 MHz and 1 mHz at an amplitude of 100.0 mV. For the CV tests, Li/β-Li_3PS_4/Pt cells were scanned at a rate of 0.1 $mV \cdot s^{-1}$ between -0.5 and 5 V *vs.* Li/Li^+ at room temperature using a Bio-Logic VSP multi-channel potentiostat. The Li/β-Li_3PS_4/Li symmetric cells were cycled on a battery system (Bio-Logic VSP) at current densities of 0.1 and 0.3 $mA \cdot cm^{-2}$.

3.5 Notes to Chapter 3

Part of this chapter is adapted from the paper "Fabrication of Submicron-thick Solid Electrolyte Membranes of β-Li_3PS_4 via Tiled Assembly of Shape-controlled Building Blocks" published in *Advanced Energy Materials* [48].

3.6 References

[1] Xu, W.; Wang, J.; Ding, F.; Chen, X.; Nasybulin, E.; Zhang, Y.; Zhang, J.-G. *Energy & Environmental Science* **2014**, *7*, 513.

[2] Guo, Y.; Li, H.; Zhai, T. *Advanced Materials* **2017**.

[3] Lin, D.; Liu, Y.; Cui, Y. *Nature Nanotechnology* **2017**, *12*, 194.

[4] Lin, Z.; Liang, C. *Journal of Materials Chemistry A* **2015**, *3*, 936.

[5] Dudney, N. J.; West, W. C.; Nanda, J. *Handbook of Solid State Batteries*; World Scientific, 2016.

[6] Hallinan Jr, D. T.; Balsara, N. P. *Annual Review of Materials Research* **2013**, *43*, 503.

[7] Wang, H.; Hood, Z. D.; Xia, Y.; Liang, C. *Journal of Materials Chemistry A* **2016**, *4*, 8091.

[8] Quartarone, E.; Mustarelli, P. *Chemical Society Reviews* **2011**, *40*, 2525.

[9] Ito, Y.; Sakuda, A.; Ohtomo, T.; Hayashi, A.; Tatsumisago, M. *Journal of the Ceramic Society of Japan* **2014**, *122*, 341.

[10] Bachman, J. C.; Muy, S.; Grimaud, A.; Chang, H.-H.; Pour, N.; Lux, S. F.; Paschos, O.; Maglia, F.; Lupart, S.; Lamp, P. *Chemical Reviews* **2015**, *116*, 140.

[11] Wang, Y.; Richards, W. D.; Ong, S. P.; Miara, L. J.; Kim, J. C.; Mo, Y.; Ceder, G. *Nature Materials* **2015**.

[12] Liu, Z.; Fu, W.; Payzant, E. A.; Yu, X.; Wu, Z.; Dudney, N. J.; Kiggans, J.; Hong, K.; Rondinone, A. J.; Liang, C. *Journal of the American Chemical Society* **2013**, *135*, 975.

[13] Rangasamy, E.; Liu, Z.; Gobet, M.; Pilar, K.; Sahu, G.; Zhou, W.; Wu, H.; Greenbaum, S.; Liang, C. *Journal of the American Chemical Society* **2015**, *137*, 1384.

[14] Rangasamy, E.; Sahu, G.; Keum, J. K.; Rondinone, A. J.; Dudney, N. J.; Liang, C. *Journal of Materials Chemistry A* **2014**, *2*, 4111.

[15] Hood, Z. D.; Wang, H.; Li, Y.; Pandian, A. S.; Paranthaman, M. P.; Liang, C. *Solid State Ionics* **2015**, *283*, 75.

[16] Hayashi, A.; Hama, S.; Mizuno, F.; Tadanaga, K.; Minami, T.; Tatsumisago, M. *Solid State Ionics* **2004**, *175*, 683.

[17] Sedlmaier, S. J.; Indris, S.; Dietrich, C.; Yavuz, M.; Dräger, C.; von Seggern, F.; Sommer, H.; Janek, J. r. *Chemistry of Materials* **2017**, *29*, 1830.

[18] Murugan, R.; Thangadurai, V.; Weppner, W. *Angewandte Chemie International Edition* **2007**, *46*, 7778.

[19] Teragawa, S.; Aso, K.; Tadanaga, K.; Hayashi, A.; Tatsumisago, M. *Journal of Materials Chemistry A* **2014**, *2*, 5095.

[20] Yamada, T.; Ito, S.; Omoda, R.; Watanabe, T.; Aihara, Y.; Agostini, M.; Ulissi, U.; Hassoun, J.; Scrosati, B. *Journal of The Electrochemical Society* **2015**, *162*, A646.

[21] Bron, P.; Johansson, S.; Zick, K.; Schmedt auf der Günne, J. r.; Dehnen, S.; Roling, B. *Journal of the American Chemical Society* **2013**, *135*, 15694.

[22] Tachez, M.; Malugani, J.-P.; Mercier, R.; Robert, G. *Solid State Ionics* **1984**, *14*, 181.

[23] Machida, N.; Yamamoto, H.; Asano, S.; Shigematsu, T. *Solid State Ionics* **2005**, *176*, 473.

[24] Cadioli, B.; Gallinella, E.; Coulombeau, C.; Jobic, H.; Berthier, G. *The Journal of Physical Chemistry* **1993**, *97*, 7844.

[25] Tanabe, K. *Chemical Physics* **1979**, *38*, 125.

[26] Minkin, V. I. *Dipole moments in organic chemistry*; Springer Science & Business Media, 2012.

[27] Homma, K.; Yonemura, M.; Kobayashi, T.; Nagao, M.; Hirayama, M.; Kanno, R. *Solid State Ionics* **2011**, *182*, 53.

[28] Villars, P., Cenzual, K., Eds.; Springer-Verlag Berlin Heidelberg & Material Phases Data System (MPDS), Switzerland & National Institute for Materials Science (NIMS), Japan.

[29] Momma, K.; Izumi, F. *Journal of Applied Crystallography* **2011**, *44*, 1272.

[30] Brinker, C. J.; Lu, Y.; Sellinger, A.; Fan, H. *Advanced Materials* **1999**, *11*, 579.

[31] Grosso, D.; Cagnol, F.; Soler-Illia, G. d. A.; Crepaldi, E. L.; Amenitsch, H.; Brunet-Bruneau, A.; Bourgeois, A.; Sanchez, C. *Advanced Functional Materials* **2004**, *14*, 309.

[32] Kitaura, H.; Hayashi, A.; Ohtomo, T.; Hama, S.; Tatsumisago, M. *Journal of Materials Chemistry* **2011**, *21*, 118.

[33] Seino, Y.; Ota, T.; Takada, K.; Hayashi, A.; Tatsumisago, M. *Energy & Environmental Science* **2014**, *7*, 627.

[34] Hood, Z. D.; Kates, C.; Kirkham, M.; Adhikari, S.; Liang, C.; Holzwarth, N. *Solid State Ionics* **2016**, *284*, 61.

[35] Minami, K.; Hayashi, A.; Tatsumisago, M. *Journal of the Ceramic Society of Japan* **2010**, *118*, 305.

[36] Burns, J.; Krause, L.; Le, D.-B.; Jensen, L.; Smith, A.; Xiong, D.; Dahn, J. *Journal of The Electrochemical Society* **2011**, *158*, A1417-A1422.

[37] Tian, Y.; Shi, T.; Richards, W. D.; Li, J.; Kim, J. C.; Bo, S.-H.; Ceder, G. *Energy & Environmental Science* **2017**, *10*, 1150-1166.

[38] Lepley, N.; Holzwarth, N. *Physical Review B* **2015**, *92*, 214201.

[39] Lepley, N.; Holzwarth, N.; Du, Y. A. *Physical Review B* **2013**, *88*, 104103.

[40] Ma, C.; Cheng, Y.; Yin, K.; Luo, J.; Sharafi, A.; Sakamoto, J.; Li, J.; More, K. L.; Dudney, N. J.; Chi, M. *Nano Letters* **2016**.

[41] Schwöbel, A.; Hausbrand, R.; Jaegermann, W. *Solid State Ionics* **2015**, *273*, 51-54.

[42] Hood, Z. D.; Wang, H.; Samuthira Pandian, A.; Keum, J. K.; Liang, C. *Journal of the American Chemical Society* **2016**, *138*, 1768-1771.

[43] Rush, L. E.; Hood, Z. D.; Holzwarth, N. A. W. *Physical Review Materials* **2017**, *1*, 075405.

[44] Wang, H.; Chen, Y.; Hood, Z. D.; Sahu, G.; Pandian, A. S.; Keum, J. K.; An, K.; Liang, C. *Angewandte Chemie International Edition* **2016**, *55*, 8551-8555.

[45] Zhu, Y.; He, X.; Mo, Y. *Journal of Materials Chemistry A* **2016**, *4*, 3253-3266.

[46] Richards, W. D.; Miara, L. J.; Wang, Y.; Kim, J. C.; Ceder, G. *Chemistry of Materials* **2015**, *28*, 266-273.

[47] Howe, J. Y.; Boatner, L. A.; Kolopus, J. A.; Walker, L. R.; Liang, C.; Dudney, N. J.; Schaich, C. R. *Journal of Materials Science* **2012**, *47*, 1572-1577.

[48] Hood, Z.D.; Wang, H.; Pandian, A.S.; Peng, R.; Gilroy, K.D.; Chi, M.; Liang, C.; Xia, Y. *Advanced Energy Materials* **2018**, 1800014.

CHAPTER 4

STRUCTURAL AND ELECTROLYTE PROPERTIES OF $Li_4P_2S_6$

4.1 Introduction

Recently, there has been renewed interest in the development of all-solid state batteries [1-3], following the discovery of highly conducting solid electrolytes such as $Li_{10}GeP_2S_{12}$ [4] and nanoporous β-Li_3PS_4 [5] as discussed in Chapter 1 of this Dissertation. Development of the all-solid-state battery technology motivates continued research on solid electrolytes, with a focus both on the continued improvement of ionic conductivity and increase in the structural and chemical stability.

As an example of a relatively stable solid electrolyte, $Li_4P_2S_6$ has been identified in several high temperature preparations of lithium thiophosphate electrolytes as a synthesis or decomposition product [6-8]. Its characteristic P–P bond may be partly responsible for its relatively good stability under ambient conditions. Early structural analysis [9] found the P sites to be disordered. Previous simulations [10] found a related low energy structure with ordered P sites. This chapter reports a re-examination of the simulation results and new measurements that reveal interesting details of the structure and electrolyte properties of $Li_4P_2S_6$.

4.2 Results and Discussion

4.2.1 Crystal properties

$Li_4P_2S_6$ was found to form at increased temperatures between 750 °C and 900 °C in vacuum. The yield of each synthesis process described in 4.4 was 99%. The purified

reaction product included particles having diameters ≥ 10 μm, which were reduced to nanosize after ball-milling for 5 minutes. SEM images of the sample after the ball-milling process at two different magnifications are shown in Fig. 4.1a,b. Producing the nano-sized powder aided in pressing dense pellets for electrochemical characterization. This method resulted in pellets as dense as 96% of the ideal density of 2.23 g/cm^3.

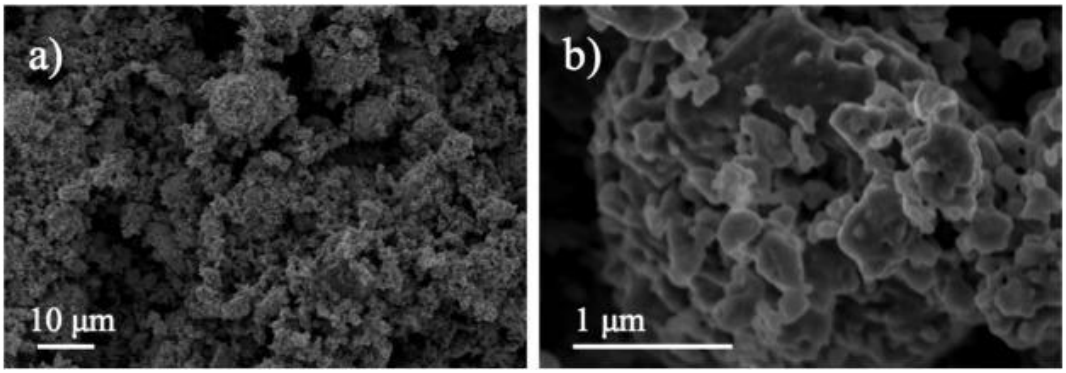

Figure 4.1 Scanning electron microscopy (SEM) images of $Li_4P_2S_6$ a) after ball milling, and b) a close-up of the ball milled material showing nanosized particles [36]. Reprinted with permission; © 2016 Elsevier.

4.2.2 Structural properties

As noted in 1982 by Mercier et al. [9], the building blocks of $Li_4P_2S_6$ crystals are P_2S_6 (hexathiohypodiphosphate) ions having D_{3d} symmetry, oriented with the P–P bond along the crystallographic *c* axis, as shown in Fig. 4.2. The left diagram of the figure shows one possible placement of a P_2S_6 ion with the origin of the unit cell at the center of the P–P bond and the coordinates of the P sites designated as $P_{\uparrow} \equiv \pm zPc$. The right diagram of the figure shows the other possible placement of the building blocks with the origin of the unit

cell located between P_2S_6 units and the coordinates of the P sites designated as P↓≡±(12−zP)c.

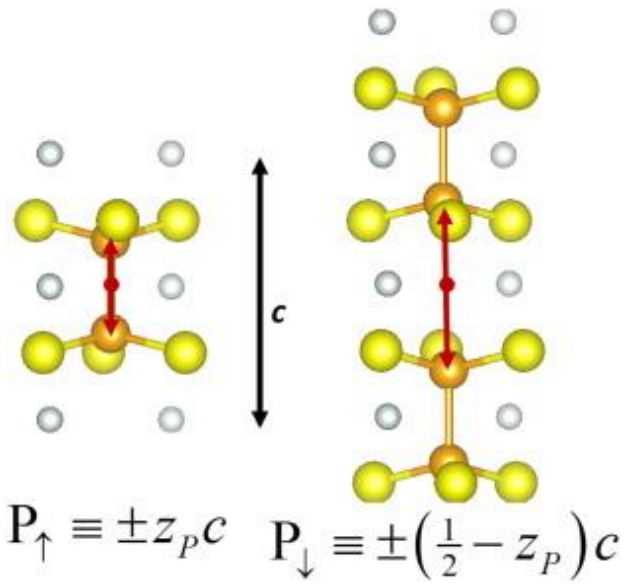

Figure 4.2 Ball-and-stick diagram of the P_2S_6 ion units comprising the $Li_4P_2S_6$ crystals. The ball designations are Li, P, and S in increasing size with gray, orange, and yellow colors, respectively. The red arrows indicate the two possible placements of the P sites within a unit cell centered at the red dot [36]. Reprinted with permission; © 2016 Elsevier.

Mercier *et al.* [9] described the overall structure of $Li_4P_2S_6$ in terms of the space group $P6_3/mcm$ (# 193) [31]. In this designation, using the site multiplicity and Wyckoff symbols, the 4*e* P sites at fractional coordinates (0, 0, z_P), and three other symmetry equivalent sites, have 0.5 occupancy. On the other hand, the 4*d* Li sites at fractional coordinates (1/3, 2/3, 0), and three other symmetry equivalent sites, and the 6*g* S sites at fractional coordinates (x_S, 0, 1/4), and five other symmetry equivalent sites, are fully occupied.

The basic structure of the crystal as projected within a hexagonal plane is shown in Fig. 4.3a. This structure is common to all of the possible structural variations. The placement of any given P–P bond within a crystal unit determines the placement of all of the P–P bonds along the same *c* axis. It is reasonable to assume, as is consistent with the experimental analysis, that the S and Li sites are insensitive to these bond placements. The likely structural variations in $Li_4P_2S_6$ crystals can be enumerated on a two-dimensional hexagonal lattice in terms of the $P_\uparrow$ or $P_\downarrow$ placements of P–P bonds on each *c* axis. Previous simulation studies [10] found a meta-stable structure which corresponds to choosing all of P–P bonds of the $P_\uparrow$ type which results in a structure with group symmetry of $\boldsymbol{P\bar{3}1m}$ (# 162) [31], which is a subgroup of the Mercier structure. This structure of ordered P–P bonds has an energy of 0.03 eV/formula unit higher than the lowest energy structure, and is shown in Fig. 4.3b. Other possible structures have P–P bonds in between alternate S layers. For example, the ordered structures shown in Fig. 4.3c,d are based on orthorhombic supercells of the hexagonal structure having an equal number of $P_\uparrow$ and $P_\downarrow$ sites. These are two examples of structures computed to have the lowest energy of the configurations considered. The configuration of Struc. (c) has two formula units per unit cell and the crystallographic space group is *Pnnm* (# 58) [31]. The configuration of Struc. (d) has four formula units per unit cell and the crystallographic space group is *Pnma* (# 62) [31]. In addition to Struc. (c) and Struc. (d), several other configurations were examined, generally finding that those configurations with equal numbers of $P_\uparrow$ and $P_\downarrow$ sites have energies equal to that of the ground state, while configurations with unequal numbers of $P_\uparrow$ and $P_\downarrow$ sites have energies between that of the ground state and 0.03 eV which characterizes the pure $P_\uparrow$ setting. While we did not have the means to explore the vast configuration space

of this system, it can be reasonably concluded that this system has many configurations corresponding to the ground state and many configurations with energies close to that of the ground state.

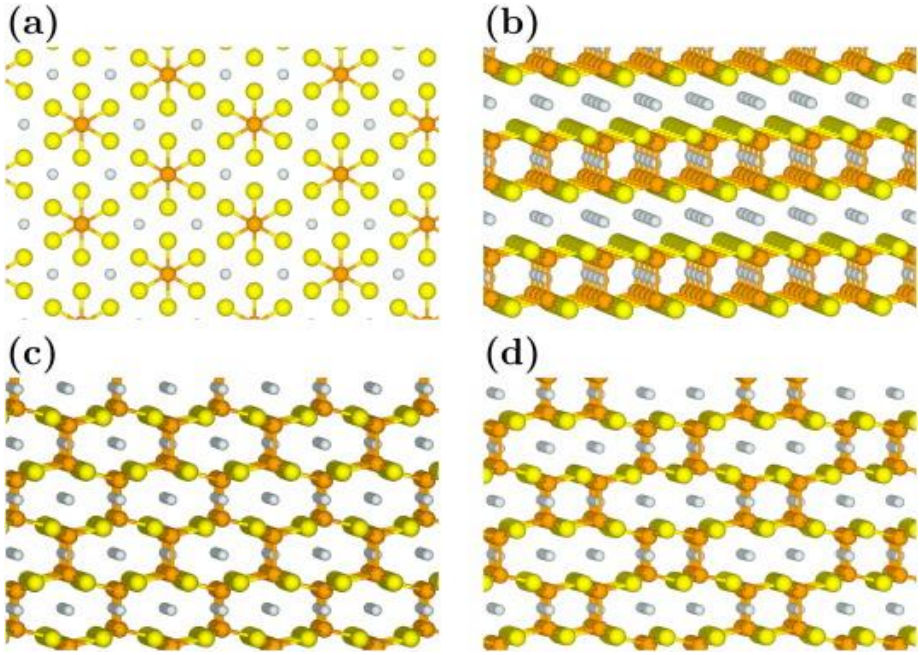

Figure 4.3 Ball-and-stick models of $Li_4P_2S_6$ with gray, orange, and yellow balls representing Li, P, and S sites, respectively. Part (a) shows a projection onto the hexagonal plane common to all of the structures. Parts (b)–(d) show a view point with perpendicular and parallel components of the hexagonal plane. Part (b) shows the ordered $\boldsymbol{P\bar{3}1m}$ structure with an energy/formula unit of 0.03 eV higher than the ground state. Part (c) shows an ordered ground state configuration having two formula units per unit cell and *Pnnm* symmetry. Part (d) shows an ordered ground state configuration having four formula units per unit cell and *Pnma* symmetry [36]. Reprinted with permission; © 2016 Elsevier.

In addition to the structural optimization, the computer simulations determine the electronic structure of the materials, the qualitative features of which are exhibited by the partial densities of states. The partial densities of states of $Li_4P_2S_6$ were found to be insensitive to the detailed structures shown in Fig. 4.3. Fig. 4.4 shows the partial densities

of states for Struc. (d) shown in Fig. 4.3d and is very similar to the result for the $\boldsymbol{P\bar{3}1m}$ structure [10]. The partial densities of states show that the P–P dimers result in valence band contributions at 1.5 eV lower energy and generally increase the overall valence band width compared to that of γ-Li_3PS_4.

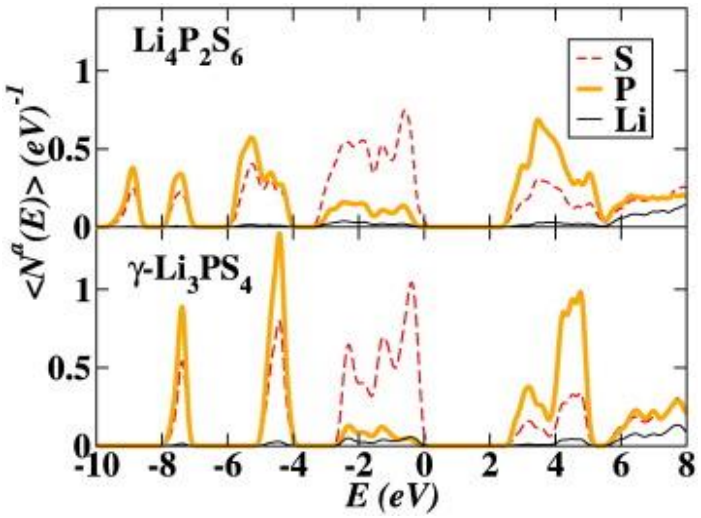

Figure 4.4 Partial density of states evaluated using Eq. (2) for $Li_4P_2S_6$ compared with that of γ-Li_3PS_4. The zero of energy is taken as the highest occupied state of the systems [36]. Reprinted with permission; © 2016 Elsevier.

X-ray analysis of the powdered sample was carried out at room temperature and at several lower temperatures and the results are shown in Fig. 4.5. The $P_{\uparrow}$ and $P_{\downarrow}$ variations in the structures were expected to result in a temperature dependence of the X-ray data. However, the fact that the 4 patterns are essentially identical indicates no structural transformation in the temperature range $15\ \mathrm{K} \leq T \leq 298\ \mathrm{K}$. This result is somewhat surprising given that calculations have identified many configurations of the P–P bonds resulting in energies in the range of $0 \leq E \leq 0.03$ eV/formula units relative to the ground state. On the other hand, one expects that there may be significant energy barriers to

changing P–P bond configurations, involving either migrations of P_2S_6 units or sequences of breaking and reforming P–P bonds. This reasoning leads to the suggestion that the P–P bond configurations might be "frozen" in at the time that the crystal is formed. The room temperature pattern in this work is essentially identical to the results reported by Mercier *et al.* [9].

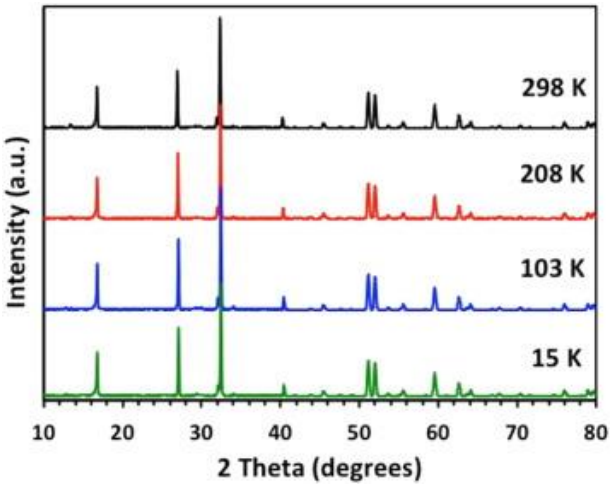

Figure 4.5 X-ray powder patterns of $Li_4P_2S_6$ measured at indicated temperatures [36]. Reprinted with permission; © 2016 Elsevier.

Fig. 4.6 compares simulated X-ray diffraction patterns for each of the structural variations shown in Fig. 4.3 with the measured pattern at 15 K. In order to easily compare with the neutron data, the scattering angle θ has been converted to the normal distance between diffracting planes d according to the Bragg condition $d = \lambda/(2 \sin \theta)$, where the X-ray wavelength is $\lambda = 1.54056$ Å. The simulated patterns for the ordered supercell structures of Fig. 4.3 reproduce the main diffraction peaks quite well, but differ from the experimental patterns and from each other with the appearance of additional small intensity diffraction peaks mostly apparent at large d. If the powder sample is assumed to be

composed of grains or domains of material each having one of the possible structures, the diffraction pattern should be composed of an incoherent superposition of diffraction patterns for each of the structures. It is apparent that the incoherent average of the simulated patterns will reduce the intensity of the extra peaks and preserve the main features of the experimental pattern. The Mercier crystal parameters [9] which describe the structure in terms of the 50% occupancy of the P sites generates the same powder diffraction pattern. However, rather than having a completely random occupation, as described in Fig. 4.2, the actual P site occupation is restricted to $P_{\uparrow}$ and $P_{\downarrow}$ configurations.

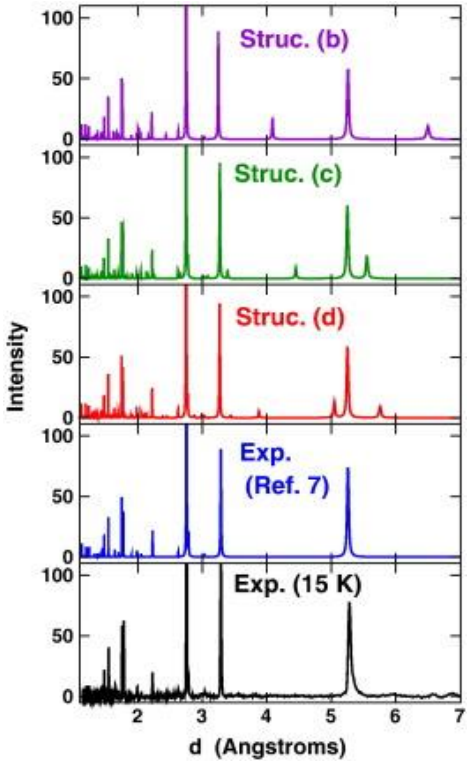

Figure 4.6 Simulated X-ray patterns from the structural models shown in Fig. 4.3, compared with the low temperature X-ray data and the room temperature X-ray data reported by Mercier *et al*. [9]. The intensity of the data and simulations were normalized so that the highest peaks at approximately $d = 2.75$ Å are fixed at the intensity of approximately 200 [36]. Reprinted with permission; © 2016 Elsevier.

A similar comparison was made with the neutron diffraction data shown in Fig. 4.7. As expected, the diffraction peak positions as a function of diffraction plane distances *d* are identical in the X-ray and neutron results, but because of the different cross section relationships, the intensity profiles of Fig. 4.7; Fig. 4.6 are quite different. The simulated patterns for Struct. (b), (c), and (d) again show extra peaks at large values of *d*. In the X-ray pattern, the largest diffraction peak occurs at $d = 2.76$ Å which corresponds to 12 equivalent $(2\bar{1}1)$ reflections in the hexagonal unit cell while another strong diffraction peak occurs at $d = 3.29$ Å corresponding to 2 equivalent (002) reflections. In the neutron pattern the largest diffraction peak occurs at $d = 5.26$ Å corresponding to 6 equivalent (100) reflections in the hexagonal unit cell. Interestingly, in these figures, the peak for the largest *d* value occurs at $d = 6.50$ Å corresponding to a (001) reflection in Struc. (b). For all the other structures and the experimental results, the *c*-axis symmetry allows only multiples of (002) reflections.

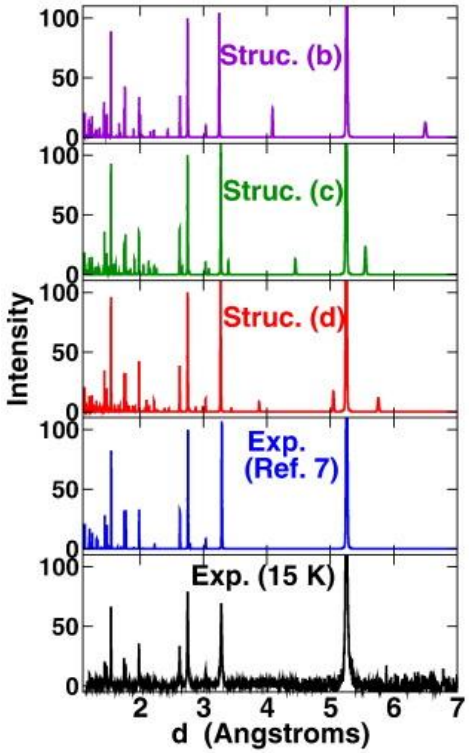

Figure 4.7 Simulated neutron diffraction patterns from the structural models shown in Fig. 4.3, compared with the low temperature neutron data and the room temperature structure by Mercier et al. [9]. The intensity of the data and simulations were normalized so that the highest peaks at approximately d = 5.25 Å are fixed at the intensity of approximately 200 [36]. Reprinted with permission; © 2016 Elsevier.

The refinement of these X-ray and neutron data and simulations for the lattice parameters a and c and fractional coordinate parameters z_P and x_S are summarized in Table 4.1 in terms of the hexagonal $P6_3/mcm$ unit cell. The numerical results are consistent with the conclusions from analysis of the X-ray patterns of Fig. 4.5, namely that the structure is invariant with temperature.

Table 4.1 Summary of structural parameters for $Li_4P_2S_6$. Calculated results were averaged from supercell simulations and the lattice parameters were scaled by 1.02 in order to account for the systematic underestimation of lattice size by the LDA exchange-correlation functional.

	***a* (Å)**	***c* (Å)**	z_P	x_S
This work at 15 K (X-ray)	6.051	6.548	0.172	0.324
This work at 15 K (neutron)	6.055	6.553	0.172	0.326
This work at 300 K (X-ray)	6.075	6.597	0.172	0.324
This work at 300 K (neutron)	6.075	6.595	0.173	0.326
Ref. [9]; X-ray at 293 K	6.07	6.577	0.1715	0.3237
Calculated structure b	6.07	6.5	0.18	0.33
Calculated structure c	6.06	6.54	0.17	0.33
Calculated structure d	6.06	6.54	0.17	0.33

4.2.3 Stability of $Li_4P_2S_6$

The $Li_4P_2S_6$ crystal was found to be thermally stable in vacuum up to 950 °C. Fig. 4.8 compares the thermal gravimetric analysis (TGA) in Ar and in air. In an atmosphere of Ar gas, there is a small amount of weight loss in the sample, presumably due to a small amount of impurities in the Ar source. By contrast, when placed in air, the sample is stable (losing a weight percent of 2% or less) up to 280 °C. At temperatures higher than 280 °C, $Li_4P_2S_6$ loses nearly 25% of its mass (Fig. 4.8). Looking at these results in more detail, X-ray diffraction data were taken on the high temperature products at 280 °C and at 350 °C (Fig. 4.9). In the latter case, reaction products of P_2O_5, $Li_4P_2O_7$, and Li_2SO_4 were identified from the X-ray data. The room temperature pattern of $Li_4P_2S_6$ differs slightly from that shown in Fig. 4.6 because of small structural changes due to air exposure. Overall, the results indicate that $Li_4P_2S_6$ is much more stable than other lithium thiophosphates. For example Li_3PS_4 decomposes at room temperature in air.

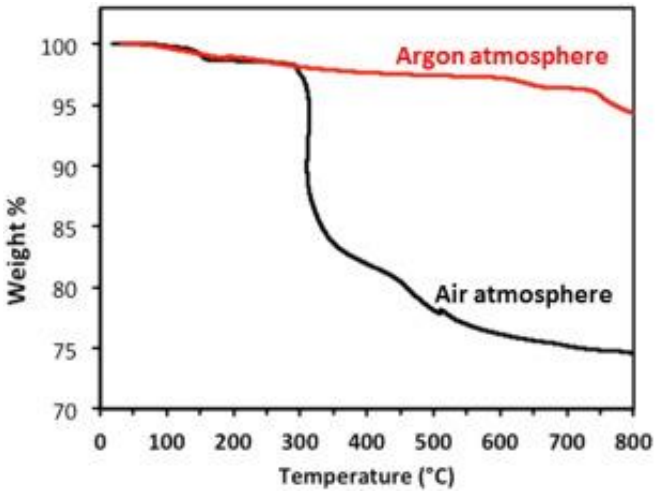

Figure 4.8 Thermal gravimetric analysis (TGA) of $Li_4P_2S_6$ showing the percentage weight remaining in the sample as a function of temperature when processed in Ar gas (red curve) or in air (black curve). $Li_4P_2S_6$ shows limited thermal stability in air until 280 °C [36]. Reprinted with permission; © 2016 Elsevier.

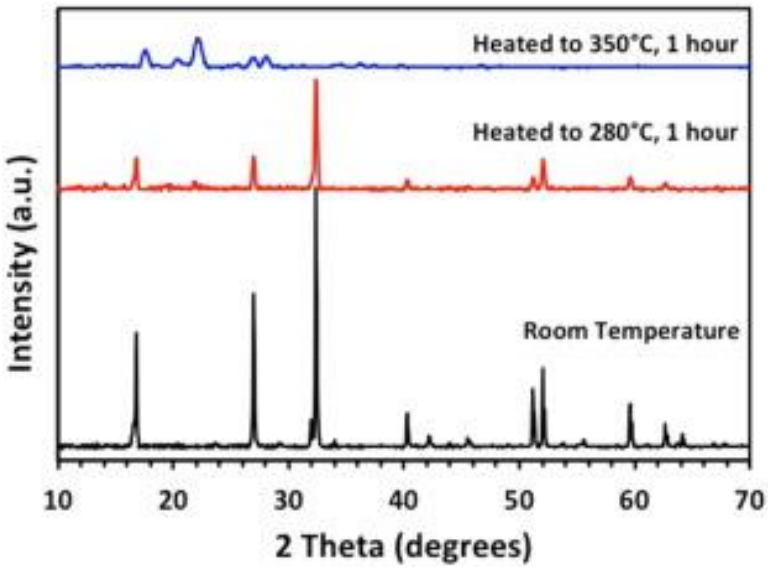

Figure 4.9 X-ray patterns of $Li_4P_2S_6$ processed at indicated temperatures in air. The $Li_4P_2S_6$ powder was heated/cooled at 100 °C/h to the indicated temperature and held at the temperature for 1 h prior to the X-ray diffraction analysis [36]. Reprinted with permission; © 2016 Elsevier.

4.2.4 Electrochemical measurements and simulations

The samples in the form of pressed pellets prepared at 300 MPa have a density of 2.14 g/cm^3. The ball-milled material allowed for the fabrication of denser pellets, which improved the ionic conductivity of $Li_4P_2S_6$. The pellets were pressed with Al/C blocking electrodes to perform all impedance and Arrhenius measurements. The impedance measurements are given in the Appendix A and the corresponding Arrhenius plot of the conductivity derived from the impedance measurements is shown in Fig. 4.10. The ionic conductivity of $Li_4P_2S_6$ is 2.38×10^{-7} S cm^{-1} at 25 °C and 2.33×10^{-6} S cm^{-1} at 100 °C. These results show that $Li_4P_2S_6$ has an activation energy (as defined by Eq. (5)) of 0.29 eV. This activation energy is smaller than that measured for nano-porous β-Li_3PS_4 ($E_m \approx 0.35$ eV) [5] but larger than the meta-stable superionic conducting material $Li_7P_3S_{11}$ ($E_m \approx 0.12 - 0.18$ eV) [32, 33, 7].

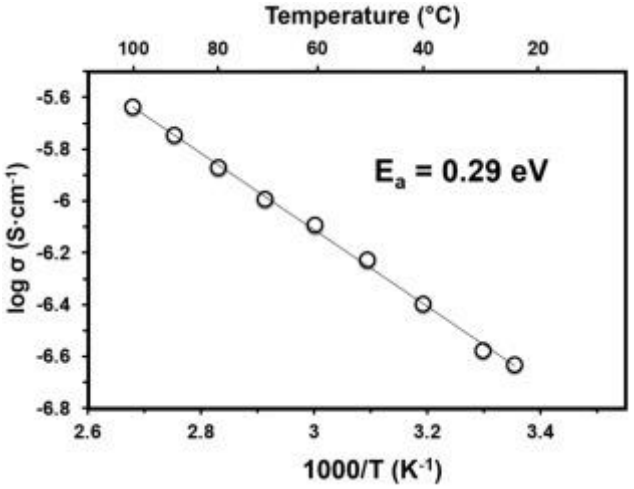

Figure 4.10 Arrhenius plot of the ionic conductivity (Eq. (5)) for $Li_4P_2S_6$ [36]. Reprinted with permission; © 2016 Elsevier.

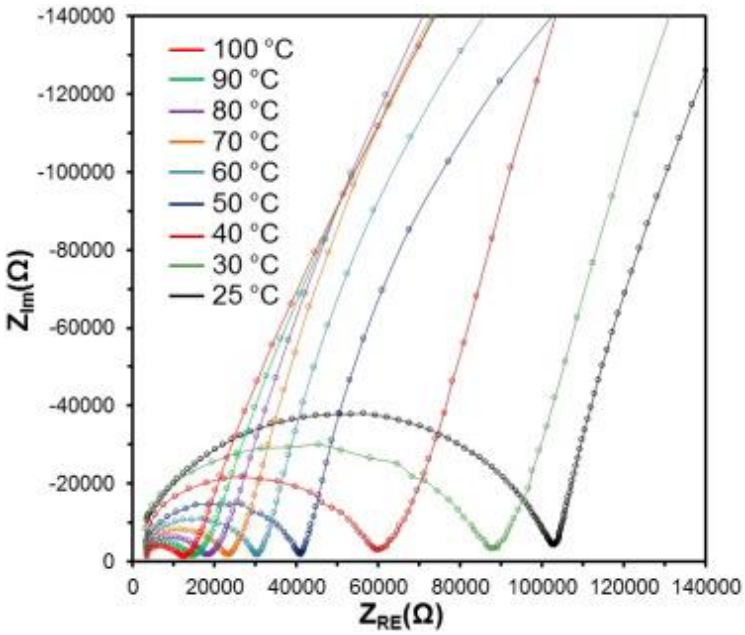

Figure 4.11. Impedance measurements for $Li_4P_2S_6$ at temperatures between 25 °C and 100 °C using blocking electrodes attached to the pellet having cross sectional area 1.27 cm^2 and thickness 0.03 cm. These impedance measurements are representative of results from other $Li_4P_2S_6$ pellets of similar size and thickness [36]. Reprinted with permission; © 2016 Elsevier.

Table 4.2 Resistances and calculated ionic conductivities of $Li_4P_2S_6$ at different temperatures.

Temperature (°C)	R (Ω)	σ (S/cm)
25	101030	2.38×10^{-7}
30	88975	2.70×10^{-7}
40	59143	4.06×10^{-7}
50	40017	6.00×10^{-7}
60	29326	8.18×10^{-7}
70	23216	1.03×10^{-6}
80	17537	1.37×10^{-6}
90	13856	1.82×10^{-6}
100	10283	2.33×10^{-6}

In order to better understand the mechanism for ion conduction, NEB calculations were carried out. First, the vacancy models based on 8 formula unit supercells of Struc. (d) shown in Fig. 4.3D were considered. For this structure, unique Li vacancy hops can occur within the hexagonal plane between sites A, B, C, and D and perpendicular to the hexagonal plane between sites C, E, and F as shown in Fig. 4.12. The corresponding energy versus configuration diagrams are shown in Fig. 4.13, indicating that the vacancy migration energies are given by $E_m = 0.6$ eV for paths both within a hexagonal plane and perpendicular to the plane. Using a supercell with a similar dimension, the migration of vacancies in the $\boldsymbol{P\bar{3}1m}$ structure shown in Fig. 4.3b were investigated, finding a minimum migration energy of $E_m = 0.5$ eV for Li vacancies in a hexagonal layer between P_2S_6 groups. The similarity of these two results suggest that for the vacancy mechanism, the effects of $P_{\uparrow}$ and $P_{\downarrow}$ disorder has little effect on Li ion migration barriers. However, by comparison of the calculated migration energies with the experimentally measured activation for $Li_4P_2S_6$, one can conclude that the Li ion conduction is unlikely to be explained by the vacancy hopping mechanism.

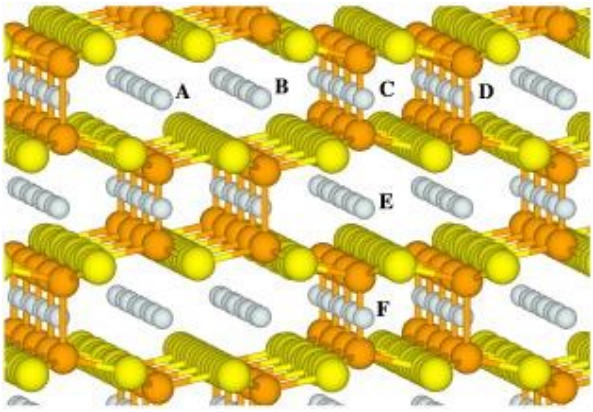

Figure 4.12 Ball-and-stick diagram of supercell of $Li_4P_2S_6$ in Struc. (d) shown in Fig. 4.3D, indicating vacancy positions A–F. The view point of this diagram is similar to that of Fig. 4.3d [36]. Reprinted with permission; © 2016 Elsevier.

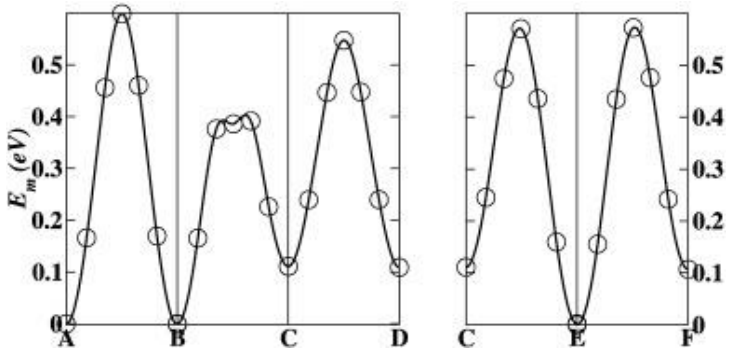

Figure 4.13 Energy path diagrams corresponding to the supercell model shown in Fig. 4.12 determined by NEB calculations of unique vacancy hops within the hexagonal plane (left graph) or along a *c* axis (right graph). The zero of energy was taken as the lowest vacancy configuration [36]. Reprinted with permission; © 2016 Elsevier.

The possible interstitial Li ion migration mechanisms were considered, focusing on the 8 formula unit supercells of Struc. (d) shown in Fig. 4.3d. In order to find possible meta-stable interstitial configurations, a sizable number of initial configurations based on a coarse grid of possible interstitial sites were relaxed with one fixed remote vacancy in order to keep the simulation cells with zero net charge. Several metastable interstitial sites were found, including the 4 neighboring sites shown in Fig. 4.13a. While these sites, which are roughly 2 Å apart from each other and from nearby host lattice Li sites, do not span the supercell, they can give a reasonable approximation to a configuration diagram for a pure interstitial mechanism of Li ion migration as shown in Fig. 4.14b. For this partial path, the migration energy is E_m = 0.1 eV, suggesting that it is likely that the interstitial Li ion migration is energetically favorable for this material. More complicated processes, such as an interstitialcy mechanism involving both interstitial and host lattice Li ions, could also be important for this system. As discussed in the experimental section of this chapter, the Arrhenius activation energy E_a also depend on the "formation" energy to produce an interstitial/vacancy pair, unless the sample has a native population of defects. Simulations

of possible interstitial/vacancy configurations result in an estimate of the formation energy to be more than 1 eV. Therefore, it is concluded that the samples must have native populations of defects such Li^+ Frenkel interstitial/vacancy pairs [34].

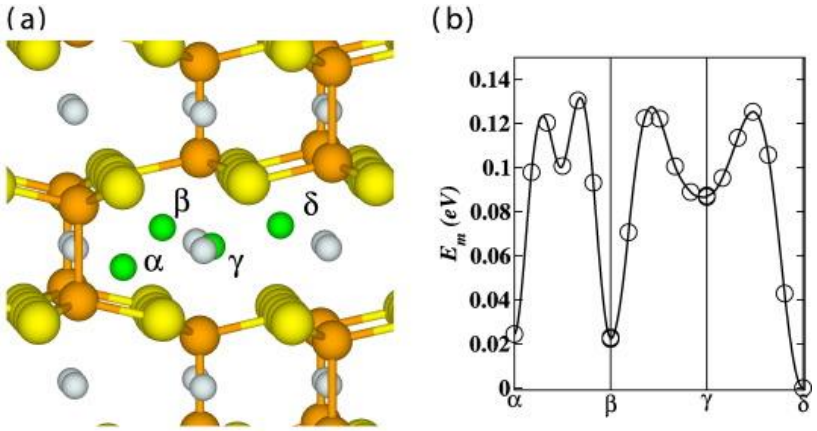

Figure 4.14 A) Ball-and-stick diagram of metastable interstitial sites of the structure shown in Fig. 4.3d labeled α, β, γ, and δ indicated in green and superposed on ideal lattice of Struc. (d). The view point of this diagram is similar to that of Fig. 4.3d and that of Fig. 4.12. B) NEB energy path diagram for interstitial Li ion migration [36]. Reprinted with permission; © 2016 Elsevier.

While it was shown that $Li_4P_2S_6$ is one of the more stable thiophosphate materials as shown in Fig. 4.8 it is interesting to ask the question of whether it is stable in the presence of a Li anode. When $Li_4P_2S_6$ is exposed to lithium metal, a noticeable reaction occurs between the solid electrolyte and the metal. While experimental attempts to cycle a $Li/Li_4P_2S_6/Li$ cell have not yet been successful, ideal interfaces of the electrolyte with a Li anode give insight into the system.

For example, one idealized cleavage of the crystal in a plane containing the hexagonal axis and containing complete P_2S_6 units was considered, as shown in Fig. 4.15a. When this surface is exposed to an idealized Li metal interface and the system was allowed to relax, the system showed some decomposition as shown in Fig. 4.15b. In this case, S–P bonds in the outer layer break in a similar way to that observed in the Li_3PS_4/Li system [13]. For $Li_4P_2S_6$/Li there seems to be a buffer layer of Li_2S formed at the interface, while the P–P bonds remained intact. The partial density of states plot for this system is shown in Fig. 4.16.

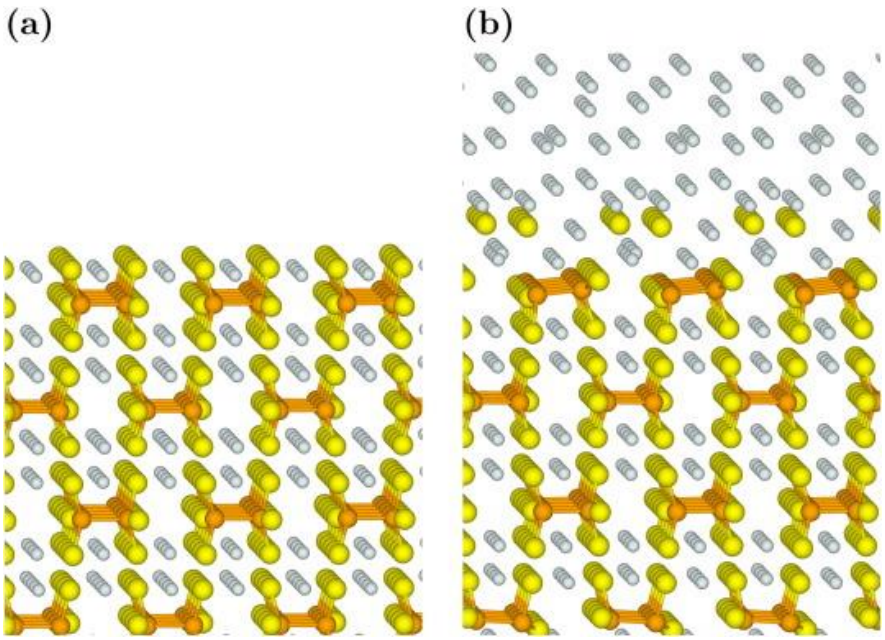

Figure 4.15 a) Relaxed surface structure of $Li_4P_2S_6$ with Struc. (c) (Fig. 4.3c) cleaved perpendicular to the hexagonal plane with vacuum shown at the top of the diagram. b) Relaxed structure of the surface in the presence of several layers of Li metal shown at the top of the diagram [36]. Reprinted with permission; © 2016 Elsevier.

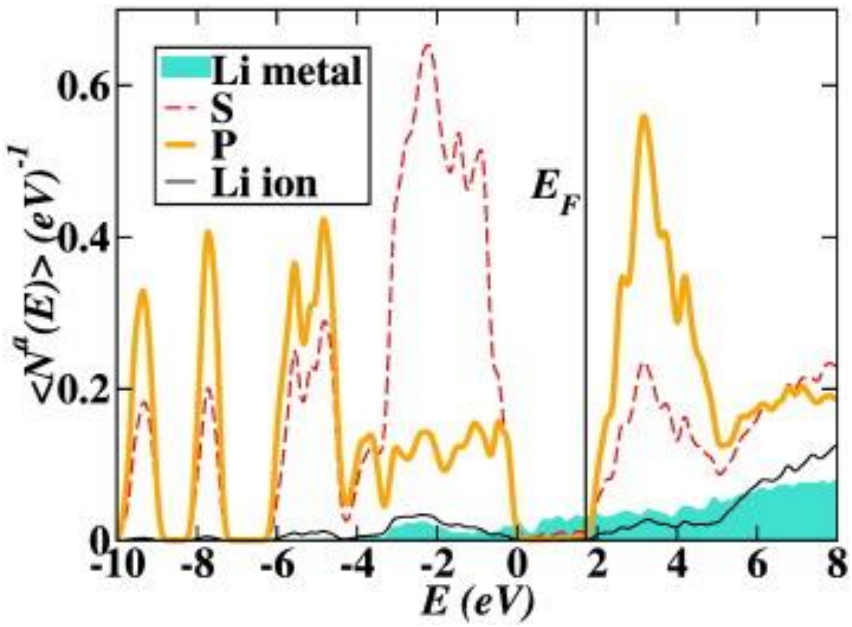

Figure 4.16 Partial density of states plot for the idealized interface shown in Fig. 4.15b. The zero of energy is adjusted to the bulk partial density of states plot of $Li_4P_2S_6$ [36]. Reprinted with permission; © 2016 Elsevier.

Another example cleave was taken parallel to the hexagonal plane. In order to maintain the P_2S_6 building blocks, this cleave results in a rough surface as shown in Fig. 4.17a. When Li metal layers are introduced into this supercell, the relaxed structure has broken P–S bonds and Li_2S groups form. The optimized geometry is very sensitive to the details of the initial structure, an example of which is shown in Fig. 4.17b. In most of the cases studied the P–P bonds remained intact. The partial density of states is shown in Fig. 4.18.

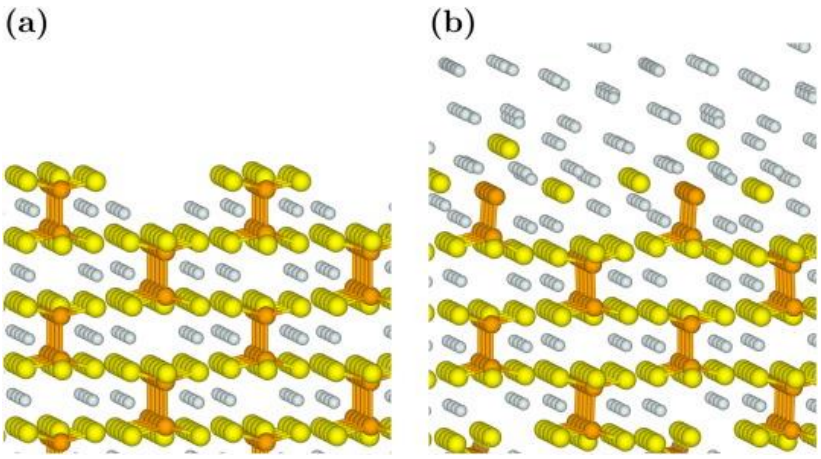

Figure 4.17 A) Relaxed surface structure of $Li_4P_2S_6$ in Struc. (c) (Fig. 4.3c) cleaved parallel to the hexagonal plane with vacuum shown at the top of the diagram. B) Relaxed structure of the surface in the presence of several layers of Li metal shown at the top of the diagram [36]. Reprinted with permission; © 2016 Elsevier.

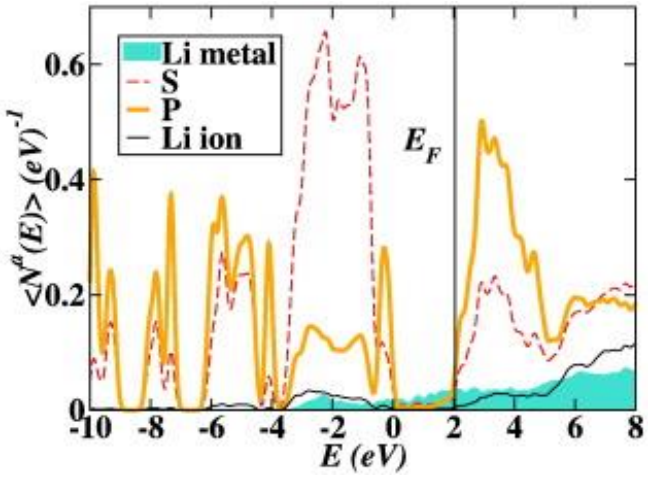

Figure 4.18 Partial density of states plot for the idealized interface shown in Fig. 4.17b. The zero of energy is adjusted to the bulk partial density of states plot of $Li_4P_2S_6$ [36]. Reprinted with permission; © 2016 Elsevier.

4.3 Summary

Samples of $Li_4P_2S_6$ were prepared and investigated. In particular, it was shown that the disorder in the structure first identified by Mercier *et al.* [9] is due to energetic degeneracy in the placement of the P_2S_6 building blocks of the structure. The simulation results are consistent with the X-ray and neutron diffraction measurements. This observation is rationalized on the basis that the structure is invariant with temperature by noting that within a given structure, transformation between the possible P–P bond placements must have a high energy barrier. The relative stability of $Li_4P_2S_6$ compared with Li_3PS_4 correlates with its increased valence band width.

The activation energy determined from the Arrhenius conductivity measurements is E_a = 0.29 eV, which is quite favorable. However for the as-prepared samples, the magnitude of the ionic conductivity is very low. Simulations indicate that the mechanism for ionic conduction in this material is likely to involve interstitial processes. If the concentration of interstitial Li ions could be increased, perhaps the ionic conductivity could be improved. The impedance measurements were made using blocking electrodes. Cells prepared with pure Li electrodes could only be cycled a few times before shorting. Simulations on ideal surfaces suggest that the $Li_4P_2S_6$/Li interface can form a meta-stable buffer layer as does Li_3PS_4 [13]. However, experiments show that for $Li_4P_2S_6$/Li, this meta-stability is very fragile and typically not realized, in contrast to the Li_3PS_4/Li system [5].

The current study has enhanced our understanding of the Li thiophosphate family of solid electrolytes, finding that $Li_4P_2S_6$ is formed at temperatures of 750 °C or higher and shows prolonged stability in air when compared to other lithium thiophosphates. The results of this study provide insights towards better understanding of the family of lithium

thiophosphate solid electrolytes as one of the very promising candidate materials for the implementation of safe high energy-dense batteries for large scale energy storage.

More generally, there are other members of the family of materials based on P_2S_6 (hexathiohypodiphosphate) building blocks as recently shown by Kuhn *et al.* [35], including $Na_4P_2S_6$, which may provide interesting comparisons to the present work and may be of interest to battery technology.

4.4 Experimental Methods

Synthesis of materials: The synthesis of $Li_4P_2S_6$ was based on high temperature solid state reaction methods similar to procedures found in the literature [9, 11]. Reagent-grade Li_2S (Alfa Aesar, 99.9%) and P_2S_5 (Sigma-Aldrich, 99%) crystalline powders were ground with a mortar and pestle for 20 min and sealed in an evacuated quartz tube to form lithium thiophosphate using the following reaction:

$$2Li_2S + P_2S_5 \rightarrow Li_4P_2S_6 + S \quad (1)$$

Since the starting materials are hygroscopic and sensitive to air, this preparation was performed in an Ar-filled glove box.

Because it was found that the same phase of $Li_4P_2S_6$ can be formed at temperatures as low as 750 °C and at temperatures as high as 900 °C, two synthetic routes were explored. For the higher temperature synthesis, the prepared powder was heated to 900 °C for 20 h and held at 450 °C for 24 h in an electric furnace with a ramp up/down of 100 °C/h. The reaction product contained elemental sulfur, which was removed by stirring the powder in anhydrous acetronitrile for 1 h. The powder was then filtered, and dried at 150 °C under vacuum for 2 h, producing a phase-pure material, as evidenced by X-ray diffraction data.

For the lower temperature synthesis, $Li_4P_2S_6$ was heated to 750 °C for 48 h with a ramp up/down at a rate of 100 °C/h, and after similar processing in anhydrous acetronitrile, the reaction yields the same phase-pure product. Both synthetic routes yielded $Li_4P_2S_6$ with the same electrolyte properties.

Temperature-dependent structural characterization: A PANalytical X'Pert Pro Powder Diffractometer with copper K_α radiation was used to complete all of the X-ray diffraction (XRD) analysis. Samples were placed on quartz slides for XRD analysis. Low temperature XRD measurements were completed using the Oxford Systems PheniX Cryostat over the range $15 \leq T \leq 298$ K. The software package HighScore Plus was used to complete Rietveld refinement and structural analysis. Scanning electron microscopy (SEM) images were collected using a Bruker Merlin SEM.

In addition, time-of-flight neutron diffraction results were collected at Oak Ridge National Laboratory using the POWGEN powder diffractometer at the Spallation Neutron Source. Samples were prepared with 700 mg of $Li_4P_2S_6$ loaded into a vanadium can (diameter 6 mm), sealed with an aluminum lid and copper gasket, and fitted with a titanium collar. The time-of-flight neutron diffraction patterns were collected at 300 K and 15 K over the range of diffraction plane d spacings of 0.4–9.0 Å. The time-of-flight neutron refinements were completed using the GSAS and EXPGUI software packages [12].

The thermal response of $Li_4P_2S_6$ was measured by using a TA Q600 differential scanning calorimeter fitted with a platinum/platinum–rhodium thermocouple. Measurements were taken on a 4.0 mg sample of $Li_4P_2S_6$ placed into a ceramic cup and heated to 970 °C at a rate of 10 °C/min under conditions of either constant flow of air or

constant flow of argon gas. The percent weight loss was calculated from the initial weight of the sample.

Electrochemical measurements: In order to prepare the sample for electrochemical measurements, further processing was undertaken in the glove box. First, ball milling with Y-ZrO_2 beads having a mixture of 3 and 5 mm diameter using a ratio of 1:25 ($Li_4P_2S_4$:ball milling media) in an 8000M Spex MixerMill was used to reduce the $Li_4P_2S_6$ particle size. Then, the powder was cold-pressed at 300 MPa to form a pellet. XRD data confirmed that the ball milling media did not react with $Li_4P_2S_6$.

Ionic conductivity measurements were completed using a Solartron 1260 impedance spectrometer over the frequency range 1 Hz–1 MHz with an amplitude of 100 mV. Arrhenius measurements used a Maccor Environmental chamber over the range 25 °C $\leq T \leq$ 100 °C. The samples were formed into pellets of diameter 1.27 cm and were pressed with Al/C blocking electrodes at 300 MPa in a pressurized cell for all electrochemical measurements.

Simulation formalisms and algorithms: The calculational methods used in this work are the same as that used in previous studies of similar materials [13]. Specifically, the calculations are based on density functional theory [14, 15], using the projector augmented wave (PAW) [16] formalism. The PAW basis and projector functions were generated by the ATOMPAW [17] code and used in both the ABINIT [18] and QUANTUM ESPRESSO [19] packages. The exchange-correlation functional was the local density approximation (LDA) [20], which has been shown to give excellent results for similar materials provided that a systematic 2% underestimate of the lattice size is taken into account for each of the 3 dimensions. The simulated results reported here (including the

simulations of the diffraction patterns) have all been adjusted by multiplying the calculated lengths by 1.02. The calculated fractional coordinates and total energies are assumed to be correct.

The electronic structure calculations were performed with plane wave expansions of the wavefunctions including $|\mathbf{k} + \mathbf{G}|^2 \leq 64$ bohr^{-2} and with a Brillouin zone sampling grid density of at least 0.003 bohr^{-3}. Structural parameters of the model systems were determined by minimizing the calculated total energies. The electronic structure results could be qualitatively analyzed in terms of partial densities of states $N^a(E)$, calculated from the expression:

$$N^a(E) = \sum_{n\mathbf{k}} W_{\mathbf{k}} Q^a_{n\mathbf{k}} \delta(E - E_{n\mathbf{k}}), \tag{2}$$

as described in previous work [13]. Here a denotes an atomic site, W_k denotes the Brillouin zone sampling weight factor for wave vector k, and E_{nk} denotes the band energy for band index n and wave vector k. In practice, the δ function is represented by a Gaussian smoothing function with a width of 0.14 eV. For each eigenstate nk and atomic site a, the local density of states factor $Q_{nk}{}^a$ is given by the charge within the augmentation sphere of radius rca which can be well approximated by:

$$Q^a_{n\mathbf{k}} \approx \sum_{ij} \left\langle \tilde{\Psi}_{n\mathbf{k}} \middle| p^a_{n_i l_i m_i} \right\rangle \left\langle p^a_{n_j l_i m_i} \middle| \tilde{\Psi}_{n\mathbf{k}} \right\rangle q^a_{n_i l_i; n_j l_i} \delta_{l_i l_j}, \tag{3}$$

in terms of the radial integrals

$$q^a_{n_i l_i; n_j l_i} \equiv \int_0^{r_c^a} \mathrm{d}\, r \varphi^a_{n_i l_i}(r) \varphi^a_{n_j l_j}(r). \tag{4}$$

In these expressions, $\left|\widetilde{\Psi}_{n\mathbf{k}}\right\rangle$ represents a pseudo-wavefunction, $\left|\tilde{p}^{a}_{n_i l_i m_i}\right\rangle$ represents a PAW atomic projector function localized within the augmentation sphere about atomic site aand characterized with radial and spherical harmonic indices nilimi [16, 21]. The function $\varphi^{a}_{n_i l_i}(r)$ represents the corresponding all-electron radial basis function. The augmentation radii used in this work are $rc^{Li} = 1.6$, $rc^{O} = 1.2$, $rc^{P} = 1.7$, and $rc^{S} = 1.7$ in bohr units. The reported partial densities of states, 〈Na(E)〉, are averaged over sites of each type *a*.

The "nudged elastic band" (NEB) method [22, 23, 24], as programmed in the QUANTUM ESPRESSO package was used to estimate the Li^{+} migration energies E_m in supercell models. For this analysis it was assumed that 5 images between each meta-stable configuration was sufficient to estimate the path energies. For these simulations, supercells consisting of 8 formula units were used. The simulations were performed on neutral supercells, either by using a compensating uniform charge, or by modeling an interstitial ion in the presence of a distant vacancy (or visa versa) within the supercell. The migration energies determined from the NEB calculations can be related to the experimental conductivity σ measurements as a function of temperature *T* through the Arrhenius relationship:

$$\sigma = \sigma_o \cdot e^{\frac{-E_A}{kT}} \qquad (5)$$

where *k* denotes the Boltzmann constant, E_A represents the activation energy for Li ion migration, and σ_0 denotes a temperature independent constant for the sample. For nearly perfect crystals, thermal processes must initiate the formation of a vacancy and interstitial

pair with energy E_f so that $E_A = E_m + 1/2\ E_f$ For crystals with a significant population of native defects, it is expected that $E_A = E_m$.

Visualizations were constructed using the XcrSDEN [26, 27] and VESTA [28] software packages. The software program FINDSYM [29] was used to help analyze the symmetry properties of the optimized structures. In order to directly compare the model structures with the diffraction measurements, powder patterns were generated from the calculated structural parameters using the program Mercury [30] for the X-ray patterns and using the program GSAS [12] for the neutron patterns. The optimized fractional coordinates were used directly, while, as mentioned above, all of the calculated lattice parameters were scaled by a uniform factor of 1.02 in order correct for the systematic size error of the local density approximation (LDA) exchange correlation functional. The diffraction results of Mercier *et al.* [9] reported here were also generated using the Mercury and GSAS programs.

4.5 Notes to Chapter 4

Part of this chapter is adapted from the paper "Structural and electrolyte properties of $Li_4P_2S_6$" that was published in Solid State Ionics [36].

4.6 References

[1] Robinson, A.L.; Janek, J. *MRS Bull.* **2014**, *39*, 1046–1047.

[2] Li, J.; Ma, Chi, M.; Liang, C.; Dudney, N.J. *Adv. Energy Materials* **2015**, *5*, 1401408.

[3] Wang, Y.; Richards, W.D.; Ong, S.P.; Miara, L.J.; Kim, J.C.; Mo, Y.; Ceder, G. *Nat. Mater.* **2015**, *14*, 1026–1031.

[4] Kamaya, N.; Homma, K.; Yamakawa, Y.; Hirayama, M.; Kanno, R.; Yonemura, M.; Kamiyama, T.; Kato, Y.; Hama, S.; Kawamoto, K.; Mitsui, A. *Nat. Mater.* **2011**, *100*, 682–686.

[5] Liu, Z.; Fu, W.; Payzant, E.A.; Yu, X.; Wu, Z.; Dudney, N.J.; Kiggans, J.; Hong, K.; Rondinone, A.J.; Liang, C. *J. Am. Chem. Soc.* **2013**, *1350*, 975–978.

[6] Minami, K.; Hayashi, A.; Tatsumisago, M. *J. Ceram. Soc. Jpn.* **2010**, *118*, 305–308.

[7] Hayashi, A.; Minami, K.; Tatsumisago, M. *J. Solid State Electrochem.* **2010**, *14*, 1761–1767.

[8] Independent private communication from Ezhiylmurugan Rangasamy and Zachary Hood, **2013**.

[9] Mercier, R.; Malugani, J.P.; Fahys, B.; Douglade, J.; Robert, G. *J. Solid State Chem.* **1982**, 43151–162.

[10] Holzwarth, N.A.W.; Lepley, N.D.; Du, Y.A. *J. Power Sources* **2011**, *196*, 6870–6876.

[11] Minami, K.; Mizuno, F.; Hayashi, A.; Tatsumisago, M. *Solid State Ionics* **2007**, *178*, 837–841.

[12] Larson, A.C.; Von Dreele, R.B. Los Alamos National Laboratory Report LAUR 86-748-748, **2004**.

[13] Lepley, N.D.; Holzwarth, N.A.W.; Du, Y.A. *Phys. Rev. B* **2013**, *88*, 104103.

[14] Hohenberg, P.; Kohn, W. *Phys. Rev.* **1964**, *136*, B864–B871.

[15] Kohn, W.; Sham, L.J. *Phys. Rev.* **1965**, *140*, A1133–A1138.

[16] Blöchl, P.E. *Phys. Rev. B* **1994**. *50*, 17953–17979.

[17] Holzwarth, N.A.W.; Tackett, A.R.; Matthews, G.E. *Comput. Phys. Commun.* **2001**, *135*, 329–347.

[18] Gonze, X.; Amadon, B.; Anglade, P.M.; Beuken, J.M.; Bottin, F.; Boulanger, P.; Bruneval, F.; Caliste, D.; Caracas, R.; Cote, M.; Deutsch, T.; Genovese, L.; Ghosez, P.; Giantomassi, M.; Goedecker, S.; Hamann, D.R.; Hermet, P.; Jollet, F.; Jomard, G.; Leroux, S.; Mancini, M.; Mazevet, S.; Oliveira, M.J.T.; Onida, G.; Pouillon, Y.;

Rangel, T.; Rignanese, G.M.; Sangalli, D.; Shaltaf, R.; Torrent, M.; Verstraete, M.J.; Zerah, G.; Zwanziger, J.W. *Comput. Phys. Commun.* **2009**, *180*, 2582–2615.

[19] Giannozzi, P.; Baroni, S.; Bonini, N.; Calandra, M.; Car, R.; Cavazzoni, C.; Ceresoli, D.; Chiarotti, G.L.; Cococcioni, M.; Dabo, I.; Corso, A.D.; Gironcoli, S.; Fabris, S.; Fratesi, G.; Gebauer, R.; Gerstmann, U.; Gougoussis, C.; Kokalj, A.; Lazzeri, M.; Martin-Samos, L.; Marzari, N.; Mauri, F.; Mazzarello, R.; Paolini, S.; Pasquarello, A.; Paulatto, L.; Sbraccia, C.; Scandolo, S.; Sclauzero, G.; Seitsonen, A.P.; Smogunov, A.; Umari, P.; Wentzcovitch, R.M. *J. Phys. Condens. Matter* **2009**, *21*, 394402.

[20] Perdew, J.P.; Wang, Y. *Phys. Rev. B* **1992**, *45*, 13244–13249.

[21] Holzwarth, N.A.W.; Matthews, G.E.; Dunning, R.B.; Tackett, A.R.; Zeng, Y. *Phys. Rev. B* **1997**, *55*, 2005–2017.

[22] Jónsson, H.; Mills, G.; Jacobsen, K.W. in: Berne, B.J.; Ciccotti, G.; Coker, D.F. (Eds.) *Classical and Quantum Dynamics in Condensed Phase Simulations, World Scientific*, Singapore **1998**, 385–404.

[23] Henkelman, G.; Uberuaga, B.P.; Jónsson, H. *J. Chem. Phys.* **2000**, *113*, 9901–9904.

[24] Henkelman, G.; Jónsson, H. *J. Chem. Phys.* **2000**, *113*, 9978–9985.

[25] Kubo, R. *J. Phys. Soc. Jpn.* **1957**, *12*, 570–586.

[26] Kokalj, A. J. Mol. *Graph. Model.* **1999**, *17*, 176–179.

[27] Kokalj, A. Comput. *Mater. Sci.* **2003**, *28*, 155–168.

[28] Momma, K.; Izumi, F. *Appl. Crystallogr*. **2011**, *44*, 1272–1276.

[29] Stokes, H.T.; Hatch, D.M. *J. Appl. Crystallogr.* **2008**, *38*, 237–238.

[30] Mercury 3.5.1, Developed and Distributed by the Cambridge Crystallographic Data Centre, http://www.ccdc.cam.ac.uk/mercury/2014.

[31] Th. Hahn (Ed.), International Tables for Crystallography, Volume A: Space-group Symmetry (Fifth revised edition), 0-7923-6590-9, Kluwer **2002**.

[32] Fuminori Mizuno, Akitoshi Hayashi, Kiyoharu Tadanaga, Masahiro Tatsumisago. *Solid State Ionics* **2006**, *177*, 2721–2725.

[33] Tatsumisago, M.; Hayashi, A. *J. Non-Cryst. Solids* **2008**, *354*, 1411–1417

[34] Hayes, W.; Stoneham. A.M. Defects and Defect Processes in Nonmetallic Solids. *John Wiley & Sons* **1985**.

[35] Alexander Kuhn, Roland Eger, Jürgen Nuss, Bettina V. Lotsch. *Z. Anorg. Allg. Chem.* **2014**, *640*, 689–692.

[36] Hood, Z. D., Kates, C., Kirkham, M., Adhikari, S., Liang, C., & Holzwarth, N. A. W. *Solid State Ionics* **2016** 284, 61-70.

CHAPTER 5

Li_2OHCl CRYSTALLINE ELECTROLYTE FOR STABLE METALLIC LITHIUM ANODES

5.1 Introduction

Advances in lithium-ion batteries within the past decade have allowed for spectacular improvements for portable computing, telecommunication, and other devices necessary for our information-rich society. These advances have also pushed our understanding of battery technology, and, more specifically, the interaction between the different components within a typical battery cell. Amongst these interactions includes the formation of the solid electrolyte interphase (SEI) layer between lithium anode and the electrolyte [1-3]. Recently, there has been an increased interest in solid electrolyte since solid electrolytes impede the formation of dendrites at the SEI, and consequently, allow for the fabrication of safer and longer-lasting batteries that can function at higher voltages [3-6]. Although various solid electrolytes show great stability with lithium anode at higher working voltages [7-9], current solid electrolytes have a number of key limitations: (1) it is difficult to synthesize and process large membranes consisting of oxides and phosphates; (2) sulfide-based solid electrolytes are air-sensitive; and (3) most oxide-based solid electrolytes are not compatible with metallic lithium anode.

The ideal anode for solid-state Li-ion batteries is metallic lithium for its increased energy density [10]. As a result, efforts have shifted to the development of solid electrolytes that show stability against metallic lithium to attain increased energy density [7, 8, 11]. Some sulfide-based solid electrolytes, such as $Li_{10}GeP_2S_{12}$, do not show stability against

metallic lithium metal, which compromises the total specific energy density of the battery [12]. $Li_7La_3Zr_2O_{12}$ (LLZO) represents the only oxide-based solid electrolyte that shows stability with metallic lithium anode, however, this electrolyte displays very high interfacial resistance and requires high processing temperatures, making its implementation into solid-state batteries difficult [13].

LiOH-LiCl electrolytes were previously explored for their increased lithium ion conductivity (10^{-4} – 10^{-3} S cm^{-1} at 200 °C) and high thermodynamic decomposition voltages [14-17]. However, it was reported that LiOH-LiCl crystalline electrolytes are not stable with metallic lithium, where an apparent interfacial reaction occurs between the metallic lithium and electrolyte [15]; this interfacial reaction was not explored further. For batteries that have increased energy density, metallic lithium anode allows for a much higher capacity, however, to achieve increased energy density, the components within the cell must work in harmony, with decreased interfacial resistance and stable SEI formation. Is it possible to have stability between Li_2OHCl crystalline electrolyte and molten lithium anode? Herein, the LiOH-LiCl system is revisited to overcome the limitations of solid electrolytes. This chapter presents the mild temperature processability, ionic conductivity, Arrhenius activation energy, and metallic lithium anode compatibility of LiOH-LiCl solid electrolytes, even at extreme temperatures. In a classic example of stability from instability, it is demonstrated that Li_2OHCl may form a stable SEI with metallic lithium anode and has the remarkable ability to cycle hundreds of times.

5.2 Results and Discussion

5.2.1 Straightforward preparation of LiOH-LiCl melt yields two distinct structures of LiOH-LiCl crystalline electrolytes

LiOH-LiCl solid electrolytes were prepared in a nickel crucible using similar methodology as previous literature [14, 17, 18]. Since LiOH, LiCl, and the LiOH-LiCl solid electrolytes are hygroscopic, all processes were completed under Argon. LiOH (Sigma Aldrich, ≥ 99%) and LiCl (Sigma Aldrich, ≥ 99%) were used to create melts the following ratios of LiOH to LiCl: 1:2, 2:3, 1:1, 3:2, and 2:1, which are referred to as Li_3OHCl_2, $Li_5(OH)_2Cl_3$, Li_2OHCl, $Li_5(OH)_3Cl_2$ and $Li_3(OH)_2Cl$, respectively. When using the same molar ratio, two distinct phases of the material may be achieved by changing the cooling treatment (Figure 5.1). The controlled cooling from 350°C to 250°C at 8°C/ hour yields an anti-perovskite structure (termed: "slow-cooled") while fast cooling from ≥ 350 °C to room temperature in approximately 20 minutes (termed: "fast-cooled") has a more complex crystal structure with increased defects due to the overcooling effect. All compounds were found to undergo a phase transition between 30°C and 50°C. This phase transition was found to significantly increase the ionic conductivity in all compounds [19]. Fast-cooled Li_2OHCl serves as a model example for this system, where the phase transition occurs reversibly, which is characterized by *in situ* powder x-ray diffraction (XRD) shown in Figure 5.2. Several peaks in the XRD pattern for Li_2OHCl are characteristic to this phase transition. Peaks at 22.0°, 23.0°, 32.0°, and 32.7° 2θ disappear when the electrolyte is heated from 30 °C to 50°C, while the peaks at 22.5°, 32.3°, 46.4°, 57.6°, and 57.7° 2θ become more pronounced during this heating process. As shown, fast-cooled Li_2OHCl

undergoes a phase change from orthorhombic to cubic at 35 °C [17]. Upon cooling the solid electrolyte from 50 °C to 30°C, the peaks return to the same position as in the parent electrolyte, supporting that that this phase transition is in fact reversible.

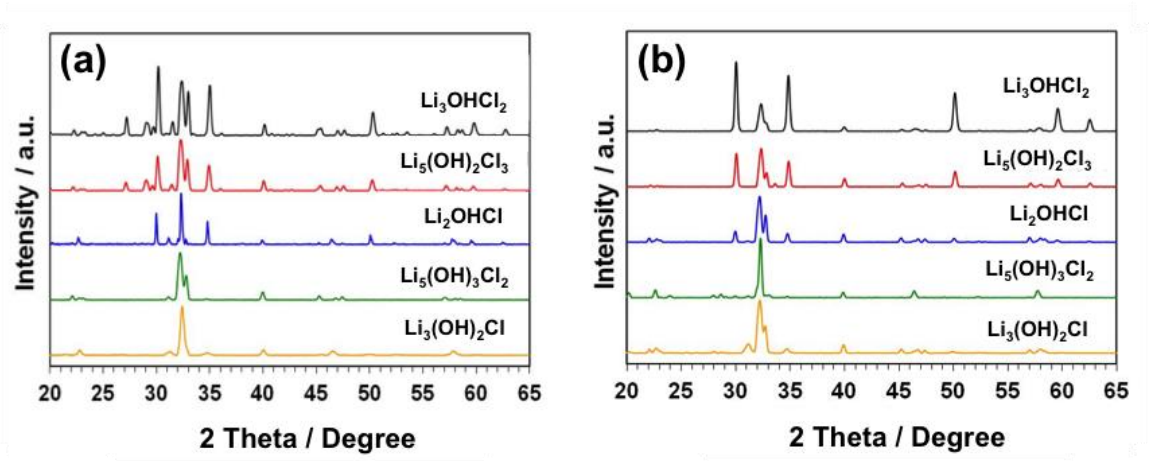

Figure 5.1 XRD patterns at room temperature for as-synthesized LiOH-LiCl crystalline electrolytes from a) uncontrolled fast cooling from ≥ 350 °C and b) slow cooling at 8 °C/ hour from 350 °C to 250 °C and holding at 250 °C for 24 hours [28]. Reprinted with permission; © 2016 American Chemical Society.

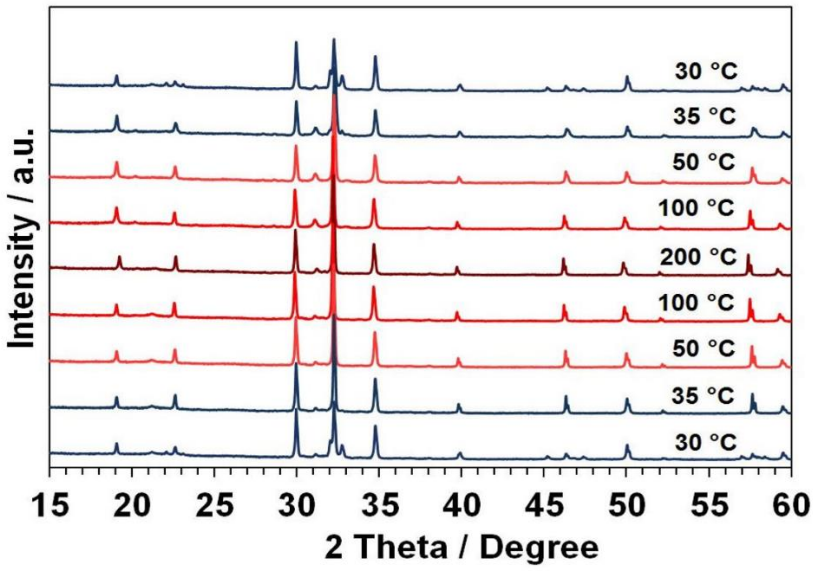

Figure 5.2 XRD patterns for the as-prepared, fast-cooled Li_2OHCl crystalline electrolyte from 30 °C to 200 °C, showing a clear phase transition from 30-50 °C. The blue line corresponds to the low temperature Li_2OHCl phase, whereas the red lines correspond to the high temperature Li_2OHCl phase. XRD confirms this phase transition is reversible [28]. Reprinted with permission; © 2016 American Chemical Society.

5.2.2 Li_2OHCl from fast cooling shows enhanced ionic conductivity and lower activation energy at increased temperatures

The ionic conductivity and Arrhenius activation energy were measured for each LiOH-LiCl compound. The crystalline electrolytes were cold-pressed in a specialized pressurized cell with Al/C blocking electrodes at 300 MPa and electrochemical impedance spectroscopy (EIS) measurements were collected between 1 MHz – 1 Hz with amplitude of 100 mV. When cold-pressed, LiOH-LiCl electrolytes form dense pellets free of fractures. Because LiOH-LiCl crystalline electrolytes exhibit a phase transition between

30 and 50 °C, the Arrhenius activation energy was calculated for temperatures ≥ 50 °C. Representative EIS measurements are shown for fast-cooled Li_2OHCl in Figure 5.3.

When comparing the resulting crystalline electrolytes from the fast cooling and slow cooling procedures, the ionic conductivities of the electrolytes at 25 °C share a similar trend. At 25 °C, fast-cooled $Li_5(OH)_2Cl_3$ yields the best ionic conductivity of 1.48×10^{-7} S cm^{-1} (Figure 5.4). When heated to 100 °C, the electrolytes from the fast cooling method maintain ionic conductivities nearly one order of magnitude higher than those from the slow cooling procedure. This enhancement in ionic conductivity from fast cooling is attributed to an increase of defects in the crystal lattice. Defects have previously been shown to enhance the ionic conductivity in crystalline electrolytes by creating an increased concentration of vacancies and interstitial spaces, and for the case of LiOH-LiCl crystalline electrolytes, creating defects through the utilization of the overcooling effect significantly improves the ionic conductivity at increased temperatures [14, 15, 17].

An equivalent stoichiometric ratio of LiOH and LiCl allows the ionic conductivity to reach a maximum at 100 °C for electrolytes from both the slow cooling and fast cooling methods. An excess of either hydroxide or chloride character yields an unfavorable charge carrier distribution after the crystalline electrolytes undergo the phase transition at increased temperatures [20, 21]. Additionally, the Arrhenius activation energy reaches a minimum (<0.60 eV) for Li_2OHCl and $Li_5(OH)_2Cl_3$ from the fast cooling method, making these electrolytes more favorable for solid-state battery applications. Fast-cooled Li_2OHCl has the highest ionic conductivity at increased temperatures and Arrhenius activation energy of 0.56 eV, rendering this electrolyte of interest for further exploration.

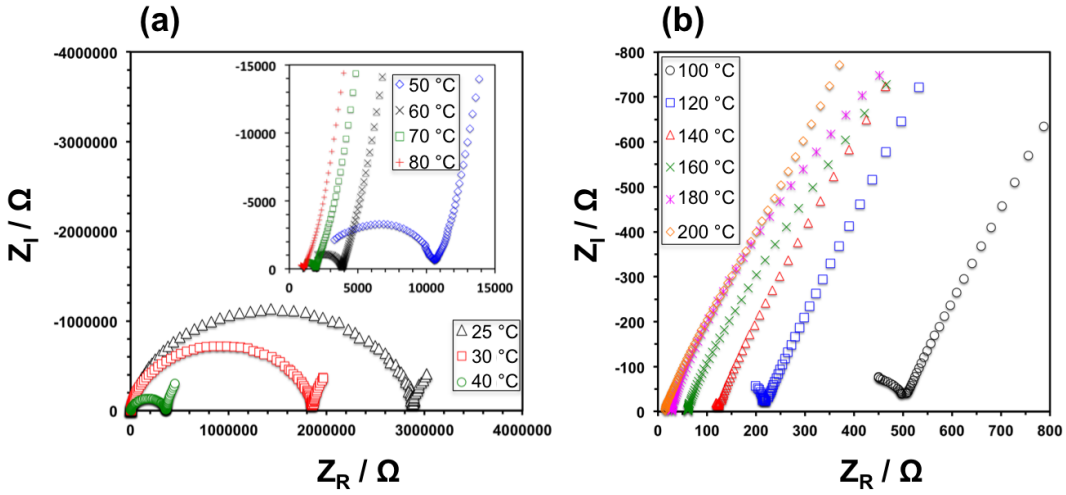

Figure 5.3 Impedance spectra of fast-cooled Li_2OHCl measured at a) 25 to 80 °C and b) 100 to 200 °C. All measurements were completed from 1 MHz – 1Hz with amplitude 100 mV. The total ionic conductivity is determined by using the intercept between the semi-circle or semi-arc and straight line as total resistance [28]. Reprinted with permission; © 2016 American Chemical Society.

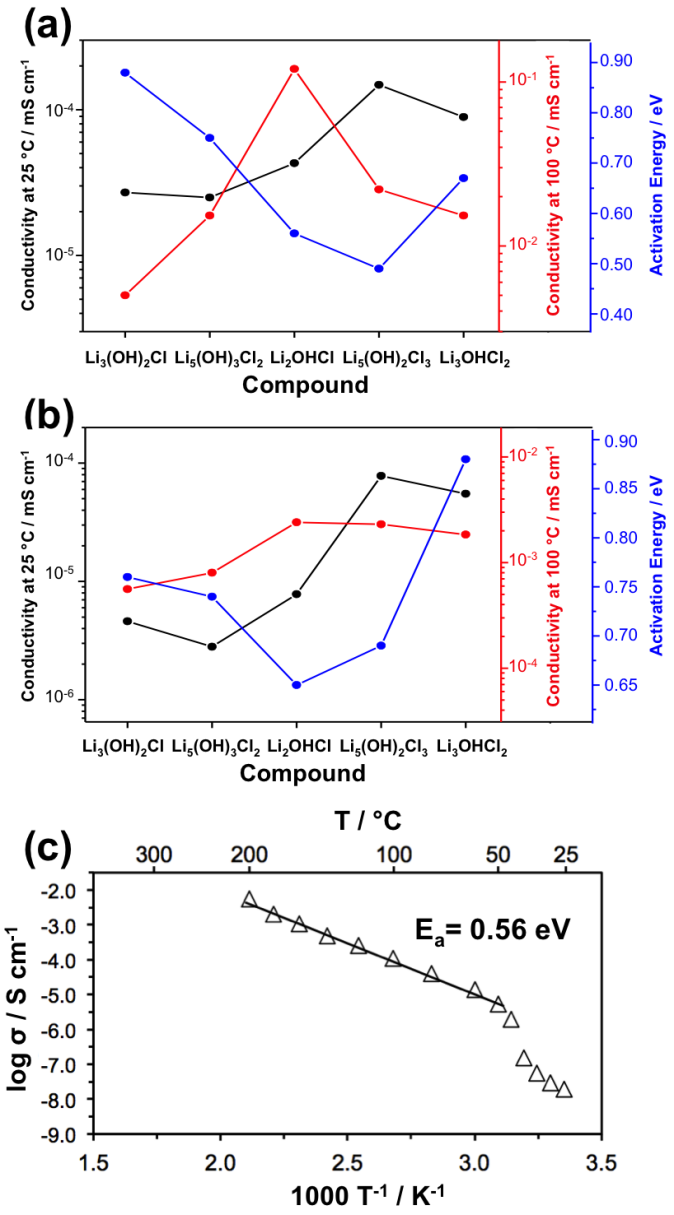

Figure 5.4 Ionic conductivity at 25 °C (black line) and 100 °C (red line), and activation energy after the phase transition (blue line) for LiOH-LiCl crystalline electrolytes from a) fast cooling procedure and b) slow cooling procedure; C) Arrhenius plot for fast-cooled Li_2OHCl, which exhibits the highest ionic conductivity at 100 °C and maintains a reasonable Arrhenius activation energy of 0.56 eV [28]. Reprinted with permission; © 2016 American Chemical Society.

5.2.3 Melt-casting Li_2OHCl yields continuous, dense membranes

A critical limitation of most oxide-based solid electrolytes exists in the fact that it is hard to process continuous, dense membranes at decreased temperatures. In fact, most oxide-based solid electrolytes require processing temperatures over 1600 °C to form dense membranes for solid-state battery applications. Li_2OHCl can be processed into continuous, dense membranes at much milder temperatures below 400 °C. To fabricate these membranes, the molten Li_2OHCl mixture was poured into a Teflon cast (Figure 5.5) and the melt was pressed slightly with a Teflon plunger (< 1MPa); the resulting membranes were dense, free of pores and cracks (Figure 5.6). When no pressure is applied to Li_2OHCl upon cooling in the Teflon mold, cracks and voids appear in the solid electrolyte membrane (Figure 5.7), which justifies the use of a Teflon plunger. Melt-casting at a mild temperature demonstrates that Li_2OHCl is a promising candidate for large-scale production of continuous, dense electrolyte membranes.

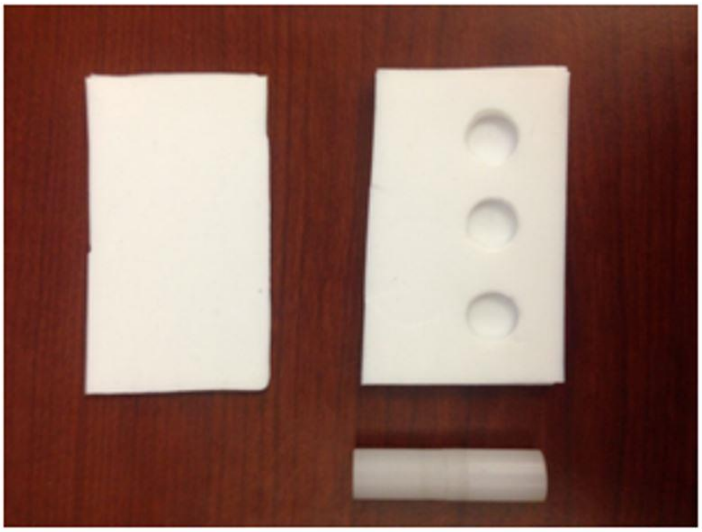

Figure 5.5 Teflon cast and plunger used to prepare LiOH-LiCl membranes [28]. Reprinted with permission; © 2016 American Chemical Society.

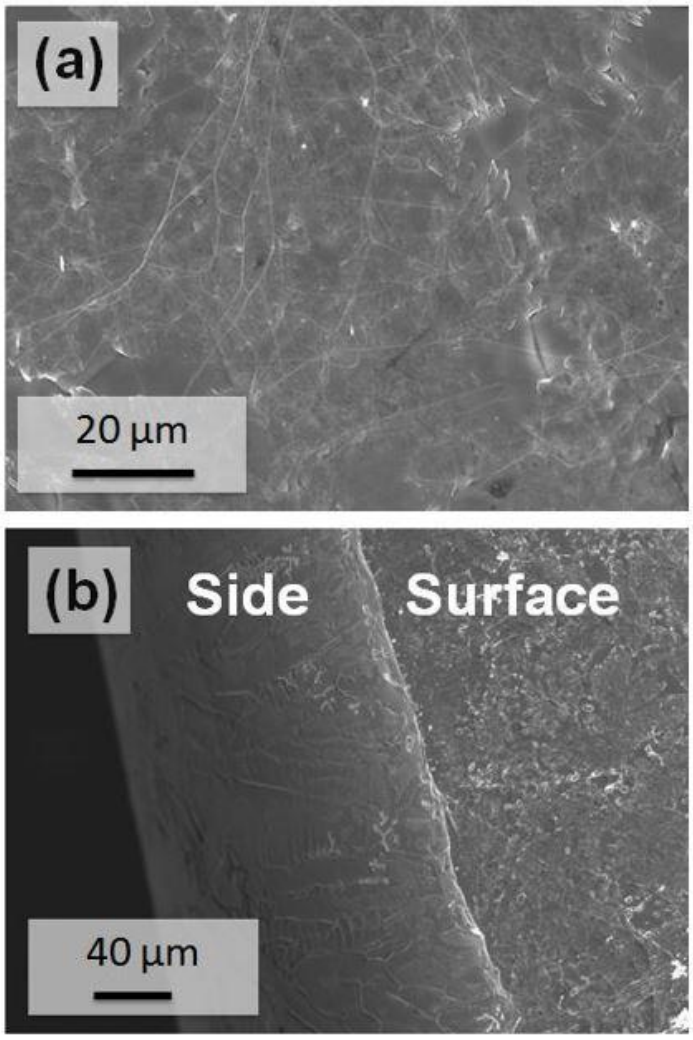

Figure 5.6 SEM images of a) the surface and b) a side view (tilt angle: 45°) of the pressed Teflon-cast Li_2OHCl membranes, yielding a continuous dense membrane [28]. Reprinted with permission; © 2016 American Chemical Society.

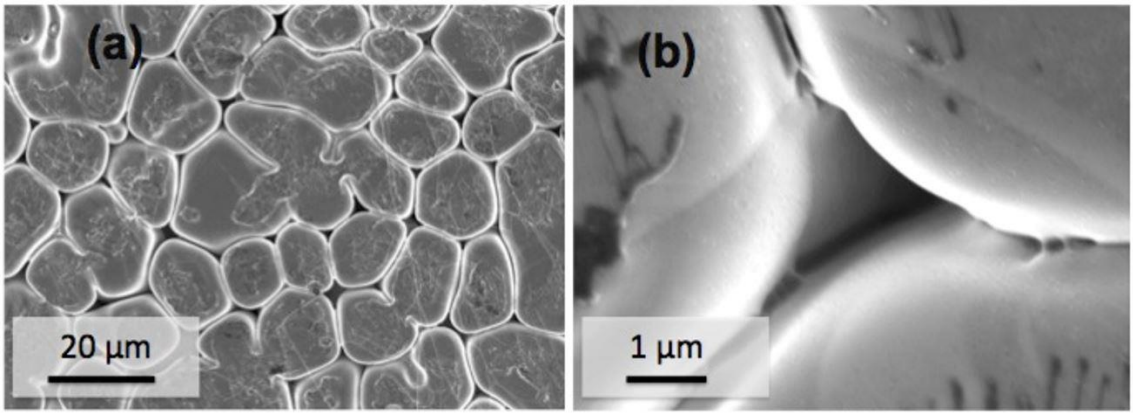

Figure 5.7 SEM images of Li_2OHCl after the molten salt was poured into Teflon casts, showing a) the surface of Li_2OHCl when no pressure was applied to the surface of the pellet, b) a close-up of (a). Applying pressure to the surface of the melt allows for a dense Li_2OHCl membrane to be fabricated [28]. Reprinted with permission; © 2016 American Chemical Society.

5.2.4 Li_2OHCl shows superior performance against molten lithium anode

To demonstrate the performance and long-term compatibility of fast-cooled Li_2OHCl against molten lithium anode, Li/Li_2OHCl/Li symmetric cells were fabricated [22]. These cells were assembled by pressing 1/2" pellet of highly ionic-conducting ball-milled Li_2OHCl at 300 MPa inside a specialized cell previously developed by our group at Oak Ridge National Laboratory [9]. For the purpose of assessing the compatibility of Li_2OHCl with molten lithium anode, cold pressing allows the solid electrolyte to form a continuous network with the body of the specialized cell. Additionally, at high pressures, the Li_2OHCl maintains good compactness (>90% of the theoretical density). Then, metallic lithium foil (≤15 mg, 12 mm in diameter and thickness of ~100 µm) was deposited with carbon mesh on each side of the pellet. A spring fixated within the cell ensured good contact between the lithium and solid electrolyte. Li_2OHCl solid electrolyte shows stability with metallic

lithium, even at temperatures above the melting point of lithium metal. Upon heating the cells to 195°C, the electrolyte shows great cyclability with molten lithium anode. Figure 5.8 demonstrates favorable lithium exchange for 4500 min with an ideal cell voltage retention of 0.06V (cycling data for 14,000 min and at different current densities are provided in Figures 5.9 and 5.10). Typically, solid electrolytes require relatively smaller current densities (0.01 mA/cm^2 – 0.2 mA/cm^2) when cycled with metallic lithium, but for the molten phase, the Li anode allows for a larger current density (1.0 mA/cm^2), which allows for faster charging kinetics.

This cycling performance is attributed to the formation of a stable SEI. The direct-current (dc) conductivity from polarization is 1.5×10^{-3} S cm^{-1} which holds a good correlation with the alternating-current (ac) conductivity of 2.8×10^{-3} S cm^{-1}, for fast-cooled Li_2OHCl at 195 °C. The differences in the dc and ac cell conductivity results relate to SEI formation and the different electrodes utilized for each measurement. Negligible interfacial resistance was observed when the Li_2OHCl crystalline electrolyte was cycled with molten lithium anode for over 400 cycles, even after SEI formation.

To further demonstrate the stability of Li_2OHCl with molten lithium anode after SEI formation, SEM images with energy-dispersive X-ray spectroscopy (EDS) of symmetric cells were collected; this method was previously shown as a powerful tool to visualize interfaces in batteries [6, 23-26]. A cross section of the Li/Li_2OHCl/Li symmetric cell cycled at 195 °C for 160 cycles shows a clear SEI formation (Figure 5.11). The SEI has a higher concentration of oxygen determined by EDS, and the thickness of this layer is 50 μm across the interface, which supports the interfacial reaction of molten lithium reacting with Li_2OHCl to form Li_2O, LiCl, and the gaseous by-product H_2 shown below:

$$2\ Li_2OHCl_{(s)} + 2\ Li_{(l)} \rightarrow 2\ Li_2O_{(s)} + 2\ LiCl_{(s)} + H_{2\ (g)}$$

LiCl remains closer to the Li_2OHCl solid electrolyte while Li_2O is in higher concentration closer to the lithium anode and constitutes the bulk of the SEI, forming an interconnected network that protects the crystalline Li_2OHCl from further reactions with molten lithium anode. H_2 evolves from the interface and does not contribute to the formation of pores or cracks in the SEI nor solid electrolyte. SEM images with EDS mapping of the surface layers in Li/Li_2OHCl/Li symmetric cells support SEI formation primarily constituting Li_2O (Figure 5.12). This SEI is believed to contain unreacted lithium metal, as the interfacial reaction between the molten lithium and Li_2OHCl is self-limiting. Simultaneously, the SEI allows the molten lithium anode to cycle hundreds of times with crystalline Li_2OHCl solid electrolyte. Still, this result raises the question: To what extent does this SEI form?

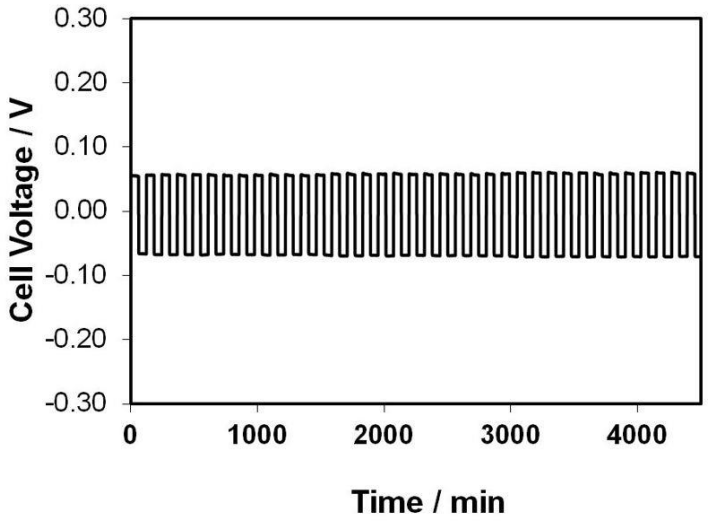

Figure 5.8 Molten lithium cyclability in a symmetric Li/Li_2OHCl/Li cell with a current density of 1.0 mA cm^{-2} at 195 °C, demonstrating stability between the molten lithium anode and the crystalline electrolyte [28]. Reprinted with permission; © 2016 American Chemical Society.

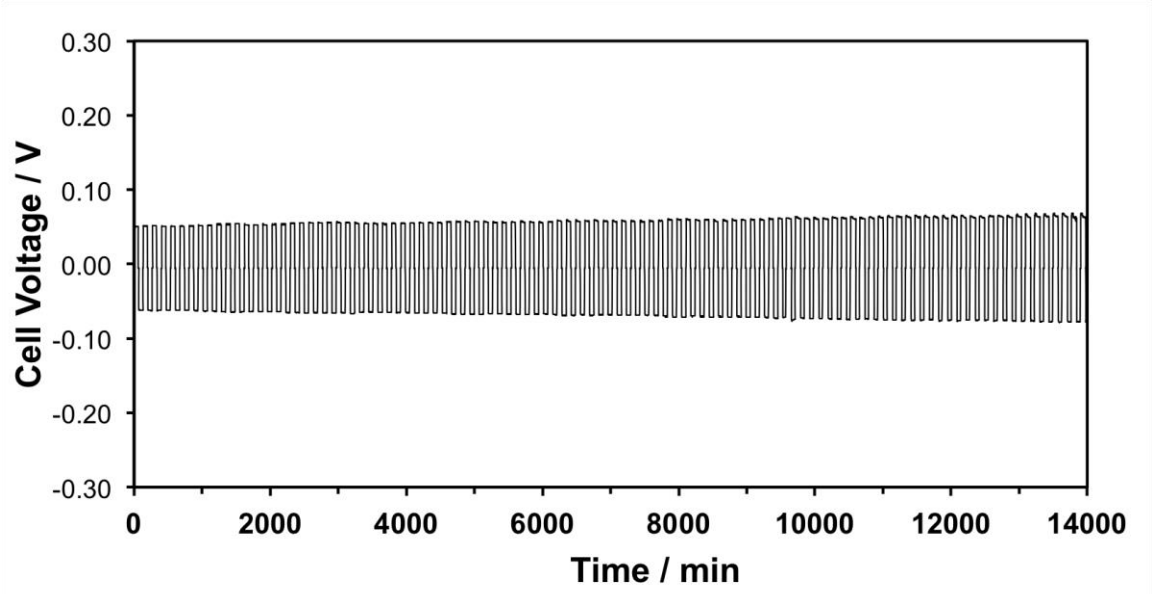

Figure 5.9 Molten lithium cyclability in a Li/Li_2OHCl/Li symmetric cell with a current density of 1.0 mA cm^{-2} at 195 °C, demonstrating stability between the molten lithium anode and the crystalline electrolyte for 14,000 minutes [28]. Reprinted with permission; © 2016 American Chemical Society.

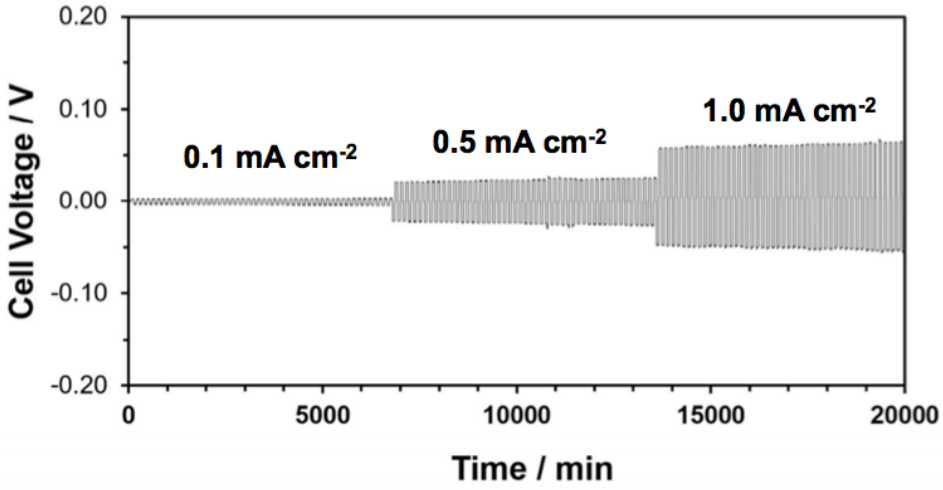

Figure 5.10 Molten lithium cyclability in a Li/Li_2OHCl/Li symmetric cell at different current densities (0.1, 0.5 and 1.0 mA cm^{-2}) at 195 °C [28]. Reprinted with permission; © 2016 American Chemical Society.

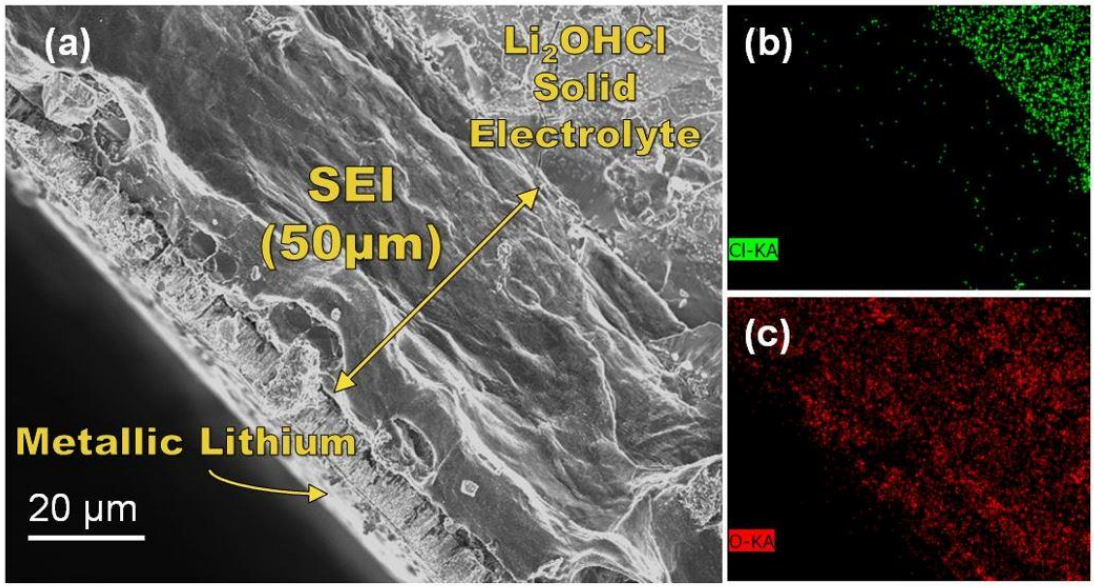

Figure 5.11 SEM image of Li/Li_2OHCl/Li symmetric cell after 160 charge/ discharge cycles showing a) the cross section of the SEI with correlating EDS mapping of b) chlorine in green and c) oxygen in red. The SEI layer is uniform and measures 50 µm in thickness [28]. Reprinted with permission; © 2016 American Chemical Society.

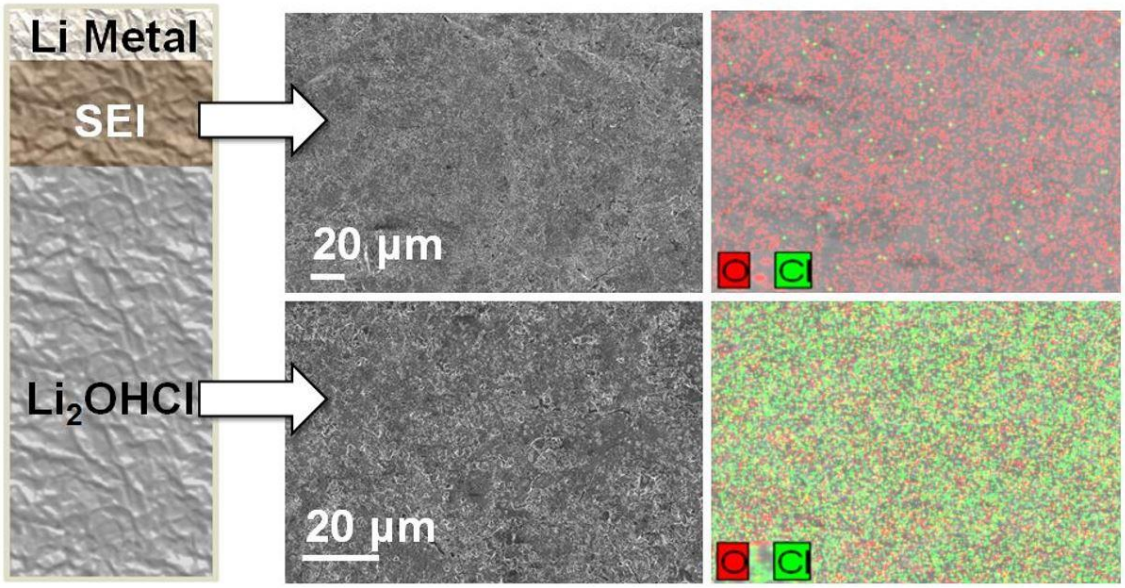

Figure 5.12 SEM images of Li/Li_2OHCl/Li symmetric cell surface layers with EDS mapping of chlorine in green and oxygen in red. The SEI is mainly composed of Li_2O [28]. Reprinted with permission; © 2016 American Chemical Society.

The formation kinetics of the SEI layer were determined by constructing similar symmetric cells with the same amount of lithium anode, charged/discharged for 40 cycles, and subsequently disassembled to measure the thickness of the SEI. After 40 cycles, the cells have the same SEI thickness as the cells cycled 160 times (Figure 5.13). The SEI layer is dense and free from pores and cracks after both 40 and 160 cycles, supporting the fact that the interfacial reaction between the Li_2OHCl solid electrolyte and the molten lithium anode occurs rapidly, which matches the criteria for an ideal SEI [27]. Since the thickness of the SEI layer does not significantly increase from cycle 40 to 160 for the symmetric cells, the interfacial reaction is believed to be self-limiting, which allows for symmetric cells of Li/Li_2OHCl/Li to cycle repeatedly and maintain a lower interfacial resistance.

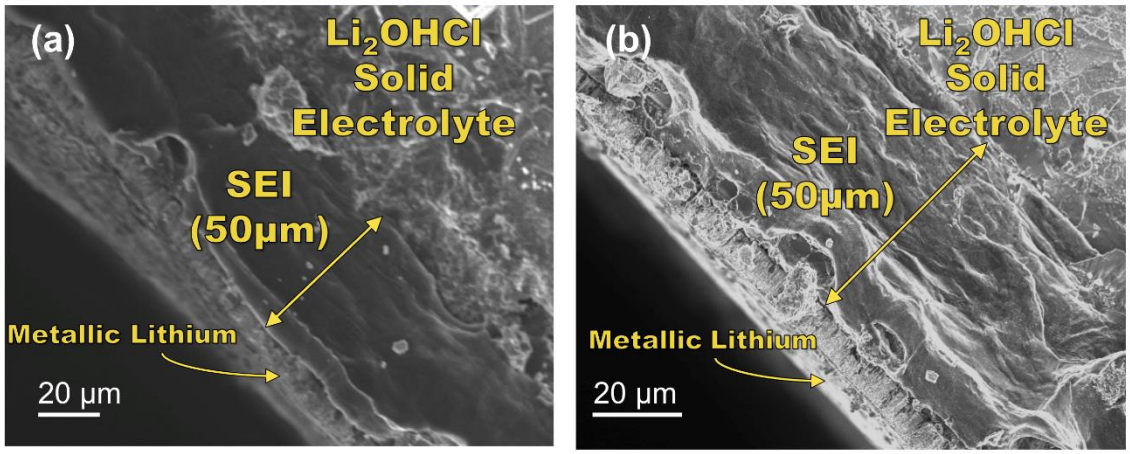

Figure 5.13 SEM image of Li/Li_2OHCl/Li symmetric cell showing a cross section of the SEI a) after 40 and b) after 160 charge/ discharge cycles. The SEI was uniform across electrolyte and measures 50 μm for both cells, demonstrating that the SEI layer forms a self-limiting passivation later between Li_2OHCl and lithium metal [28]. Reprinted with permission; © 2016 American Chemical Society.

5.3 Summary

To summarize, the LiOH-LiCl system was explored in order to overcome the limitations of solid electrolytes. It was found that fast-cooled Li_2OHCl had a number of excellent properties for solid-state batteries plus an extremely stable interface with metallic lithium anode through self-limiting interfacial reactions. Cold-pressed Li_2OHCl from fast cooling exhibited the highest ionic conductivity and practical Arrhenius activation energy at increased temperatures. Li_2OHCl shows compatibility with metallic lithium, even in extreme temperatures. Li/Li_2OHCl/Li cells cycled at 195 °C show stability between the solid electrolyte and molten lithium anode upon SEI formation, where the electrolyte and lithium show little interfacial resistance and can cycle hundreds of times. The SEI was

found to have a higher concentration of oxygen, supporting the formation of a lithium oxide layer, which stabilizes the molten lithium anode with the solid electrolyte without adversely compromising the ionic conductivity. This finding opens ample opportunities for advancements in batteries that employ metallic lithium anode.

5.4 Experimental Methods

Synthesis of the LiOH-LiCl electrolytes: Fast-cooled LiOH-LiCl crystalline electrolytes were prepared in a nickel crucible by mixing appropriate molar ratios of LiOH (Sigma Aldrich, ≥ 98%) and LiCl (Sigma Aldrich, ≥ 99%) and heating to ≥ 350 °C for 30 minutes to achieve a homogeneous melt, and then cooled quickly to room temperature (this process took about 20 minutes). All reagents were used without further purification. The precursors were dried on a Schlenk line for 4 hours prior to moving the powders to the Argon-filled glove box. Slow-cooled anti-perovskite LiOH-LiCl crystalline electrolytes were prepared in a nickel crucible using the same precursors; the nickel crucible was then sealed with a copper gasket in a bomb reactor and heated to 350 °C for 24 hours and cooled slowly at 8 °C/ hour to 250 °C, held at this temperature for 24 additional hours, and cooled to room temperature at 25 °C/ hour. The samples were then ground to a fine powder with a mortar and pestle and ball milled (8000M Spex Mixer Mill) using a mixture of 3 mm and 5 mm Y-ZrO_2 ball milling media in a 1:25 (solid electrolyte: media) mass ratio in a HDPE vial. All processes were carried out under Argon, as the LiOH-LiCl electrolytes and precursors are sensitive to moisture and air.

Structural and electrolyte characterization: Crystallographic phase characterization was conducted with a PANalytical X'Pert Pro Powder Diffractometer with Cu-K_α radiation. All

samples were prepared in an Argon-filled glove box and sealed with Kapton® films on quartz slides. Rietveld refinement was completed using HighScore Plus, a software package developed by PANalytical. To investigate the phase transitions, LiOH-LiCl crystalline electrolytes were sealed with Kapton® films and silver paste on quartz slides. The quartz slides were places in an Anton Paar Align.Stage Hot Stage, which was heated between 30 °C-200°C in 10 °C increments; the temperature was maintained for 30 minutes prior to collecting crystallographic data. Phase transition reversibility was also confirmed by ramping the hot stage from 200 °C to 30 °C in 10 °C increments. A Zeiss® Merlin Scanning Electronic Microscope (SEM) was used to collect images of the pellet surface at 5.0kV. Energy-dispersive X-ray spectroscopy (EDS) was completed with a gun acceleration of 10.0kV to observe surface and cross-sectional elemental distribution in the molten lithium exposed Li_2OHCl crystalline electrolyte. Samples were placed on carbon conductive tape and sealed under Argon prior to collecting SEM images.

After ball milling the LiOH-LiCl samples, about 140 mg of each sample were cold-pressed at 300 MPa into a pellet with a diameter of 1/2" and sealed in a pressurized cell developed by our group. For electrochemical impedance spectroscopy (EIS), pellets were pressed with Al/C blocking electrodes and a Solartron 1260 coupled with a Maccor environmental chamber was used to determine Arrhenius activation energy measurements from 20-100 °C. All EIS measurements were completed from 1 MHz – 1Hz with amplitude 100 mV. Phase reversibility was confirmed through EIS by ramping cells from 100-20 °C.

A Maccor multifunction Model 4200 battery cell cycler collected all cell cycling data. Specialized pressurized cells developed by our group were used to assemble Li/Li_2OHCl/ Li symmetric cells. First, ball-milled Li_2OHCl was cold-pressed at 300 MPa

to form a continuous membrane across the pressurized cell's dye. Next, lithium foil (≤ 15 mg) was placed on each side of the solid electrolyte membrane. Carbon mesh was placed on each side of the lithium to prevent molten lithium leakage into the cell. After sealing the cell, the symmetric cell was moved to a Fischer Scientific™ Isotemp™ forced air oven at 195°C for 2 hours prior to collecting data. All processes for cell fabrication (for cell cycling and EIS measurements) were completed under inert atmosphere as LiOH-LiCl electrolytes are sensitive to moisture and air.

5.5 Notes to Chapter 6

This chapter is based on the paper "Li_2OHCl Crystalline Electrolyte for Stable Metallic Lithium Anode" published in the Journal of the American Chemical Society [28].

5.6 References

[1] Peled, E. *Journal of The Electrochemical Society* **1979**, 126, 2047.

[2] Peled, E. *Journal of Power Sources* **1983**, 9, 253.

[3] Winter, M. *Zeitschrift für Physikalische Chemie International journal of research in physical chemistry and chemical physics* **2009**, 223, 1395.

[4] Li, J.; Baggetto, L.; Martha, S. K.; Veith, G. M.; Nanda, J.; Liang, C.; Dudney, N. J. *Advanced Energy Materials* **2013**, 3, 1275.

[5] Li, J.; Dudney, N. J.; Nanda, J.; Liang, C. *ACS Applied Materials & Interfaces* **2014**, 6, 10083.

[6] Unemoto, A.; Ikeshoji, T.; Yasaku, S.; Matsuo, M.; Stavila, V.; Udovic, T. J.; Orimo, S.-I. *Chemistry of Materials* **2015**, 119, 13459.

[7] Rangasamy, E.; Liu, Z.; Gobet, M.; Pilar, K.; Sahu, G.; Zhou, W.; Wu, H.; Greenbaum, S.; Liang, C. *Journal of the American Chemical Society* **2015**, 137, 1384.

[8] Liu, Z.; Fu, W.; Payzant, E. A.; Yu, X.; Wu, Z.; Dudney, N. J.; Kiggans, J.; Hong, K.; Rondinone, A. J.; Liang, C. J*ournal of the American Chemical Society* **2013**, 135, 975.

[9] Wang, H.; Ma, C.; Chi, M.; Liang, C. *Advanced Materials Interfaces* **2015**, 2.

[10] Zu, C.-X.; Li, H. *Energy & Environmental Science* **2011**, 4, 2614.

[11] Li, J.; Ma, C.; Chi, M.; Liang, C.; Dudney, N. J. *Advanced Energy Materials* **2015**, 5, 1401408.

[12] Kamaya, N.; Homma, K.; Yamakawa, Y.; Hirayama, M.; Kanno, R.; Yonemura, M.; Kamiyama, T.; Kato, Y.; Hama, S.; Kawamoto, K. *Nature Materials* **2011**, 10, 682.

[13] Wolfenstine, J.; Allen, J.; Read, J.; Sakamoto, J. *Journal of Materials Science* **2013**, 48, 5846.

[14] Hartwig, P.; Rabenau, A.; Weppner, W. *Journal of the Less Common Metals* **1981**, 78, 227.

[15] Hartwig, P.; Weppner, W. *Solid State Ionics* **1981**, 3, 249.

[16] Zhao, Y.; Daemen, L. L. *Journal of the American Chemical Society* **2012**, 134, 15042.

[17] Schwering, G.; Hönnerscheid, A.; van Wüllen, L.; Jansen, M. *ChemPhysChem* **2003**, 4, 343.

[18] Friese, K.; Hönnerscheid, A.; Jansen, M. *Zeitschrift für Kristallographie/International journal for structural, physical, and chemical aspects of crystalline materials* **2003**, 218, 536.

[19] Eilbracht, C.; Kockelmann, W.; Hohlwein, D.; Jacobs, H. Physica B: *Condensed Matter* **1997**, 234, 48.

[20] Maier, J.; Münch, W. *Zeitschrift für anorganische und allgemeine Chemie* **2000**, 626, 264.

[21] Braga, M. H.; Stockhausen, V.; Oliveira, J. C.; Ferreira, J. A. *MRS Proceedings, Cambridge Univ Press* **2013**, Vol. 1526, p mrsf12.

[22] Burns, J.; Krause, L.; Le, D.-B.; Jensen, L.; Smith, A.; Xiong, D.; Dahn, J. *Journal of The Electrochemical Society* **2011**, 158, A1417.

[23] Unemoto, A.; Chen, C.; Wang, Z.; Matsuo, M.; Ikeshoji, T.; Orimo, S.-i. *Nanotechnology* **2015**, 26, 254001.

[24] Kotobuki, M.; Suzuki, Y.; Munakata, H.; Kanamura, K.; Sato, Y.; Yamamoto, K.; Yoshida, T. *Electrochimica Acta* **2011**, 56, 1023.

[25] Ota, H.; Sato, T.; Suzuki, H.; Usami, T. *Journal of Power Sources* **2001**, 97, 107.

[26] Lu, P.; Li, C.; Schneider, E. W.; Harris, S. J. *The Journal of Physical Chemistry C* **2014**, 118, 896.

[27] Verma, P.; Maire, P.; Novák, P. *Electrochimica Acta* **2010**, 55, 6332.

[28] Hood, Z. D., Wang, H., Samuthira Pandian, A., Keum, J. K., & Liang, C. *Journal of the American Chemical Society* **2016** 138(6), 1768-1771.

CHAPTER 6

AN AIR-STABLE, WATER-PROCESSABLE SODIUM THIOPHOSPHATE SOLID ELECTROLYTE

6.1 Introduction

Solid electrolytes based on sodium (Na), phosphorus (P), and sulfur (S) have attracted considerable interest for their high ionic conductivity, earth-abundance, increased safety, and promise to enable high-capacity anodes for next-generation energy-storage systems, especially in applications where energy density is critical [1-3]. Exploration of the Na-P-S system has introduced a number of novel solid electrolytes, including cubic/tetragonal-Na_3PS_4 [4, 5], Na_2S-P_2S_5 glass-ceramics [6, 7], and doped Na_3PS_4 [8-11], amongst others [12], yet one of the key concerns of this system of electrolytes is their relative low air and water stability, complicating the processing and handling of the materials. To this end, a number of approaches have been applied to increase the water and air stability of sulfide-based electrolytes with the most successful centered on hard and soft acids and bases (HSAB) theory [13]. According to HSAB theory, the hard acid of P^{5+} is generally replaced with a softer element such as S^{2-} with a larger atomic radius such that a stronger interaction is achieved. Though substituting P^{5+} with aliovalent and softer elements has led to the identification of solid electrolytes with enhanced ionic conductivity and air stability [13-16], larger aliovalent elements can result in relatively large solid-electrolyte interphase (SEI) layers at the solid electrolyte/Na interface as a result of a multitude of redox or decomposition processes [13, 17]. Furthermore, many of these previously reported sulfide-based sodium solid electrolytes necessitate rather stringent

synthetic conditions, including intense ball milling and solid-state reactions at elevated temperatures (>300 °C) in evacuated Pyrex or Quartz ampules [4, 6, 7, 11, 18]. These conventional solid-state synthetic procedures have served well in the identification of new phases and the synthesis of novel materials, but limited breakthroughs for achieving intimate contact amongst the battery components and the formation of thin films from top-down approaches are expected for large-scale processing of solid-state electrolytes that utilize such synthetic procedures.

The Na-P-S system contains multiple important, and often overlooked, compounds that are structurally and chemically intriguing for battery-related applications. Materials based on the hexathiohypodiphosphate ($P_2S_6^{4-}$) have been previously investigated since this anion forms complexes with a number of alkali, transition, and post-transition metal ions that hold unique optical, magnetic, structural, and electrochemical properties.[4,19-24] In particular, the structure of several alkali-metal hexathiohypodiphosphates $M_4P_2S_6$ (M = Li, Na, and K) have be experimentally identified in previous literature [19-22, 24]. Although the structural and electrolyte properties of crystalline $Li_4P_2S_6$ were reported [19-21], previous investigations detailing the sodium analog ($Na_4P_2S_6$) were largely limited to crystallographic and theoretical studies [22, 25, 26]. While the pursuit of enhanced electrolyte properties through innovative chemical structures remains a force for advanced ion-conductors, the Na-P-S system of electrolytes is revisited and it is demonstrated that applying soft chemistry methodology to synthesize sodium hexathiohypodiphosphate offers an effective approach to the production of an air- and water-stable solid electrolyte. To the best of my knowledge, this work represents the first report of the electrolyte

properties of an air- and water-stable nanostructured sodium thiophosphate material purely within the Na-P-S system.

6.2 Results and Discussion

6.2.1 Decomposition of $Na_4P_2S_6 \cdot 6H_2O$ forms nanostructured $Na_4P_2S_6$

The creation of $Na_4P_2S_6$ is quite unique among the hexathiohypodiphosphate materials. In many cases, hexathiohypodiphosphates necessitate solid-state syntheses at increased temperatures (generally between 350 and 950 °C) and synthesis times between 1 day and 3 months [19, 22, 27-30]. In the case of $Na_4P_2S_6$, the phase is acheived at significantly lower temperatures and in solution. The synthesis of $Na_4P_2S_6$ relies on the formation of high-quality $Na_4P_2S_6 \cdot 6H_2O$ from $Na_2S \cdot 9H_2O$ and PCl_3 in D.I. H_2O, similar to that first reported by Falius in 1968 [23]. In short, $Na_2S \cdot 9H_2O$ (83.70 mmol) is stirred in water for 48 hours under ambient conditions. Next, PCl_3 (20.85 mmol) is slowly added dropwise to the stirred solution that is chilled by an ice bath. After stirring for an additional 2 hours, white $Na_4P_2S_6 \cdot 6H_2O$ is collected and washed with 20 mL of chilled (2 °C) D.I. H_2O. Crystallized H_2O is removed from $Na_4P_2S_6 \cdot 6H_2O$ by heating the white powder under vacuum on a Schlenk line for 1 hour. Thermogravimetric analysis (TGA) was utilized to monitor the dehydration process of $Na_4P_2S_6 \cdot 6H_2O$. The TGA curve in Figure 6.1A shows one main step between 40 and 80 °C, corresponding to a 23.6 wt.% loss, which is very close to the theoretical weight loss of H_2O from $Na_4P_2S_6 \cdot 6H_2O$ [25]. The as-synthesized $Na_4P_2S_6$ powder becomes nanocrystalline after H_2O removal, as displayed by *in situ* XRD patterns at increased temperatures (25-200 °C) shown in Figure 6.1B. $Na_4P_2S_6 \cdot 6H_2O$ displays strong diffraction peaks at $2\theta \approx 15.4°$ and 30.8°, indicating that the complex

contains co-crystallized water molecules. After heating $Na_4P_2S_6 \cdot 6H_2O$ to ≥ 80 °C, the material decomposes to $Na_4P_2S_6$ (Figure 6.2). The XRD pattern for nanostructured $Na_4P_2S_6$ is close to the monoclinic structure as reported by Kuhn and coworkers (space group: *C2/m*, *a* = 6.611(3) Å, *b* = 11.348(5) Å, *c* = 7.548(3) Å, *alpha* = 90°, *beta* = 106.43(4), *gamma* = 90°, volume = 543.12 $Å^3$) [22].

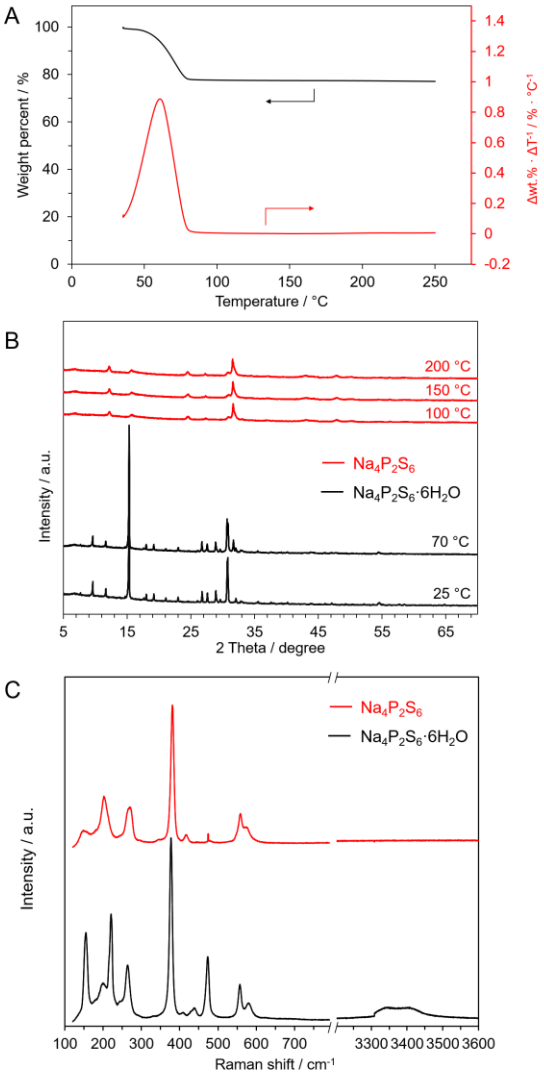

Figure 6.1 A) Thermogravimetric analysis of $Na_4P_2S_6 \cdot 6H_2O$, showing removal of water below 100 °C. B) XRD patterns with *in situ* heating and C) Raman spectra of $Na_4P_2S_6$ and $Na_4P_2S_6 \cdot 6H_2O$.

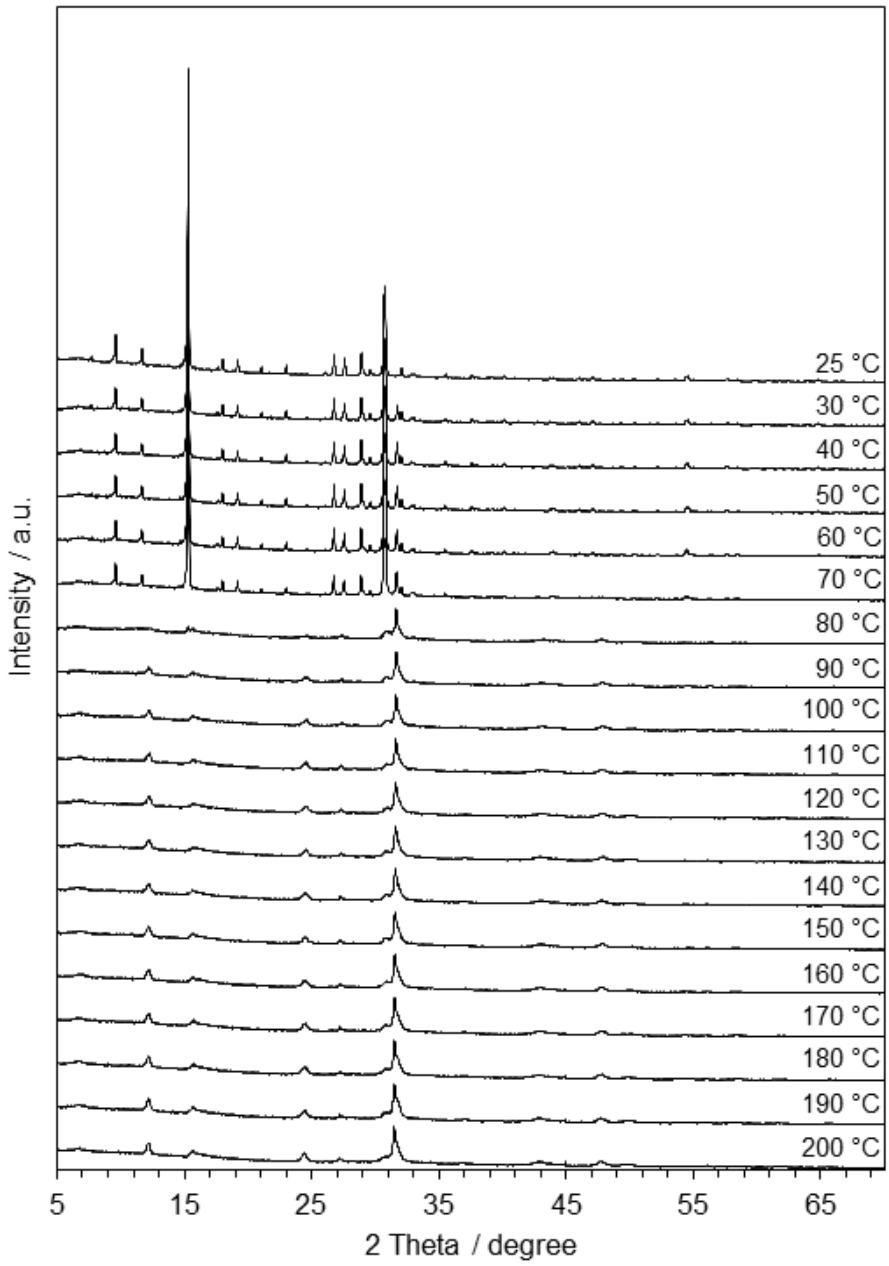

Figure 6.2 XRD patterns from *in situ* XRD heating experiments from 25 to 200 °C.

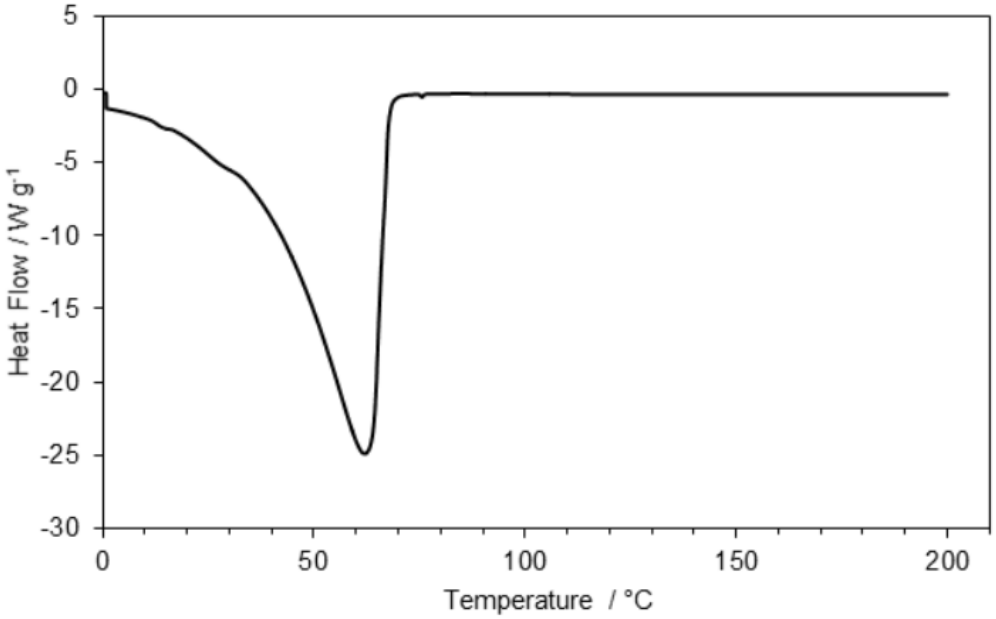

Figure 6.3 Differential scanning calorimetery of $Na_4P_2S_6 \cdot 6H_2O$, highlighting the removal of co-crystalized H_2O from $Na_4P_2S_6$.

The Raman spectrum of $Na_4P_2S_6 \cdot 6H_2O$ in Figure 6.1C show the characteristic stretching modes at 156, 172, 202, 266, 377, 556, and 577 cm^{-1} for the $P_2S_6^{4-}$ anion that adopts the D_{3d} symmetry, corresponding to the lattice vibrations ν_9/E_g, $A_g + B_g$ in C_{2h}, ν_3/A_{1g}, ν_8/Eg, ν_2/A_{1g}, ν_1/A_{1g}, and ν_7/E_g, respectively [31-33]. Additionally, the Raman spectrum for $Na_4P_2S_6 \cdot 6H_2O$ has a broad hump at 3300 – 3500 cm^{-1} signifying that the material contains co-crystallized H_2O. After decomposing $Na_4P_2S_6 \cdot 6H_2O$ to $Na_4P_2S_6$ on a Schlenk line at 175 °C, no stretches were found at 3300 – 3500 cm^{-1} suggesting that all H_2O was removed from the sample. The main vibrational modes were found to be centered at 152, 203, 273, 383, 560, and 577 cm^{-1} for as-prepared $Na_4P_2S_6$.

The removal of H_2O under high vacuum on a Schlenk line causes a subtle yet important nanostructure in $Na_4P_2S_6$. The micrograph in Figure 6.4A displays particles of

$Na_4P_2S_6 \cdot 6H_2O$ that exhibit prismatic-shaped particles ranging in size from 5 to 30 µm in length and 1 to 10 µm in width. The as-synthesized $Na_4P_2S_6 \cdot 6H_2O$ powder has a Brunauer-Emmett-Teller (BET) [34] surface area of less than 1.5 $m^2\ g^{-1}$ (Figure 6.4C). Heating at 175 °C results in a 24 % weight loss due to the removal of H_2O, and the particles were found to generally break into small units ranging from 250 nm to 15 µm in one dimension. The inset in Figure 6.4C reveals that the $Na_4P_2S_6$ particles have a porous structure. To this end, the as-prepared $Na_4P_2S_6$ (at 175 °C) was found to exhibit significant nitrogen adsorption at relative pressures above 0.9, as shown in the isotherm in Figure 6.4C. The BET surface area of $Na_4P_2S_6$ was determined to be 5.3 $m^2\ g^{-1}$, together with an average pore size between 8 and 40 nm. When the nanoporous structure is introduced to $Na_4P_2S_6$, the overall surface energy is significantly increased, potentially inducing lattice distortion; this distortion can, in turn, affect the overall electrochemical properties of material. This phenomenon is akin to other nanostructured solid electrolytes, such as nanostructured β-Li_3PS_4 [35] and α-AgI [36, 37].

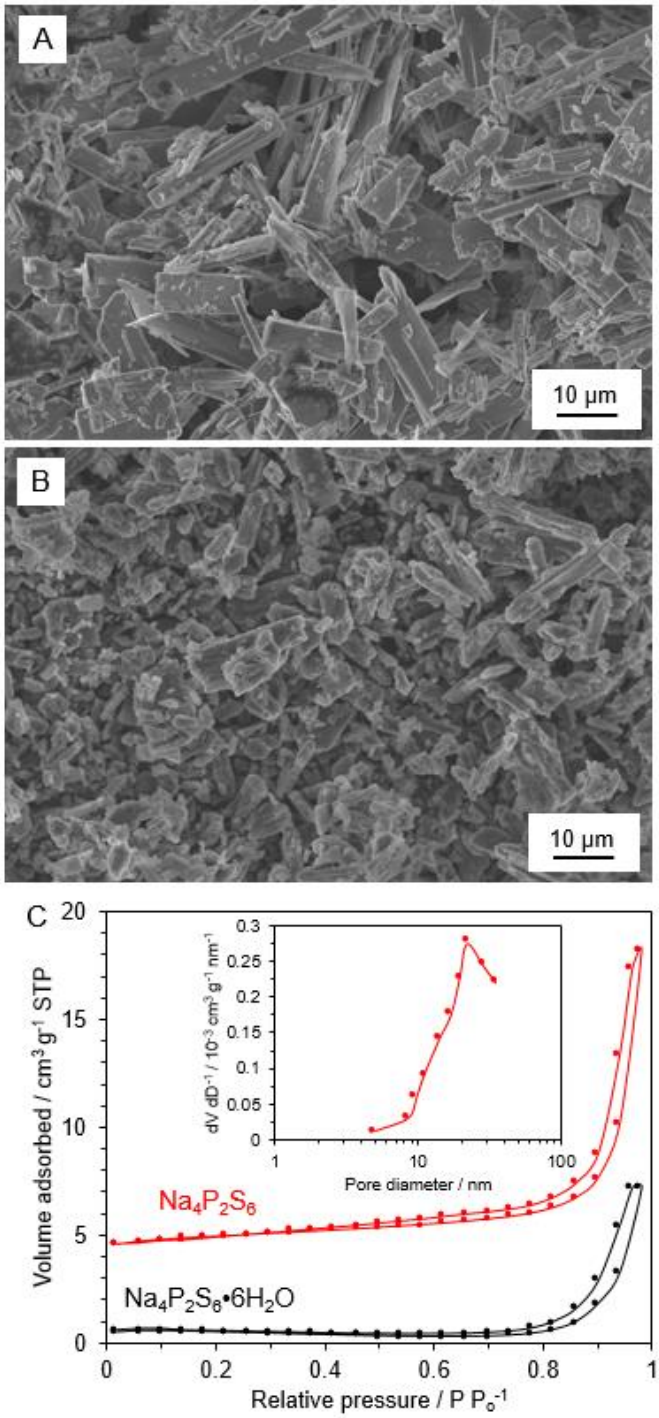

Figure 6.4 Characterization of $Na_4P_2S_6$ grains. SEM images displaying the morphology of A) $Na_4P_2S_6 \cdot 6H_2O$ and B) $Na_4P_2S_6$. C) N_2 adsorption-desorption isotherms at 77 K, and inset shows the pore size distribution of $Na_4P_2S_6$ after heat treatment at 175 °C.

High-resolution transmission electron microscopy (HR-TEM) and energy-dispersive x-ray spectroscopy (EDS) allow for direct interrogation of the structure and composition of $Na_4P_2S_6$. Figure 6.5A displays the typical morphology of a representative particle of $Na_4P_2S_6$ dispersed on lacey carbon and exposed to ambient conditions for ~3 min. Generally, sulfide-based solid electrolytes suffer from instability when exposed to the electron beam [38]. By carefully controlling the beam irradiation and exposure, the structure of $Na_4P_2S_6$ could be interrogated at the atomic scale, which is amongst the first sulfide-based solid electrolytes that could be characterized with such spatial resolution. A typical HR-TEM of $Na_4P_2S_6$ is presented in Figure 6.5B, illustrating the presence of multiple nanosized crystallites in the sample. A majority of the crystallites displayed a d-spacing of 0.280 nm corresponding to the (20-1 observed XRD diffraction peak at $2\theta \approx 31.7°$ that the as-synthesized $Na_4P_2S_6$ has an monoclinic crystal structure similar to that as reported by Kuhn *et al*. [22] and Rush *et al*. [26]. Energy-dispersive x-ray spectroscopy (EDS) analysis allowed for further interrogation of the composition of $Na_4P_2S_6$ (Figure 6.5C). Elemental mapping shows that particles of $Na_4P_2S_6$ contain an even dispersion of Na, P, and S, together with an average P:S ratio of 1 : 2.97.

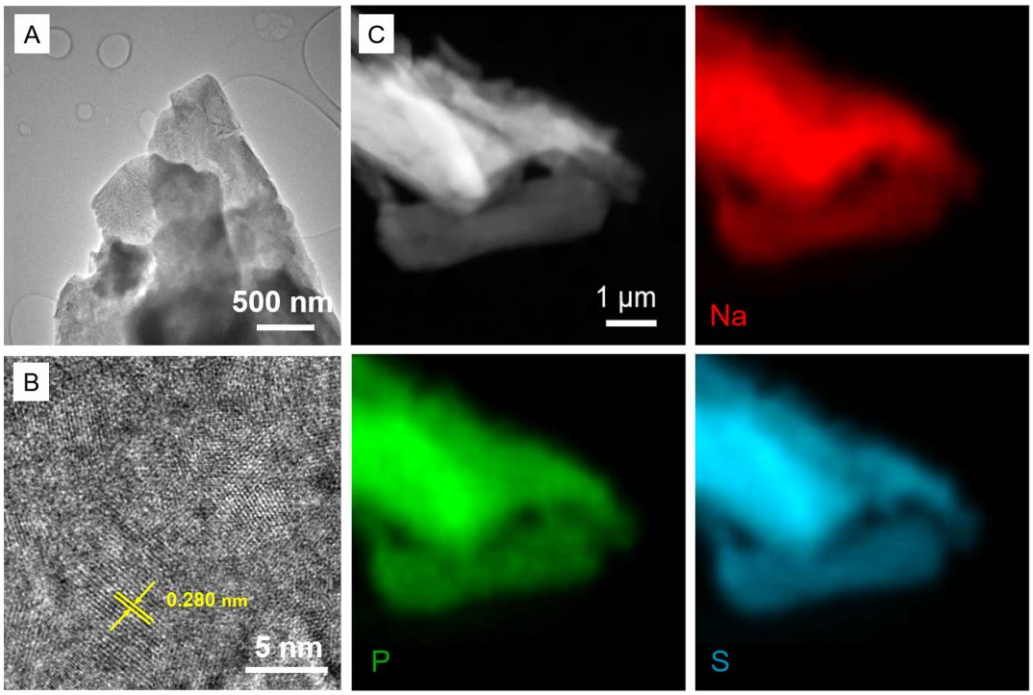

Figure 6.5 A,B) High-resolution transmission electron microscopy at different magnifications of $Na_4P_2S_6$. C) HAADF-STEM image and EDS elemental mappings of $Na_4P_2S_6$.

6.2.2 Surface conduction enhances the overall ionic conductivity of nanostructured $Na_4P_2S_6$

The bulk ionic conductivity of cold-pressed $Na_4P_2S_6$ was measured to be 3.4×10^{-6} S cm^{-1} at 25 °C using electrochemical impedance spectroscopy (EIS) and Al/C blocking electrodes in a specialized pressurized electrochemical cell that was developed by our group [39]. The calculated activation energy displays an Arrhenius behavior between 20 and 175 °C according to the following relationship (Equation 1):

$$\sigma = \sigma_o \cdot e^{\frac{-E_a}{kT}} \qquad (1)$$

where σ_o denotes the temperature independent ionic conductivity, k represents the Boltzmann constant, and E_a denotes the activation energy. The Arrhenius activation energy of $Na_4P_2S_6$ and was determined to be 0.35 eV (Figure 6.6A), which is lower than previously reported cold-pressed cubic/tetragonal-Na_3PS_4 and Na_2S-P_2S_5 glasses [4, 6, 7]. To unravel the dependence of ionic conductivity and sample preparation temperature, a series of samples were prepared at different processing temperatures for the dehydration step under vacuum, ranging from 75 - 225 °C (Figure 6.6B). Nanostructured $Na_4P_2S_6$ reaches an optimized ionic conductivity at a processing temperature of 175 °C. At temperatures past 175 °C, some S in $Na_4P_2S_6$ is expected to be lost to the volatility of this element, which leads to a decreased overall ionic conductivity. It is expected that the ionic conductivity can be further increased by the addition of NaX (X = Cl, Br, I) or iso-/aliovalent doping/substitution for the solution-processed $Na_4P_2S_6$ solid electrolyte.

Water removal is critical to the achievement of enhanced ionic conductivity in nanostructured $Na_4P_2S_6$. Interestingly, co-crystalized H_2O was found to reversibly exchange with $Na_4P_2S_6$, and similar ionic conductivities were achieved after nanostructured $Na_4P_2S_6$ is rehydrated and dehydrated at 175 °C. Figure 6.6C presents XRD patterns of as-prepared $Na_4P_2S_6{\cdot}6H_2O$ and dehydrated $Na_4P_2S_6$ (at 175 °C). When $Na_4P_2S_6$ is placed in air with a relative humidity of 30%, the material starts to absorb water, leading to a change in its crystal structure. After exposing $Na_4P_2S_6$ to air with a relative humidity of 30% for 4 weeks, the material completely reverts back to $Na_4P_2S_6{\cdot}6H_2O$. Dehydrating this material at 175 °C leads to nanostructured $Na_4P_2S_6$ with a similar ionic conductivity and Arrhenius activation energy as the $Na_4P_2S_6$ from the first dehydration (Figure 6.6D),

indicating that the ionic conductivity is maintained even after $Na_4P_2S_6$ is exposed to humid air and subsequently dehydrated.

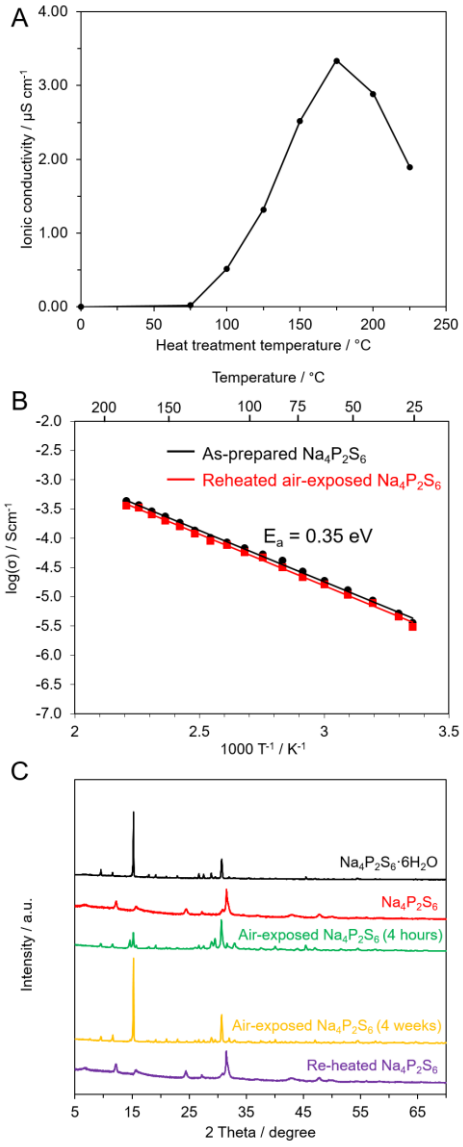

Figure 6.6 A) Correlation of room-temperature ionic conductivity to the processing temperature for samples of $Na_4P_2S_6$ treated at temperatures ranging 75 to 225 °C, B) Arrhenius plots of $Na_4P_2S_6$ after heat treatment at 175 °C and reheated (at 175 °C) air-exposed $Na_4P_2S_6$. C) XRD patterns of $Na_4P_2S_6{\cdot}6H_2O$, $Na_4P_2S_6$, and air-exposed $Na_4P_2S_6$.

6.2.3 Nanostructure allows for straightforward fabrication of dense membranes of $Na_4P_2S_6$ and does not compromise the electrochemical compatibility with a metallic Na anode

The soft nature of the sulfide-based $Na_4P_2S_6$ and the nanostructure allow for the fabrication of dense films from straightforward cold pressing at 320 MPa for 5 minutes. These membranes achieved relative densities greater than 92% of the calculated theoretical density (2.15 g cm^{-3} as derived from the monoclinic structure as proposed by Kuhn and coworkers). SEM images of the surface (Fig. 6.7A,B) and the cross section (Fig. 6.7C,D) of a typical pellet of $Na_4P_2S_6$ display that dense membranes can be achieved by facile cold pressing procedures. In comparison, many oxide-based solid-state ion conductors necessitate temperatures well above 1000 °C (and high pressure in some cases) for densification [40-42], but here, high temperature is not necessarily needed to achieve dense membranes. Such a low processing temperature enables the possibility of stable and unreactive polymeric additives to form flexible and dense membranes for industrial scale processing of next-generation solid-state sodium ion conductors.

Symmetric Na/$Na_4P_2S_6$/Na cells were constructed to demonstrate the compatibility of nanostructured $Na_4P_2S_6$ with a metallic Na anode. The interfacial stability of solid electrolytes with such electrodes is of utmost importance, as any undesired reactions could potentially lead to thick interphases that increase the charge-transfer resistance at the interface [13, 43-46]. Figure 6.7E shows the voltage profile of cells cycled at room temperature (~23 °C) at a current density of 10, 20, and 50 μA cm^{-2}. The direct current (dc) ionic conductivity was determined to be 2.4×10^{-6} S cm^{-1} at 23 °C, which is close to the

room temperature ionic conductivity of nanostructured $Na_4P_2S_6$, suggesting that the material preserves a conductive interphase at the $Na_4P_2S_6$/Na interface. With increased cycling, the interfacial resistance does not appear to significantly increase with time, suggesting that $Na_4P_2S_6$ is compatible with a metallic Na anode.

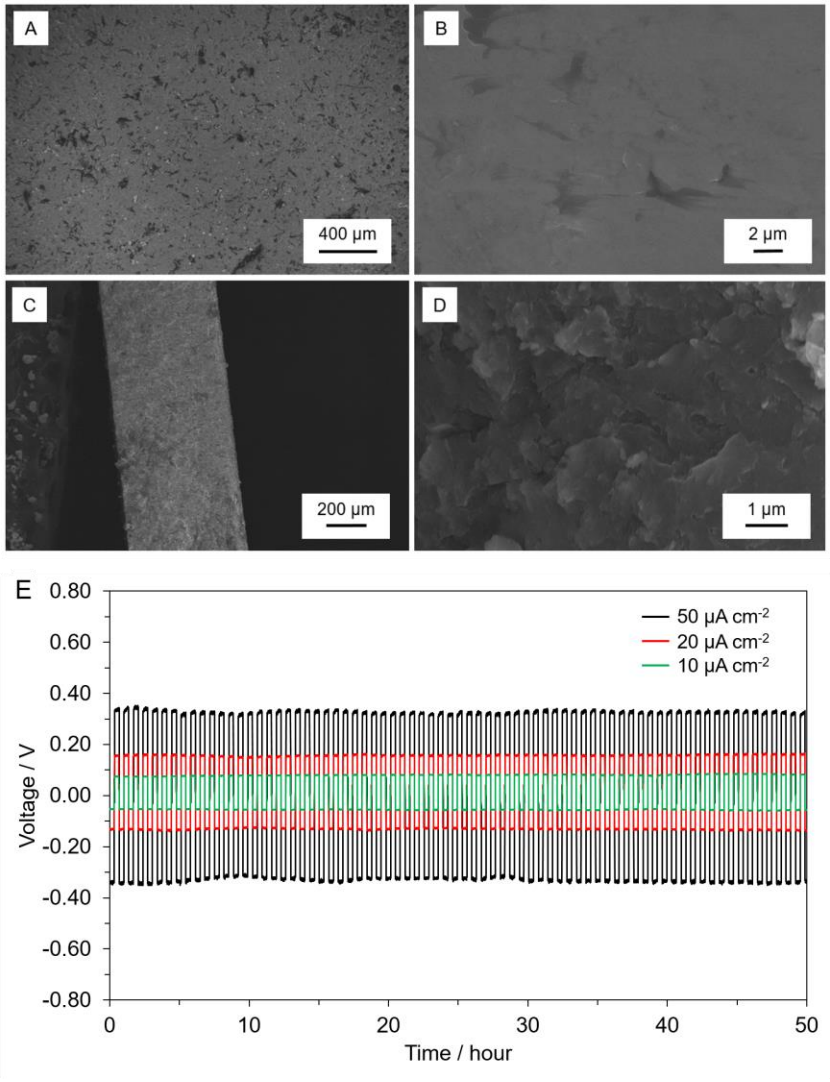

Figure 6.7 SEM images of the A,B) surface and C,D) cross section of a cold-pressed $Na_4P_2S_6$ pellet. E) Metallic sodium cyclability in a symmetric cell configuration (Na/$Na_4P_2S_6$/Na) with a current density of 10, 20, and 50 µA cm^{-2} at room temperature, demonstrating compatibility between the metallic sodium anode and sulfide-based solid electrolyte.

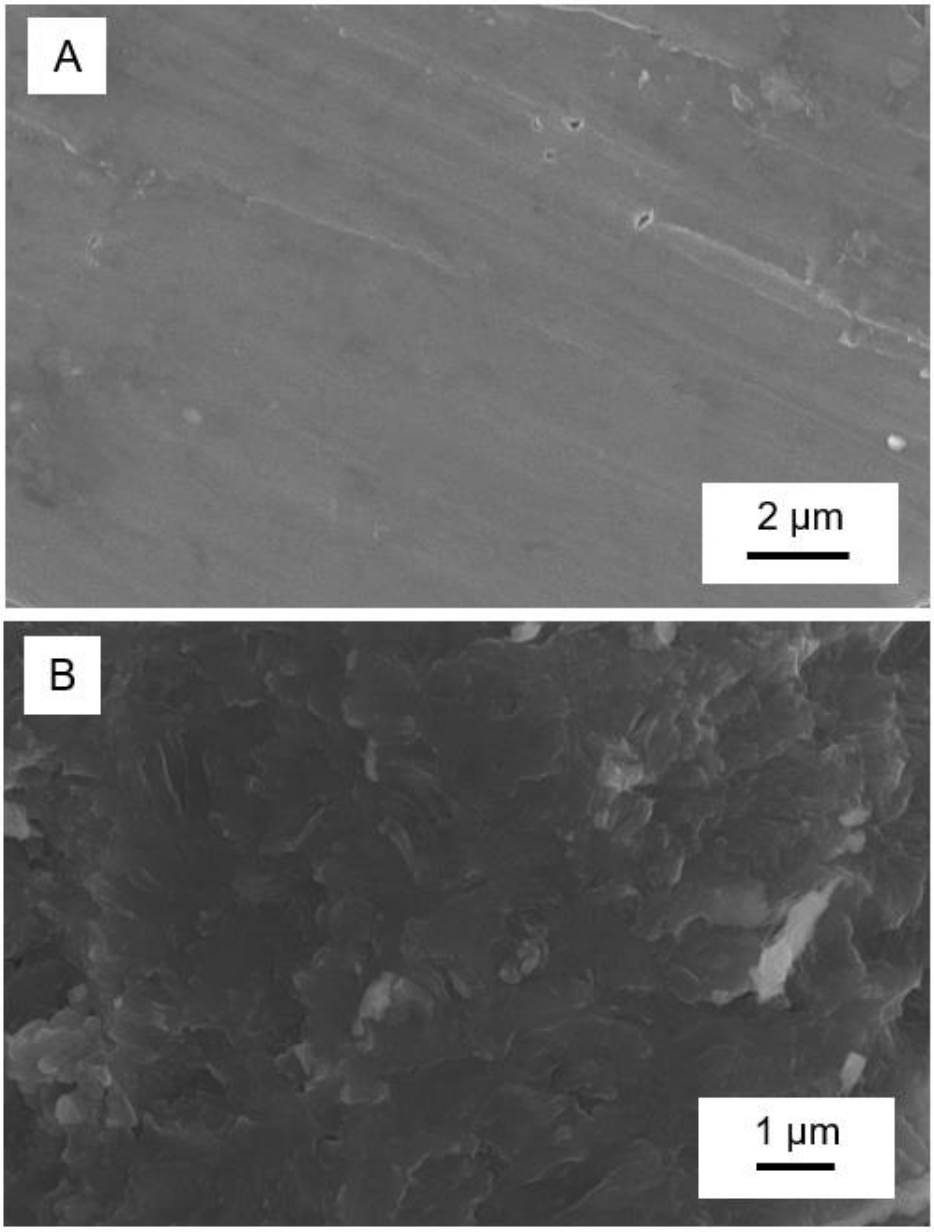

Figure 6.8 SEM images of the A) surface and B) cross section of a cold-pressed $Na_4P_2S_6$ pellet.

6.3 Summary

In summary, sulfide-based Na-ion-conducting solid electrolytes hold promise to improve battery chemistries on the basis of energy density, safety, and cost. It is shown that $Na_4P_2S_6$ offers a number of advantages over previously explored solid-state ion conductors, namely the ability to synthesize the material through a facile water-based synthetic approach and subsequent dehydration at relatively low temperatures. Additionally, rehydrating and subsequent dehydration does not lead to significant degradation of the electrochemical performance of nanostructured $Na_4P_2S_6$; this property is expected to be of utmost importance for solution processing of next-generation solid electrolyte membranes and composite cathodes. It is also demonstrated that nanocrystalline $Na_4P_2S_6$ holds compatibility with high-capacity metallic Na anode. This work not only shows $Na_4P_2S_6$ as a promising solid electrolyte, but also points out a strategy to utilize facile solution-based processing of solid-state sodium ion conductors.

6.4 Experimental Methods

Chemicals and materials: $Na_2S{\cdot}9H_2O$ (≥ 99.99 %, trace metals basis) PCl_3 (99%), and sodium cubes (99.9%) were purchased from Sigma Aldrich and were used as received. Carbon-coated aluminum foils (Al/C) were purchased from Exopack. Deionized (DI) water with a resistivity of 18.2 MΩ·cm was used for all aqueous-based syntheses. Ultrahigh purity Argon (99.999%) was purchased from AirLiquide.

Synthesis of $Na_4P_2S_6{\cdot}6H_2O$: In a typical synthesis, 20.10 g $Na_2S{\cdot}9H_2O$ (83.70 mmol) was dissolved in 25 mL of D.I. H_2O and stirred for 48 hours under ambient conditions in an Erlenmeyer flask. Next, 1.82 mL PCl_3 (20.85 mmol) was added dropwise to the solution

over approx. 30 minutes (Caution: PCl_3 reacts vigorously with H_2O to form HCl_g, so it is important to add PCl_3 slowly to the mixture). After all PCl_3 was added, the reaction was stirred for an additional 2 hours by placing the Erlenmeyer flask in an ice bath (~ 0 °C). The white precipitate was collected by vacuum filtration using a Whatman® Anodisc inorganic filter membrane (pore size 0.02 µm) and the precipitate ($Na_4P_2S_6 \cdot 6H_2O$) was washed with 5 mL of chilled D.I. H_2O (2 °C).

Synthesis of $Na_4P_2S_6$: In a typical synthesis $Na_4P_2S_6 \cdot 6H_2O$ was loaded into a glass Schlenk line vessel and heated under vacuum to 175 °C (ramp rate 5 °C min^{-1}) for 1 hour to remove water from the complex. A heat treatment temperature of 75, 100, 125, 150, 175, 200, or 225 °C (ramp rate 5 °C min^{-1}) were also used for 1 hour to investigate the electrolyte properties of $Na_4P_2S_6$.

Characterization of materials: Identification of the crystalline phase for Na_3SbS_4 was conducted on a PANalytical X'pert Pro Powder Diffractometer with Cu Kα radiation (λ = 1.54056 Å). All samples were prepared in a glovebox and the quartz slides were sealed with Kapton® films. Scanning electron microscopy (SEM) images were collected on a field-emission scanning electron microscope (SEM, Zeiss Merlin) at an acceleration voltage of 10.0 kV equipped with a custom-designed stage for handling air-sensitive materials such as metallic sodium [47]. High-resolution transmission electron microscopy (HR-TEM) was performed on an aberration-corrected FEI Titan S 80-300 STEM/TEM microscope equipped with a Gatan OneView camera at an acceleration voltage of 300 kV. Scanning transmission electron microscopy (STEM) with energy-dispersive x-ray spectroscopy (EDS) elemental mappings were collected on a JEOL JEM 2200FS STEM/TEM microscope at an acceleration voltage of 200 kV equipped with a CEOS probe

corrector (Heidelberg, Germany) to provide nominal resolution of ~0.07 nm. A Bruker-AXS silicon drift detector (SDD) was used for all EDS elemental analysis.

Electrochemical characterization: $Na_4P_2S_6$ was cold-pressed at 300 MPa in an airtight cell designed by our group with Al/C blocking electrodes for all electrochemical impedance spectroscopy (EIS) measurements (Bio-Logic, VSP). EIS measurements were measured between 1 MHz – 1 mHz with an amplitude of 100.0 mV in a temperature-controlled chamber. For Arrhenius measurements, the temperature control chamber was ramped from 10 to 110 °C and allowed to equilibrate for 2 hours before EIS measurements were collected. The activation energy (E_a) was calculated through the Arrhenius relationship (Equation 1):

$$\sigma = \sigma_o \cdot e^{\frac{-E_a}{kT}} \qquad (1)$$

where σ_o denotes the temperature independent ionic conductivity of the film, *k* represents the Boltzmann constant, and E_a denotes the activation energy. Symmetric $Na/Na_4P_2S_6/Na$ cells were constructed by cold-pressing $Na_4P_2S_6$ at 300 MPa and carefully affixing two polished metallic sodium foils to each side of the pellet in a Swagelok® cell. The symmetric cells was cycled at a current density of 50, 100, or 150 μA cm^{-2} for >1000 cycles (30 minutes on each side) at room temperature.

6.5 Notes to Chapter 6

This chapter is based on a paper entitled "An Air-Stable, Water-Processable, Sodium Thiophosphate Solid Electrolyte" that is currently under review.

6.6 References

[1] Yabuuchi, N.; Kubota, K.; Dahbi, M.; Komaba, S. *Chemical Reviews* **2014**, *114*, 11636.

[2] Kundu, D.; Talaie, E.; Duffort, V.; Nazar, L. F. *Angewandte Chemie International Edition* **2015**, *54*, 3431.

[3] Kim, S. W.; Seo, D. H.; Ma, X.; Ceder, G.; Kang, K. *Advanced Energy Materials* **2012**, *2*, 710.

[4] Jansen, M.; Henseler, U. *Journal of Solid State Chemistry* **1992**, *99*, 110.

[5] Zhu, Z.; Chu, I.-H.; Deng, Z.; Ong, S. P. *Chemistry of Materials* **2015**, *27*, 8318.

[6] Hayashi, A.; Noi, K.; Tanibata, N.; Nagao, M.; Tatsumisago, M. *Journal of Power Sources* **2014**, *258*, 420.

[7] Tanibata, N.; Noi, K.; Hayashi, A.; Kitamura, N.; Idemoto, Y.; Tatsumisago, M. *ChemElectroChem* **2014**, *1*, 1130.

[8] Chu, I.-H.; Kompella, C. S.; Nguyen, H.; Zhu, Z.; Hy, S.; Deng, Z.; Meng, Y. S.; Ong, S. P. *Scientific Reports* **2016**, *6*, 33733.

[9] de Klerk, N. J.; Wagemaker, M. *Chemistry of Materials* **2016**, *28*, 3122.

[10] Krauskopf, T.; Pompe, C.; Kraft, M. A.; Zeier, W. G. *Chemistry of Materials* **2017**, *29*, 8859.

[11] Hibi, Y.; Tanibata, N.; Hayashi, A.; Tatsumisago, M. *Solid State Ionics* **2015**, *270*, 6.

[12] Dehnen, S.; Duchardt, M.; Roling, B.; Ruschewitz, U.; Adams, S. *Angewandte Chemie International Edition* **2017**.

[13] Wang, H.; Chen, Y.; Hood, Z. D.; Sahu, G.; Pandian, A. S.; Keum, J. K.; An, K.; Liang, C. *Angewandte Chemie International Edition* **2016**, *55*, 8551.

[14] Yu, Z.; Shang, S. L.; Seo, J. H.; Wang, D.; Luo, X.; Huang, Q.; Chen, S.; Lu, J.; Li, X.; Liu, Z. K. *Advanced Materials* **2017**, *29*.

[15] Zhang, L.; Zhang, D.; Yang, K.; Yan, X.; Wang, L.; Mi, J.; Xu, B.; Li, Y. *Advanced Science* **2016**, *3*.

[16] Banerjee, A.; Park, K. H.; Heo, J. W.; Nam, Y. J.; Moon, C. K.; Oh, S. M.; Hong, S. T.; Jung, Y. S. *Angewandte Chemie* **2016**, *128*, 9786.

[17] Rush, L. E.; Hood, Z. D.; Holzwarth, N. A. W. *Physical Review Materials* **2017**, *1*, 075405.

[18] Berbano, S. S.; Seo, I.; Bischoff, C. M.; Schuller, K. E.; Martin, S. W. *Journal of Non-Crystalline Solids* **2012**, *358*, 93.

[19] Hood, Z. D.; Kates, C.; Kirkham, M.; Adhikari, S.; Liang, C.; Holzwarth, N. *Solid State Ionics* **2016**, *284*, 61.

[20] Mercier, R.; Malugani, J.; Fahys, B.; Douglande, J.; Robert, G. *Journal of Solid State Chemistry* **1982**, *43*, 151.

[21] Dietrich, C.; Sadowski, M.; Sicolo, S.; Weber, D. A.; Sedlmaier, S. J.; Weldert, K. S.; Indris, S.; Albe, K.; Janek, J. r.; Zeier, W. G. *Chemistry of Materials* **2016**, *28*, 8764.

[22] Kuhn, A.; Eger, R.; Nuss, J.; Lotsch, B. V. *Zeitschrift für anorganische und allgemeine Chemie* **2014**, *640*, 689.

[23] Falius, H. *Zeitschrift für anorganische und allgemeine Chemie* **1968**, *356*, 189.

[24] Schäfer, H.; Schäfer, G.; Weiss, A. *Zeitschrift für Naturforschung B* **1965**, *20*, 811.

[25] Fincher, T.; LeBret, G.; Cleary, D. *Journal of Solid State Chemistry* **1998**, *141*, 274.

[26] Rush, L. E.; Holzwarth, N. *Solid State Ionics* **2016**, *286*, 45.

[27] Svirskaya, S.; Lupeiko, T.; Pakhomov, A.; Medvedeva, E. *Russian Journal of Applied Chemistry* **2011**, *84*, 762.

[28] Clement, R.; Garnier, O.; Jegoudez, J. *Inorganic Chemistry* **1986**, *25*, 1404.

[29] Sourisseau, C.; Forgerit, J.; Mathey, Y. *Journal of Solid State Chemistry* **1983**, *49*, 134.

[30] Kliche, G. *Journal of Solid State Chemistry* **1984**, *51*, 118.

[31] Bischoff, C.; Schuller, K.; Haynes, M.; Martin, S. W. *Journal of Non-Crystalline Solids* **2012**, *358*, 3216.

[32] Menzel, F.; Ohse, L.; Brockner, W. *Heteroatom Chemistry* **1990**, *1*, 357.

[33] Menzel, F.; Brockner, W.; Ystenes, M. *Journal of molecular structure* **1993**, *294*, 53.

[34] Brunauer, S.; Emmett, P. H.; Teller, E. *Journal of the American chemical society* **1938**, *60*, 309.

[35] Liu, Z.; Fu, W.; Payzant, E. A.; Yu, X.; Wu, Z.; Dudney, N. J.; Kiggans, J.; Hong, K.; Rondinone, A. J.; Liang, C. *Journal of the American Chemical Society* **2013**, *135*, 975.

[36] Guo, Y. G.; Lee, J. S.; Maier, J. *Advanced Materials* **2005**, *17*, 2815.

[37] Liang, C.; Terabe, K.; Tsuruoka, T.; Osada, M.; Hasegawa, T.; Aono, M. *Advanced Functional Materials* **2007**, *17*, 1466.

[38] Ma, C.; Chi, M. *Frontiers in Energy Research* **2016**, *4*, 23.

[39] Wang, H.; Ma, C.; Chi, M.; Liang, C. *Advanced Materials Interfaces* **2015**, *2*.

[40] Murugan, R.; Thangadurai, V.; Weppner, W. *Angewandte Chemie International Edition* **2007**, *46*, 7778.

[41] Rangasamy, E.; Wolfenstine, J.; Sakamoto, J. *Solid State Ionics* **2012**, *206*, 28.

[42] Ma, C.; Cheng, Y.; Chen, K.; Li, J.; Sumpter, B. G.; Nan, C. W.; More, K. L.; Dudney, N. J.; Chi, M. *Advanced Energy Materials* **2016**, *6*.

[43] Wenzel, S.; Leichtweiss, T.; Weber, D. A.; Sann, J.; Zeier, W. G.; Janek, J. r. *ACS Applied Materials & Interfaces* **2016**, *8*, 28216.

[44] Hood, Z. D.; Wang, H.; Samuthira Pandian, A.; Keum, J. K.; Liang, C. *Journal of the American Chemical Society* **2016**, *138*, 1768.

[45] Rush Jr, L. E.; Hood, Z. D.; Holzwarth, N. *Physical Review Materials* **2017**, *1*, 075405.

[46] Tian, Y.; Shi, T.; Richards, W. D.; Li, J.; Kim, J. C.; Bo, S.-H.; Ceder, G. *Energy & Environmental Science* **2017**, *10*, 1150.

[47] Howe, J. Y.; Boatner, L. A.; Kolopus, J. A.; Walker, L. R.; Liang, C.; Dudney, N. J.; Schaich, C. R. *Journal of Materials Science* **2012**, *47*, 1572.

CHAPTER 7

CONCLUSIONS AND FUTURE DIRECTIONS

7.1 Conclusions

The past few years have witnessed tremendous progress in the development of highly conductive SEs and techniques for understanding their interfaces [1-5]. Thanks to the efforts of many research groups, SEs have found uses in next-generation battery systems. It is clear that various experimental and characterization techniques have all allowed researchers to introduce new superionic conductors and better understand their use as SEs. In addition to experimental studies, theoretical modeling has also progressed to provide a better understanding of different phenomena observed in ionic conductors, as well as an enhanced understanding of predictive synthesis of highly conductive SEs. These research activities have guided researchers in designing better ionic conductors, improving interfaces within batteries, and clarifying long-standing misconceptions of structure-property relationships within ionic conductors.

However, designing interfaces that are highly conductive and stable with electrodes is still very challenging. Although some strategies have been reported to enhance interfacial properties as discussed earlier, the root origin of these phenomena are currently unknown, and many of the explorations are still in a trial-and-error stage. The lack of a clear mechanistic understanding of the interfacial mass transport and charge transfer behavior is significantly hindering our ability to design and fabricate high-performance interfaces between electrodes and SE in a controlled manner. This lack in mechanistic understanding

is due to the complex nature of interfacial phenomenon, especially under electrochemical cycling, in which the interfaces are dynamic and move away from equilibrium states.

7.2 Future Directions

There is no doubt that the design of new, high-voltage, safer batteries will be realized if our understanding of SEs and their interfaces is improved. To achieve this understanding, several technical issues must be further explored to better understand the interfacial phenomena: (1) atomic-scale characterization techniques have to be spatially correlated in order to elucidate key descriptors of SEs, including charge, ions, structure, and chemistry, among others, (2) improvements are necessary to advance *in situ* and *in operando* TEM and XPS studies of electrode/SE interfaces, (3) theoretical modeling and simulations should provide insight as to the interfacial changes between the different interfaces associated with SEs and be compared with experiment, where possible, and (4) correlative technique developments, which can precisely correlate atomic-scale parameters with global performance in practical batteries, are important for the future developments of SE-based energy storage research. It must be emphasized that one technique cannot bridge the gap between our mechanistic understanding with the performance of SEs and their interfaces, but rather, theoretical and experimental approaches should be highly corroborated to develop clear descriptors for interfacial phenomena for SEs (*e.g.* at the SE/electrode interface and grain boundaries of SEs).

It is expected that further advancements in solid-state ionic conductors and their interfaces will allow for exciting, new energy-storage technologies that can transform modern-day life. Traditionally, the study of SEs has been dominated by electrochemists

and solid-state physicists. As evidenced in recent years, researchers from various backgrounds have pushed our understanding of SEs and introduced multiple promising materials for electrochemical energy systems. Bridging theoretical modeling with both *ex situ* and *in situ* experimental studies will only improve our mechanistic understanding of ionic conductors, and with the involvement of the larger scientific and engineering communities, SEs will surely become some of the most important materials for next-generation commercial batteries.

7.3 References

[1] Dudney, N. J.; West, W. C.; Nanda, J. Handbook of Solid State Batteries; *World Scientific*, **2016**.

[2] Lin, Z.; Liang, C. Lithium–sulfur batteries: from liquid to solid cells. *Journal of Materials Chemistry A* **2015**, *3*, 936-958.

[3] Hagenmuller, P.; Van Gool, W. Solid Electrolytes: General Principles, Characterization, Materials, Applications; *Elsevier*, **2015**.

[4] Quartarone, E.; Mustarelli, P. Electrolytes for solid-state lithium rechargeable batteries: recent advances and perspectives. *Chemical Society Reviews* **2011**, *40*, 2525-2540.

[5] Bachman, J. C.; Muy, S.; Grimaud, A.; Chang, H.-H.; Pour, N.; Lux, S. F.; Paschos, O.; Maglia, F.; Lupart, S.; Lamp, P.;Giordano, L.; Shao-Horn, Y. Inorganic Solid-State Electrolytes for Lithium Batteries: Mechanisms and Properties Governing Ion Conduction. *Chemical Reviews* **2015**, *116*, 140-162.